ENHANCING SEISMIC RESILIENCY OF STEEL BUILDINGS THROUGH THREE-DIMENSIONAL MODELING OF DIAPHRAGM SYSTEM INTERACTION WITH BRACED FRAME

by

Hamid Foroughi

A dissertation submitted to Johns Hopkins University in conformity with the requirements for the degree of Doctor of Philosophy

Baltimore, Maryland

March 2021

Abstract

The design objectives of early seismic codes were mainly achieved by using acceptable construction materials, and minimum levels of strength and stiffness largely derived based on roughly estimated demands. Early seismic design provisions resulted in sometimes adequate levels of performance for buildings, efficient and reliable building performance was not accomplished with the simplistic demand-based design process adopted. Consequently, capacity-based design approaches and later performance-based design approaches have been adopted and developed for new seismic design provisions.

To achieve a certain performance level for conventional steel buildings during seismic events, all the members should be designed to meet the component deformation and force capacities. The lateral-force resisting system, key for developing successful seismic performance, has two main parts: 1) the Vertical Lateral-force resisting system (VLFRS) of which a common example in steel buildings is the braced frame, and 2) the Horizontal lateral-force resisting system (HLFRS) consisting of the floor and roof diaphragm. The floor diaphragm acts as a critical element that distributes the demands developed in a building during an extreme event to the vertical lateral-force resisting systems and eventually to the building foundation. Compared to the VLFRS, far less attention has been paid to the role of the diaphragm in seismic building response, particularly for steel framed buildings.

The first part of this dissertation contributes to developing fundamental understanding of steel deck diaphragms as structural systems integrated within the overall building performance and improved strategies for accurate modeling of floor systems within three-dimensional building models to enhance the overall structural resilience of a building. In this study, the effect of different diaphragm designs on the behavior of steel buildings is investigated using three-dimensional computational building models that consider nonlinear behavior in both the vertical and horizontal elements of the seismic force resisting system. Different diaphragm design scenarios based on *ASCE 7-16,* are investigated for a series of 1, 4, 8, and 12-story archetype buildings with special concentrically braced frames (SCBFs) as the vertical lateral force resisting system: 1) traditional design, 2) alternative design with $R_s = 1.0$, 3) alternative design with $R_s = 2.0$ or 2.5, and 4) alternative design with $R_s = 3.0$ are all considered. For the studied buildings first, modal analyses were conducted to study their basic dynamic properties. Second, nonlinear pushover analyses were investigated to analyze their static overstrength and ductility. Third, nonlinear response history analyses were conducted to evaluate building seismic performance. Finally, the *FEMA P-695* methodology is used to assess the seismic performance and propose a reasonable R_s values for conventional SCBF steel buildings.

The second part of this dissertation addresses rod bracing, which has a wide application in metal buildings as a truss diaphragm including the sidewalls to provide the lateral stiffness in longitudinal direction, and also the roof by providing the lateral bracing for the rafters in the out-of-plane direction. In this part of the dissertation, an experimental program is conducted to establish the stiffness, strength and applicable limit states for rod bracing. Twelve rod brace assemblages with differing details related to the geometry of the primary frame members, anchorage of the rod into the frame member, and angle of the rod relative to the framing member were tested in tension until failure. Finally, a framework is presented for future evaluation of seismic performance for rod-braced metal buildings by implementing the experimentally established stiffness and strength values and three-dimensional computational modeling of metal building systems.

Advisor: Dr. Benjamin W. Schafer; **Readers:** Dr. James K Guest and Dr. Thomas Gernay

Acknowledgements

Up and Dowwwn, this is "The End" of an era for me. I am remembering first days of PhD, and the road I passed through the defense day. Of course, we are living in a world full of uncertainties. It's even more fun when you are doing a PhD started with something like Travel (Muslim) Ban, which trapped you in US for 4 years, and ends with a global pandemic! If I wanted to look at the bright side, of course, I am much stronger than before. It was definitely not possible without the support and love I received from many people here in US and specially my family who were patient with my PhD while they could not see me for many years. Thank you!

I owe a debt of gratitude to all those individuals who made this work possible. First and foremost, I would like to express my appreciation to my advisor Prof. Benjamin Schafer for his continuous support during my PhD study, for his patience, motivation, and immense knowledge.

I have worked and learned from so many brilliant people at JHU. Dr. Shahabeddin Torabian, for his kind support like my elder brother. Thank you, Shahab!

Prof. Rachel Sangree, for whom I was a teaching assistant for 4 courses. I learned a lot from you about all aspects of teaching and communicating with students. Additionally, I would like to state my appreciation for Assoc. Prof. Matthew R. Eatherton and Prof. Jerome F. Hajjar for providing me with their expertise and experience, and specifically helping us on the SDII project.

I would be remiss without mentioning the current and former Thin-walled Structures Lab members and friends—Dr. Abdullah Mahmud, Dr. Guanbo Bian, Dr. David Fartamico, Dr. Xi Zhao, Marzieh Bahreman, Astrid W. Fischer, Zhidong Zhang, Chu Ding, Victoria

Ding, Mohammed Elady, Dr. Aakash Bangalore Satish, Amartya Bhattacharjee, Farzin Ahmadi, Dr. Saeed Ashrafinia, Dr. Alireza mortezavi, Dr. Pegah Ghahremani, Dr. Hossein Hezaveh, Ali Ebrahimi, Fardin Ganjekhanloo and many others.

My special thanks to my best friends, Dr. Farshid Alambeigi and Dr. Fardad Haghpanah, who gave me a lot of support and helped me to never give up in difficult moments. I really appreciate the time you've taken out of your busy schedule to help me out. Thank you!

I also should thank the technician of the Thin-walled Structures Lab, Nick Logvinovsky for all his kind support during the metal building experimental test.

.

Contents

Abstract ii

Acknowledgements iv

Contents vi

List of Tables x

List of Figures xii

Chapter 1 1

Introduction to Seismic Resilient Design of Steel Structures 1

1.1. Overview on Seismic Design Provisions 1
  1.1.1. Resilience and the National Model Building Codes 1
  1.1.2. Advancing Resilience through Seismic Design Provisions 2
1.2. Research Objectives and Motivation 3
  1.2.1. Conventional Steel Buildings Seismic Design 3
  1.2.2. Metal Building Systems Design 8
1.3. Thesis outline 11

Chapter 2 15

Seismic Performance of Conventional Structural Steel Buildings 15

2.1. Introduction 15
2.2. Steel Braced Frame Design 16
  2.2.1. Ordinary Concentrically Steel Braced Frames (OCBF) 17
  2.2.2. Buckling Restrained Braced Frames (BRBF) 18
  2.2.3. Special Concentrically Steel Braced Frames (SCBF) 20
  2.2.4. Design Comparison for Different CBF Braces 23
2.3. Diaphragm, Chords and Collectors 24
  2.3.1. Diaphragm Flexibility Assumptions 25
  2.3.2. Diaphragm Design Procedure 27
2.4. FEMA P-695 Methodology for Building Seismic Performance 32
  2.4.1. Overview on FEMA P-695 Methodology 32
  2.4.2. Literature Review on Archetypes Evaluated by FEMA P-695 Methodology 36

2.5. Conclusion 40

Chapter 3 42

Three-Dimensional Modeling of SCBF Archetype Buildings 42

3.1. Introduction 42
3.2. Three-dimensional Computational Modeling 43
  3.2.1. Introduction 43
  3.2.2. Literature Review with Focus on Diaphragm Design 45
  3.2.3. Development of Computational models 48
  3.2.4. Gravity Loads, Masses, Materials, Geometric Nonlinearity and Boundary Condition Modeling 54
  3.2.5. Damping and System Convergence in Dynamic Analysis 55
  3.2.6. Special Concentrically Braced Frame (SCBF) Modeling 56
  3.2.7. Modeling of Diaphragm systems 59
3.3. Computational Modeling of BRBF Archetype 68
3.4. Conclusion 69

Chapter 4 70

Fundamental Response of SCBF Steel Archetypes 70

4.1. Introduction 70
4.2. Response Validation for Simulation 71
  4.2.1. Story Drift Ratio Calculation 71
  4.2.2. Diaphragm Shear Angle Calculation 72
4.3. Modal Analysis 73
  4.3.1. Estimated Natural Periods and Mode Shapes 73
4.4. Nonlinear Static Pushover Analysis 76
4.5. Conclusion 85

Chapter 5 87

Nonlinear Time History Response of SCBF Archetype Buildings 87

5.1. Introduction 87
5.2. Ground Motion Scaling 87
5.3. Collapse Criteria for SCBF Archetypes 93
5.4. Dynamic Response Analysis Examples and Discussions 96
  5.4.1. Four-story SCBF Building Response Subjected to One Ground Motion Pair 96
5.5. Statistical Results and Discussion 106
  5.5.1. Story Drift Analysis 106

5.5.2. Elastic Diaphragm Shear 112
5.5.3. Collapse Ratio Analysis Based on *FEMA* P695 114
5.6. Conclusion 129
Chapter 6 132
Lateral Performance of Metal Building Systems 132
6.1. Introduction 132
6.2. Metal building Systems 133
6.2.1. Seismic Design of Metal Building Systems 134
6.2.2. Moment Frame Response 135
6.2.3. Rod Bracing Response 137
6.3. Seismic Performance Evaluation for Metal Building Systems 139
6.3.1. Fundamental Response of Metal Building Systems 139
6.3.2. Nonlinear Response History Analysis 140
6.4. Conclusion 141
Chapter 7 142
Fundamental Response of Metal Building Rod Bracing 142
7.1. Introduction 142
7.2. Industry Survey of Rod Anchor Details in Metal Buildings 143
7.2.1. Rod and cable bracing – industry survey results 143
7.2.2. Hillside washer type and details – industry survey results 145
7.2.3. Primary frame web and flange dimensions and details – industry survey results 146
7.2.4. Rod brace anchor location and details in primary frame – industry survey results 149
7.3. Test specimens 150
7.4. Test setup, loading and instrumentation 152
7.5. Specimen measurements and material properties 154
7.6. Rod anchorage connection limit states 156
7.7. Overall load-deformation response 158
7.8. Localized response 163
7.9. Rod brace assemblage connection stiffness 165
7.10. Discussion and implications for design 167
7.11. Conclusion 170
Chapter 8 171
Preliminaries for Metal Building System Archetype Three-Dimensional Modeling with Rod Bracing 171

8.1. Introduction 171
8.2. Development of Computational Models for Metal Building Archetypes 172
8.3. Damping, Elements, Geometric Nonlinearity and Material Modeling 173
8.4. Rod Bracing Connection, Panel Zone, and Base Plate Modeling 175
8.5. Metal Building Roof System 176
8.6. Basic Ideas and Future Work 177
8.7. Conclusion 177

Chapter 9 178

Conclusion and Future work 178

9.1. Major Contribution 178
  9.1.1. SCBF Archetype Building Designed with Different Diaphragm Design Procedures 179
  9.1.2. Lateral Response of Metal Building 182
9.2. Future work 183
  9.2.1. Semi-Rigid Diaphragm System 183
  9.2.2. Metal Building System 184

References 185

Appendix 196

A1. Member Sizes of Archetype Buildings 196
A2. Modification of Pinching4 Backbone Parameters for Diaphragm Models 199
A3. Lognormal Cumulative Distribution Function (CDF) fitting 202
A4. Median of Peak Story Drifts and Diaphragm Shear Demands 204

List of Tables

Table 2-1. CBF brace design summary [40] 24

Table 2-2. Mode shape factor (z_s) for Alternative design approach 31

Table 3-1. List of SCBF Archetype Buildings for the Study 50

Table 3-2. Archetype Building Loading and Design Information 51

Table 3-3. Prototype Building Seismic Design Information 51

Table 3-4. Diaphragm Design Shear per Unit width at Diaphragm Edge along Short Dimension of Building.. 53

Table 3-5. Masses at Typical Node Locations 54

Table 3-6. Calibrated *Steel02* Material Parameters in *OpenSees* Software 58

Table 3-7. Calibrated Pinching4 Material Model Parameters 65

Table 3-8. Diaphragm Design Shear per Unit width at Diaphragm Edge along Short Dimension of Building.. 66

Table 3-9. Diaphragm Design specification for different diaphragm design 67

Table 4-1. Natural Periods of SCBF Archetype Models in *OpenSees* [56] and *SAP2000* [39] 74

Table 4-2. Overstrength and period-based ductility for archetype buildings 83

Table 5-1. Far-Field Ground Motions Used for Nonlinear Response History Analysis 88

Table 5-2. Ground Motion Scaling for all Buildings 93

Table 5-3. Base Shear of 4-story Archetype Building with Traditional / R_s = 2.0 or 2.5 diaphragm design under DE and MCE-level Ground Motions 103

Table 5-4. Medians of Diaphragm Shear Demand for four-story Archetype Buildings 113

Table 5-5. Collapse ratio for archetype with rigid and R_s = 1.0 diaphragm design procedure 115

Table 5-6. Triggered collapse ratio for archetype with rigid and R_s = 1.0 diaphragm design procedure 117

Table 5-7. Collapse ratio for all archetype with different diaphragm design procedure 121

Table 5-8. Triggered collapse ratio for all archetype with different 122

Table 5-9. Mean spectral acceleration corresponding to MCE and DE level 125

Table 5-10. Overstrength, period-based ductility and total system collapse uncertainty (β_{total}) 126

Table 5-11. Summary of evaluation of SCBF archetype buildings using *FEMA P695* methodology 127

Table 7-1. List of SCBF Archetype Buildings for the Study 144

Table 7-2. Industry survey results - cable brace material, diameter, and washer details 145

Table 7-3. Industry survey results - web dimensions and details for a metal building primary frame 147

Table 7-4. Industry survey results - flange dimensions and details for a metal building primary frame 148

Table 7-5. Industry survey results – anchor hole dimensions and details for a metal building primary frame .. 150

Table 7-6. Test matrix and nominal specimen dimensions 151

Table 7-7. Measured specimen dimensions 154

Table 7-8. Specimen steel yield stress, ultimate stress, and elongation 155

Table 7-9. Summary of tested response and observed limit states including flange local buckling and peak test load 159

Table 7-10. Rod brace anchor connection deformation and stiffness 166

Table 8-1. Metal Building Archetype Building Loading and Design Information 173

Table 8-2. Material designations for metal building archetype 175

List of Figures

Figure 1-1. Building Collapse During 1994 Northridge Earthquake: (a) Concrete Parking Garages; (b) Storage Building with Rigid Wall Flexible Diaphragm (RWFD). 5

Figure 1-2. Diaphragm interaction with whole lateral force resisting system [9]. 5

Figure 1-3. Application of concrete-filled steel deck diaphragm in steel building [11]. 6

Figure 1-4. SCBF application in three-story steel building in Palo Alto, CA [13]. 7

Figure 1-5. Typical Metal Building System [33]. 8

Figure 1-6. Metal Building Structural System. 9

Figure 1-7. Application of rod bracing in the roof of metal building systems [36] 11

Figure 2-1. Typical OCBF configurations. 17

Figure 2-2. (a) Typical BRB; (b) BRB axial force response [48]. 19

Figure 2-3. Gusset plate connection design: (a) Rectangular gusset plate; (b) Tapered gusset plate [44]. 23

Figure 2-4. Typical diaphragm: (a) Bare deck roof [52]; (b) Composite deck [51]. 25

Figure 2-5. Design procedure for the diaphragm. 28

Figure 2-6. Alternative design procedure for diaphragm 30

Figure 3-1. Design procedure for the diaphragm. 49

Figure 3-2. Typical Floor Framing Plan. 52

Figure 3-3. Typical Roof Framing Plan 52

Figure 3-4. Elevation view of four-story building braced frames. 53

Figure 3-5. Flow chart of the algorithm for convergence tests [49]. 56

Figure 3-6.Configuration of a typical SCBF and computational model. 57

Figure 3-7. Hysteretic response of CBF from experiment and simulation: *(a)* Fell *et al.* [78] Spec. HSS 1-1, *(b)* Popov and Black [77] Strut 17 58

Figure 3-8. Fracture strain limit for *MINMAX* material: *(a)* Fell *et al.* [78] Specimen HSS 1-1; *(b)* Popov and Black [77] Strut 17 59

Figure 3-9. Test setup and computational model of cantilever diaphragm test. 61

Figure 3-10. Diaphragm meshing in computational models of archetype buildings. 61

Figure 3-11. Pinching4 material model [56]. 63

Figure 3-12. Hysteretic response of diaphragm from experiment and simulation. 64

Figure 4-1. Mode shapes for the 1st mode of four-story archetype models: (a) *OpenSees* [56] model; (b) *SAP2000* [39] model. 75

Figure 4-2. Mode shapes of four-story archetype models. 75

Figure 4-3. Schematic load pattern direction: (a) Transverse direction pushover (Short direction); (b) Longitudinal direction pushover (Long direction). 77

Figure 4-4. Lateral force distribution on four-story archetype building for pushover analysis in transverse direction (Load distributed along the longer span). 77

Figure 4-5. Pushover curves in transverse direction with different diaphragm design procedures. 81

Figure 4-6. Pushover curves in longitudinal direction with different diaphragm design procedures. 82

Figure 4-7. Deformed shapes of archetype buildings with Trad diaphragm design procedures (deformation amplification factor: 10). 85

Figure 5-1. Spectral acceleration with 5% damping ratio for P695 far-field record suite: (a) Raw records; (b) Normalized records. 89

Figure 5-2. Example ground motion scaling for DE and MCE (4-story building) 90

Figure 5-3. Example time history of maximum story drift for analysis with convergence failure considered as building collapse (4-story Trad. / Rs= 2.0 or 2.5, Ground Motion Set 21)[49] 95

Figure 5-4. Example time history of maximum story drift for analysis with convergence failure excluded from collapse ratio calculation (8-story Trad. / Rs= 2.0 or 2.5, Ground Motion Set 26) 96

Figure 5-5. Time history response of 4-story building with the Traditional / R_s = 2.0 or 2.5 diaphragm design procedure under three levels of ground motions 99

Figure 5-6. Deformed shapes of 4-story archetype building with the Traditional /R_s = 2.0 or 2.5 diaphragm design procedure under three levels of ground motions 100

Figure 5-7. Column buckling for 4-story archetype building with the Traditional /R_s = 2.0 or 2.5 diaphragm design procedure 100

Figure 5-8. Time history of peak story drift four-story building with Traditional / diaphragm design with R*s* = 2.0 or 2.5 under MCE-level ground motion: total story drift vs. SCBF story drift. 101

Figure 5-9. Base shear of four-story building with Traditional / R_s = 2.0 or 2.5 diaphragm design under DE and MCE-level ground motions: total base shear vs. SCBF base shear. 102

Figure 5-10. Base shear vs. story drift hysteretic curves of four-story building with Traditional / R_s = 2.0 or 2.5 diaphragm design under MCE-level ground motion. 103

Figure 5-11. Contour of normalized diaphragm shear angle and normalized SCBF strain of four-story building with Traditional /R_s = 2.0 or 2.5 diaphragm design under MCE-level ground motion. 105

Figure 5-12. Contour of normalized diaphragm shear angle demand and normalized SCBF strain demand of 4-story building with different diaphragm designs under MCE-level ground motions. 106

Figure 5-13. Distribution of median peak story drifts at each story along building height of twelve-story archetype buildings with R_s = 2.0 or 2.5 diaphragm design under three levels of ground motions 107

Figure 5-14. Distribution of median peak resultant story drift along building height 111

Figure 5-15. Distribution of median peak story drift in longitudinal (x) direction along building height 111

Figure 5-16. Distribution of median peak story drift in transverse (y) direction along building height............. 112

Figure 5-17. Diaphragm shear demand of archetype buildings with R_s = 1.0 diaphragm design normalized by diaphragm design shear. 114

Figure 5-18. Cumulative distribution function (CDF) plots for SRSS drift for $ACMR_{10\%}$ hazard level: (*a*) One-story steel bare deck roof; (*b*) Four-story; (*c*) Eight-story; (*d*) Twelve-story. 123

Figure 5-19. Cumulative distribution function (CDF) plots for shear angle for $ACMR_{10\%}$ hazard level: (*a*) One-story steel bare deck roof; (*b*) Four-story; (*c*) Eight-story; (*d*) Twelve-story. 124

Figure 5-20. Lognormal cumulative distribution (CDF) plots for diaphragm design with Rs = 2.0 or 2.5: (a) Four-story archetype; (b) Eight-story archetype. 127

Figure 6-1. Typical Metal Building System: (a) Three-dimensional view; (b) Front view 133

Figure 6-2. Application of rod bracing in metal building system: top view rod bracing detail 137

Figure 6-3. Reduced order modeling of metal building archetype using *OpenSees* software 141

Figure 7-1. Rod brace diameter industry survey results – min and max reported ranges. 144

Figure 7-2. Rod brace angle industry survey results – min and max reported ranges where θ is the angle from the web plane to the rod (0 degree result was probably misreported and should be 90 degrees). 145

Figure 7-3. Hillside washer types reported in the survey: (a) hardened steel with an oversized bearing surface and nipple for engaging web edge; and (b) an aluminum hillside washer. 146

Figure 7-4. Primary frame web depth industry survey results – min and max reported ranges. 147

Figure 7-5. Primary frame web thickness industry survey results – min and max reported range. 148

Figure 7-6. Primary frame flange thickness industry survey results – min and max reported ranges. 149

Figure 7-7. Primary frame flange width industry survey results – min and max reported ranges. 149

Figure 7-8. Metal building primary frame steel plate girder specimen dimension nomenclature. 151

Figure 7-9. Dimensions and details for the hillside washer used for all tests in this research. 152

Figure 7-10. Metal building primary frame test setup with rod anchor. 153

Figure 7-11. Position transducer plan designed to isolate specimen local web and flange deformation, weak axis bending, and torsion deformation. 154

Figure 7-12. Typical flange local buckling deformation (W1 test shown). 157

Figure 7-13. Typical web bearing deformation at the hillside washer nipple bearing point 157

Figure 7-14. Typical web tearing deformation at the hillside washer nipple bearing point 158

Figure 7-15. Hillside washer nipple bearing failure (C3 test shown) 158

Figure 7-16. Tested specimen group C: (a) Front side view (b) Back side view. 160

Figure 7-17. Test group C (control) load-deformation response 161

Figure 7-18. Test group W (reduced web thickness) load-deformation response 161

Figure 7-19. Test group F (increased flange width and thickness) load-deformation response 162

Figure 7-20. Test group A (decreased rod angle) load-deformation response 162

Figure 7-21. Load-flexural deformation ($\delta_{flexure}$) response: (a). W1 Specimen (b). A1 Specimen 164

Figure 7-22. Load-web deformation (δ_{web}) response: (a). W1 Specimen (b). A1 Specimen 164

Figure 8-1. Metal Building Archetype (*VP Buildings 3200 Club Circle Memphis TN*): (a) Designed Archetype with Rod Bracing (MBMA); (b) Top View of Archetype; (c) Computational model [105] 172

Figure 8-2. Wall rod layout and sizing for metal building archetype [105] 174

Figure 8-3. Roof rod layout and sizing for metal building archetype [105] 174

Figure 8-4. Typical juncture of rafter-to-column and rod bracing to rafter and column connections 176

Figure 8-5. Typical hillside washer detail for rod-brace systems based on rod diameter [105] 176

Figure 8-6. Typical through fastened panel detailing for roof and walls [105] 177

This page is intentionally left blank.

Chapter 1

Introduction to Seismic Resilient Design of Steel Structures

1.1. Overview on Seismic Design Provisions

1.1.1. Resilience and the National Model Building Codes

Resilience is an extensive concept embracing different aspects of communities such as economy, infrastructure, and public well-being. As the built environment represents the major component of societies, sustainable structures play a significant role in the whole sustainability approach. When it comes to the natural hazard context, resilient design of infrastructures and community resilience are in a harmony. Damage to critical infrastructure and facilities can have unfavorable consequences for the society and welfare system and represents the deficiency of sustainability and resilience. Therefore, seismic resilient design has become an important subject in the past decades.

Among natural hazards, earthquake is one of the most destructive natural phenomena causing large number of fatalities and adverse economic losses. According to the United States Geological Survey (USGS), around half of Americans are exposed to potentially damaging ground shaking from earthquakes [1]. Annualized Earthquake Losses (AEL) are estimated to be $6.1 billion by the Federal Emergency Management Agency (FEMA) [2]. By having the evidence from past earthquakes and knowledge provided by engineers and researchers, updating the building design provisions is one of the most effective seismic mitigation strategies available for the communities.

Building regulation has been adopted and used in the United States since the late 1800s after occurring frequent events in some densely populated cities [3]. The first objective of building codes was protecting the big cities from fire. Later on, building regulations broadened their scope to some other issues such as safety and public health. In response to the earthquake hazard, building regulations are developed and known as "building codes" since they reflect the community concerns. In 1950s, three different building codes had been developed and adopted for three different regions across United States. By evolving the building codes, different industries established professional associations to develop technical criteria and construction. Guidance documents, issued by industries associations, are adopted as codes of references after the American National Standards Institute (ANSI) approval [4]. The model building codes continually updated after different events across the country.

1.1.2. Advancing Resilience through Seismic Design Provisions

To implement the seismic resilient design, model building codes are primarily developed based on performance objectives of the building. During early years of seismic code provision development, observation of the damage and performance of the buildings during earthquakes was the main reason for code revisions. Earthquakes such as 1925 Santa Barbara, CA and 1933 Long Beach, CA led to the development of regulations to provide for minimum levels of lateral strength. The design objectives of the early codes have been mainly achieved by using acceptable construction materials, minimum levels of strength and stiffness [5]. The design requirements have been established based on classifications of the buildings. Also, demand-based design concept has been developed based on fixed values of different specifications related to structural design such as dead loads, live loads, snow loads, rain loads, earthquake loads, wind loads, etc.

Although demand-based design concept in early seismic design provisions resulted in a certain level of performance for the buildings, the actual performance capability of the building is not reached using the demand-based design process. In 1971, the observations from San Fernando Earthquake revealed that, in addition to strength, buildings needed to have the ability to deform (ductility) without catastrophic failure. In addition, the evidence from other severe seismic events like 1994 Northridge, CA and 1995 Kobe, Japan reported significant damage and losses of the buildings designed based on minimum levels of strength and stiffness demands. The findings from previous earthquakes finally led to evolution of seismic design provisions toward predictive methods for assessing potential seismic performance. Consequently, capacity-based design approach, later implemented as performance-baseddesign, was adopted and developed for new seismic design provisions.

1.2. Research Objectives and Motivation

1.2.1. Conventional Steel Buildings Seismic Design

To achieve a certain performance level for conventional steel buildings during seismic events, all the members should be designed to meet the component deformation and force capacities. Lateral-force resisting system has two main parts: 1) Vertical Lateral-force resisting system (VLFRS) which usually is known as the primary lateral-load resisting system in buildings. There are different types of braced frames available as VLFRS for conventional steel buildings. These frames have beams, columns and brace members. To assure that the VLFRS can achieve the inelastic deformation level without premature failure, design codes require the capacity-based design approach for the beams, columns and connections to meet the tensile and compressive capacity of the brace in dynamic load. 2) Horizontal lateral-force resisting system (HLFRS) known as diaphragm is the floors and roof of the building. The floor diaphragm acts as a critical element that distributes the demands developed in a building during an extreme event to the vertical lateral-force resisting systems and eventually to the building foundation. Steel deck diaphragms are made of thin corrugated steel panels typically with concrete fill, forms one of the most commonly used diaphragm elements in multi-story steel conventional buildings. Compared to VLFRS, little attention has been paid to the role of the diaphragm systems of buildings. The objectives of this study can be introduced as: 1) develop fundamental understanding of steel deck diaphragms as structural systems integrated within the overall building performance; 2) improve strategies for accurate modeling of floor systems within three-dimensional building models to enhance the overall structural resilience of the building.

1.2.1.1. Steel Deck Diaphragm, HLFRS

To simulate the response of floor deck diaphragm in conventional steel buildings, considering rigid diaphragm assumption is a common design approach. To create the computational model for the steel buildings with rigid diaphragm, all the nodes on the floor level could be connected to a mater node which is the center of mass/stiffness of the diaphragm on each level of the building. This assumption has some advantages like being simple and computationally efficient and accepted by *ASCE 7-10* [6] design provision for conventional steel buildings. However, this design approach has significant shortcomings. Floor systems could not behave completely rigid in a severe seismic event even if the diaphragm is designed as rigid. The observation from previous earthquakes such as 1994 Northridge earthquake shows that utilizing rigid diaphragm assumption can cause significant inelasticity during design level earthquakes. Figure 1-1 shows the collapse of several concrete parking garages with precast concrete diaphragms during the 1994 Northridge earthquake [7], [8].


(a) (b)

Figure 1-1. Building Collapse During 1994 Northridge Earthquake: (a) Concrete Parking Garages; (b) Storage Building with Rigid Wall Flexible Diaphragm (RWFD).

In addition, the floor diaphragm system is a major part of the lateral force resisting systems. Having a semi-rigid diaphragm experiencing inelastic deformation could be beneficial for overall seismic performance of the building since it can reduce the inelastic deformation in the braces. Figure 1-2 illustrates a schematic figure of interaction between diaphragm and different parts of lateral force resisting system [9].

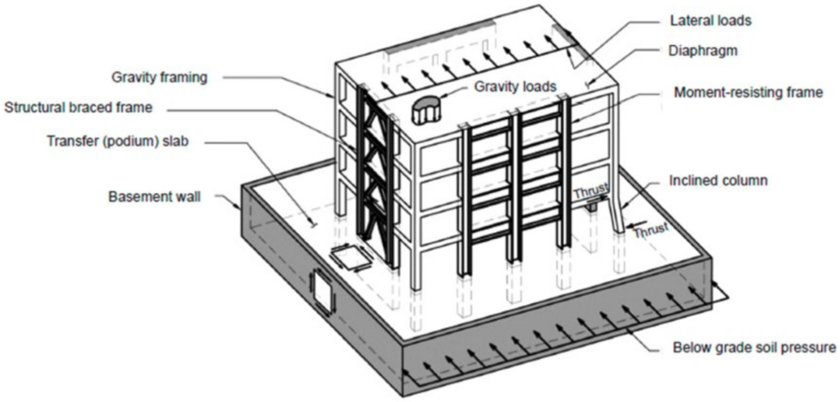

Figure 1-2. Diaphragm interaction with whole lateral force resisting system [9].

Figure 1-2 shows the coupled behavior of diaphragm system with VLFRS. Semi-rigid assumption for diaphragm behavior could be described in performance-based design framework. Current U.S. seismic design provisions, i.e., *ASCE 7-16* [10] provide two strategies to design the diaphragm system: 1) Demand-based design approach using forces reduced by the response modification factor of vertical system (R)., and 2) Capacity-based design approach which is consistent with performance-based design methodology which incorporates a diaphragm design force reduction factor (R_s). Both methodologies are described in Chapter 2.

In this study, a computational study using three-dimensional building models is conducted to capture the precise diaphragm behavior and its interaction with whole building during earthquake. Also, the performance of steel building is evaluated for different proposed values of R_s for bare steel deck and concrete-filled steel deck diaphragms. Figure 1-3 shows the application of concrete-filled steel deck diaphragm in a steel conventional building [11].

Figure 1-3. Application of concrete-filled steel deck diaphragm in steel building [11].

1.2.1.2. Special Concentrically Braced Frames (SCBF), VLFRS

Different types of braced frames could provide different levels of stiffness and ductility in steel buildings. Although studying the braced frames response is not the focus of this study, it is shown the interaction of diaphragm with different braced frames could provide different levels of seismic performance. In the current study, Special Concentrically Braced Frames (SCBFs) are selected as the VLFRS. Special Concentrically Braced Frames (SCBFs) can provide large amount of stiffness and strength for high seismic regions [12]. Capacity-based design approach with detailing and ductility requirements is the typical design methodology for SCBF braces. The details of SCBF design are explained in Section 2.2.3. Figure 1-4 illustrates the application of SCBF braces in a three-story steel conventional building in Palo Alto, California [13].

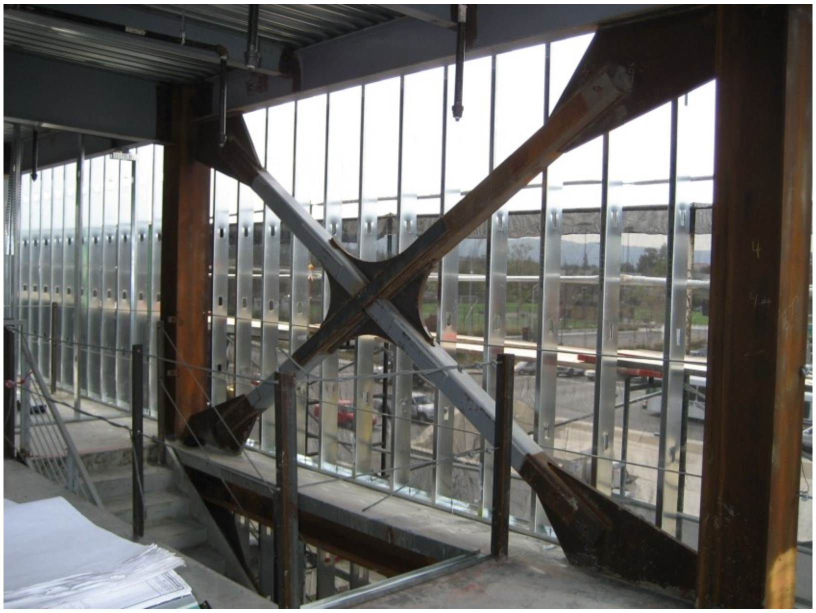

Figure 1-4. SCBF application in three-story steel building in Palo Alto, CA [13].

Seismic performance of special concentrically braced frames has been investigated by many researchers [14–20]. There are several studies with the focus on improving the inelastic behavior of the braces [21–24]. Full-scale experimental studies are conducted to study the response of a full special concentrically braced frame system [25–28]. In addition, computational models of SCBF are studied and calibrated using the experimental response of the structure [22,29–31]. Noted that the focus of current study is not on response evaluation of SCBF braces and is mostly on diaphragm system modeling and its interaction with SCBF as vertical lateral force resisting system.

1.2.2. Metal Building Systems Design

Metal building systems are a very common type of non-residential steel structures account for approximately 50% of the total low-rise construction market in the U.S. [32]. Metal building industry is able to offer economical and reliable structures that could be extremely customizable based on a wide range of applications including industrial, office, educational storage, etc. Metal building systems could be designed for the regions of high seismicity U.S. [32]. Figure 1-5 shows a typical metal building system construction [33].

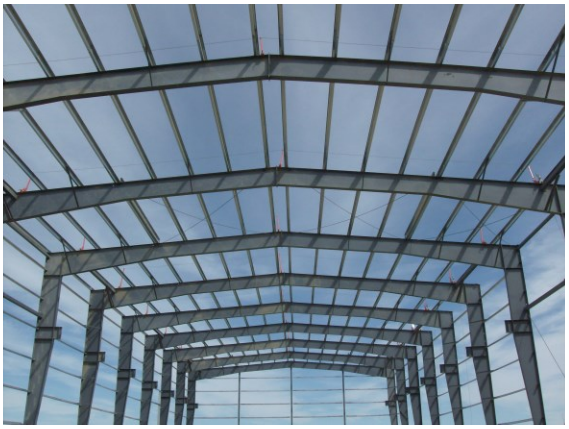

Figure 1-5. Typical Metal Building System [33].

Metal building systems consist of primary steel frames fabricated into I-sections from welded plates with the web depth of the members tapered to match the dominant demands, and secondary cold-formed steel purlins and girts running perpendicular to the primary frames as depicted in Figure 1-6 . The building skin typically consists of metal roof cladding, while the walls employ a variety of solutions from lightweight metal cladding to brick, concrete, or masonry. For lateral loads parallel to the primary frames the frames themselves provide lateral stability and strength. For lateral loads perpendicular to the primary frames, and for diaphragm action in the roof plane, rods in an X-configuration are typically employed within a given bay of the building. The rods are connected to the primary frames by running through holes in the web and are anchored by large hillside washers that fit within the holes in the web of the primary frame and are designed to accommodate the X-bracing approach angle that varies based on the building height and bay spacing (Figure 1-6).

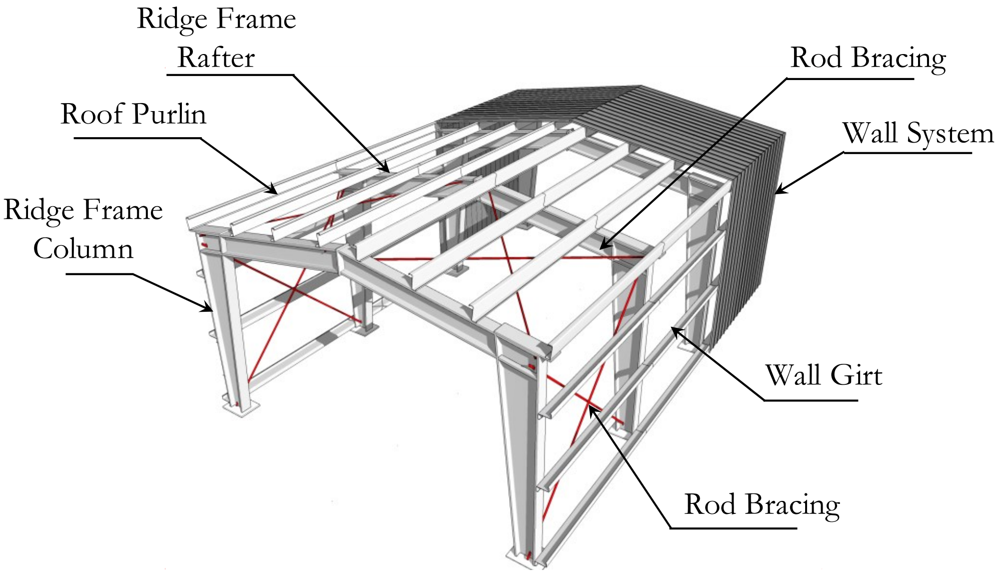

Figure 1-6. Metal Building Structural System.

Seismic design of metal building systems is based on equivalent lateral force approach in *ASCE 7-10* [6] through the use of different seismic performance factors including the Response Modification Coefficient, *R*, the Overstrength Factor, Ω, and the Deflection Amplification Factor, C_d. Primary frame flanges, web, and taper are designed and optimized based on the moment envelope developed from the seismic base shear [34].

In metal building systems, moment frames are the lateral force resisting system in transverse direction while tension-only rod bracing system provides the lateral stiffness for metal building systems in longitudinal direction. The rod anchorage connection assemblage consists of the rod, the anchorage (hillside washer), and the primary frame member that is penetrated by the rod. Deformation of the web of the primary frame member, accommodation in the hillside washer anchorage, and of the rod itself all contribute to the brace flexibility. The rod, its anchorage, or elements of the primary frame all can potentially be associated with the final limit state of the rod brace assemblage [35].

The research objectives in the current study are: 1) conducting an experimental study on the stiffness and strength of rod brace anchorage connection in metal building systems. 2) evaluation the seismic performance of the metal building system's design by implementing the actual stiffness and strength of rod brace anchorage connection in three-dimensional computational models.

1.2.2.1. Anchorage Rod Bracing, LFRS

In addition to the application of rod bracing in sidewalls for providing the lateral stiffness in longitudinal direction of the building, tension-only rod bracing is the main part of roof system by providing the lateral bracing for frame rafters in the out-of-plane direction. Figure 1-7 shows the application of rod bracing in the roof of metal building system [36].

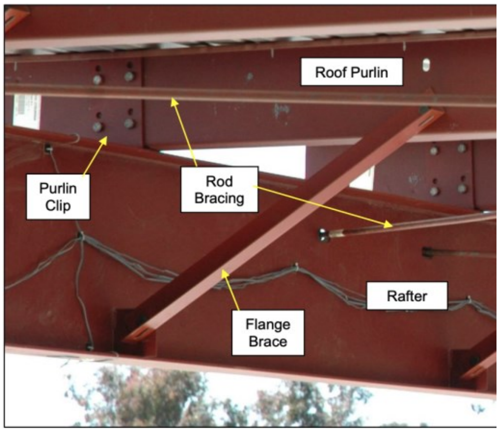

Figure 1-7. Application of rod bracing in the roof of metal building systems [36].

Seismic response of a full-scale metal building system can be evaluated as a combination of primarily moment frames, rod bracing, purlins, and girts behavior. Although metal building systems performed well in sever seismic events based on the observations from previous earthquakes, some experimental studies revealed a concerning lack of ductility in the cyclic behavior of metal building systems [36]. The current research study aims to investigate the seismic performance of the metal buildings using three-dimensional computational models, focusing on implementing the actual strength and stiffness of rod bracing anchorage connection, obtained from an experimental program was conducted at Johns Hopkins University [37].

1.3. Thesis outline

This thesis has nine chapters, including this introduction, and appendices.

Chapter 2 reviews the current seismic design strategies for conventional steel buildings. First, three types of different steel braced frames are reviewed by examining their design and performance in terms of seismic resilience. Then, a summary is provided to compare the design and requirements for three types of steel braced frame systems. In addition, diaphragm design procedure including both traditional and alternative design methods are presented and discussed. Finally, *FEMA P-695* [38] methodology to evaluate the seismic performance of steel building is introduced and discussed. Also, a literature review on SCBF steel archetypes buildings is given in this chapter.

Chapter 3 provides the details for three-dimensional modeling of SCBF archetype buildings. A literature review with focus on diaphragm design and rigidity is presented. In addition, details of one-, four-, eight-, and twelve-story archetype buildings such as number of buildings, software, building heights, building layout, and loading are discussed. Details of SCBF brace modeling are presented by calibrating the computational model against previous experimental data. Moreover, diaphragm system modeling including diaphragm design and modeling procedure are described. The computational model for diaphragm is calibrated and verified against experimental data. Finally, a short discussion on computational modeling of BFRF steel archetype building is presented in this chapter.

Chapter 4 presents the fundamental responses for SCBF steel archetype buildings. This chapter begins with a discussion on response validation of computational models and post-processing the outputs. Estimated natural periods and mode shapes are given and compared with *SAP2000* [39]rigid diaphragm model. The impact of different diaphragm procedures on natural periods and mode shapes of the steel buildings are discussed. In addition, overstrength, period-based ductility and static response of SCBF steel archetypes with different diaphragm procedures are presented using static nonlinear pushover analysis. A discussion is provided to evaluate the response of SCBF archetype buildings compared to previous studies.

Chapter 5 presents the nonlinear time history analysis results for SCBF steel archetype buildings designed with different diaphragm design force reduction factors. First, ground motion scaling and collapse criteria are introduced for SCBF archetype buildings. Then, a response example of four-story archetype building subjected to one ground motion pair is presented and discussed. Statistical analysis of the SCBF archetype buildings performed to compare the dynamic response of the buildings with different diaphragm design procedures. Finally, *FEMA P-695* [38] methodology is used to evaluate the overall seismic response of buildings with different diaphragm design procedures. Also, a diaphragm design procedure for SCBF archetype building is proposed based on *FEMA P-695* [38] assessment.

Chapter 6 provides a discussion on fundamental response of metal building systems. A literature review on metal building modeling is presented in this chapter. Also, the role of moment frames and other components of metal building systems are discussed. In addition, a discussion is provided on rod bracing response in metal buildings. Finally, lack of knowledge on both fundamental and seismic response of the metal buildings with focus on performance of rod bracing connection is discussed.

Chapter 7 concentrates on the experimental determination of stiffness and strength for metal building system rod bracing. A literature review is provided for rod bracing anchorage connection. The details for test matrix and specimens including the dimensions and material properties are provided. Moreover, different limit states are described and discussed based on the results of experimental program. Finally, rod brace assemblage connection strength and stiffness are obtained and discussed.

Chapter 8 describes the preliminaries for metal building system modeling with rod bracing. The ideas, basic inputs for archetype model and a framework for future modeling of three-dimensional metal building archetypes is provided in this chapter.

Chapter 9 includes general conclusion for the behavior of SCBF archetype building with different diaphragm design procedures. In addition, a summary on experimental findings of rod brace assemblage connection strength and stiffness is provided. Finally, the potential future work is discussed in this chapter.

Chapter 2

Seismic Performance of Conventional Structural Steel Buildings

2.1. Introduction

Today's tendencies toward seismic performance-based design of steel structural buildings places increasing emphasis upon developing efficient lateral and horizontal force resisting systems. Different types of braced frame systems such as concentrically steel braced frame provides a unique solution to fulfill multiple design criteria for lateral force resisting system in steel structures. In addition, capacity-based design approach for diaphragm as horizontal lateral force resisting system offers an attractive solution for a better performance-based design for conventional steel structures. This chapter refers to the design methods for both brace and diaphragm and following building codes and standards for conventional steel braced buildings:

- AISC 341-10, *Seismic Provisions for Structural Steel Buildings and Commentary*, 2010 [40].
- AISC 360-10, *Specification for Structural Steel Buildings and Commentary*, 2010 [41].
- ASCE 7, *Minimum Design Loads for Buildings and Other Structures*, 2010 [6].
- IBC *International Building Code*, 2012 [42].
- AISI S310-16, *North American Standard for the Design of Profiled Steel Diaphragm Panels*, 2016 [43].

In addition, *FEMA P-695* [38] methodology is introduced and discussed with details for seismic performance evaluation of steel framed buildings and different methods to design the diaphragm.

2.2. Steel Braced Frame Design

Brace frames are known as vertical lateral force resisting system (VLRFS) in steel structures. Brace frames provide the lateral strength and stiffness to achieve the desired structural performance during natural hazards like earthquakes. Braced frames are capable to develop the inelastic deformation and dissipate the earthquake energy to assure the life safety of the building.

Concentrically steel braced frames (CBFs) are axially loaded members that could be designed for different levels of strength and ductility based on seismic hazard levels. Three common types of CBFs are introduced in this chapter: (1) Ordinary Concentrically Steel Braced Frame (OCBF); (2) Special Concentrically Steel Braced Frame (SCBF), and (3) Buckling Restrained Braced Frames (BRBF).

Capacity-based design is the conventional design approach for CBF braces [44]. Design forces includes both tension and compression. Different types of CBF braces experience various limit states regarding their configuration, specific design and detailing. Ductility is the major property of all types of CBF braces which gives them the ability to sustain large inelastic deformations without significant loss in strength. Braces should be designed for ductile limit states such as yielding and buckling and avoid brittle limit states like fracture in the gusset plate. Three major types of braces and their design limit states are discussed in the following sections. It should be noted that special concentrically steel braced frame (SCBF) is discussed with more details since it has been used as VLFRS for the archetype buildings in this study.

2.2.1. Ordinary Concentrically Steel Braced Frames (OCBF)

Ordinary Concentrically Steel Braced Frames (OCBF) are usually made of hollow structural sections (HSS) and designed for larger seismic design force due to their lower ductility and deformation demand. The design principle for the OCBFs focuses on increasing the brace strength and stiffness using a higher design forces in order to minimize the inelastic demand. OCBFs have relatively few specific seismic requirements which provide more economical benefits, less amount of complication, and construction limitations [45]. OCBFs are developed in different layouts (see Figure 2-1). It should be noted that K-type braced frames are not permitted for OCBFs in *AISC 341-16* [40] specification.

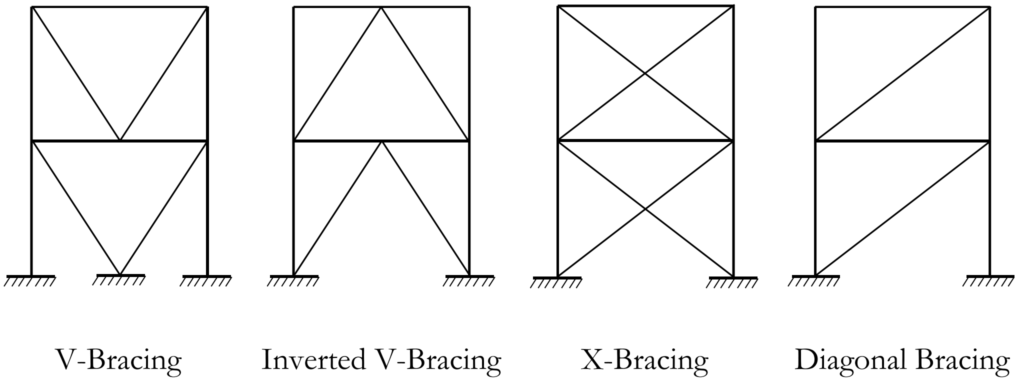

Figure 2-1. Typical OCBF configurations.

Compared to other types of CBF braces such as SCBF and BRFB, OCBF must be designed for lower response modification factor and for the regions with low seismicity. The provisions required OCBFs to have greater stiffness (lower kl/r ratio) and greater strength by having lower response modification factor, *R*. Based on *ASCE7* provision, OCBFs are only permitted for the building height less than 35 feet due to their lack of ductility. Hollow

Structural Sections (HSS) are usually used for OCBFs and must be designed for moderate ductile member requirements in *AISC 341* [40] specification. Moreover, OCBFs must fulfil the slenderness requirements provided by the *AISC* Specification in Chapter E. To design the OCBF connections, the *AISC Seismic Provisions* [40] specifies that diagonal brace connections must be designed for the amplified seismic load effect using the overstrength factor, Ω_o. It should be noted that the maximum tension force is the expected yield strength of the brace. The maximum compression force is the minimum value of $R_y F_y A_g$, and $1.14 F_{cr} A_g$ is gross area of the section. F_{cr} is the expected critical buckling stress in the *AISC* Specification Chapter E with yield stress, F_y, replaced by the expected yield stress, $R_y F_y$.

2.2.2. Buckling Restrained Braced Frames (BRBF)

The concept of steel core element which can yield in compression as well as tension is developed in Japan many years ago [46]. The first construction project in the United states that used BRBs was the Plant and Environment Science Building at University of California, Davis [47]. In 2005, BRBFs were officially adopted as LFRS in ASCE7 and AISC 341 building provisions. Thereafter, BRBs used in many structures across United States due to their exclusive inelastic seismic response in the regions with high seismic hazard. Figure 2-2 shows a typical BRBF and force-deformation response of BRB compared to other CBF braces in steel structures.

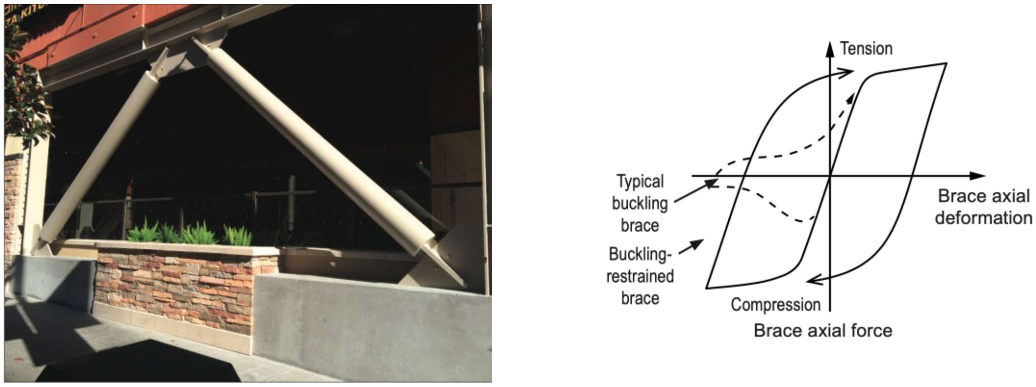

(a) (b)

Figure 2-2. (a) Typical BRB; (b) BRB axial force response [48].

Buckling restrained braced frames (BRBF) are very similar to ordinary concentrically steel braced frames (OCBF) and special concentrically steel braced frames (SCBF) in member properties, connections, and their role as vertical lateral force resisting system in conventional steel buildings. However, the structural performance of BRBFs is significantly unlike the other types of CBFs. BRBFs are fabricated members in steel framed buildings [48]. These braces consist of a steel core, as yielding element, which is surrounded by a steel tube casing filled with grout or concrete. The core restrains the buckling phenomenon under compressive loading and achieves a compressive yield strength that is approximately equal to its tensile yield strength. In despite of other types of CBFs, BRBFs yield axially in both tension and compression which result in a symmetric cyclic response with strain hardening (See Figure 2-2). This specific feature in BRBFs is the primarily source of ductility and allows the engineers to design the steel structure buildings with a larger response modification factor, R. BRBFs could be designed within the regions of moderate and high seismic hazard. In *ASCE 7* [6], the BRBF system is assigned the largest response modification coefficient ($R = 8$), indicating that the system is expected to withstand large inelastic deformation demands. BRBF must be designed based on three major steps: (1) the BRB's sized should be selected based on *ASCE*

7 [6] load combinations, where the earthquake loads have been reduced by response modification factor, R; (2) inelastic design-level drift and BRB strain should be checked to ensure compliance with *ASCE 7* [6] and *AISC 341* [40]; and (3) the adjusted brace strengths for BRBs should be determined and used to design beams, columns, and connections based on capacity-design approach.

Table 12.6-1 in *ASCE 7* [6] provision provides different options for the analysis procedure in BRBF. Equivalent Lateral Force (ELF) procedure, Modal Response Spectrum Analysis (MRSA) procedure, and Seismic Response History procedure are three methods which contain both linear and nonlinear procedures. It should be noted that ELF procedure is used to design the BRBF archetype buildings as another part of this research project [49].

For the connection design, *AISC 341* [40] requires BRBF gusset plates to be designed for 1.1 times the adjusted brace strength in compression. BRBF gusset plates are not intended to develop a hinge zone the way SCBF gusset plates are detailed to develop. In SCBFs, gusset plate hinging is part of the brace buckling mechanism, but in BRBFs, the design objective is to limit the inelastic deformation of the BRB cores. Principles for design of gusset plates are discussed in *AISC* Design Guide 29 [50].

2.2.3. Special Concentrically Steel Braced Frames (SCBF)

Buckling restrained braced frames offer high level of brace ductility and performance for the design of conventional steel structures. However, BRBFs may not be economical for low-rise steel structures due to the cost of fabrication and construction limitations. In addition, ordinary concentrically steel braced frames are not able to provide desired ductility for the regions of high seismic hazard. For all these reasons, Special Concentrically Steel Braced

Frames (SCBF) have been used extensively compared to both OCBFs and BRBFs across the North America [44].

SCBFs are special type of CBF braces which are capable to provide a reasonable level of ductility to maximize the inelastic drift capacity in steel structures. The main source of inelastic deformation capacity in SCBFs is through buckling and yielding of the brace members. Proportioning and detailing rules for SCBF's ensure adequate axial ductility, which translates into lateral drift capacity for the system. Since the SCBF braces work as fuses of the structural system, capacity-based design procedure has been applied for their design. Braces must be designed for small range of demand-to-capacity ratios which gives the LFRS the opportunity to spread the yielding over multiple stories in the building. To control the torsion of the building during earthquake, the braces are desired to be located in the building perimeter. Based on *ASCE 7-10* [6] provision, SCBFs could be designed for a relatively large response modification factor, R. To achieve the design objective, *AISC 341*[40] seismic design provisions require significant ductile detailing for SCBFs. Brace fracture is a dominant limit state due to the large amount of inelastic deformation. However, brace fracture does not cause an immediate collapse in SCBFs because of capacity-based design of gusset plates which allows the structure to experience a significant lateral resistance after the brace fracture. This lateral resistance could be 20% to 40% of original braced frame resistance [44].

To design conventional steel buildings with SCBF, factored force demands from *ASCE 7-10* [6] must be used for the members of the system while *AISC 360 Load and Resistance Factor Design* [41] provisions used to size the brace. In addition, braces should meet the requirements for local and global slenderness. Local slenderness limits for beams and columns are proposed by *AISC 341* seismic design provisions [40].

Similar to other types CBF braces, *ASCE 7* Table 12.6-1 allows Equivalent Lateral Force (*ELF*), Modal Response Spectrum Analysis (*MRSA*), and Seismic Response History design procedures for SCBFs. *ELF* procedure has some limitations like irregularity in the building or building height. In the current study, ELF procedure has been used to design the SCBF archetype buildings since there is no major irregularity in the archetype layout. Moreover, the total height of highest archetype building (twelve-story) is 151.5 feet which falls within the 160 feet height limitation by *ASCE 7* Table 12.6-1. *ELF* design procedure enables the static analysis procedure to estimate the performance of the building in earthquake. Similar to OCBF, the expected tensile strength of the brace may be taken as $R_y F_y A_g$. Also, the maximum compression force is the minimum value of $R_y F_y A_g$, and $1.14 F_{cr} A_g$, where A_g is gross area of the section. F_{cr} is the expected critical buckling stress in the *AISC Specification Chapter E* with yield stress, F_y, replaced by the expected yield stress, $R_y F_y$.

The connections joining the brace to the frame must be designed to maintain their integrity even when the brace undergoes buckling and yielding in cyclic dynamic load. Gusset plates and resistance of the bolts and welds connecting the gusset plates to the steel frames must be designed for tension and preclude block shear rupture limit states. Moreover, bolts or welds joining the gusset plate to the frames must have sufficient strength to resist force demands corresponding to the expected strength of the brace. For compression, out-of-plane buckling of the brace is accommodated using geometric limits on the gusset plate relative to the end of the brace. The *AISC* Seismic Design Manual [40] provides several illustrations of the application of member design and connection design for SCBFs. The thickness of the gusset plate must be adequate to resist both the brace expected tension strength and buckling when the gusset plate is subjected to the expected brace compression strength. Beam-column connections must be designed to be consistent with gusset plate design. Figure 2-3 shows the detailing of gusset plate connection in SCBF braces.

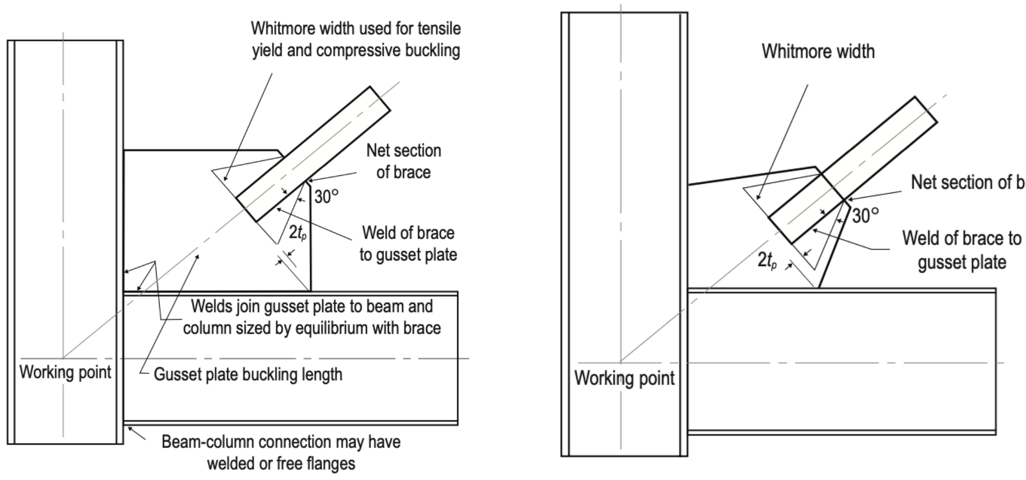

(a) *(b)*

Figure 2-3. Gusset plate connection design: (a) Rectangular gusset plate; (b) Tapered gusset plate [44].

2.2.4. Design Comparison for Different CBF Braces

To summarize and highlight the major difference for the design, Table 2-1 shows a summary of the design for three types of the CBF braces. It should be noted that, in this study, SCBF brace with response modification factor of $R = 6$, has been selected to study the structural performance of the diaphragm and braces during earthquake.

Table 2-1. CBF brace design summary [40]

	OCBF (R =3.25)	BRBF (R = 8)	SCBF (R = 6)
Brace layout	K shape bracing not allowed, extra requirements for V and inverted-V	No limitation, extra requirements for V and inverted-V	K shape bracing not allowed, extra requirements for V and inverted-V
Braces	KL/r < ~100 for K, V, inverted-V configurations; seismic b/t	$P_{ysc} = A_{sc}\ F_{ysc}$, $ØP_{ysc}$ adjust KF required. Reanalyze only if needed.	$KL/r <$ ~100 with exceptions; seismic b/t
Gross section	Design for factor load	Design for factor load	Design for $R_yF_yA_g$ of the brace
Connection	Design for minimum of $R_yF_yA_g$ of brace or amplified seismic load	Design for $\beta\omega R_y\ F_{ysc}$ in compression, and $\omega R_y\ F_{ysc}$ in tension	Design for $R_yF_yA_g$ and $1.1R_yP_n$ of brace & permit end rotation of brace
Columns	Design for minimum of maximum load of $1.1R_y$ times brace strength or amplified seismic load	Design for minimum of maximum load of $1.1R_y$ times brace strength or amplified seismic load	Design for minimum of maximum load of $1.1R_y$ times brace strength or amplified seismic load
Column Splices	Column design axial loads, special weld requirements, flanges splice 50% of flange strength	Column design axial load, $0.5M_p$ flexure, plastic shear strength	Column design axial load, $0.5M_p$ flexure, plastic shear strength; special weld requirements

2.3. Diaphragm, Chords and Collectors

Lateral force resisting system consists of two major components: (1) Vertical Lateral Force Resisting System (VLFRS) which is known as braced frame system in the conventional steel buildings (discussed in section 2.2), and (2) Horizontal Lateral Force Resisting System (HLFRS) which is the diaphragm. Steel diaphragms are made of cold-formed steel materials which are fabricated in different configurations [51,52]. The most common profile of steel diaphragms is corrugated plates. Steel diaphragms could be used as either steel bare deck or composite concrete on top of the bare deck which is also known as composite diaphragm. Figure 2-4 shows the bare deck and composite deck in conventional steel buildings.

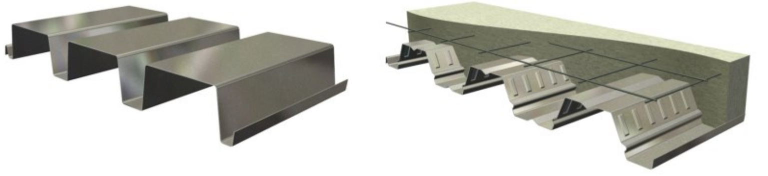

(a) (b)

Figure 2-4. Typical diaphragm: (a) Bare deck roof [52]; (b) Composite deck [51].

2.3.1. Diaphragm Flexibility Assumptions

To ensure the life safety during the extreme events, HLFRS with combination of the chord and collectors should be work as a coupled system with VLFRS to transfer the lateral load to the foundation of the buildings. There are various assumptions to simulate the behavior of the diaphragm in the buildings. However, having a precise computational model which can simulate the real response of the braced steel building is a challenge especially due to the current trends toward having a better performance-based design [53]. To achieve the capacity-based design approach for diaphragm system, significant updates have been added to *ASCE 7-16* [10] for designing the diaphragm system. However, these design updates are only applicable for concrete and wood diaphragms. This study is focused on investigating the structural performance of diaphragms in steel braced frame structures with similar design methodology introduced in *ASCE 7-16* [10] known as Alternative design. *ASCE 7-10* [6] provision classifies the diaphragm behavior as follows,

(1) Flexible diaphragm:

This assumption could be considered for structures with diaphragm constructed of untopped steel decking or wood panels by considering the following conditions as mentioned in *ASCE 7-10* [6]: *"(a) if vertical elements are steel braced frames, steel and concrete composite braced frames or concrete, masonry, steel, or steel and concrete composite shear walls; (b) one- and two-family dwellings; (c) light-frame construction where topping of concrete or similar materials is not placed over wood structural panel diaphragms except for nonstructural topping no greater than 1 1/2 in. thick and Each line of vertical elements of the seismic force-resisting system complies with the allowable story drift of ASCE 7-10 Table 12.12-1".* By considering this assumption, two-dimensional analysis is permitted by *ASCE 7-10* [6] due to uncoupled response in the building.

(2) Rigid diaphragm:

Structures with concrete slabs or concrete filled metal deck with span-to-depth ratios of 3 or less in structures that have no horizontal irregularity could be considered as structures with rigid diaphragm. Diaphragms are permitted to be idealized as flexible diaphragm (*ASCE 7-10* [6] Sections 12.3.1.1) when the computed maximum in-plane deflection of the diaphragm under lateral load is more than two times the average story drift of adjoining vertical elements of the seismic force resisting system of the associated story under equivalent tributary lateral load. *ASCE 7-10* [6] Tables 12.3-1 and 12.3-2 requirements should be considered for structures with horizontal and vertical irregularity.

Assumption of rigid diaphragm for the floors could significantly reduce the number of degrees of freedom of the structures by having a fully coupled response in the simulation. This assumption is accepted by *ASCE 7-10* [6] and is widely used by designers. However, in-plane floor deformation is neglected in this assumption which is in contrary with capacity-based design approach.

(3) Semi-rigid diaphragm:

A semi-rigid diaphragm is permitted by *ASCE 7-10* [6] to be used in structural analysis if the diaphragm is not belonging to neither of rigid nor flexible diaphragm. In *ASCE 7-10* section 12.3.4, the design forces determined from *ASCE 7-10* [6] section 12.10.1.1 shall be increased by a redundantly factor equal to 25 percent for the design of relative structural components in diaphragms.

Semi-rigid assumption for the diaphragm should be considered in design to provide more accurate simulation of the braced frame structures with contribution of diaphragm to LRFS. Semi-rigid diaphragm with a finite in-plane rigidity could work as coupled system with VLFRS during the earthquake load. There is comparatively little research on the semi-rigid diaphragm's models in steel braced structures. The goal of this study is to investigate the influence of different diaphragm designs on the seismic performance of special concentrically steel braced frame (SCBF) systems. [43]

2.3.2. Diaphragm Design Procedure

Design procedure for the diaphragm and collectors could be simply explained using Figure 2-5. To design the diaphragm, the base shear of the building, V , could be calculated by reducing the earthquake force using modification response factor, *R*, which is selected based on vertical lateral force resisting system in the building. For SCBFs, modification response factor is equal to 6. In the next step, the design seismic forces at each level of diaphragm must be calculated using the individual design concepts in *ASCE 7-10* [6] and *ASCE 7-16*[43]. According to *ASCE 7* provision [6] , "*Floor and roof diaphragms shall be designed to resist the design seismic forces at each level. The diaphragm is required to transfer design seismic forces from the vertical-resisting elements above the diaphragm to other vertical-resisting elements below the diaphragm due* *to changes in relative lateral stiffness in the vertical elements*". There are two design approach for the diaphragm: (1) Demand-based design approaches for diaphragms on *ASCE 7-10* [6] provision, known as Traditional design method, and (2) Alternative design method is a capacity-based design approach for diaphragms which is added to *ASCE 7-16* [10]. It should be noted that there is a similar minimum value for both Traditional and Alternative design methods to calculate the design seismic forces for diaphragm. Moreover, collector elements should be designed to transfer the seismic forces into the element providing the resistance to those forces such as VLFRS for both design approaches.

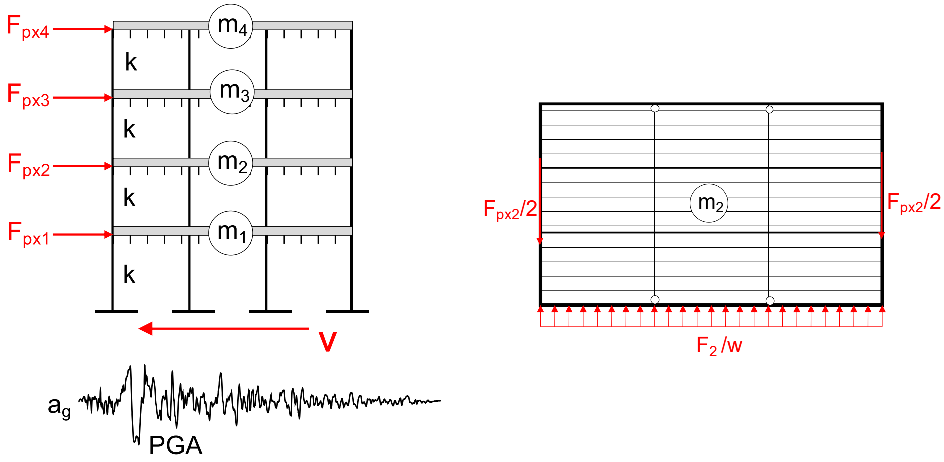

Figure 2-5. Design procedure for the diaphragm.

2.3.2.1. Traditional Design Method

Demand-based design approach on *ASCE 7-10* [6] provision, known as Traditional design method, states that "*Diaphragms shall be designed for both the shear and bending stresses resulting from design forces.*" Floor and roof diaphragms shall be designed to resist the design seismic forces at each level, F_{px}, as follows,

$$F_{px} = \frac{\sum_{i=x}^{n} F_i}{\sum_{i=x}^{n} w_i} w_{px} \tag{2-1}$$

where F_{px} is the diaphragm design force at level *x*, w_{px} is the weight tributary to the diaphragm at level *x*. F_i and w_i are design force and weight tributary applied to the level *i*, respectively. The minimum and maximum values of F_{px} could be introduced as $0.2S_{DS}I_e w_{px}$ and $0.4S_{DS}I_e w_{px}$, respectively. S_{DS} is the spectral acceleration as determined from Section *ASCE 7-10* [6] Section 11.4.4, and I_e is the component importance factor that varies from 1.00 to 1.50 (*ASCE 7-10* [6] Section 13.1.3).

2.3.2.2. Alternative Design Method

Alternative design approach on *ASCE 7-16* [10] provision states that "*Diaphragms including chords and collectors and their connections shall be designed for to resist in-plane seismic design force.*" In this method, the in-plane stiffness of the diaphragm is assumed to be finite. This assumption gives the diaphragm the opportunity to contribute to the structural system. Equation (2-2) introduces the in-plane seismic design force in the diaphragm.

$$F_{px} = \frac{C_{px}}{R_s} w_{px} \tag{2-2}$$

where the maximum value of F_{px} is $0.2S_{DS}I_e w_{px}$. S_{DS} is the spectral acceleration as determined from Section *ASCE 7-10* [6] Section 11.4.4, and I_e is the component importance factor that varies from 1.00 to 1.50 (*ASCE 7-10* [6] Section 13.1.3). R_s values could be chosen based on diaphragm design. In the current study, three designs are considered based on Alternative design approach: (1) Diaphragm design procedures with R_s = 1.0, (2) Diaphragm design procedures with R_s = 2.0 for composite concrete on steel deck diaphragm and R_s = 2.5 for bare steel deck diaphragm, and (3) Diaphragm design procedures with R_s = 3.0 for both composite concrete on steel deck and bare steel deck diaphragm.

Values of C_{px} could be determined using Figure 2-6 by knowing design acceleration coefficients C_{p0} and C_{pn} as follows,

$$C_{p0} = 0.4 S_{DS} I_e \tag{2-3}$$

$$C_{pn} = \sqrt{\left(\Gamma_{m1}\Omega_0 C_s\right)^2 + \left(\Gamma_{m2} C_{s2}\right)^2} \geq C_{pi} \tag{2-4}$$

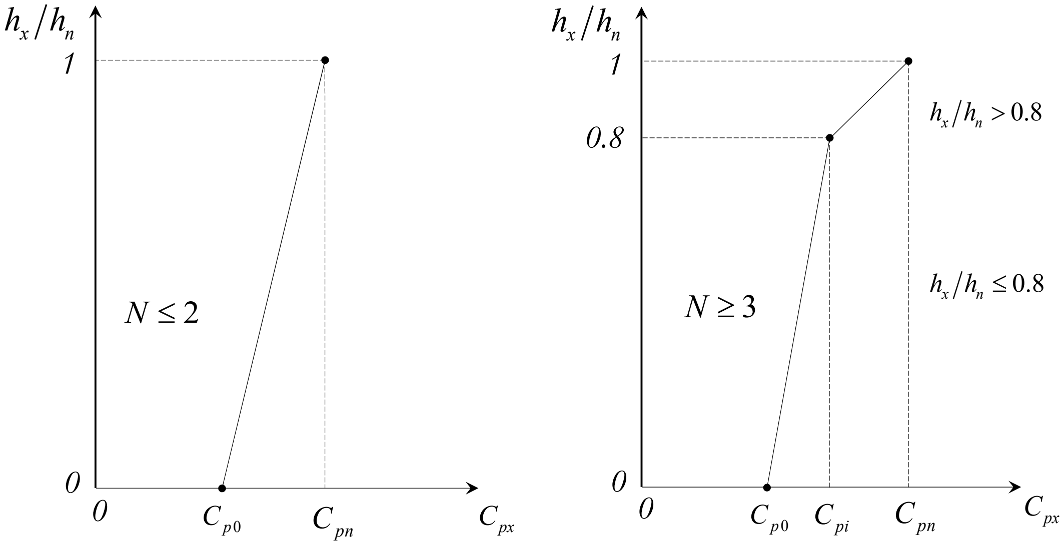

Figure 2-6. Alternative design procedure for diaphragm.

In addition, design acceleration coefficient, C_{pi}, should be greater than both $C_{pi} = 0.8 C_{p0}$, and $C_{pi} = 0.8 \Gamma_{m1} \Omega_0 C_s$.

Ω_0 is the overstrength factor which is given in *ASCE 7-16* [10] Table 12.2-1. Seismic response coefficient, Cs, can be calculated using *ASCE 7-16* [10] Section 12.8 and Section 12.9. Also, C_{s2} is the minimum values of $C_{s2} = \left(0.15N + 0.25\right) S_{DS} I_e$, $C_{s2} = S_{DS} I_e$,

$C_{s2} = \dfrac{I_e S_{D1}}{0.03(N-1)}$ For $N \geq 2$, and $C_{s2} = 0$ For $N = 1$. It should be noted that N is the story number in the building.

The modal contribution factors, Γ_{m1} and Γ_{m2} could be introduced as,

$$\Gamma_{m1} = 1 + \frac{z_s}{2}\left(1 - \frac{1}{N}\right) \tag{2-5}$$

$$\Gamma_{m2} = 0.9 z_s \left(1 - \frac{1}{N}\right)^2 \tag{2-6}$$

where the mode shape factor, z_s, could be chosen based on the lateral force resisting system in Table 2-2.

Table 2-2. Mode shape factor (z_s) for Alternative design approach

z_s	Lateral Force Resisting system
0.3	Buildings designed with Buckling Restrained Braced Frame (*ASCE 7-16* [10] Table 12.2-1)
0.7	Buildings designed with Moment-Resisting Frame (*ASCE 7-16* [10] Table 12.2-1)
0.85	Buildings designed with Dual System defined in *ASCE 7-16* [10] Table 12.2-1 with special or Intermediate Moment Frame capable of resisting at least 25% of the prescribed seismic forces
1.0	Buildings designed with all other seismic-resisting systems

In Figure 2-6, higher stories ($h_x/h_n > 0.8$)experience the effects of the higher modes for the buildings with larger number of stories. According to Table 2-2, higher modes effects depend on mode shape factor (z_s). The values of the mode shape factor (z_s) have more than 70% difference from BRBF (z_s = 0.3) to SCBF (z_s = 1) systems. This difference could make a significant change in the response of the steel frame buildings which shows the importance of the diaphragm design in structures. To evaluate the performance of the steel frame buildings with different diaphragm design and VLFRS system, two sets of archetypes with SCBF and BRBF systems have been studied by considering different diaphragm designs. The current study of focuses on SCBF archetypes buildings. The results for BRBF system is provided by Gengrui et al. [49]. It should be noted that all the design forces for different diaphragm designs in SCBF archetypes buildings could be find in Chapter 3 of this study.

2.4. FEMA P-695 Methodology for Building Seismic Performance

As it discussed in previous sections, there are various seismic performance factors such as response modification coefficient (R), the system overstrength factor (Ω_0), and deflection amplification factor (C_d). These factors are fundamentally important for evaluating the reliability and adoption of current and new seismic designs for force-resisting systems. The Federal Emergency Management Agency (FEMA) report, *FEMA P-695 Quantification of Building Seismic Performance Factors* [38], outlines a procedural methodology to evaluate the seismic performance of the buildings using statistical and probabilistic methods.

This section aims to provide an overview on *FEMA P-695* [38] methodology to evaluate the braced frame building archetypes with focus on SCBF as vertical lateral force resisting system and different diaphragm designs based on design approaches available in *ASCE 7* [6] provision.

2.4.1. Overview on FEMA P-695 Methodology

FEMA P-695 [38] methodology provides a rational foundation to evaluate the structural performance using nonlinear analysis techniques and explicitly considers uncertainties in ground motion, modeling, design, and test data in the probabilistic assessment of collapse risk.

The process needed for *FEMA P-695* methodology could be summarized in 6 steps: "*(a)* ***Obtain Required Information.*** *Obtain required system information in the form of detailed design requirements and system and component test data; (b)* ***Characterize Behavior.*** *Characterize system behavior through consideration of configuration issues and behavioral effects, development of index archetype configurations, definition of an archetype design space, and identification of performance groups; (c)* ***Develop Models.*** *Develop nonlinear models by applying design requirements and using test data to prepare index archetype designs, develop mathematical models for explicit simulation of collapse modes, calibrate models, and establish criteria for non-simulated collapse modes; (d)* ***Analyze Models.*** *Perform nonlinear static (pushover) and nonlinear dynamic (response history) analyses using a set of predefined (Far-Field) ground motion records; (e)* ***Evaluate Performance.*** *Evaluate system collapse performance by assessing total uncertainty (based on the quality of test data, design requirements, and analytical models), determining the collapse margin ratio, and comparing an adjusted collapse margin ratio to acceptable values based on an acceptably low probability of collapse; (f)* ***Document Results.*** *Identify sources of required system information, and document information on system behavior, development of index archetype designs, nonlinear model development, analytical results, quality ratings, and system performance evaluation criteria."*

To evaluate the performance of the structural system the collapse probability of structure should be evaluated at Maximum Considered Earthquake (MCE) ground motions. MCE ground motion is an earthquake that is expected to occur once in approximately 2,500 years; that is, it has a two-percent probability of being exceeded in 50 years (*ASCE 7-10* [6] Section 11.4). Structural system must meet the requirements for ten-percent collapse probability across all archetypes in the performance groups. The evaluation procedure based on *FEMA P-695* [38] methodology could be explained as,

(1) Calculating Collapse margin ratio (*CMR*) which is "*the ratio of median collapse intensity,* $\hat{S}_{CT}$ *, obtained from nonlinear dynamic analysis to the MCE ground motion spectral demand,* S_{MT} ".

$$CMR = \frac{\hat{S}_{CT}}{S_{MT}} \tag{2-7}$$

In Equation (2-7), S_{MT} is calculated by knowing the spectral response acceleration parameters of the archetype building (*ASCE 7-10* [6] Section 11.4). $\hat{S}_{CT}$ is obtained by calculating the 50% collapse probability using Incremental Dynamic Analysis (IDA) results where the horizontal axis is spectral acceleration and vertical axis is collapse probability of the archetype. It should be noted that, in this study, $\hat{S}_{CT}$ is calculated using the best fitting of lognormal cumulative distribution function (CDF) to three values of collapse probability for DE, MCE and ACMR10% ground motions. The details are provided in Chapter 4 of this study.

(2) Obtaining Adjusted collapse margin ratios (*ACMR*) by multiplying the CMR, which is calculated in step 1, by a spectral shape factor, SSF .

$$ACMR = SSF \times CMR \tag{2-8}$$

where a spectral shape factor, SSF is calculated using Table 7-1 of *FEMA P-695* [38], based on fundamental period, *T*, and period-based ductility, μ_T . Period-based ductility is obtained using static pushover analysis and by dividing the ultimate roof drift, δ_u, by the effective yield drift, $\delta_{y,eff}$ (See Equation (2-9)). The results for static pushover analysis are presented Chapter 3 of this study.

$$\mu_T = \frac{\delta_u}{\delta_{y,eff}} \tag{2-9}$$

In addition, the overstrength factor, Ω, could be calculated by dividing the maximum shear force obtained from static pushover analysis, $V_{\max}$, by the design shear force, V :

$$\Omega = \frac{V_{\max}}{V} \tag{2-10}$$

(3) Comparing the obtained values of $ACMR$ for each archetype in step 2 and the mean of $ACMR$ values for each performance group with accepted values of $ACMR_{20\%}$ and $ACMR_{10\%}$, respectively.

$$\overline{ACMR_i} \geq ACMR_{10\%} \tag{2-11}$$

$$ACMR_i \geq ACMR_{20\%} \tag{2-12}$$

Total system collapse uncertainty, β_{total}, has been used to calculate the values of $ACMR_{10\%}$ and $ACMR_{20\%}$ which are specified in Table 7-3 of *FEMA P-695* [38]. Collapse uncertainty is a function of the quality ratings associated with the design requirements, test data, and nonlinear models, as well as record-to-record uncertainty. β_{total} is determined from Table 7-2 of *FEMA P-695* [38] and can be introduced as,

$$\beta_{total} = \sqrt{\beta_{RTR}^2 + \beta_{DR}^2 + \beta_{TD}^2 + \beta_{MDL}^2} \tag{2-13}$$

In Equation (2-13), values of design requirements-related uncertainty, β_{DR}, test data uncertainty, β_{TD}, and model uncertainty, β_{MDL}, should be chosen based on their respective quality ratings from Table 7-2 of *FEMA P-695* [38]. It should be noted that the quality rate is selected as *"Good"* with the values of 0.2 for all the archetype buildings (*FEMA P-695* [38] Section 7.3.4). Record-to-record uncertainty, β_{RTR}, could be obtained as following,

$$\beta_{RTR} = 0.1 + 0.1\mu_T \leq 0.4 \tag{2-14}$$

Most steel structures are relatively ductile and period-based ductility, μ_T, has a value greater than 3.0. In this case, β_{RTR} should be taken as 0.40 and the totally system collapse uncertainty is given in Table 7-2 of *FEMA P-695* [38]. It should be noted that β_{RTR} should not be less than 0.2.

2.4.2. Literature Review on Archetypes Evaluated by FEMA P-695 Methodology

There are several studies on evaluating the performance of steel braced archetypes in earthquake. Most of the studies in the literature are considering two-dimensional frame analysis. Different limit states like buckling, post-buckling behavior, yielding and fracture have been investigated to predict the dominant failure mode and seismic performance of SCBFs.

In 2010, Chen and Mahine [54] studied a series of two-, three-, six-, twelve-, and sixteen-story archetypes with SCBF and BRBF lateral load resisting system. Archetypes were designed based on *ASCE 7-05* for two seismic design categories, D_{min} and D_{max}. *ATC-63* methodology, which is identical with *FEMA P-695* [38] methodology, has been used for dynamic analysis. Each of the archetypes was subjected to the far-field ground motion set as described in *FEMA P695* [38]. For the purpose of assessing uncertainty, the archetype was given a *FEMA P695 (ATC-63)* [38] rating of "*B-Good*". The results demonstrated that in general, SCBF archetypes with shorter period (two- and three- story) had lower *ACMR* values and might be more prone to collapse. The group performance of two and three-story SCBF archetypes buildings designed using *ELF* method did not pass the *FEMA P-695* [38] criteria. However, Mid- and high-raised SCBF archetypes designed using *RSA* method did pass the *FEMA P-695* [38] criteria. NIST GCR 10-917-8 [38] also reported the results for same archetype buildings studied in [54]. The results show average collapse probability of 17 percent for an average design period of (T = 0.38 seconds) for two-story and three-story archetype buildings. Both archetypes have similar amount of overstrength ($\Omega = 1.4$) and designed for same seismic coefficient ($C_s = 0.167g$). The individual collapse probabilities for the two-story and three-story archetype models were 35 percent and 8.6 percent, respectively. It has been reported that the main reason for lower percentage of collapse in the three-story archetype is probably because if longer period (T = 0.58 seconds) compared to the two-story archetype. Based on *FEMA P-695* [38], this difference can decrease the response level of the *FEMA P-695* [38] ground motion records about 0.8 of the response for the two-story archetype. Moreover, the results show that all archetypes designed with seismic design categories, D_{min} passed the *FEMA P-695* [38] criterion. The results also showed that all long period SCBF archetypes (6, 12, and 16-story) passed this criterion regardless of seismic design level. Drift controlled the design for taller buildings which resulted in oversized members in the archetype compared to the buildings designed based on modification response factor. This has been described as the main reason for better performance of taller buildings. It should be noted that, all BRFB archetypes passed this criterion in this study.

In another recent study, Hsiao et al. [19] developed advanced computational models for SCBF to provide an approximate prediction of local damage to the beams, columns and SCBF braces. Equal lateral force (ELF) method was used for three-story and twenty-story archetypes with different values of response modification factor. The analysis showed that the brace buckling is a common phenomenon for all levels of hazard. The results demonstrated that the brace fracture in shorter buildings in 2% in 50 years (Design Earthquake level, DE) events was more common compared to twenty -story archetype. The results also showed that three-story archetype, with response modification factor of $R = 6$, did not pass the *FEMA P-695* [38] criterion. For twenty-story archetype, the buckling deformation distributed in different levels resulted in fewer brace fracture in higher buildings with longer period. The results revealed that significant buckling deformation usually happened in upper levels of the taller buildings due to the contribution of higher building modes. The observations also demonstrated that twenty-story archetype, with response modification factor of $R = 6$, did not pass the *FEMA P-695* [38] criterion. However, both archetypes (three- and twenty-story), with a lower response modification factor of $R = 3$, did pass the *FEMA P-695* [38] criterion. Therefore, Hsiao et al. [19] suggested a smaller response modification factor for the SCBF buildings to control the effects of brace buckling and fracture.

In 2020, *FEMA P-2139-4* [55] studied *"Short-Period Building Collapse Performance and Recommendations for Improving Seismic Design: Study of One-to-Four Story Steel Special Concentrically Braced Frame Buildings"*. Three-dimensional models for a group of four SCBF archetypes (1, 2, 3, and 4-story) have been studied with high and very high seismic design category, different foundation flexibility, and brace configurations. All archetypes are commercial buildings designed for modification response factor of $R = 6$ and seismic response coefficient (C_s) of $0.167g$, and $0.25g$, for archetypes with high and very high seismic design category, respectively. Archetypes are modeled with SuperX and chevron bracing configurations. The results showed that all archetypes with high seismic design category passed the *FEMA P-695* [38]criterion. However, for archetypes with very high seismic design, two- and four-story buildings have 20% and 19% collapse ratios which is not permitted by *FEMA P-695* [38]criterion. The results also explained the importance of using different bracing configurations by comparing the results of two- and four-story archetypes with SuperX and chevron bracing systems. The results showed that four-story chevron braced-frame archetype has a probability of collapse (21 precent) that exceeds 10 percent for the MCE spectral acceleration of $1.5g$. The reason has explained as formation of plastic hinges and subsequent deterioration at the tops of the first-story column. Collapse probability for two- and four-story archetypes with high seismic design category are 3.4% and 6%, respectively, which passed the *FEMA P-695* [38] criterion. This observation is in contrary to the results of previous studies [38,54]. To explain the reasons for the discrepancy between analytical prediction of collapse performance of this study and observations of the previous studies, two-story archetype building is selected for comparison. The comparison showed that the significant difference in collapse performance of the two-story archetype is primarily due to the large difference in the overstrength of archetypes. The overstrength of the two-story archetype in [54] was 1.4 compared to 5.96 for [55]. Another reason might be rooted in the brace configuration if buildings include larger number of braced frames, in order to provide a symmetrical and redundant system. This study proposed a better design for the braces based on optimizing the structural strength instead of material availability, economy or construction limitations.

2.5. Conclusion

Seismic design of conventional steel structures in the modern building codes follows the capacity-based design approach. Concentrically steel braced frames (CBFs) are efficient lateral force resisting systems and commonly used in conventional steel structures. Each type of CBFs has different design limit states and limitations. Ordinary Concentrically steel braced frames (OCBFs) have relatively few specific seismic requirements which provides more economical benefits, less amount of complication, and construction limitations. However, their low ductility makes them suitable for the regions of high seismic hazard. Buckling restrained braced frames (BRBFs) offer high level of brace ductility and performance for the design of conventional steel structures. However, BRBFs may not be economical for low-rise steel structures due to the cost of fabrication and construction limitations. Special Concentrically Steel Braced Frames (SCBF) have a reasonable amount of ductility and have been used extensively compared to both OCBFs and BRBFs across the North America.

Floor and roof diaphragms shall be designed to resist and transfer the seismic forces at each level to the vertical lateral force resisting system. There are three different assumptions for diaphragm flexibility. Traditional design is a demand-based design approach which considers the diaphragm with significant in-plane deformation rigidity. To have a coupled response in the buildings, Alternative design methodology is introduced by *ASCE7-16* [10]. Alternative design is a capacity-based design approach which is only available for wood and concrete diaphragms. The alternative design methodology shows the importance of diaphragm design in seismic performance of the steel braced frame buildings. This study focused on performance of SCBF archetypes buildings with different diaphragm design based on Alternative design methodology in *ASCE7-16* [43].

To evaluate the seismic structural performance of SCBF archetypes, *FEMA P-695* [38] methodology provides a rational foundation to assess the collapse probability in the buildings. *FEMA P-695* [38] methodology has been described. Moreover, a literature review with focus on studies with SCBF and BRFB as lateral force resisting system has been done in this chapter. The results showed that SCBF archetypes with shorter period and lower overstrength values are more vulnerable during earthquakes. Brace buckling and fracture is reported as the main reason for the collapse in shorter buildings. Moreover, the results also showed that brace configuration and design could affect the general performance of the building. For taller buildings, the seismic performance was relatively better due to the distribution of earthquake load in different levels of building. The observation revealed that buckling and fracture in higher stories cause failure in most of the previous SCBF archetype models. It should be noted that all BRBF archetypes passed *FEMA P-695* [38] criterion and showed significantly better performance compared to SCBF archetypes. P-delta effect reported as the main reason of collapse in BRBF archetypes.

Chapter 3

Three-Dimensional Modeling of SCBF Archetype Buildings

3.1. Introduction

In seismic engineering studies, simulation is widely used to explore the response of the building in extreme events. Computational modeling for structures has emerged during 1960s by developing Finite Element Method (FEM). After Northridge earthquake in 1994, computational modeling received great attention due to loss of life and billions of dollars in destruction to buildings and the entire built infrastructure. In a same time, by evolving new electronical technologies, supercomputers became available for structural engineers. Different building codes and standards has developed based on the simulations supported by experimental evidence. The low cost of simulation compared to experiments, made simulation a significant part of research projects.

By developing performance-based design for structures, different computational tools have developed for dynamic and reliability analysis of structures in earthquake. The results from finite element packages such as *SAP2000* [39], made a substantial improvement in response prediction of the buildings. However, the major problem structural engineers faced, was analyzing complex structural models with high level of uncertainty in material and behavior.

Also, most of the available packages were commercial software that are not made for researchers wishing to implement advanced modeling for reliability analysis of current and new designs in structures.

None of the commercial software is obviously made available for researchers wishing to implement these reliability methods in the application. To acknowledge this demand, *OpenSees* software [56], is developed as an opensource framework for the earthquake engineering research. *OpenSees* [56] provides a powerful tool for the purpose of nonlinear analysis of structures. Reduced-order modeling approach in *OpenSees* [56] provides computational tool to alleviate the burden of high computational costs of nonlinear dynamic analysis problems by considering uncertainty in both material and geometry.

In this chapter, computational modeling detail is discussed for different components of the SCBF steel braced frame model. Literature reviews on modeling methods of SCBF and diaphragm system are performed. Different components of SCBF archetype models are calibrated versus the available experimental database. Finally, a short summary on modeling of BRBF archetype is described.

3.2. Three-dimensional Computational Modeling

3.2.1. Introduction

Conventional steel structural systems with special concentrically steel braced frames (SCBF), bare steel deck roof, and concrete-filled steel deck floor diaphragms are one of the most common type of steel building systems in United States. During an extreme event like earthquake, lateral inertial forces are transferred through the diaphragms systems to the vertical lateral force resisting system (LFRS). Seismic design of conventional buildings is based on assuming the VLFRS as primarily element to control the dynamics of the building by experiencing large inelastic deformation and high level of hysteretic energy dissipation due to ductility. However, it has been proven that roof and floors systems in the steel buildings which designed using traditional design procedures may be subject to inelasticity during design level earthquakes. Also, the observations from previous earthquake damages such as Northridge earthquake shows that extreme inelastic deformation happing in diaphragms could cause collapse such as happened for several concrete parking garages with precast concrete diaphragm.

As it is discussed in Chapter 2, *ASCE 7-16* [10] design provision provides two methodologies for seismic design of diaphragms: (1) Traditional diaphragm design procedures which uses reduced forces, associated with the VLFRS, and (2) Alternative diaphragm design procedures with larger and more accurate "elastic" design forces for diaphragms. The alternative diaphragm design procedures incorporate a diaphragm design force reduction factor, R_s, that reduces the diaphragm demands based on the ductility and overstrength in the diaphragm. However, there is no available R_s factor in *ASCE 7-16* [10] steel diaphragms including both bare steel deck and concrete-filled steel deck diaphragms. Although there is a significant update in the upcoming edition of NEHRP Recommended Seismic Provisions and *ASCE 7-22* to adopt $R_s = 2.5$ for bare steel deck diaphragms by satisfying specific special detailing requirements, and $R_s = 2.0$ for concrete-filled steel deck diaphragms.

A majority of previous computational models did not consider the effects of inelastic deformation in diaphragms because of rigid diaphragm assumption. In addition, seeking simplicity in computational models, two-dimensional models are primarily considered in the literature. However, two-dimensional models are not capable to consider the inelastic deformation and in-plane shear the diaphragm systems. To evaluate the seismic performance of the conventional steel buildings with various diaphragm design procedures, a computational study using three-dimensional models is conducted to capture the nonlinear diaphragm behavior, and its interaction with the nonlinear vertical VLFRS. In this study, a series of 1, 4, 8, and 12-story archetype buildings with special concentrically braced frames (SCBF) for the vertical system and four designs for the diaphragms is presented. The modeling scheme uses computationally efficient calibrated frame and truss elements to capture the realistic nonlinear behavior of both the SCBFs and the diaphragms. The objectives of this study include: 1) to examine the effect of diaphragms on the dynamic properties of buildings, 2) to understand the extents of diaphragm inelasticity at specified diaphragm hazard levels, 3) to investigate the probability of collapse for buildings designed using different diaphragm design approaches, and 4) to evaluate whether the use of proposed values of Rs for bare steel deck and concrete-filled steel deck diaphragms have a significant effect on the seismic behavior of buildings. This chapter focused on details of modeling and calibration for braces, diaphragms, and gravity columns.

3.2.2. Literature Review with Focus on Diaphragm Design

The analysis of steel framed buildings is mostly focused on vertical lateral force resisting system. Floor and roof diaphragms must resist lateral forces and transfer them to VLFRS. Seismic codes and standards usually design the diaphragms based on the base shear strength in LFRS. Distribution of the base shear forces to each level of the building in low-rise and mid-rise buildings, is usually based on equivalent lateral force (ELF) method in which the elastic mode shapes of structures with rigid diaphragm assumption is used to design the LFRS. This can cause an inaccurate prediction for the response of the structure during earthquake by considering the fact of having semi-rigid diaphragm in the building [55,57]. In addition, the evidence from previous studies shows that diaphragm force calculated using rigid diaphragm assumption may not always be conservative [58,59].

Having an inaccurate prediction of semi-rigid diaphragm response, especially for structures with irregularity, resulted in severe damage in structures [60,61]. Jain and Jennings [62] studied dynamic analysis of single span one-story and multistorey structures with flexible diaphragms supported by end walls. Their results showed that first two symmetric mode of vibration has the most contribution to the total base shear. Ju and Lin [63] investigated the effects of diaphragm flexibility on moment-resisting frame buildings. The findings revealed that the assumption of rigid diaphragm only works if there is no shear wall as LFRS and the stiffness of diaphragm is significantly larger than VLFRS. In another study, Tremblay and Stiemer [64] studied the nonlinear response of rectangular one-story steel buildings with flexible diaphragm designed based on 1990 National Building Code of Canada. Nonlinear time history analysis results showed that the relative drift is significant due to diaphragm flexibility. The authors also found that increasing diaphragm flexibility would increase the fundamental natural period of the structure which is not consistent with the period estimation according to Canadian standard. This study recommended applying a dynamic amplification factor of 2.3 to diaphragm static force-based bending moments and roof deformations. Fleischman *et al.* [65]conducted a study on three- and six-story archetype with varied diaphragm flexibility. Diaphragm flexibility varied by changing in dimension of the building. Time history analysis results showed that for a certain level of diaphragm flexibility the mass tributary to the lateral-system and the remainder of the diaphragm mass act independently. Tremblay and Rogers [66] studied the seismic design of one-story steel buildings with metal roof deck roof using equivalent static force (ELF) method. Simulation results showed that the natural period of building get larger by increasing the flexibility of the roof diaphragm. Sadashiva *et al.* [67] proposed an approximate displacement prediction equation for different diaphragm in-plane stiffness based on elastic and inelastic time history analyses of symmetric structures. The results showed that deformation of one-story building mostly affected by diaphragm flexibility.

Koliou *et al.* [68,69] investigated the probability of collapse of rigid wall-flexible diaphragm structures based on the *FEMA P-695* [38] methodology. The findings indicated that the current design provision cannot meet the performance limits under the maximum considered earthquake (MCE) ground motions. This study also developed the of using weakening specified diaphragm zones to improve the collapse capacity of the structures through. Fang and Leon [53] conducted an study on a series of six four-story archetypes with different diaphragm stiffness and horizontal torsional and vertical irregularities for symmetric and asymmetric braced frame structures. The nonlinear static and time history analyses demonstrated that the ultimate strength of the structures with rigid diaphragm constraints is higher than the ultimate strength of those with semirigid diaphragms. Moreover, the findings showed that for the asymmetric structures, compared to rigid diaphragm models, the higher mode significantly effects the semirigid models under biaxial earthquake loads.

Nearly all the related models applying the *FEMA P-695* [38] methodology on steel moment and steel braced frame buildings have continued the use of two-dimensional models of the vertical lateral force resisting system and ignoring the diaphragm in the modeling by assuming a rigid diaphragm for the archetypes [17,19,20,70–74]. There are also small number of studies which considered three-dimensional modeling with a rigid diaphragm assumption [55,75].

To evaluate the diaphragm design using three-dimensional models, Wei *et al.* [49] evaluated the performance of a series of one-, four-, eight- and twelve-story archetypes, with BRBF as vertical lateral resisting force system, designed according to both traditional and alternative design concept in *ASCE 7-22*. The results revealed that steel bare deck and concrete-filled deck diaphragms are capable to experience inelastic deformation and improve the seismic performance of the building by decreasing the large inelastic deformation in the braces. It should be noted that current study is an individual but identical phase of [49] study to evaluate and compare the seismic performance of the building with SCBF as vertical lateral resisting force system and different diaphragm design.

3.2.3. Development of Computational models

To perform the nonlinear dynamic analysis, three-dimensional computational models were created using the *OpenSees* software [56]. Figure 3-1 illustrates a schematic view of the one-, four-, eight-, and twelve-story SCBF archetype building models used in this study. Details of the archetype simulation are provided in this section.

Current US building codes are applied to design the conventional steel buildings with SCBFs as vertical lateral force resisting system [76]. Four various diaphragm design scenarios are used: (1) Traditional design using conventional diaphragm design procedures from Section 12.10.1 of *ASCE 7-16* [10]; (2) diaphragm design procedures from Section 12.10.3 of *ASCE 7-16* [10] with R_s = 1.0 providing a “near elastic” design; (3) diaphragm design procedures based on Section 12.10.3 of *ASCE 7-16* [10] but with new values of R_s = 2.0 for concrete-filled steel deck floor diaphragms and R_s = 2.5 for bare steel deck roof diaphragms; and (4) diaphragm design procedures based on Section 12.10.3 of *ASCE 7-16* [10], but with an upperbound ductile R_s = 3.0 assumed for both concrete-filled steel deck and bare steel deck diaphragm. It should be noted that two types of roof are used for one-story SCBF archetype: (1) one-story SCBF archetype with concrete-filled steel deck roof; and (2) one-story SCBF archetype with bare steel deck roof. Concrete-filled steel deck roof may be less common than those with bare steel deck roof, but they are included to enable comparison to multi-story archetype buildings with concrete-filled steel deck floors. All other SCBF multi-story archetypes are designed with concrete-filled steel deck for all the floors and bare steel deck roof for the roof of the building.

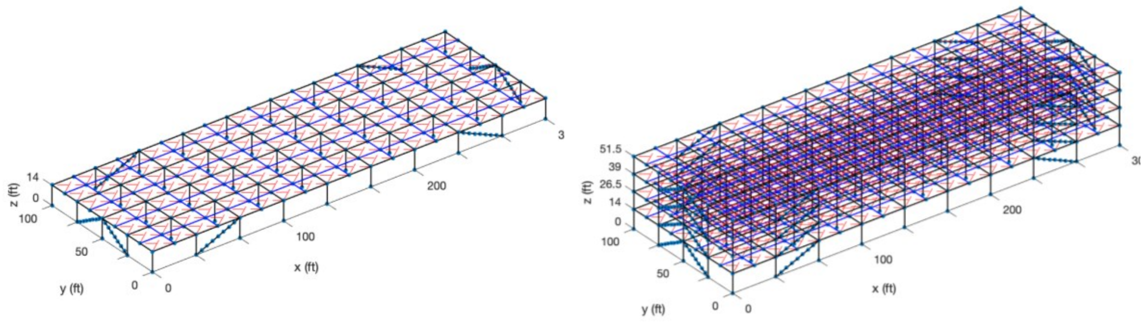

(a) 1-story building

(b) 4-story building

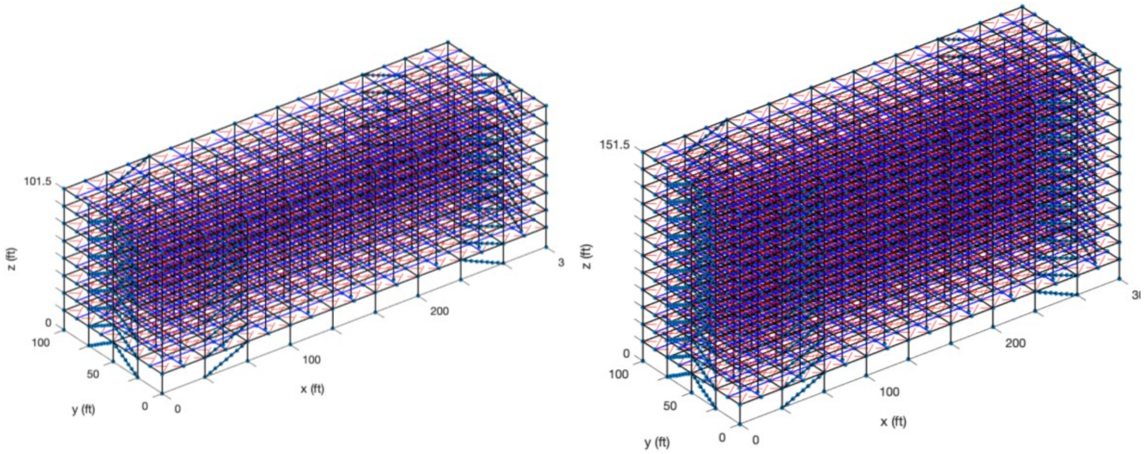

(c) 8-story building

(d) 12-story building

Figure 3-1. Design procedure for the diaphragm.

Table 3-1 illustrates a list of the buildings analyzed in this study. Note that the diaphragm force demands in some cases (e.g., traditional design, design with Rs = 2.5 and Rs = 3 for the one- story archetype with bare steel deck roof) are controlled by the minimum value allowed for diaphragm design forces (see

Table 3-4 for details), and therefore the archetype buildings designed with these different diaphragm design procedures were identical.

Table 3-1. List of SCBF Archetype Buildings for the Study

	Diaphragm Design			
Archetype Building	Traditional	$R_s = 1.0$	$R_s = 2.0$* / 2.50**	$R_s = 3.0$
1-story[a]	1	2	2	2
1-story[b]	3	4	5	6
4-story	7	8	7	9
8-story	10	11	12	12
12-story	13	14	15	15

[a]: bare steel deck roof; [b]: composite deck roof

*: $R_s = 2.0$ with concrete-filled steel deck; **: $R_s = 2.5$ with bare steel deck (roof)

Detailed site information and design parameters are given in Table 3-2, including the loading information, the location, risk category, importance factor I_e, spectral response acceleration parameter at short periods S_s, spectral response acceleration parameter at a period of 1 sec S_1, site class, response modification coefficient R, overstrength factor Ω_0, and deflection amplification factor C_d . Table 3-3 shows approximate fundamental period of the building T_a, upper limit on approximate fundamental period C_uT_a, fundamental period of the building obtained from a *SAP2000* model T_{model}, effective seismic weight of the building W, and design base shear V.

Table 3-2. Archetype Building Loading and Design Information

Concrete-filled steel deck Floor / Roof	Bare Steel Deck Roof	Seismic Weight	Site Information	Design Parameters
Dead Load = 56.5 psf slab + 22 psf superimposed = 78.5 psf	Dead Load = 3 psf slab + 22 psf superimposed = 25 psf	Typical Floor = 2545 kips	Irvine, CA Risk Category 2 $I_e = 1.0$ $S_s = 1.55$ $S_1 = 0.57$ Site Class D	$R = 6$ $\Omega_0 = 2$ $C_d = 5$
Live Load = 50 psf + 15 psf partition = 65 psf	Live Load = 20 psf + 15 psf partition = 35 psf	Composite Concrete on Steel Deck Roof = 2630 kips		
Exterior wall = 40 psf	Exterior wall = 40 psf	Bare Steel Deck Roof = 1271 kips		

Table 3-3. Prototype Building Seismic Design Information

Design Parameter	1-story Bare Deck Roof	1-story Concrete-filled Deck Roof	4-story	8-story	12-story
T_a (sec)	0.217	0.145	0.384	0.640	0.864
C_uT_a (sec)	0.304	0.203	0.538	0.895	1.209
T_{model} (sec)	0.417	0.500	0.640	1.246	1.770
W (kip)	1271	2630	8906	19086	29266
V (kip)	218	451	1529	2021	2295

The buildings all use the same plan dimensions, shown in Figure 3-2 and Figure 3-3, 300 ft by 100 ft with a story height of 14 ft at the first story and 12.5 ft for a typical story. Four bays of SCBFs are located on the perimeter of the building in each orthogonal direction designated as braced frame with BF, and Figure 3-4 shows an elevation view of the SCBFs in the 4-story building. Typical details for the floor and roof diaphragms are given in the notes on Figure 3-2 and Figure 3-3, as designed based on the diaphragm design forces tabulated in

Table 3-4. Member sizes for each archetype building are provided in the appendix A.1. Additional details for the design of the archetype buildings can be found in Torabian *et al.* [76].

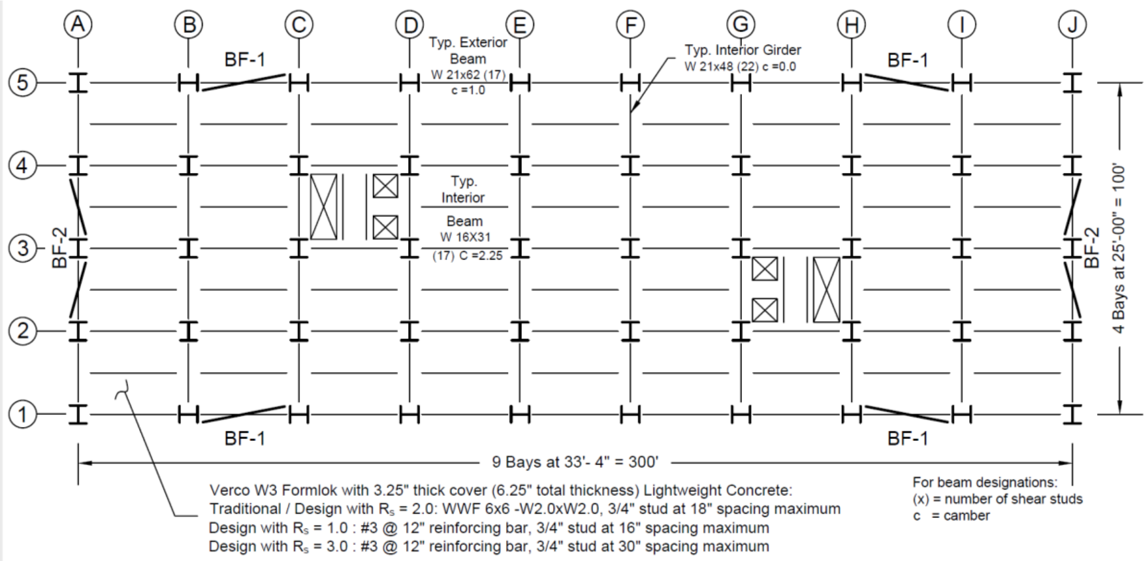

Verco W3 Formlok with 3.25" thick cover (6.25" total thickness) Lightweight Concrete:
Traditional / Design with R_S = 2.0: WWF 6x6 -W2.0xW2.0, 3/4" stud at 18" spacing maximum
Design with R_S = 1.0 : #3 @ 12" reinforcing bar, 3/4" stud at 16" spacing maximum
Design with R_S = 3.0 : #3 @ 12" reinforcing bar, 3/4" stud at 30" spacing maximum

For beam designations:
(x) = number of shear studs
c = camber

Figure 3-2. Typical Floor Framing Plan.

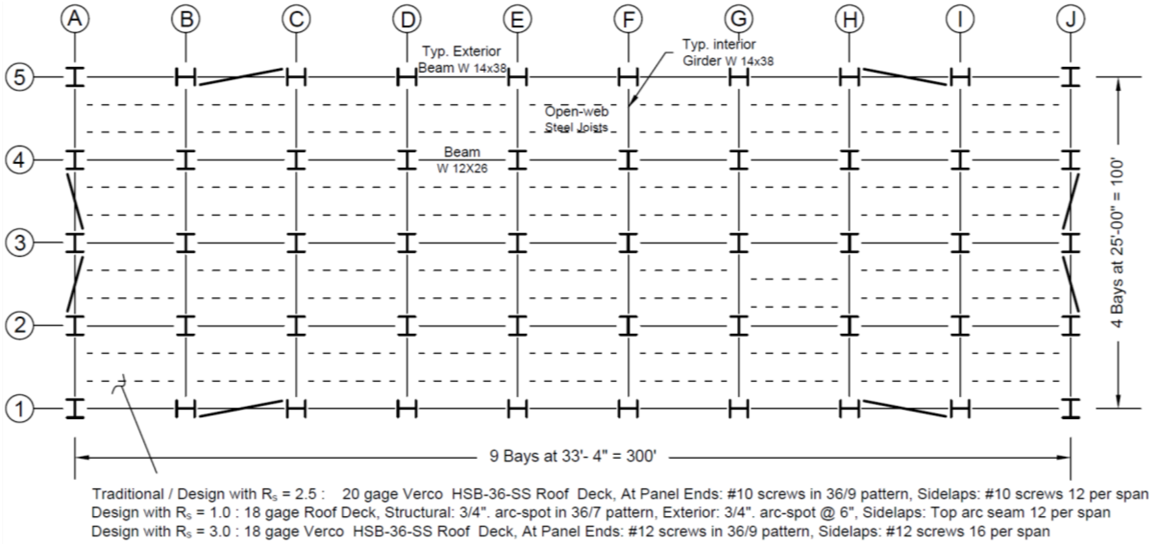

Traditional / Design with R_S = 2.5 : 20 gage Verco HSB-36-SS Roof Deck, At Panel Ends: #10 screws in 36/9 pattern, Sidelaps: #10 screws 12 per span
Design with R_S = 1.0 : 18 gage Roof Deck, Structural: 3/4". arc-spot in 36/7 pattern, Exterior: 3/4". arc-spot @ 6", Sidelaps: Top arc seam 12 per span
Design with R_S = 3.0 : 18 gage Verco HSB-36-SS Roof Deck, At Panel Ends: #12 screws in 36/9 pattern, Sidelaps: #12 screws 16 per span

Figure 3-3. Typical Roof Framing Plan.

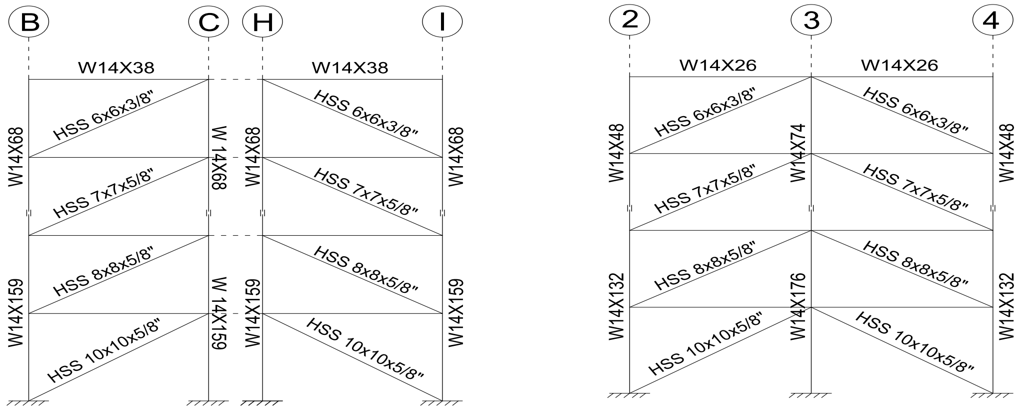

(a) SCBF frame on gridlines 1 and 5 (b) SCBF frame on gridlines A and J

Figure 3-4. Elevation view of four-story building braced frames.

Table 3-4. Diaphragm Design Shear per Unit width at Diaphragm Edge along Short Dimension of Building

Archetype Building	**Level**	**Diaphragm Design Forces (kip/ft)**			
		Traditional	**R_S =1**	**R_S =2/2.5**	**R_S =3**
1-story[a]	Roof	1.31	2.10	1.31	1.31
1-story[b]	Roof	2.70	4.33	2.70	2.70
4-story	Roof	1.88	4.11	1.64	1.31
	4	3.15	5.39	2.69	2.62
	3	2.62	5.34	2.67	2.62
	2	2.62	5.29	2.64	2.62
8-story	Roof	1.36	4.90	1.96	1.63
	8	2.62	6.35	3.17	2.62
	7	2.62	4.25	2.62	2.62
	6	2.62	4.42	2.62	2.62
	5	2.62	4.57	2.62	2.62
	4	2.62	4.73	2.62	2.62
	3	2.62	4.90	2.62	2.62
	2	2.62	5.06	2.62	2.62
12-story	Roof	1.31	5.15	2.06	1.72
	12	2.62	7.80	3.90	2.62
	11	2.62	5.26	2.63	2.62
	10	2.62	4.26	2.62	2.62
	9	2.62	4.36	2.62	2.62
	8	2.62	4.47	2.62	2.62
	7	2.62	4.58	2.62	2.62

6	2.62	4.69	2.62	2.62
5	2.62	4.80	2.62	2.62
4	2.62	4.91	2.62	2.62
3	2.62	5.01	2.62	2.62
2	2.62	5.12	2.62	2.62

[a]: bare steel deck roof; [b]: composite deck roof

3.2.4. Gravity Loads, Masses, Materials, Geometric Nonlinearity and Boundary Condition Modeling

FEMA P695 provision is implemented for the gravity loads in steel building. A combination of factored dead (*D*) and live loads (*L*), 1.05D+0.25L, is applied in the computational model. Masses were determined from the dead loads and lumped at the column nodes on each floor (See Table 3-5).

Table 3-5. Masses at Typical Node Locations

Level	Masses at Different Locations (kip-sec^2/in.)			
	Corner	Left/Right Edge	Top/Bottom Edge	Interior
Roof	0.046	0.059	0.067	0.070
Typical Floor	0.077	0.110	0.121	0.155
2nd Floor	0.079	0.112	0.123	0.155

Both material and geometric nonlinearity were considered in the analysis. In addition to the aforementioned nonlinear material models used for diaphragms and SCBF's, the columns and beams were represented by nonlinear beam-column elements with fiber-section formulation and kinematic hardening material with a hardening modulus equal to 450 *ksi* (or 0.0155E). Geometric nonlinearity was considered by including the gravity loads and using the *P-Delta* coordinate transformation algorithm in *OpenSees* [56] for the columns. For the SCBF braces, Corotational coordinate transformation algorithm in *OpenSees* [56] is applied to capture a precise response in the braces due to buckling and low-cycle fatigue in the brace.

3.2.5. Damping and System Convergence in Dynamic Analysis

To perform the nonlinear time history analyses, Rayleigh damping with a critical damping ratio equal to 2% for the 1st and 4th modes was used for the SCBF archetype building models. To overcome the convergence issue which is common for dynamic analysis with both nonlinearity in material and geometry, an algorithm with multiple steps is developed as follows: (1) Implying "*EnergyIncr*" convergence criterion with tolerance value equal to 1e-12 *kip-in*; (2) Try different *OpenSees* software numerical solver algorithms: "*Newton"*, *"ModifiedNewton"*, *"NewtonLineSearch"*, *"Broyden"*, and *"KrylovNewton"*; (3) Reduce the applied displacement increment for static analysis or time step for response history analysis by 10; (4) Reduce the applied displacement increment for static analysis or time step for response history analysis by 100; (5) Temporarily relax convergence criterion with the tolerance amplified by a factor of 10; (6) Temporarily relax convergence criterion with the tolerance amplified by a factor of 100; (7) Change the convergence criterion to the one based on the norm of unbalanced forces "*NormUnbalance*" with an initial value of tolerance equal to 1e-5 (unit in *kip* and *kip-in.*); (8) Go through Steps 2 to 6 again; (9) Change the convergence criterion to the one based on the norm of displacement increment "*NormDispIncr*" with an initial value of tolerance equal to 1e-6 (unit in *in.* and *rad.*)"; (10) Go through Steps 2 to 6 again; (11) For response history analysis, increase the Rayleigh damping ratio of the whole structure to 5% and then 10% to facilitate the convergence of a certain time step; (12) If all these attempts do not work, the simulation is considered to have experienced convergence failure and the analysis is terminated. A flow chart of the convergence algorithm is shown in Figure 3-5.

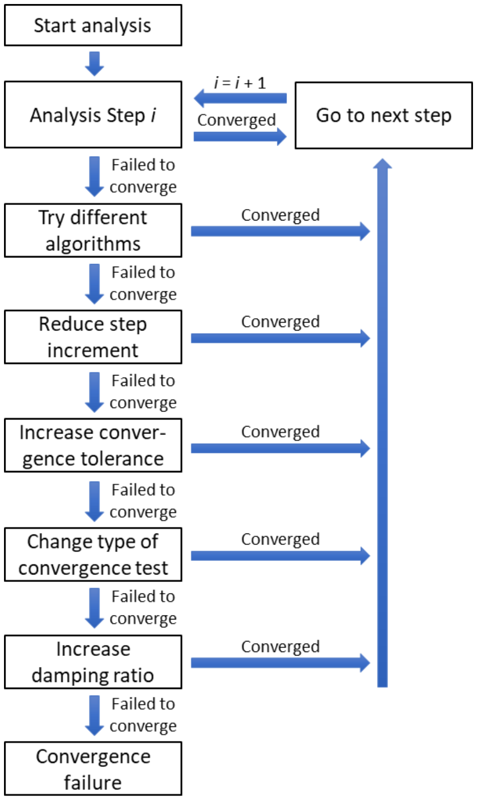

Figure 3-5. Flow chart of the algorithm for convergence tests [49].

3.2.6. Special Concentrically Braced Frame (SCBF) Modeling

Concentric braces are prone to buckle when they are under compression load. In addition, both post-buckling response of the SCBF and tensile yielding of the brace are sensitive to the gusset plates and other details and lead to nonlinear behavior which is key in the seismic response of a SCBF building. To employ an accurate model to simulate the SCBF response in both tension and compression, a computational *OpenSees* [56] model is developed and calibrated against experimental results. Figure 3-6 shows the detail of the concentric brace model which consists of a fiber element model for the hollow structural section (HSS) brace and rotational springs at the two ends to account for the rigidity of the connecting gusset plates. Similar studies in the literature have verified the benefits of using the discrete brace model and modeling rigid end zones at the connections on the simulation of SCBFs and mentioned the concept of using rotational spring at the ends of the brace element [29–31]. Typical modeling approaches for SCBFs use either fully restrained or fully pinned models for the gusset plate connections. However, test results show that the gusset plate connection is neither pinned nor fixed and its flexibility must be modeled explicitly to capture the nonlinear response. The zero-length nonlinear rotational spring element using *Steel02* material model at the end of the brace simulated the out-of-plane deformational stiffness of the connection. A rigid beam to column connection is considered to simulate the effects of rigid end zones in gusset plates. A fiber cross section creates the steel brace cross section with the assumption of plane strain compatibility. Displacement-based nonlinear beam–column elements with four integration points were used to model the braces. The *Giuffre–Menegotto–Pinto* model with the *Steel02* material was the nonlinear constitutive law used for material in the braces. Geometric imperfections equal to $L/1000$ formed by a single half-sine wave (in-plane) are included. To capture the brace buckling the corotational transformation is used in *OpenSees* [56]. The direction of the coordinate transformation vector must be normal to the buckling plane. It should be noted that six elements are considered along the brace length in all computational models.

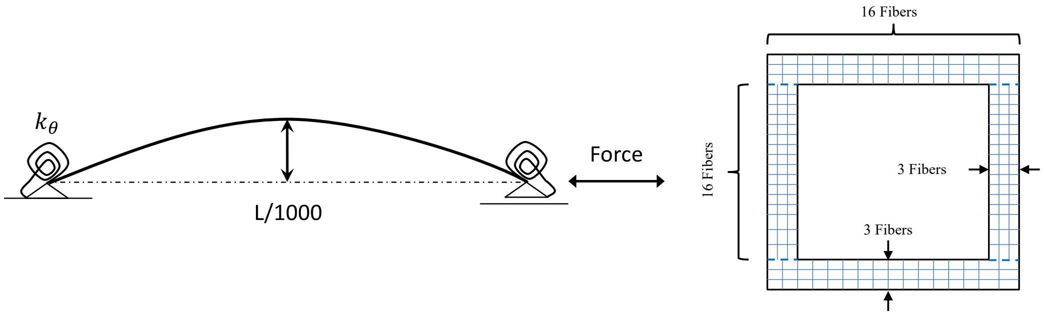

Figure 3-6.Configuration of a typical SCBF and computational model.

The calibration of the HSS fiber material model has been conducted against test data to match the behavior of specimens tested by Popov and Black [77] and Fell *et al.* [78]. For

Popov and Black [77], no rotational springs were used at the ends because the experiments used a mechanical pin. Table 3-6 presents the selected *Steel02* material model and rotational spring parameters for three different studies. As can be observed in Figure 3-7, the model can capture the behavior of the brace in both tension and compression.

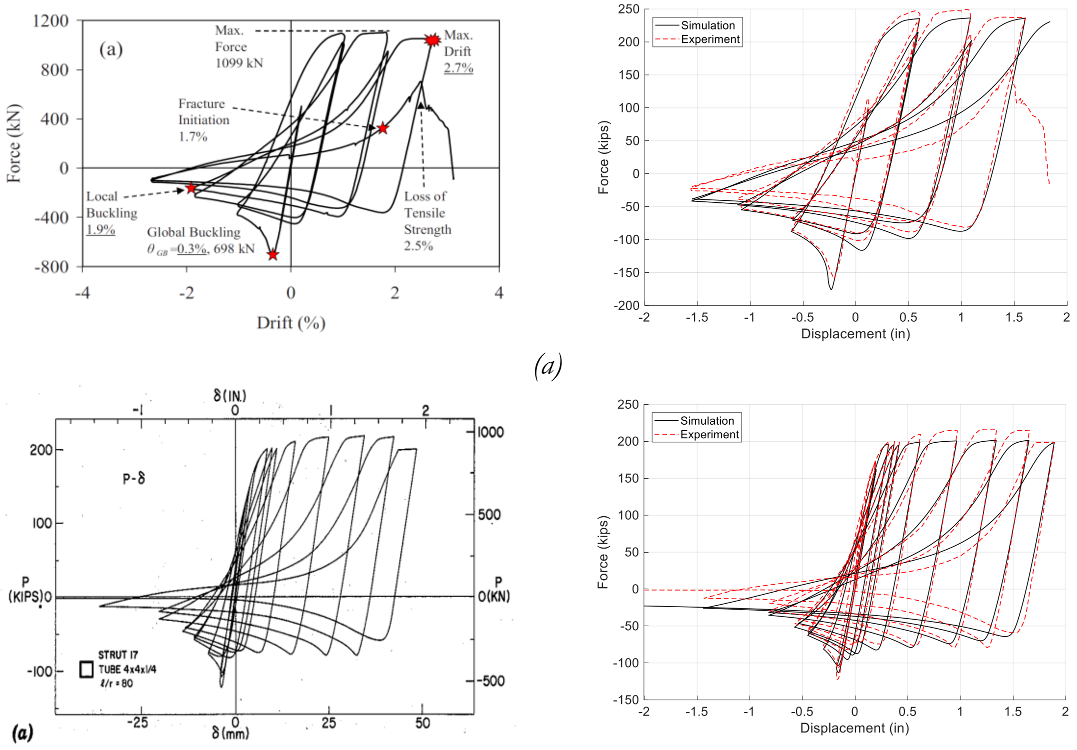

(a)

(b)

Figure 3-7. Hysteretic response of CBF from experiment and simulation: *(a)* Fell *et al.* [78] Spec. HSS 1-1, *(b)* Popov and Black [77] Strut 17

Table 3-6. Calibrated *Steel02* Material Parameters in *OpenSees* Software

SCBF material	*F_y (ksi)*	*b*	*R0*	*CR1*	*CR2*	*a1*	*a2*	*a3*	*a4*	-
	70.2	0.005	20.1	0.90	0.15	0	1	0	1	-
Rotational Springs	*M_y (k-in)*	*k_{spring}*	*R0*	*CR1*	*CR2*	*a1*	*a2*	*a3*	*a4*	*Hard.*
	414	0.002	20	0.9	0.15	0	1	0	1	0.005

Although the concept of performance-based seismic design is widely accepted, capacity evaluation of SCBF including fracture is difficult to conduct in a practical manner. In particular, it is difficult to predict brace fracture, which is a common failure mode of SCBFs due to low-cycle fatigue. The out-of-plane displacement of the brace increases with the story drift of the frame, which results in a concentration of inelastic deformation at the midspan of the brace and eventual formation of a plastic hinge which then leads to low-cycle fatigue fracture in the brace. To capture the effects of fracture in the SCBF model the *MINMAX* material is used in *OpenSees [56]*. This model eliminates the fiber at a user selected strain value.

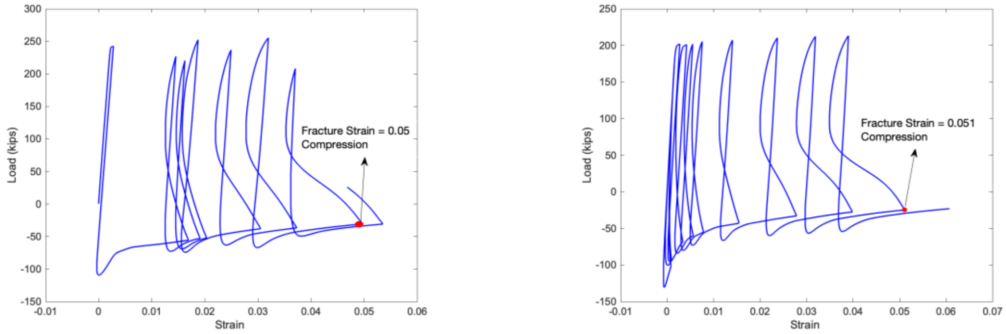

(a) *(b)*

Figure 3-8. Fracture strain limit for *MINMAX* material: *(a)* Fell *et al.* [78] Specimen HSS 1-1; *(b)* Popov and Black [77] Strut 17

Figure 3-8 shows the fracture strain for Popov and Black and Fell et al. Based on these results, the *MINMAX* strain is selected as 0.05 *in./in.* in the models. The selected model of the brace neglects explicit modeling of local buckling effects.

3.2.7. Modeling of Diaphragm systems

The significant advantage of three-dimensional modeling is being capable to evaluate the in-plane shear in the diaphragm. To simulate the in-plane diaphragm behavior in the archetype buildings, diagonal truss elements were used in the computational model. To validate the accuracy of computational model, test results from previous experimental studies have been used un this study. The load-deformation behavior of a diaphragm is typically derived through cantilever diaphragm tests in which a steel deck diaphragm with or without concrete fill is supported with one edge fixed and the parallel edge subjected to a shear loading (See Figure 3-9a). Force-displacement data from cantilever diaphragm tests are used to calibrate the diagonal nonlinear truss elements of unit cross-section area (See Figure 3-9b). All connections were modeled as pinned, and the perimeter framing beams were modeled as nonlinear beam-column elements with kinematic hardening material and with the same size of cross sections as the test. Figure 3-10 shows the meshing of diaphragms in the computational models of the archetype buildings. The dimension of the diaphragm unit in the mesh is 200 in. × 150 in., which is similar in scale to the test specimens used for calibration.

Having a data base including all valid cantilever diaphragm tests is a key parameter for having an accurate computational model. The cantilever diaphragm test database provided by O'Brien *et al.* [79] is utilized as a tool to help select specimens for diaphragm model calibration. For the bare deck roof diaphragm, the specimen labeled as Test 33 by Martin [80] with 20-gage P3615 1.5 in. B-deck was selected to satisfy the force demand for the archetype building roof diaphragm with traditional ASCE design or alternative diaphragm design with R_s =2.5 procedures (herein denoted as SP1). For the design with R_s =1.0 in the eight- and twelve-story archetype buildings, SP1 bare steel deck is not sufficient for the roof demand. To have sufficient design strength to match the roof demands for those archetypes, specimen 12 with 22-gage 1.5 in deep B-deck and welded sidelaps is chosen based on the testing of Essa *et al.* [81], herein denoted as SP2. For the concrete-filled steel deck floor diaphragm, test specimen 3/6.25-4-L-NF-DT tested by Avellaneda Ramirez *et al.* [82] was used, which consisted of 3 in. deck, with lightweight concrete fill and 6.25 in. total thickness (herein denoted as SP3). The dimensions of the test specimens (240 in. × 144 in. for SP1 and 180 in. × 144 in. for SP2) are close to those of the diaphragm units in the mesh of the building models.

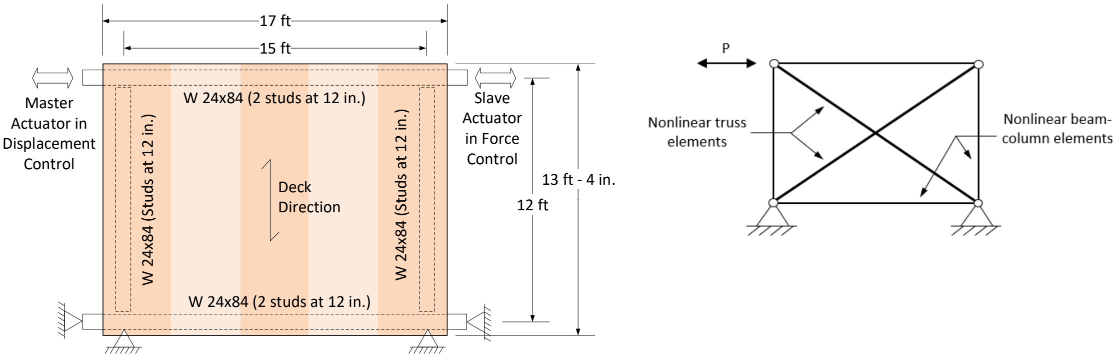

(a) Schematic view of SP2 test setup (b) Computational model

Figure 3-9. Test setup and computational model of cantilever diaphragm test.

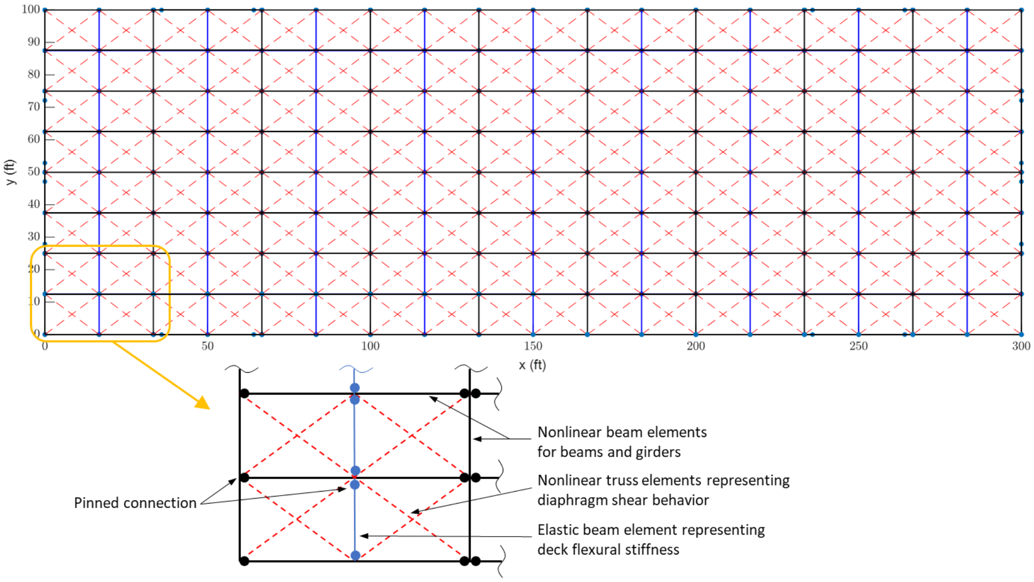

Figure 3-10. Diaphragm meshing in computational models of archetype buildings.

As is shown in Figure 3-11, the *Pinching4* material model in *OpenSees* [56] is used for the diagonal truss elements. This model is capable of capturing the hysteretic pinching, cyclic strength degradation, and cyclic stiffness degradation behavior of the diaphragms. Material parameters for the *Pinching4* model, including backbone stresses and strains and cyclic strength and stiffness degradation parameters, are calibrated through a multi-objective optimization algorithm with six steps to achieve an optimal match between hysteretic response from the simulation and test that minimizes the objective functions:

1) The backbone curve of a selected experimental stress-strain is obtained for the Pinching4 material calibration.
2) The four needed stress-strain points for a curve with linear segments are calculated to meet the requirements for *Pinching4* material according to the selected experimental stress-strain back bone curve. Third point of Pinching4 material is chosen based the peak load on the selected experimental stress-strain back bone curve. Then, the first, second, and fourth points were obtained by interpolation at 40%, 80%, and 40% (for SP1 and SP2) or 30% (for SP3), respectively, of the peak load on the backbone.
3) Multi-level optimization algorithm is used with different objectives functions such as the sum of the errors for peak forces, reloading stiffness, unloading stiffness, and cumulative energy dissipation of the hysteretic loops, considering different weights for each type of error. To have a robust optimization results, the initial values of four stress-strain points are obtained by scaling the backbone of the cyclic cantilever test data with a factor equal to 1.3.
4) Five levels of optimization are achieved as follows: (1) the strength degradation parameters considering displacement and energy history are optimized to achieve a minimum error for the peak forces of the hysteretic loops; (2) the reloading stiffness degradation parameters considering displacement and energy history are optimized to achieve a minimum error for the reloading stiffness of the hysteretic loops; (3) the unloading stiffness degradation parameters considering displacement and energy history are optimized to achieve a minimum error for the unloading stiffness of the hysteretic loops; (4) the parameters for reloading / unloading are optimized to achieve a minimum error for the cumulative energy dissipation in the hysteretic loops; and finally (5) all the Pinching4 parameters are optimized together to achieve a minimum

value for an objective function defined as the sum of the errors for peak forces, reloading stiffness, unloading stiffness, and cumulative energy dissipation of the hysteretic loops, considering different weights for each type of error.

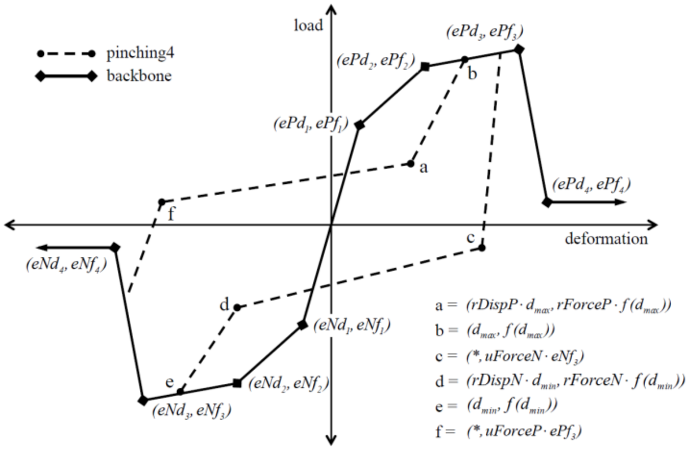

Figure 3-11. Pinching4 material model [56].

Table 3-7 shows the resulting values of the *Pinching4* material model parameters for the three selected diaphragm specimens. It should be noted that the dimensions of the archetype building diaphragm units do not coincide with those of the test specimens, and therefore the backbone parameters were modified using the strategy described in the Appendix A.2 so that the diaphragm shear strength per unit length is consistently represented. A comparison of the hysteretic response from the calibrated diaphragm simulation and that from the experiment is shown in Figure 3-12.

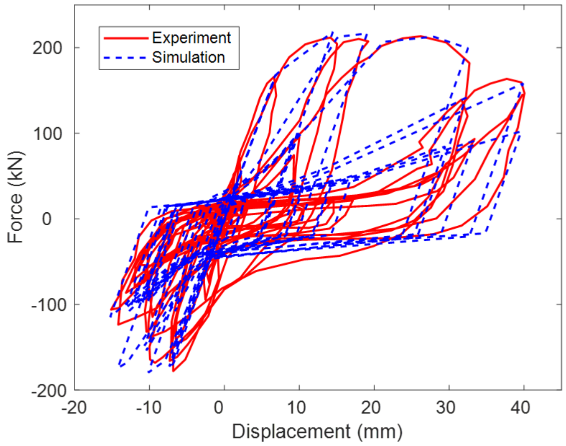

(a) SP1

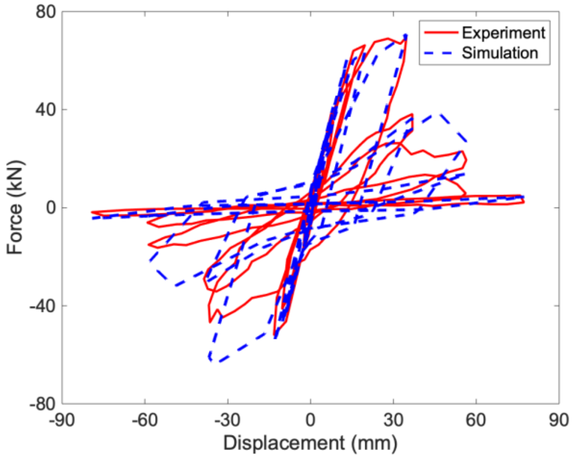

(b) SP2

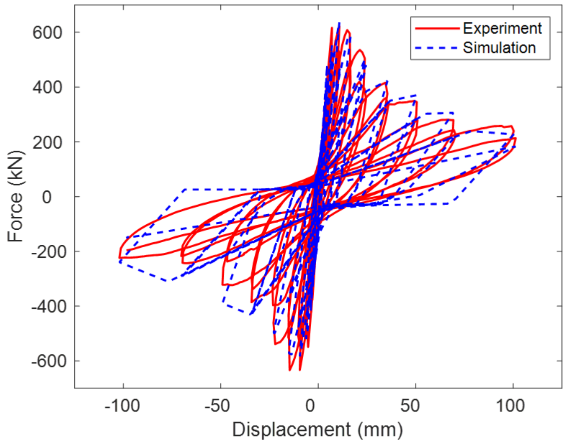

(a) SP3

Figure 3-12. Hysteretic response of diaphragm from experiment and simulation.

Table 3-7. Calibrated Pinching4 Material Model Parameters

Test	Backbone				Pinching			Strength Degradation					Stiffness Degradation					Energy Dissipation
	ε_1, σ_1 (ksi)	ε_2, σ_2 (ksi)	ε_3, σ_3 (ksi)	ε_4, σ_4 (ksi)	$r_{\Lambda+}$ $r_{\Lambda-}$	r_{F+} r_{F-}	u_{F+} u_{F-}	gF_1	gF_2	gF_3	gF_4	gF_{lim}	gK_1, gD_1	gK_2, gD_2	gK_3, gD_3	gK_4, gD_4	gK_{lim}, gD_{lim}	gE
SP1	0.0008, 22.18	0.0017, 28.90	0.0033, 30.69	0.0053, 23.97	0.20, 0.35	0.20, 0.35	0.10, 0.12	0	0.35	0	0.70	0.90	0, 0	0, 0.50	0, 0	0, 0.75	0, 0.90	4.31
SP2	0.0009, 5.80	0.0015, 7.77	0.0041, 9.28	0.0073, 4.31	0.05, 0.35	0.28, 0.35	0.12, 0.12	0	0.45	0.0	0.50	0.87	0.32, 0	0.60, 0.38	0.52, 0	1.52, 0	1.07, 1.08	2.02
SP3	0.0005, 63.46	0.0006, 76.41	0.0014, 107.40	0.0143, 48.33	-0.06, -0.06	0.12, 0.12	0.11, 0.11	0	0.83	0.0	0.46	0.33	1.09, 0.14	0.76, 0.47	0.32, 0.12	0.75, 0.10	1.04, 0.61	4.29

Table 3-8 provides the diaphragm demands and designs for the archetype buildings, where v is the shear demand per unit width of the diaphragm (as given in Table 3-4 in detail). $v_{n\_Estimated}$ is the expected nominal strength of the diaphragm design (note uppercase V refers to force while lower case v is force/length), and V_{exp} is the experimental peak strength from the hysteretic response curve in a given test. For the models of the same archetype building with different diaphragm designs that are not a good match with past testing, the same Pinching4 model parameters were used except that the backbone stresses were scaled so that the peak strength equals the expected nominal strength of the diaphragm from design. In this case, no additional overstrength of the diaphragm is considered. The expected nominal strength is calculated with prediction equations to the best knowledge of the authors. For bare For bare steel deck diaphragm, DDM04 [83] and AISI 310-16 [43] are used to calculate the nominal strength. For concrete-filled steel deck diaphragm, the nominal strength is determined as the lesser of: the strength associated with concrete slab diagonal tension cracking limit state calculated with the proposed equations (for AISI S310 2022 edition) in O'Brien et al. [79], in addition where appropriate the contribution of reinforcing steel is calculated with ACI 318-14 [84]; and the strength associated with the perimeter fastener (shear stud) limit state is calculated per AISC 360-16 [43].

The limit states that control the nominal strength calculation and the experimental strength are also provided in Table 3-8 . While it would be ideal to use test specimens that match the predicted limit states, test data was not available for some of the diaphragm configurations and limit states considered herein at the time this study was conducted. Therefore, the test specimens selected were used to represent some of the diaphragm designs even though their limit states do not match exactly. This was deemed acceptable for concrete-filled steel deck diaphragms as while the limit states change the post-peak force-deformation response is not substantially altered. Note, Table 3-9 provides the final selected details for the different diaphragm designs.

Table 3-8. Diaphragm Design Shear per Unit width at Diaphragm Edge along Short Dimension of Building

Building Model	Diaphragm Design	Level	v_{Design} (kip/f)	v_{n_Design} (kip/ft)	$v_{n\_Estimated}$ (kip/ft)	Estimated Limit state	v_{exp} (kip/f)	Experimental Limit State	Scale Factor
1-story[a]	Trad. / R_s =2.5 / R_s =3.0	Roof	0.92	2.30	2.07	Sidelap fastener	2.45	Sidelap fastener	0.84
	R_s =1.0		1.32	3.30	3.31	Sidelap fastener	2.45	Sidelap fastener	1.35
1-story[a]	Trad. / R_s = 2.5	Roof	1.81	5.88	12.70	Diag. Tension Cracking	9.55	Diag. Tension Cracking	1.33
	R_s = 1.0		2.96	9.62	16.80	Diag. Tension Cracking	9.55	Diag. Tension Cracking	1.76
	R_s = 3.0		1.81	5.88	11.40	Shear stud	9.55	Diag. Tension Cracking	1.19
4-story	Trad. / R_s = 2.5	Roof	1.32	3.30	3.31	Sidelap fastener	2.45	Sidelap fastener	1.35
	R_s = 1.0		2.90	8.70	8.70	Connection (Weld)	0.53	Connection (Weld)	16.42
	R_s = 3.0		0.92	2.30	2.07	Sidelap fastener	2.45	Sidelap fastener	0.84
	Trad. / R_s =2.5	Floor	2.96	9.62	11.40	Shear stud	9.55	Diag. Tension Cracking	1.19

	R_s = 1.0		4.74	15.41	16.80	Diag. Tension Cracking	9.55	Diag. Tension Cracking	1.76
	R_s = 3.0		1.81	5.88	11.40	Shear stud	9.55	Diag. Tension Cracking	1.19
8-story	Trad.	Roof	0.92	2.30	2.07	Sidelap fastener	2.45	Sidelap fastener	0.84
	R_s = 1		3.76	11.28	11.28	Connection (Weld)	0.53	Connection (Weld)	21.28
	R_s = 2.5 / R_s = 3.0		1.32	3.30	3.31	Sidelap fastener	2.45	Sidelap fastener	1.35
	Trad.	Floor	1.81	5.88	11.40	Shear stud	9.55	Diag. Tension Cracking	1.19
	R_s = 1		4.74	15.41	17.10	Shear stud	9.55	Diag. Tension Cracking	1.79
	R_s = 2.0 / R_s = 3.0		1.81	5.88	11.40	Shear stud	9.55	Diag. Tension Cracking	1.19
12-story	Trad.	Roof	0.92	2.30	2.07	Sidelap fastener	2.45	Sidelap fastener	0.84
	R_s = 1.0		3.76	11.28	11.28	Connection (Weld)	0.53	Connection (Weld)	21.28
	R_s = 2.5 / R_s = 3.0		1.32	3.30	3.31	Sidelap fastener	2.45	Sidelap fastener	1.35
	Trad.	Floor	1.81	5.88	12.70	Diag. Tension Cracking	9.55	Diag. Tension Cracking	1.33
	R_s = 1.0		2.96	9.92	17.10	Shear stud	9.55	Diag. Tension Cracking	1.79
	R_s = 2.0 / R_s = 3.0		1.81	5.88	12.70	Diag. Tension Cracking	9.55	Diag. Tension Cracking	1.33

Table 3-9. Diaphragm Design specification for different diaphragm design

Building Model	Level	Diaphragm Design	Design Specification
1-story (bare steel deck roof)	Roof	Trad. / R_s = 3.0/ R_s = 2.5	1.5 in. B deck, 20 gauge, 36/9 pattern, structural connection: PAF @ 5.8 in. sidelap connection: #12 @ 10.7 in.
		R_s = 1.0	1.5 in. B deck, 18 gauge, 36/9 pattern, structural connection: PAF @ 4.4 in. sidelap connection: #12 @ 8.3 in.
1-story (comp. deck roof)	Roof	Trad. / R_s = 3.0/ R_s = 2.0	3.25 in LW fill above 1.5 in. B deck, 0.00075 reinforcing ratio, 3/4 in. shear studs @ 18 in. o.c. or less
		R_s = 1.0	3.25 in LW fill above 1.5 in. B deck, 0.0025 reinforcing ratio, 3/4 in. shear studs @ 30 in. o.c. or less
4-story	Roof	Trad. / R_s = 2.5	1.5 in. B deck, 18 gauge, 36/9 pattern, structural connection: PAF @ 4.4 in. sidelap connection: #12 @ 8.3 in.
		R_s = 1.0	1.5 in. B deck, 18 gage Roof Deck, structural connection: 3/4". arc-spot in 36/7 pattern, Exterior: 3/4". arc-spot @ 6", sidelap connection: Top arc seam 12 per span
		R_s = 3.0	1.5 in. B deck, 20 gauge, 36/9 pattern, structural connection: PAF @ 5.8 in. sidelap connection: #12 @ 10.7 in.
	Floor (4)	Trad. / R_s = 2.0	3.25 in LW fill above 1.5 in. B deck, 0.0025 reinforcing ratio, 3/4 in. shear studs @ 30 in. o.c. or less
		R_s = 1	3.25 in LW fill above 1.5 in. B deck, 0.0025 reinforcing ratio, 3/4 in. shear studs @ 16 in. o.c. or less

		R_s = 3	3.25 in LW fill above 1.5 in. B deck, 0.00075 reinforcing ratio, 3/4 in. shear studs @ 18 in. o.c. or less
8-story	Roof	Trad.	1.5 in. B deck, 20 gauge, 36/9 pattern, structural connection: PAF @ 5.8 in. sidelap connection: #12 @ 10.7 in.
		R_s = 1.0	1.5 in. B deck, 16 gage Roof Deck, structural connection: 3/4". arc-spot in 36/7 pattern, Exterior: 3/4". arc-spot @ 6", sidelap connection: Top arc seam 12 per span
		R_s = 2.5 / R_s = 3.0	1.5 in. B deck, 18 gauge, 36/9 pattern, structural connection: PAF @ 4.4 in. sidelap connection: #12 @ 8.3 in.
	Floor (8)	Trad.	3.25 in LW fill above 1.5 in. B deck, 0.00075 reinforcing ratio, 3/4 in. shear studs @ 18 in. o.c. or less
		R_s = 1.0	3.25 in LW fill above 1.5 in. B deck, 0.0025 reinforcing ratio, 3/4 in. shear studs @ 16 in. o.c. or less
		R_s = 2.0 / R_s = 3.0	3.25 in LW fill above 1.5 in. B deck, 0.0025 reinforcing ratio, 3/4 in. shear studs @ 30 in. o.c. or less
12-story	Roof	Trad.	1.5 in. B deck, 20 gauge, 36/9 pattern, structural connection: PAF @ 5.8 in. sidelap connection: #12 @ 10.7 in.
		R_s = 1	1.5 in. B deck, 16 gage Roof Deck, structural connection: 3/4". arc-spot in 36/7 pattern, Exterior: 3/4". arc-spot @ 6", sidelap connection: Top arc seam 12 per span
		R_s = 2.5 / R_s = 3.0	1.5 in. B deck, 18 gauge, 36/9 pattern, structural connection: PAF @ 4.4 in. sidelap connection: #12 @ 8.3 in.
	Floor (12)	Trad.	3.25 in LW fill above 1.5 in. B deck, 0.00075 reinforcing ratio, 3/4 in. shear studs @ 18 in. o.c. or less
		R_s = 1.0	3.25 in LW fill above 1.5 in. B deck, 0.0025 reinforcing ratio, 3/4 in. shear studs @ 12 in. o.c. or less
		R_s = 2.0 / R_s = 3.0	3.25 in LW fill above 1.5 in. B deck, 0.0025 reinforcing ratio, 3/4 in. shear studs @ 30 in. o.c. or less

3.3. Computational Modeling of BRBF Archetype

As a complimentary work to investigate the conventional steel buildings with different diaphragm design, an identical series of archetypes are analyzed by Wei *at al.* [49]. All the modeling assumption are chosen, as same as the current study with SCBF as VLFRS, to compare the results. BRB brace is calibrated based on the stress-strain experimental database tests. The details related to BRB calibration can be found in [49]. In addition, different diaphragm designs with different scale factors are provided in [49] to evaluate the seismic performance of the steel buildings. It should be noted that three diaphragm design (Traditional, R_s = 1.0, and R_s = 2.0 /2.5) are selected for analysis is BRB archetypes versus four diaphragm design for SCBF (Traditional, $R_s = 1.0$, $R_s = 2.0$ /2.5, and $R_s = 3.0$). For BRBF archetypes the number of cases for based on diaphragm design decreased to Traditional or $R_s = 2.0$ /2.5, and $R_s = 1.0$ due to the minimum values controlling the design. More information can be find in [49].

3.4. Conclusion

The details for three-dimensional modeling of SCBF archetypes with different diaphragm design procedures are presented in this chapter. A series of one-, four-, eight-, and twelve-story archetypes with different diaphragm systems are introduced. To do the simulation, the computational model for the SCBF braces is calibrated versus available studies in the literature. To capture the accurate response of SCBF brace, corotational geometric transformation is with six nonlinear beam-column elements along the brace length are assigned to *OpenSees* [56] model. Geometric imperfection equal to *L/1000* is utilized in the computational model to simulate the buckling behavior of SCBF brace. Since low-cycle fracture is a dominant failure mode for SCBF braces, a fracture strain value equal to 0.05 is assigned to *MINMAX* Uniaxial material in *OpenSees* [56] . The simulated response of the SCBF brace shows a good agreement with experimental results.

Diaphragm system is simulated using two diagonal truss elements and *Pinching4* material in *OpenSees* [56]. Different parameters of *Pinching4* material are obtained using a multi-level optimization algorithm with different objectives. Three cantilever diaphragm tests are considered to calibrate the computational model. The result from simulation shows a good agreement with experimental results. Finally, a brief description is provided for complementary work for this study which focus on same archetype building with BRBF as vertical lateral force resisting system.

Chapter 4

Fundamental Response of SCBF Steel Archetypes

4.1. Introduction

Fundamental response of SCBF steel archetypes is needed to assess the seismic performance of the buildings and make comparisons for different diaphragm design procedures. Dynamic characteristics of steel buildings such as fundamental natural periods and mode shapes are two key parameters for the design of steel structures. Unrealistic values of fundamental natural periods could affect the design of SCBF building and result in inaccurate design and poor seismic performance.

The recent advent of performance-based design shows that nonlinear static pushover analysis is a powerful tool to evaluate the response and failure modes in the buildings. In pushover analysis is a displacement-controlled method in which the magnitude of the structural loading is incrementally increased in accordance with a certain predefined pattern which is usually based on 1st mode shape of the structure. Period-based ductility, overstrength and general response of the structure could reveal the static response of the structure and use for time history response evaluation.

In this chapter, the fundamental natural periods and mode shapes of SCBF archetypes with different diaphragm design procedures are presented using modal analysis in *OpenSees*

[56] software. The effects of diaphragm flexibility are investigated by comparing the results from *OpenSees* [56] with *SAP2000* [39] structural analysis software. In addition, Period-based ductility, overstrength and general response of the structure are presented by nonlinear static pushover analysis in both transverse and longitudinal direction of the SCBF archetype buildings.

4.2. Response Validation for Simulation

Post-processing of structural response is one of the key parameters of all computational models. By having a wide range of quantities for structural response such as nodal displacements, element deformations, element forces, and reactions, it is necessary to post-process the quantities and derive the critical values needed to evaluate the performance of the building. In this study, drift ratios related to different locations of the building and diaphragm shear angle (i.e., shear strain), are two main parameters which are described in this section

4.2.1. Story Drift Ratio Calculation

In static nonlinear pushover analysis, roof drift ratio is obtained as the applied displacement at the roof level divided by the total building height. For nonlinear time history analysis, story drift ratio (SDR) at any timestep is calculated for the transverse and longitudinal directions at each story, which is defined as the transverse and longitudinal relative displacements of any two nodes on the adjacent floors with the same coordinates, divided by the story height. The resultant story drift ratio at any time in the record is derived by taking the square root of the sum of the squares (SRSS) of the story drift ratios in the transverse and longitudinal directions at that time. The peak story drift ratio is then determined by the largest value of the resultant story drift ratio at any time during the motion and at any location of the building.

4.2.2. Diaphragm Shear Angle Calculation

Diaphragm in-plane shear strain, at the center of each diaphragm unit, can be calculated based on fundamental continuum mechanics using displacement fields. Equation (4-1) shows the shear strain formula.

$$\gamma = \frac{\partial u_x}{\partial y} + \frac{\partial u_y}{\partial x} \tag{4-1}$$

where u_x and u_y are the displacement at the center of diaphragm unit along *x* and *y* direction, respectively. u_x and u_y are obtained using piecewise finite element approximation.

$$u_x = \sum_{i=1}^{4} N_i\left(x,y\right)u_{x,i} \tag{4-2}$$

$$u_y = \sum_{i=1}^{4} N_i\left(x,y\right)u_{y,i} \tag{4-3}$$

where $u_{x,i}$ and $u_{y,i}$ are displacement fields along longitudinal and transverse direction of the building. $N_i\left(x,y\right)$ are the shape functions as follows,

$$N_1\left(x,y\right) = \frac{\left(x-x_2\right)\left(y-y_2\right)}{A} \tag{4-4}$$

$$N_2\left(x,y\right) = -\frac{\left(x-x_1\right)\left(y-y_2\right)}{A} \tag{4-5}$$

$$N_3\left(x,y\right) = \frac{\left(x-x_1\right)\left(y-y_1\right)}{A} \tag{4-6}$$

$$N_4\left(x,y\right) = -\frac{\left(x-x_2\right)\left(y-y_2\right)}{A} \tag{4-7}$$

In Equations (4-4) to (4-7), (x_1, y_1) and (x_2, y_1) are the coordinates of Node 1 and Node 2. In addition, Node 3 and Node 4 coordinates are (x_2, y_2) and (x_1, y_2), respectively.

4.3. Modal Analysis

Natural period of steel structures has a significant role in seismic design of the building. Inaccurate values for natural period and the mode shapes of the building can result in an overestimation or underestimation in seismic response of structure. Diaphragm systems as a part of lateral force resisting system could affect the values of natural period. As described in 3, different assumption for diaphragm design could change the response prediction of structures. Considering flexible diaphragm assumption results in larger natural period for structures compared to rigid diaphragm assumption for the building. In this section, modal analysis is performed for the archetype buildings in *OpenSees* software [56] to derive the natural periods and mode shapes. The results from *OpenSees* software are compared to the natural periods of the structural models in *SAP2000* [56]software provided by Torabian *et al.* . [76] based on rigid diaphragm assumption.

4.3.1. Estimated Natural Periods and Mode Shapes

Eigenvalue analysis is performed for the SCBF archetype buildings to obtain their estimated natural periods and mode shapes. To study the effect of the rigid diaphragm assumption on modal properties of the building structure, linear elastic models are also created using the commercial structural analysis program *SAP2000* [39]. Table 4-1 shows the 1st and 2nd estimated natural periods of SCBF archetype buildings derived from eigenvalue analysis in *OpenSees* and *SAP2000* [39] software. Elastic diaphragm assumption has been used for the analysis in *OpenSees* [56] software. In *SAP2000* [39] software, SCBF archetypes are modeled and analyzed by considering rigid diaphragm assumption. In Table 4-1, one-story archetype building with bare steel deck roof has a more flexible diaphragm, so the fundamental period is most affected by the rigid diaphragm assumption in the *SAP2000* [39] model. It can be observed that diaphragm deflections can have a substantial effect on building natural period (up to 66% larger than rigid). This is consistent with results from Sadashiva *et al.* [67] and Tremblay and Rogers [66]where the one-story building mostly affected by diaphragm flexibility. The results also demonstrate that archetypes with concrete-filled deck floor diaphragms which has more rigid diaphragm are less affected in modal analysis. The results also shows that the diaphragm flexibility have smaller effect on natural period of structure with increasing the total height of the building. The reason can be attributed to the dominancy of vertical lateral force resisting system stiffness, SCBF, in the building compared to horizontal lateral force resisting system stiffness, diaphragm systems. In addition, as it was excepted, the natural periods increase for taller archetypes due to the lower lateral stiffness in the building.

Table 4-1. Natural Periods of SCBF Archetype Models in *OpenSees* [56] and *SAP2000* [39]

Building Model	Long Dimension Mode 1 (sec)			Short Dimension Mode 1 (sec)		
	Elastic Diaphragm (*OpenSees*)	Rigid Diaphragm (*SAP2000*)	Difference	Elastic Diaphragm (*OpenSees*)	Rigid Diaphragm (*SAP2000*)	Difference
1-story[a]	0.36	0.18	50%	0.89	0.30	66%
1-story[b]	0.37	0.32	15%	0.59	0.34	42%
4-story	0.75	0.69	8%	0.90	0.70	22%
8-story	1.46	1.39	5%	1.50	1.33	11%
12-story	2.12	1.96	8%	2.07	1.83	11%

[a]: bare steel deck roof; [b]: composite deck roof

Figure 4-1 Shows the 1st mode shape of four-story archetype building for both *OpenSees* [56] and *SAP2000* [39] software. It can be observed that the 1st mode shape is transverse direction of the building for both models. In addition, first four model shapes of four-story archetype building are provided in Figure 4-2.

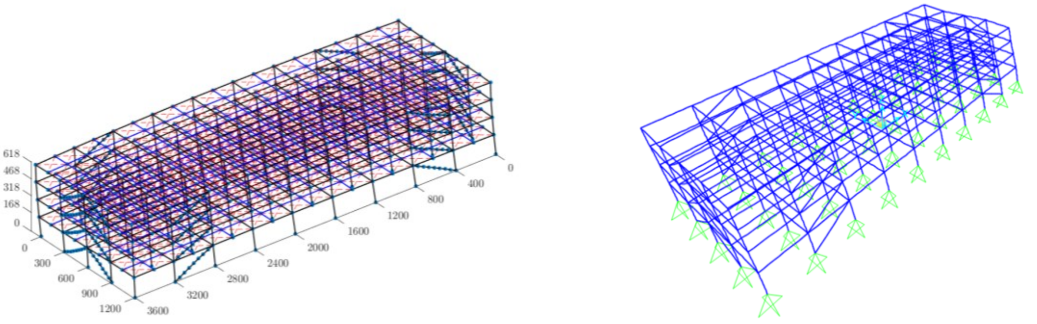

(a) (b)

Figure 4-1. Mode shapes for the 1st mode of four-story archetype models: (a) *OpenSees* [56] model; (b) *SAP2000* [39] model.

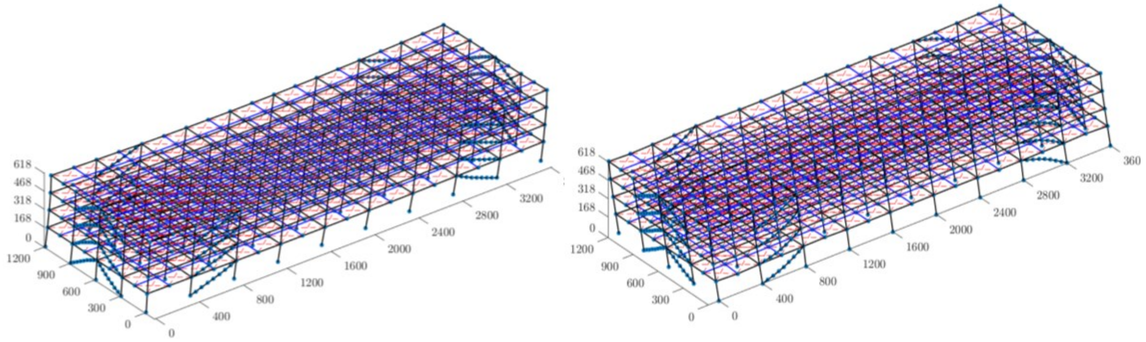

(a) Short dimension Mode 1 ($T = 0.90$ sec) (b) Long dimension Mode 1 ($T = 0.75$ sec)

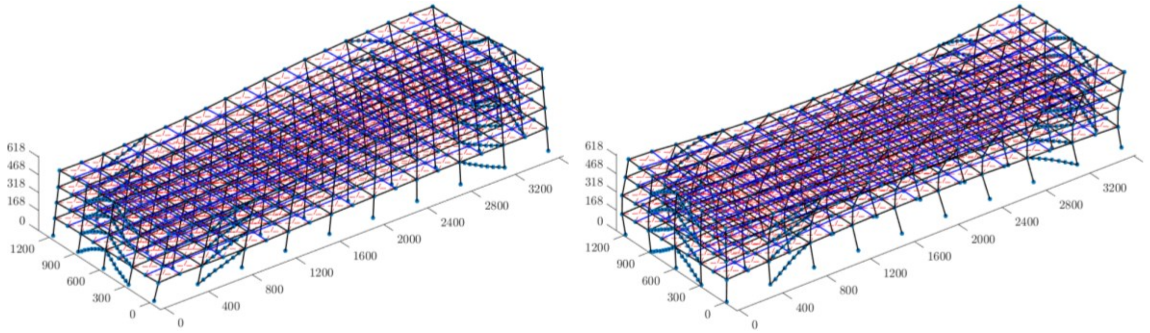

(c) Short dimension Mode 2 ($T = 0.59$ sec) (d) Torsional mode ($T = 0.48$ sec)

Figure 4-2. Mode shapes of four-story archetype models.

4.4. Nonlinear Static Pushover Analysis

To evaluate the static behavior of SCBF archetype buildings, nonlinear static pushover analysis is performed. Ductility and Overstrength of the archetypes with different diaphragm design are derived as two key parameters to predict the seismic performance of the buildings. Based on FEMA P-695 [38] provision, vertical distribution of lateral force at each node is assigned proportional to the product of the tributary mass and the fundamental mode shape coordinate at the node: $F_x \alpha m_x \phi_{1,x}$, where F_x is the relative magnitude of force applied at node x, m_x is the mass associated with node x, and $\phi_{1,x}$ is the fundamental mode shape coordinate at node x. To apply the static load for the nonlinear static pushover analysis in short direction of the building, a displacement control load pattern is used in transverse direction where the displacement of the center node on the roof in the short direction controlled the solution. Similar to nonlinear static pushover analysis in short direction, a displacement control load pattern is used in longitudinal direction to do the nonlinear static pushover analysis in long direction of the archetype building. Figure 4-3 shows a schematic drawing of four-story archetype with the displacement control load pattern in two different direction of the building. In addition, a view of the lateral force distribution on transverse direction of the four-story archetype building is shown in Figure 4-4, in which the arrow length denotes the relative magnitude of the applied force.

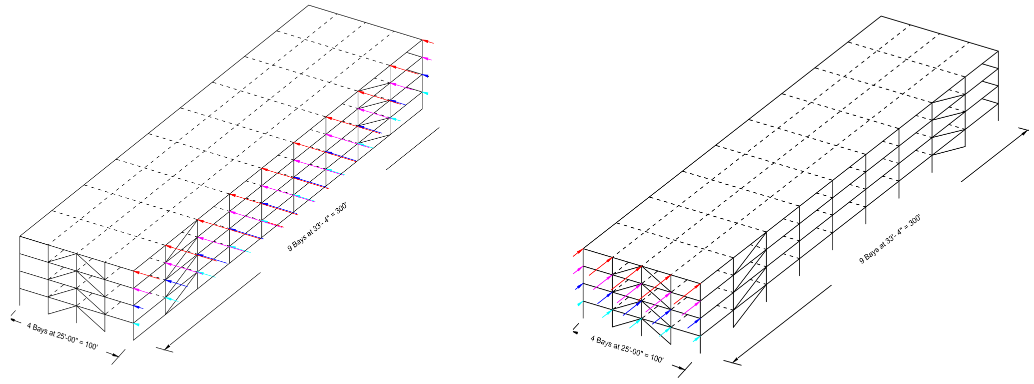

(a) (b)

Figure 4-3. Schematic load pattern direction: (a) Transverse direction pushover (Short direction); (b) Longitudinal direction pushover (Long direction).

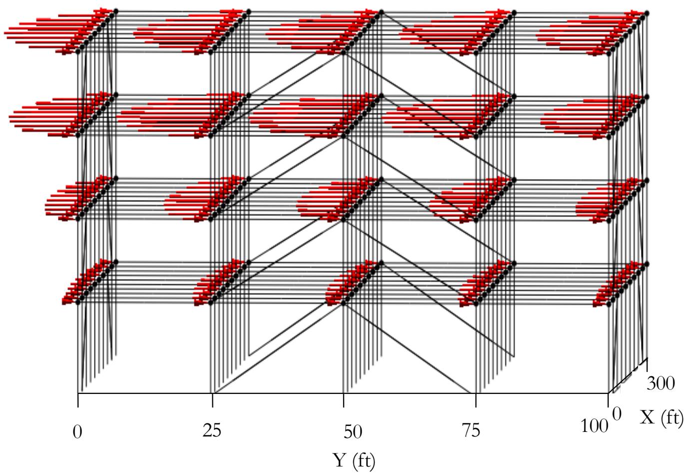

Figure 4-4. Lateral force distribution on four-story archetype building for pushover analysis in transverse direction (Load distributed along the longer span).

Figure 4-5 shows the static response of SCBF archetype buildings with different diaphragm design procedures for the transverse direction of the building. The drift ratio is calculated as the applied displacement at the center of roof divided by the building height. Generally, the system behavior of SCBF archetypes could be explained using three individual regions: (1) an elastic stiffness region in which the frame response usually reaches the design base shear and typically ends with SCBF buckling in a story. Noted that the buckling of the

SCBF usually occurs in the first story of the building; (2) a secondary stiffness region in which the SCBF experiences a combination of buckling and yielding, and the maximum brace capacity is attained; (3) in the third region the frame exhibits response until P-Δ completely destabilizes the structure and causes collapse. In Figure 4-5, one-story with bare deck roof for both R_s = 1.0 and Traditional/ R_s = 2.5/ R_s = 3.0 diaphragm design procedures, the system behavior deviated from elastic region with the onset of SCBF buckling. For R_s = 1.0 diaphragm design procedure, the failure dominated by SCBF brace buckling and yielding. In addition, the initial stiffness is larger compared to Traditional / R_s = 2.5/ R_s = 3.0 diaphragm design. The reason could be attributed to the nature of the capacity design procedure for SCBF braces. The SCBF braces are not designed based on the actual end-to-end length which results in a larger size for SCBF braces. The explained design procedure for SCBF also can cause a significant increase in overstrength value. The SCBF also must be checked for satisfying the high-ductility limits. Hollow structural section (HSS) size limitation can cause an increase on the size of the brace beyond the strength requirement (*b*/*t* limits). For Traditional / R_s = 2.5/ R_s = 3.0 diaphragm design, the diaphragm experiences substantial inelastic deformation. In this case, he failure mode is dominated by loss of rigidity in the roof diaphragm. Significant inelastic deformation in diaphragm is the reason for having a smaller value for the peak strength of Traditional / R_s = 2.5/ R_s = 3.0 diaphragm design procedure.

For both one-story with concrete-filled deck and four-story SCBF archetypes, in all the diaphragm design procedure analysis, the observation is the brace buckling in the first story. The SCBF buckling and yielding happens until the archetype reaches the maximum applied load value. Developing story mechanism in the first story cause collapse due to P-Δ effect and yielding of the brace. four-story SCBF archetype shows lower ultimate deformation compared to one-story with concrete-filled deck-story archetype because of less amount of ductility. The large reduction in frame ductility as the number of stories increases can described by worsening of the P-Δ effect for taller structures. In should be noted that in static nonlinear pushover analysis, SCBF archetypes usually experience unrealistic large amount of deformation due to lack of energy dissipation and fracture happening in dynamic behavior of structure. The results from the current study shows similar behavior to the pushover analysis results for SCBF steel building in the literature such as [16] and [85].

In Figure 4-5, eight- and twelve-story SCBF archetypes response appears bilinear because of the distribution of lateral stiffness through the height of building. This observation is attributed to the behavior of SCBF braces work in tension that results in no loss of system stiffness or strength until yielding happens in tension brace. Another reason is the designing the SCBFs with the size beyond the strength requirement. These results are consistent with previous study from [86],which shows that the tension braces failure could be the dominant limit state for nonlinear pushover analysis of SCBF archetype buildings.

The results also show that except one-story with bare deck roof with Traditional / $R_s = 2.5$/ $R_s = 3.0$ diaphragm design, the limit state of all archetypes with various diaphragm design procedure is dominated by yielding and buckling of the SCBF braces in first floor of the building. Noted that buckling and yielding of the braces are also occurred for the braces in higher levels of the building.

Figure 4-6 shows the static response of SCBF archetype buildings with different diaphragm design procedures for the longitudinal direction of the building. It can be seen that except one-story with bare deck roof with Traditional / $R_s = 2.5$/ $R_s = 3.0$ diaphragm design, which has a clear deviation between the first region of elastic stiffness and second region of buckling and yielding of the braces, the failure mode of the other archetypes is yielding in the tension braces while compression braces buckled. This behavior was excepted due to high in-plane stiffness for the diaphragm in longitudinal direction. Moreover, for the eight-story archetype diaphragm design of R_s = 1.0, the peak value of applied load is larger than other diaphragm designs. As it discussed before, the reason could be described by the design philosophy of SCBF braces and oversized SCBF braces designed for more than the strength requirement.

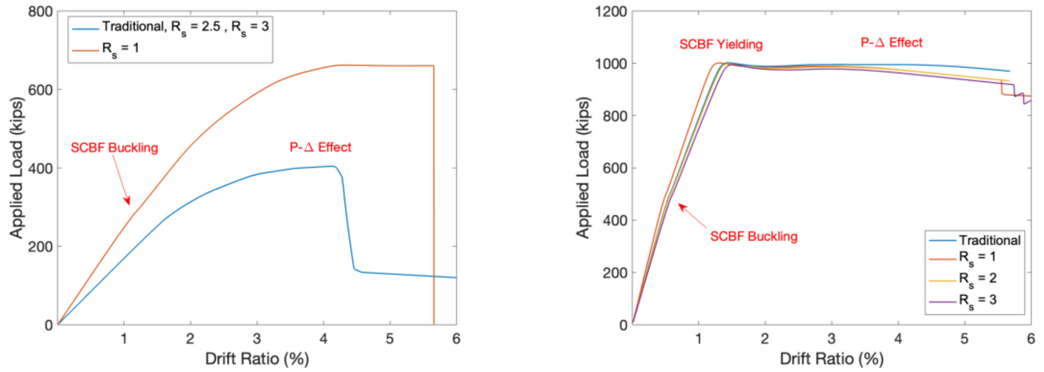

(a) One-story with bare steel deck roof

(b) One-story with concrete-filled steel deck roof

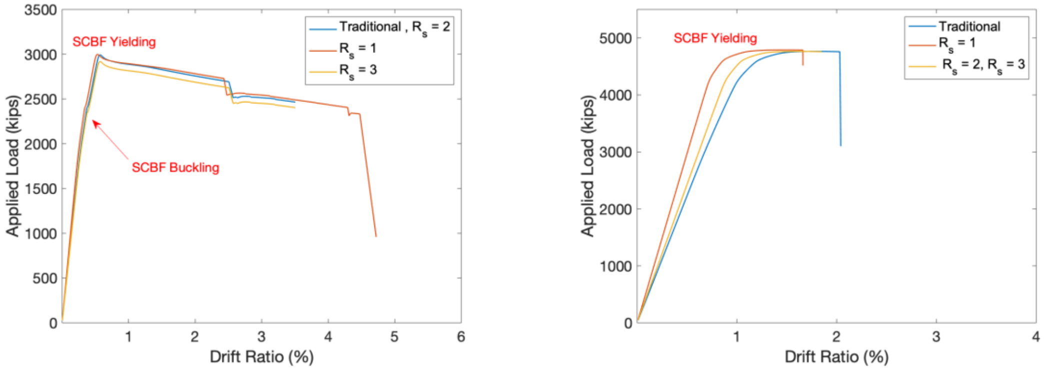

(c) Four-story

(d) Eight-story

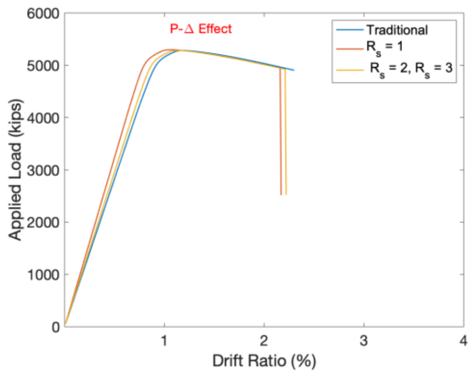

(e) Twelve-story

Figure 4-5. Pushover curves in transverse direction with different diaphragm design procedures.

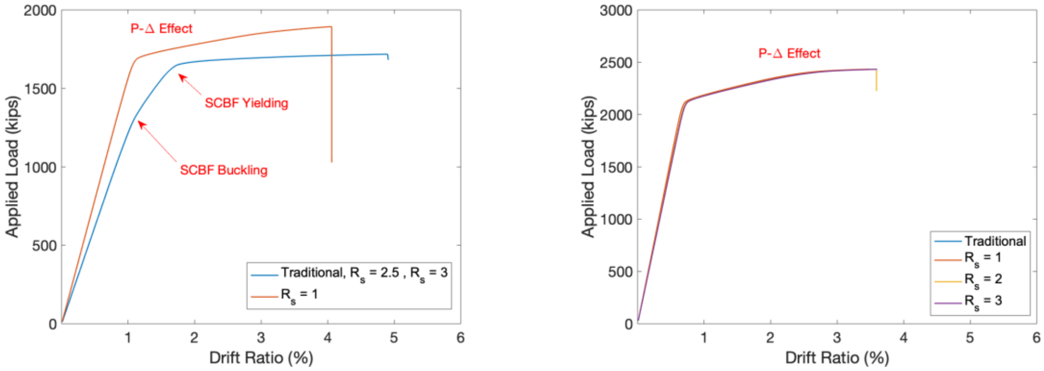

(a) One-story with bare steel deck roof

(b) One-story with concrete-filled steel deck roof

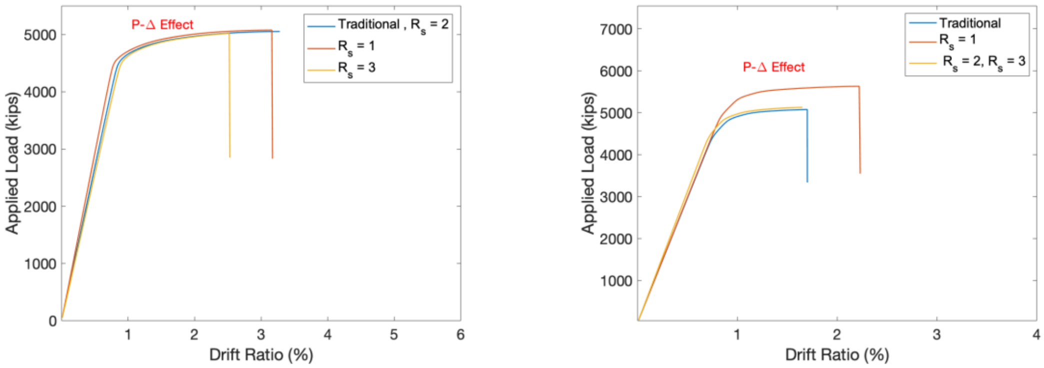

(c) Four-story

(d) Eight-story

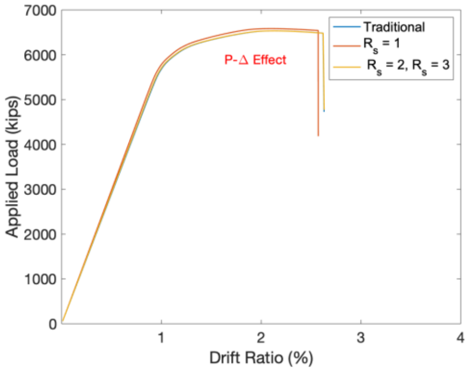

(e) Twelve-story

Figure 4-6. Pushover curves in longitudinal direction with different diaphragm design procedures.

Period-based ductility (μ_T) and overstrength (**Ω**) are obtained from pushover analyses for both transverse and longitudinal directions of the archetype buildings. The period-based ductility (μ_T) defined as the ratio of the post-peak roof displacement ($\delta_{u\ 80\%}$), at the point of 20% strength loss (0.8Pmax) to the effective yield roof displacement ($\delta_{y,eff}$), which can be obtained using Equation (2-9) which is the Equation B-2 in *FEMA P-695* [38]. For the models with convergence issues, the roof displacement in the last step of analysis (δ_u) is used instead of the post-peak roof displacement ($\delta_{u\ 80\%}$). The overstrength (**Ω**) of the building is calculated by dividing the peak load by the design base shear (See Equation 2-10).

The period-based ductility and overstrength for both transverse and longitudinal directions are tabulated in Table 4-2. The overstrength values for archetypes with different diaphragm design except one-story archetype with bare deck roof and four-story archetypes, are generally larger than the overstrength factor, $\Omega_0 = 2$, specified by *ASCE 7-16* [10].

Table 4-2. Overstrength and period-based ductility for archetype buildings

Building Model	Diaphragm Design	Design Shear (kips)	Transverse Direction		Longitudinal Direction	
			Ductility (μ_T)	Overstrength (Ω)	Ductility (μ_T)	Overstrength (Ω)
1-story[a]	R_s = 1.0	218	2.70	3.04	5.23	1.24
	Trad. / R_s = 2.5 / R_s = 3.0		2.40	1.85	3.85	1.12
1-story[b]	R_s = 1.0	451	8.81	4.59	2.06	1.59
	Trad.		5.83	2.22	2.18	1.59
	R_s = 2.0		5.74	4.58	2.19	1.59
	R_s = 3.0		6.50	2.21	2.21	1.59
4-story	R_s = 1.0	1529	4.11	1.96	4.60	3.32
	Trad. / R_s = 2.0* or 2.5**		3.51	1.96	4.70	3.31
	R_s = 3.0		3.8	1.96	3.61	3.28
8-story	R_s = 1.0	2021	3.25	2.37	2.57	3.36
	Trad.		3.38	2.36	2.60	2.32
	R_s = 2.0* or 2.5** / R_s = 3.0		3.39	2.36	2.60	3.32
12-story	R_s = 1.0	2295	2.55	2.31	3.31	2.87
	Trad.		2.86	2.30	3.33	2.85
	R_s = 2.0* or 2.5** / R_s = 3.0		2.86	2.30	3.35	2.85

[a]: bare steel deck roof; [b]: composite deck roof

*: R_s = 2.0 with concrete-filled steel deck; **: R_s = 2.5 with bare steel deck (roof)

As it discussed, the large overstrength values can be attributed to the confluence of capacity design process for SCBFs and the modeling assumption where the design length of the brace is smaller than the brace length in the computational model. In 2019, Grabner and Fahnestock [16] reported high overstrength values for SCBF frames. For one-story archetype with bare deck roof and four-story archetypes, the overstrength is less than $\mathbf{\Omega}_0$ = 2. In

Addition, Kircher *et al.* [55] results revealed that the SCBF archetypes with smaller values of overstrength compared to the design overstrength factor are more vulnerable and demonstrated poor seismic performance during earthquakes.

The period-based ductility varied across the SCBF archetypes with different diaphragm design procedures. Generally, the period-based ductility decreases by increasing the number of stories in the building. The reduced ductility capacity for the taller archetypes is because of the P-Δ effects for higher stories. The results also show that for taller archetypes in which the dominant limit state is related to vertical lateral force resisting system, the diaphragm design procedures do not affect the ductility values. For one-story and four-story archetypes, diaphragm design procedures could change the ductility values where the $R_s = 1.0$ diaphragm design procedures has larger values for ductility. For pushover analysis in longitudinal direction, the values for both ductility and overstrength are directly related to the SCBF design since the in-plane stiffness of the diaphragm is significant in longitudinal direction. The deformed shapes of the building models at the end of the pushover analysis are shown in Figure 4-7. As it can be seen, the deformed shapes of the archetypes are mostly due to the lower stories' deformation. However, significant inelastic deformation of diaphragm system is observed in Figure 4-7a.

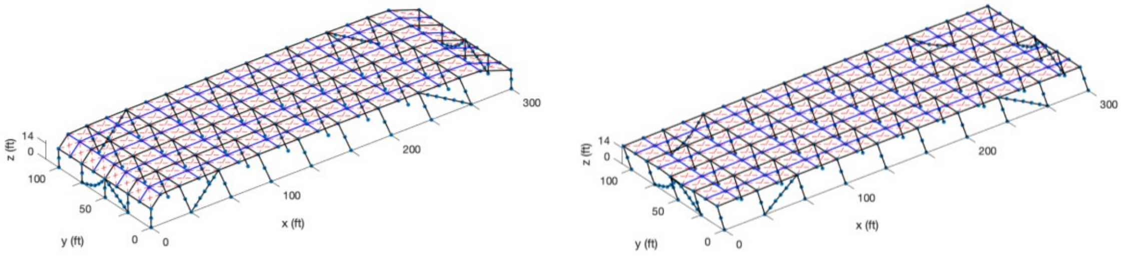

(a) One-story with bare steel deck roof

(b) One-story with concrete-filled steel deck roof

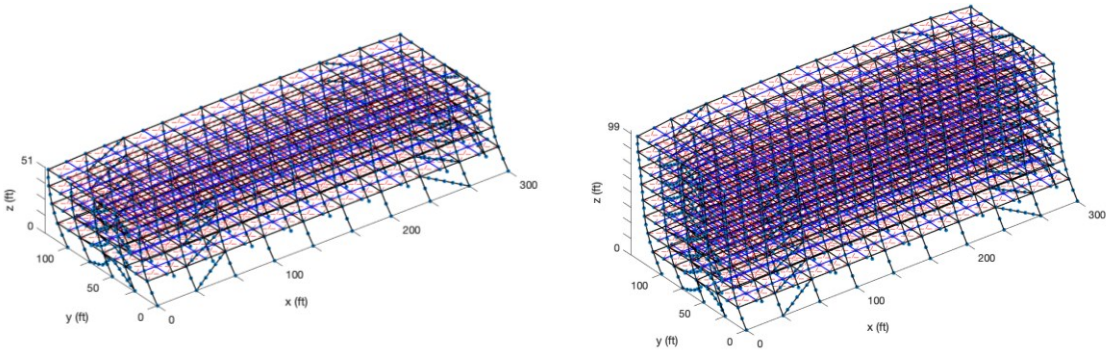

(c) Four-story

(d) Eight-story

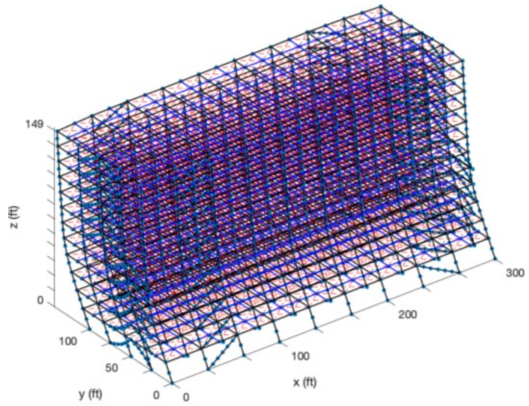

(e) Twelve-story

Figure 4-7. Deformed shapes of archetype buildings with Trad diaphragm design procedures (deformation amplification factor: 10).

4.5. Conclusion

Fundamental response of SCBF archetypes with different diaphragm procedures are presented and discussed in this chapter. Modal analysis and nonlinear static pushover analysis are investigated. Based on the results from modal analysis, rigid diaphragm assumption for the design can result in an inaccurate seismic performance prediction for SCBF steel archetypes due to the imprecise values for natural period of the structure. Natural period of SCBF archetypes could vary more than 66 precent compared to rigid diaphragm assumption in *SAP2000* [39] model for one-story building with bare steek deck roof system. The difference in natural period values also shows the contribution of the diaphragm to the lateral force resisting system as it was expected for alternative design procedure available in *ASCE 7-22*.

The nonlinear static pushover analysis results are presented for SCBF archetypes with different diaphragm procedures in both transverse and longitudinal directions. The results show that generally the SCBF archetype response starts with an elastic stiffness region where the braces in compression experience buckling. The tension braces yield while the compression braces buckle in compression. The response continues and ends by P-Δ effects in the archetype building. For taller buildings, the response could be bilinear due to yielding of tension braces in a system with distributed stiffness in different levels of the building. The findings demonstrate the effects of SCBF design procedure on nonlinear static pushover analysis results. Different diaphragm design procedures in SCBF archetypes does not have significant impact on behavior of the building except one-story building with steel bare deck roof system.

Moreover, he overstrength and period-based ductility values are presented and discussed. The results show that in general the ductility of the building decrease for taller buildings due to P-Δ effects. For one-story and four-story archetypes, diaphragm design procedures could change the ductility values where the $R_s = 1.0$ diaphragm design procedures has larger values for ductility. For pushover analysis in longitudinal direction, the values for both ductility and overstrength are directly related to the SCBF design since the in-plane stiffness of the diaphragm is significant in longitudinal direction.

Chapter 5

Nonlinear Time History Response of SCBF Archetype Buildings

5.1. Introduction

To evaluate the seismic performance of the archetype buildings with different diaphragm design procedures, nonlinear response history analysis was performed with the archetype models subjected to the suite of *FEMA P-695* [38] far-field earthquake motions. This section provides some details for the scaling of ground motion records to desired hazard levels and the criteria adopted to define building collapse.

In addition, the performance of SCBF archetypes with different diaphragm design procedures are investigated and discussed based on *FEMA P-695* [38] Methodology.

5.2. Ground Motion Scaling

To represent different hazard levels in nonlinear response history analysis (NRHA), 22 pairs of ground motion records from the *FEMA P-695* [38] far-field record suite are scaled to different intensities and applied orthogonal directions of the building. Table 3-1 shows the magnitude, year, location and other information of the 22 ground motion pairs.

Table 5-1. Far-Field Ground Motions Used for Nonlinear Response History Analysis

ID No.	Earthquake			Recording Station	
	Magnitude	Year	Name	Name	Owner
1	6.7	1994	Northridge	Beverley Hills - Mulhol	USC
2	6.7	1994	Northridge	Canyon Country - WLC	USC
3	7.1	1999	Duzke, Turkey	Bolu	ERD
4	7.1	1999	Hector, Mine	Hector	SCSN
5	6.5	1979	Imperial Valley	Delta	UNAMUCSD
6	6.5	1979	Imperial Valley	El Centro Array #11	USGS
7	6.9	1995	Kobe, Japan	Nishi-Akashi	CUE
8	6.9	1995	Kobe, Japan	Shin-Osaka	CUE
9	7.5	1999	Kocaeli, Turkey	Duzce	ERD
10	7.5	1999	Kocaeli, Turkey	Arcelik	KOERI
11	7.3	1992	Landers	Yermo Fire Station	CDMG
12	7.3	1992	Landers	Coolwater	SCE
13	6.9	1989	Loma Prieta	Capitola	CDMG
14	6.9	1989	Loma Prieta	Gilroy Array #3	CDMG
15	7.4	1990	Mnajil, Iran	Abbar	BHRC
16	6.5	1987	Superstition Hills	El Centro Imp. Co.	CDMG
17	6.5	1987	Superstition Hills	Poe Road (temp)	USGS
18	7.0	1992	Cape Mendocino	Rio Dell Overpass	CDMG
19	7.6	1999	Chi-Chi, Taiwan	CHY101	CWB
20	7.6	1999	Chi-Chi, Taiwan	TCU045	CWB
21	6.6	1971	San Fernando	LA – Hollywood Star	CDMG
22	6.5	1976	Friuli, Italy	Tolmezzo	-

Three scale levels were considered for nonlinear response history analysis as follows,

- Design earthquake (DE)
- Maximum considered earthquake (MCE)
- A scale level based on adjusted collapse marginal ratio ($ACMR_{10\%}$)

Ground motion scaling involves two steps for *DE* and *MCE* levels. In the first step, individual records are normalized by their respective peak ground velocities, as described in *Appendix A* of *FEMA P-695* [38]. This step is intended to remove unwarranted variability between records due to inherent differences in event magnitude, distance to source, source type and site condition, without eliminating overall record-to-record variability. To be consistent with the *FEMA P-695* [38] methodology, spectral acceleration with 5% damping ratio is considered in the ground motion scaling. shows the unnormalized and normalized spectral acceleration for the 22 pairs of ground motions and 5% damping ratio.

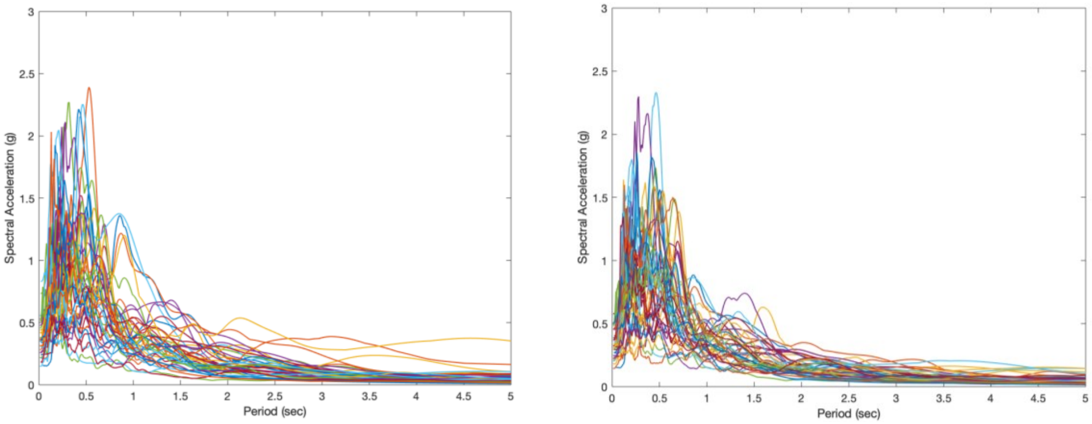

(a) (b)

Figure 5-1. Spectral acceleration with 5% damping ratio for P695 far-field record suite: (a) Raw records; (b) Normalized records.

In the second step, normalized values for spectral accelerations are collectively scaled to a specific intensity (e.g., *MCE*) such that the median spectral acceleration of the record set matches the spectral acceleration of the target spectrum at the fundamental period, T, of the archetype building. Per *FEMA P-695* [38] methodology, the value of the fundamental period is obtained by the product of the coefficient for upper limit on calculated period (C_u) and the approximate fundamental period (T_a) as defined in *ASCE 7-16* [10] Section 12.8.2, which is provided in Table 3-3. The median spectral accelerations of the ground motion record set are calculated as the median of a lognormal distribution fit to the ground motion spectral accelerations at each period. That means that the median spectral acceleration at a given period is taken as the exponential of the mean of the set of logarithms of the ground motion spectral accelerations at that period.

In this study, Seismic Design Category (SDC) D_{max} from *FEMA P-695* [38] is considered. The design spectral acceleration parameters S_{DS} = 1.0, and S_{D1} = 0.6 are used to create the target design earthquake (DE) spectrum. The maximum considered earthquake (MCE) spectrum was obtained using 1.5 times the S_{DS} and S_{D1} values. The third scale level ($ACMR_{10\%}$) is related to median collapse for acceptability according to *FEMA P-695* [38] and assumptions about the uncertainty as detailed further below. $\text{ACMR}_{10\%}$ scale level is considered to evaluate the conformance of the archetype buildings with the acceptance criteria in *FEMA P-695* [38] for a single building, i.e., less than 50% of ground motions causing collapse implies conformance with the acceptance criteria. Figure 5-2 shows an example for *DE* and *MCE* level where the ground motions were scaled such that the median spectrum matches the design spectrum at the fundamental design period of the building.

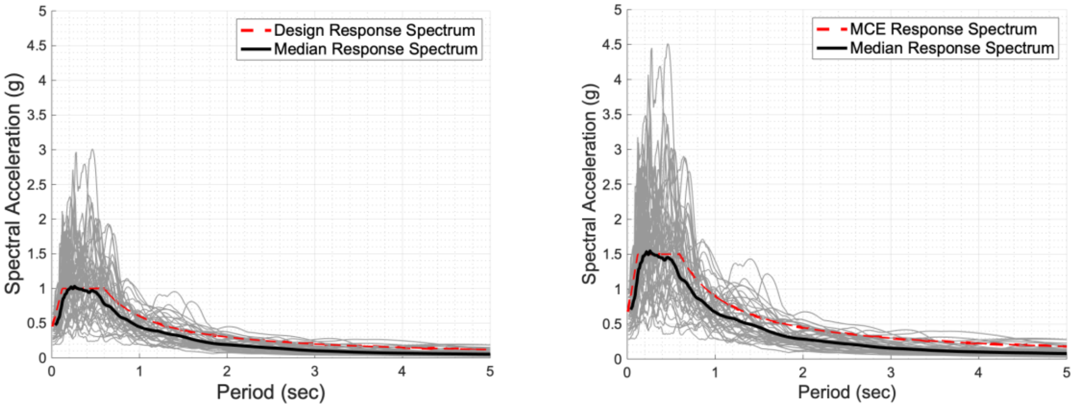

(a) DE (b) MCE

Figure 5-2. Example ground motion scaling for DE and MCE (4-story building)

For the third intensity ($ACMR_{10\%}$), the scale factor is obtained using the method described in Appendix F.3 of *FEMA P-695* [38]:

1) Period-based ductility (μ_T) is obtained from a pushover analysis for the short direction of the archetype building. The period-based ductility (μ_T) defined as the ratio of the post-peak roof displacement ($\delta_{u\ 80\%}$), at the point of 20% strength loss ($0.8P_{max}$) to the effective yield roof displacement ($\delta_{y,eff}$), which can be obtained using

Equation B-2 in *FEMA P695*. For the models with convergence issue, the roof displacement in the last step of analysis (δ_u) is used instead of the post-peak roof displacement ($\delta_{u\ 80\%}$).

2) Total system collapse (β_{total}) is calculated by assuming Good quality rating for design requirements, test data, and modeling, and using the period-based ductility (δ_u). β_{DR} = 0.2, β_{TD} = 0.2, and β_{MDL} = 0.2.

3) An acceptable value of the adjusted collapse margin ratio for acceptable collapse probability equal to 10%, $ACMR_{10\%}$, is obtained from Table 7-3 in Appendix F.3 of *FEMA P695* [38].

4) Spectral shape factor (*SSF*) is obtained from Table 7-1b using the period-based ductility (δ_u) and period of the building.

5) Finally, the scale factor based on $ACMR_{10\%}$ is obtained using Equation G-1 in Appendix F.3 of *FEMA P-695* [38] as follows,

$$SF_{ACMR_{10\%}} = \frac{ACMR_{10\%}}{C_{3D}SSF}\left(\frac{S_{MT}}{S_{NRT}}\right) = \frac{ACMR_{10\%}}{C_{3D}SSF} SF_{MCE} \tag{5-1}$$

Example calculation of $ACMR_{10\%}$ scale factor for 4-story archetype buildings with traditional diaphragm design:

- Period-based ductility, μ_T, is obtained from the pushover analysis. Values of the Coefficient, C_0, maximum base shear $V_{\max}$, building weight W, fundamental period T (equal to $C_u T_a$), fundamental period obtained from modal analysis T_1, effective yield roof drift displacement $\delta_{y,eff}$, ultimate roof drift displacement δ_u, and period-based ductility μ_T, are given as follows (see *FEMA P695* for details):

a. $C_0 = 1.66$

b. $V_{\max} = 1529$ kip

c. $W = 8983$ kip

d. $T = 0.54$ sec

e. $T_1 = 0.91$ sec

f. $\delta_{y,eff} = 4.50$ in.

g. $\delta_u = 21.54$ in.

h. $\mu_T = 4.82$

- Assumed total system collapse uncertainty, $\beta_{total} = 0.529$ based on the following

  a. Total system collapse uncertainty is calculated based on Equation 7-5 per FEMA P695:

  b. $\beta_{total} = \sqrt{\beta_{RTR}^2 + \beta_{DR}^2 + \beta_{TD}^2 + \beta_{MDL}^2}$

  where β_{total} = total system collapse uncertainty, β_{RTR} = record-to-record collapse uncertainty, β_{DR} = design requirements-related collapse uncertainty, β_{TD} = test data-related collapse uncertainty, β_{MDL} = modeling-related collapse uncertainty.

  c. Assuming the quality ratings for design requirements, test data, and modeling are all Good, we have (Section 7.3.4): $\beta_{DR} = 0.2$, $\beta_{TD} = 0.2$, and $\beta_{MDL} = 0.2$.

  d. β_{RTR} is a function of period-based ductility δ_u (Equation 7-2): $\beta_{RTR} = 0.1 + 0.1\mu_T \le 0.4$, but for μ_T bigger than 3.0, β_{RTR} is equal to 0.4.

e. By considering the values explained in items b and c, β_{total} is 0.529. This value can also be obtained directly from Table 7-2b of FEMA P695.

- Find acceptable level of ACMR: ACMR for 10%

  a. Using Table 7-3 with β_{total} = 0.529, and 10% collapse probability

  b. $ACMR_{10\%}$ =1.97

- Spectral shape factor, *SSF*

  a. Table 7-1b of FEMA P695 is used to get *SSF*

  b. Based on period, $T = C_u T_a$ = 0.54 sec for SCBF building and period-based ductility, μ_T = 3.51

  c. *SSF* = 1.25

- Find scale factor as scale factor for MCE multiplied by *CMR* using Equation (5-1):

  $SF_{ACMR10\%}$ = (1.97 x 2.12) / (1.2 x 1.25) = 2.78

The values for the other buildings are provided in as follows,

Table 5-2. Ground Motion Scaling for all Buildings

Building	$C_u T_a$ (sec)	T_1 (sec)	μ_T	β_{total}	$ACMR_{10\%}$	*SSF*	DE Scale Factor, SF_{DE}	MCE Scale Factor, SF_{MCE}	$ACMR_{10\%}$ Scale Factor, $SF_{ACMR10\%}$
1-story[a]	0.30	0.89	2.40	0.485	1.86	1.15	1.29	1.94	2.61
1-story[b]	0.20	0.59	5.83	0.529	1.97	1.27	1.29	1.94	2.50
4-story	0.54	0.91	3.51	0.529	1.97	1.25	1.42	2.12	2.78
8-story	0.89	1.50	3.38	0.529	1.97	1.22	1.66	2.49	3.33
12-story	1.21	2.77	2.86	0.514	1.94	1.30	1.66	2.49	3.10

5.3. Collapse Criteria for SCBF Archetypes

To evaluate the seismic performance of SCBF archetype building using statistical analysis of the nonlinear response time history analysis results, three criteria listed in the following are considered, and if any of them is satisfied, the building is considered as collapsed. It should be noted that some limit states such as SCBF fracture were explicitly captured in the models and result in triggering one of the three criteria below and therefore not included in these criteria.

1) Peak resultant story drift ratio exceeds 10%. This limit is consistent with the evaluation of two-dimensional SCBF collapse performance by NIST [38].
2) Maximum diaphragm shear angle exceeds 4%. This limit is determined based on the evaluation of the cantilever diaphragm test and connector test database, in which the majority of the specimens exhibited little residual strength at an average shear angle equal to 4%.
3) Convergence failure occurs in the analysis. There are potentially many reasons for convergence failure during the analysis, and one of them is that large displacements cause local or global instability. For those runs of analysis that fail to converge, criteria 1) and 2) are first checked. If neither of these two criteria is met, the time history of story drift at the location where the maximum story drift occurs is examined on a case-by-case basis. Examples for determining the occurrence of building collapse in an individual analysis are provided as follows.
    i) If the building collapses under the same pair of ground motions with a smaller scale factor, then the building is considered collapsing and is included in the calculation of collapse ratio of all runs (with the reasoning that smaller magnitude of ground motions typically cause less damage to the building). Alternative, a run may be considered a collapse if the building undergoes substantial amount of inelastic deformation at the early stage of analysis (e.g., before the peak ground

acceleration is applied). Figure 5-3 shows an example time history of maximum story drift for the runs of analysis with two different scale levels of ground motions. The analysis fails to converge for $ACMR_{10\%}$-level ground motions. However, because the building is considered to collapse for the analysis with the same pair of ground motions at *MCE* level (the story drift ratio exceeds 10%), it is also considered to collapse for the $ACMR_{10\%}$ level since the ground motions are scaled to a higher hazard level.

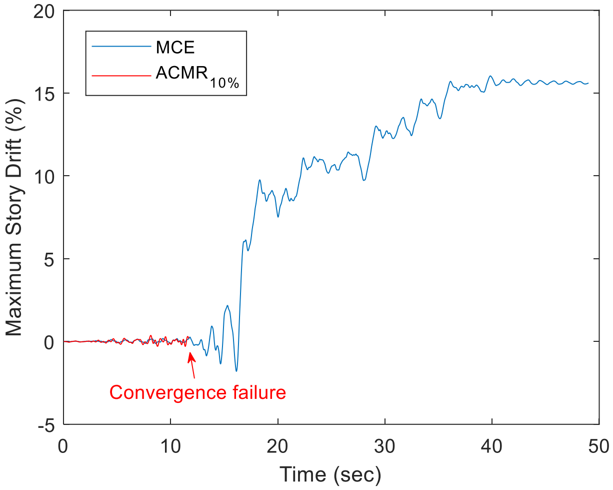

Figure 5-3. Example time history of maximum story drift for analysis with convergence failure considered as building collapse (4-story Trad. / Rs= 2.0 or 2.5, Ground Motion Set 21)[49]

ii) If the building does not collapse under the same pair of ground motions with a larger scale factor, then the building is considered non-collapsing and is included in the calculation of collapse ratio of all runs. The reasoning is that smaller magnitude of ground motions typically causes less damage to the building.

iii) If it cannot be determined whether the building collapses or not, the run is excluded from the calculation of collapse ratio of all runs. This happens if neither i) nor ii) is satisfied. In this case, the analysis is considered incomplete, and is deemed inappropriate to be included in the calculation of collapse ratio. An example is shown in Figure 5-4.

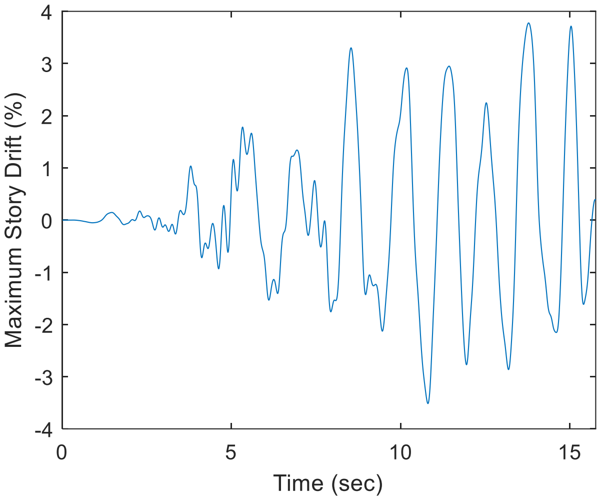

Figure 5-4. Example time history of maximum story drift for analysis with convergence failure excluded from collapse ratio calculation (8-story Trad. / Rs= 2.0 or 2.5, Ground Motion Set 26)

5.4. Dynamic Response Analysis Examples and Discussions

This section has two main parts including a detailed investigation of building behavior in the nonlinear response history analysis using a single building height subjected to one ground motion pair, and statistical performance evaluation of all archetypes based on different diaphragm design procedures.

5.4.1. Four-story SCBF Building Response Subjected to One Ground Motion Pair

To investigate the detailed behavior of SCBF archetypes buildings, a four-story SCBF building model with different diaphragm designs subjected to the ground motion with ID No. 7 (Kobe earthquake of the magnitude 6.9, occurred on January 17, 1995) at different earthquake hazard levels is considered.

Figure 5-5 demonstrates response history analysis results including peak story drift at the location of maximum story drift, SCBF at the location of maximum SCBF brace force, and diaphragm truss hysteresis at the point of maximum diaphragm shear angle, for the building designed with Traditional / R_s = 2.0 or 2.5 diaphragm design procedure. It can be seen that peak story drift of the building subjected to DE-level ground motion is less than 4% which could be explained as the building not collapsed. This is consistent with what was expected to for DE-level ground motion. For the MCE-level ground motion, the peak story drift is larger than the 10% limit for collapse definition. While the building is still considered as collapsed the reserve strength of the building keeps the peak story drift between 11% to 14% during the earthquake. Finally, under $\mathrm{ACMR}_{10\%}$-level ground motion the building experiences significant increasing in peak story drifts, which indicates building collapse. It should be noted that the building loss the strength and completely collapsed with the ground motion duration between 14 to 15 seconds which is about 30% of total ground motion duration.

The SCBF's and diaphragms both undergo inelastic deformation at all three hazard levels. The SCBF hysteresis response of DE level ground motion shows that energy is dissipated by SCBF inelastic deformation where the braces experience both buckling and yielding. For MCE- and $\mathrm{ACMR}_{10\%}$-level ground motions, excessive SCBF deformation occurs and cause the building to collapse. The SCBF hysteresis response shows that the brace loss the strength at 0.05 strain value due to defining a fracture strain to simulate the low-cycle fatigue which is dominant limit state for SCBF braces. Previous studies such as Sabeli *et al.* [44] described that the brace fracture is the dominant limit state for SCBF braces. However, the lateral resistance after initial brace fracture may be the range of 20% to 40 % of the original braced frame resistance. It should be noted that the current computational model in this study uses *MINMAX* material with a strain values and is not able to simulate the reserved lateral resistance of the building after initial brace fracture.

In Figure 5-5, floor diaphragms remain relatively elastic compared to the roof diaphragms under the *DE* and MCE-level ground motions, whereas at the $ACMR_{10\%}$ level, the floor diaphragms are affected by the large story drift due to the excessive deformation of the SCBF and also undergo large deformation. Similar to floor diaphragms, roof diaphragms also experience large story drift at $ACMR_{10\%}$ level which is because of the extreme inelastic deformation in SCBF brace.

Figure 5-6 shows the deformed shapes of the building, at the moment of peak story drift, under the three levels of the ground motion. The deformed shapes further illustrate the cause of building collapse at the *MCE* level ground motions which is failure of SCBF's particularly at the first story where story drifts concentrate. For $\mathrm{ACMR}_{10\%}$-level ground motions, column buckling also occurs in the collapse. Figure 5-7 shows the column buckling of perimeter a few steps before the peak story drift which is the collapse time. The reason for column buckling may attributed to axial-flexural interaction in the columns due to P- Δ effects.

The importance of gravity column behavior also reported in several studies in the literature [15]. Rai *et al.* [87] studied the gravity column participation in resisting lateral loads for OCBF braced frame buildings. The authors reported that gravity column participation is about 30% of total shear following the loss of strength due to brace failure. Flores *el al.* [88] also studied the influence of gravity columns modeling on performance of steel buildings during earthquake.

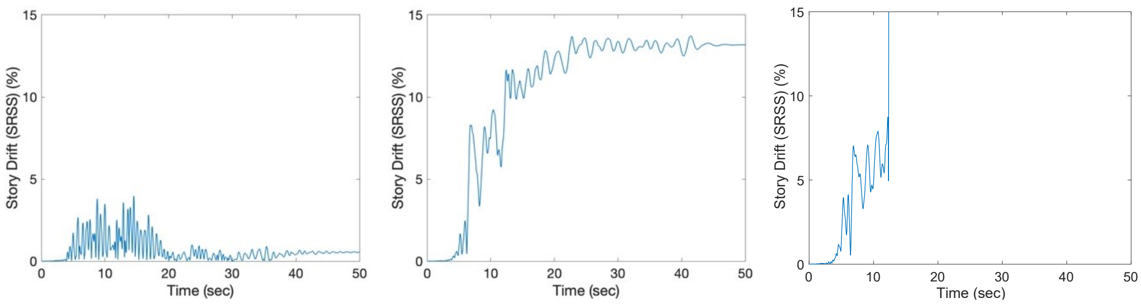

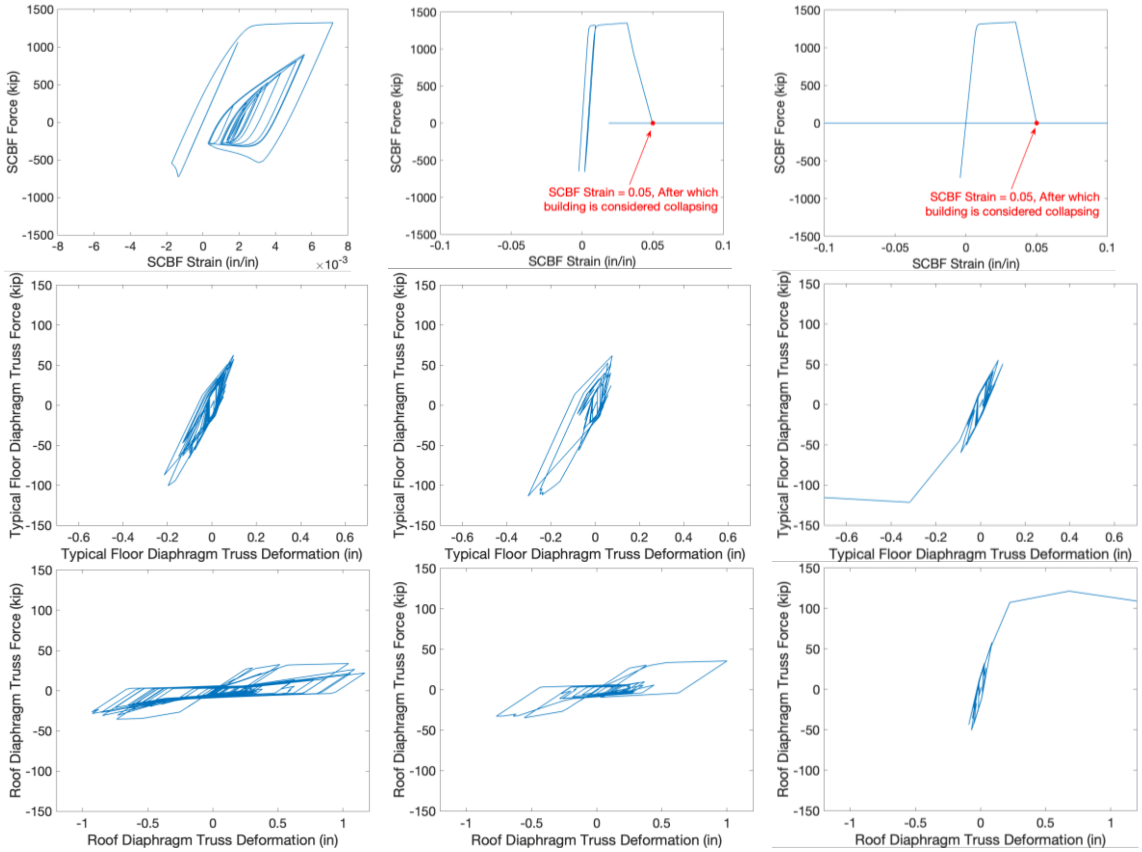

(a) DE (b) MCE (c) ACMR10%

Figure 5-5. Time history response of 4-story building with the Traditional / R_s = 2.0 or 2.5 diaphragm design procedure under three levels of ground motions

Time history analysis per *FEMA P-695* [38] revealed the contribution of gravity columns to lateral force resisting system and sustain the flexural demand. In addition, unlike the first-mode based pushover analysis in which inelasticity focuses in the SCBF's, the participation of higher modes in the response history analysis leads to diaphragm inelasticity. The total story drifts include inelastic deformations in the vertical LFRS and the diaphragm such that the two compound each other (i.e., interact) to exacerbate the P-Δ effect which eventually leads to the collapse of the buildings.

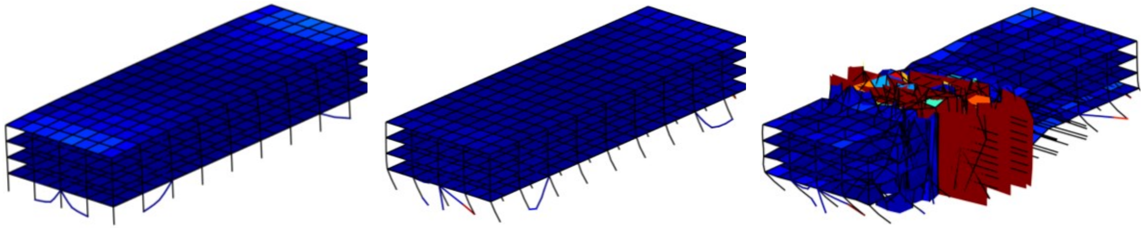
(a) DE (b) MCE (c) ACMR*10%*

Figure 5-6. Deformed shapes of 4-story archetype building with the Traditional /R_s = 2.0 or 2.5 diaphragm design procedure under three levels of ground motions (deformation amplification factor: 10)

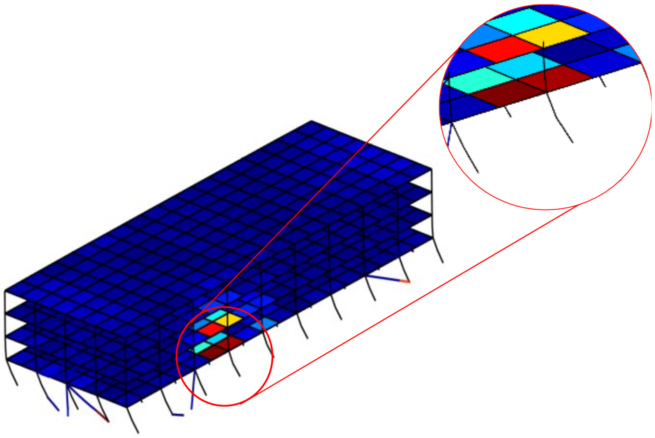

Figure 5-7. Column buckling for 4-story archetype building with the Traditional /R_s = 2.0 or 2.5 diaphragm design procedure

Figure 5-8 shows the time history of the maximum total story drift (at any location of the building including diaphragm deformation) and the maximum story drift at the SCBF frames plotted separately for the longitudinal (x) and transverse (y) directions of the archetype building with Traditional / R_s = 2.0 or 2.5 diaphragm design procedure subjected to the ground motion at MCE level. It can be observed that the building experiences larger story drift in the transverse direction than in the longitudinal direction, possibly likely because the stiffness of the building in the longitudinal (x) direction is larger than in the transverse (y) direction. Also, the total story drift in the longitudinal (x) direction is close to the story drift at the SCBF frames throughout the time history, indicating negligible in-plane diaphragm deformation in this direction, which is due to the large in-plane stiffness of the diaphragm along the longer dimension of the building. However, the in-plane stiffness of the diaphragm in the transverse (y) direction is smaller, resulting in significantly larger in-plane diaphragm deformations and thus the total story drift is larger than the story drift at the SCBF frames in this direction. This is worth some attention as in conventional structural analysis where diaphragms are assumed infinitely rigid or elastic in plane with zero or small deformation, the story drift of the building could be underestimated.

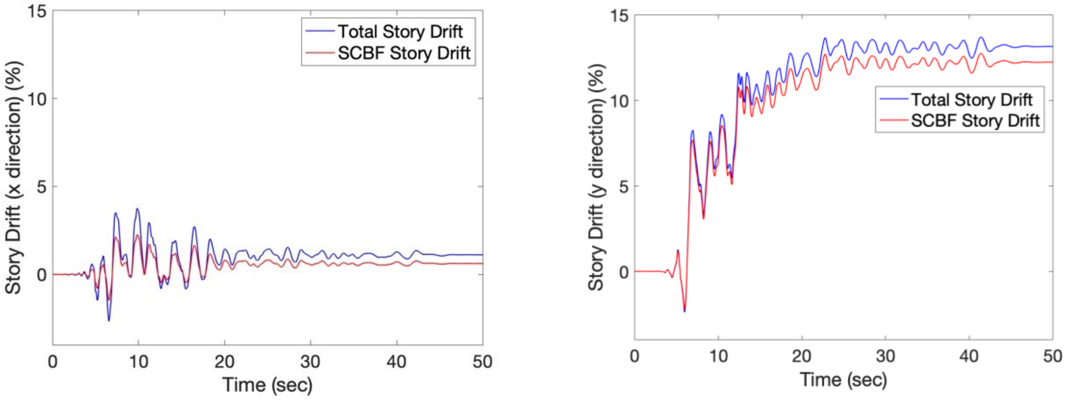

(a) Longitudinal direction (x)

(b) Transverse direction (y)

Figure 5-8. Time history of peak story drift four-story building with Traditional / diaphragm design with R_s = 2.0 or 2.5 under MCE-level ground motion: total story drift vs. SCBF story drift.

Figure 5-9 shows the time history of the maximum total base shear (including the shear in the columns at the base story) and the maximum base shear at the SCBF frames plotted separately for the longitudinal (x) and transverse (y) directions of the 4-story archetype building with Traditional / R_s = 2.0 or 2.5 diaphragm design procedure subjected to the ground motion at DE and MCE levels. The peak values of these base shears are provided in Table 5-3. It can be observed that although the scale factor for MCE ground motion accelerations is 1.5 times larger than that for DE ground motions, the peak base shear is an average of 1.2 times larger for MCE (2640 kip) compared to DE (2212 kip) because the SCBF strength limits the force that can transfer through the vertical LRFS. It is also noted that the peak total base shear in the transverse (y) direction is close to the peak base shear at the SCBF frames, while in the longitudinal (x) direction these two quantities are approximately 20% different, with the peak total base shear being smaller than the peak base shear at the SCBF frames direction opposite to the SCBF base shear.

In Figure 5-9 at MCE level, the total base shear is mostly carried by the SCBF braces until the fracture of the SCBF brace. After losing the SCBF strength, the rests of the building including gravity columns most attempt to carry the shear, but the significant increase in the drift due to P- Δ effects leading to the collapse of the archetype building.

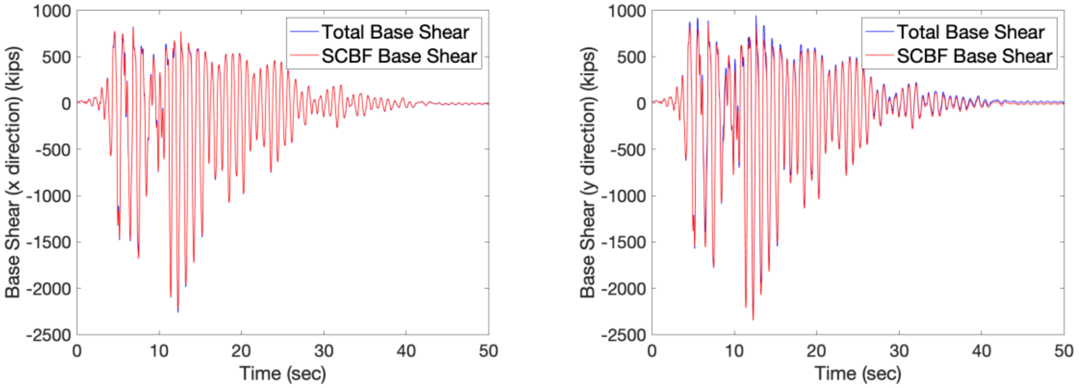

(a) Longitudinal (x) base shear, DE (b) Transverse (y) base shear, DE

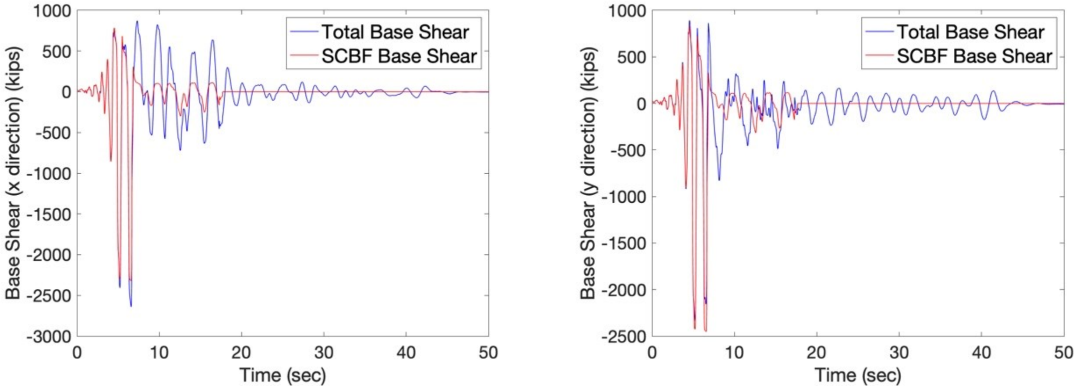

(c) Longitudinal (x) base shear, MCE (d) Transverse (y) base shear, MCE

Figure 5-9. Base shear of four-story building with Traditional / R_s = 2.0 or 2.5 diaphragm design under DE and MCE-level ground motions: total base shear vs. SCBF base shear.

Table 5-3. Base Shear of 4-story Archetype Building with Traditional / R_s = 2.0 or 2.5 diaphragm design under DE and MCE-level Ground Motions

Ground motion scale	Peak total base shear in x direction (kip)	Peak SCBF base shear in x direction (kip)	Peak total base shear in y direction (kip)	Peak SCBF base shear in y direction (kip)
DE	2212	2257	2259	2348
MCE	2640	2229	2270	2450

Figure 5-10 shows the total base shear versus the story drift at the location of peak story drift, under the MCE-level ground motion. It is noted that the peak base shear typically does not occur at the same time as the peak story drift, which are both selected for further investigation.

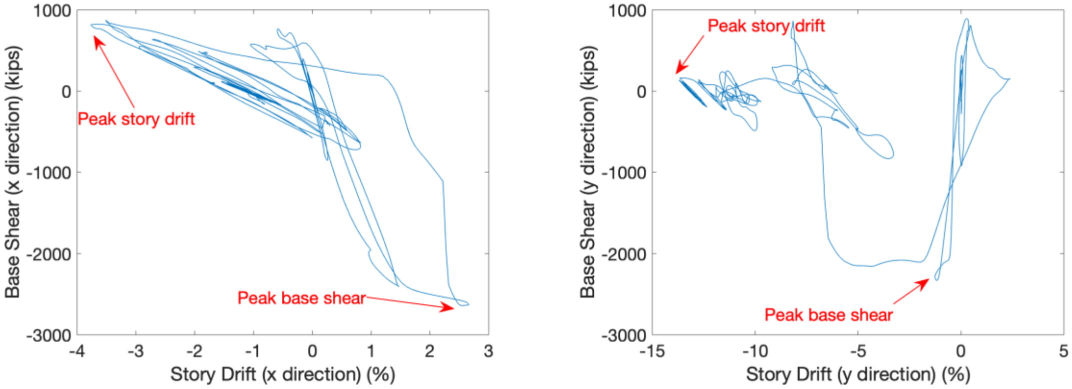

Figure 5-10. Base shear vs. story drift hysteretic curves of four-story building with Traditional / R_s = 2.0 or 2.5 diaphragm design under MCE-level ground motion.

Figure 5-11 shows the contour of the normalized shear angles of the diaphragm units and the normalized strain of the SCBF's plotted at different moments in the time history, i.e., at peak story drift and peak base shear in the longitudinal (x) and transverse (y) directions. The longitudinal (x) direction displacement appears small in the contour plotted at the peak story drift because the story drifts in the longitudinal direction are smaller than those in the transvers direction, as shown in Figure 5-11. The diaphragm shear angles (γ_{diaph}) are normalized by γ_1

which is the shear angle reached when the diagonal trusses of the diaphragm unit undergo an axial strain equal to $\varepsilon_1$of the Pinching4 parameters, i.e., the elastic regime. The normalized strain demand of each SCBF is obtained by dividing the SCBF strain ($\varepsilon_{\mathrm{SCBF}}$) by ε_y, which is the yield strain of the SCBF given by $\varepsilon_y = F_y/E$ where $F_y = 62.5$ *ksi* is the yield stress of the SCBF and E = *29000 ksi* is the elastic modulus of steel. The normalization is done such that the contours provide a visualization of the inelastic strain distribution for the horizontal and vertical systems. It can be observed from Figure 5-11 that the diaphragm deformation is relatively small at the moment when the peak story drift in the longitudinal (x) direction is reached. However, at the moment when the peak story drift or peak base shear in the transverse (y) direction occurs, there is significant inelastic deformation in the roof diaphragm and it is concentrated at its two edges where the shear demand is largest. The extent of diaphragm inelasticity at the peak base shear levels is extensive.

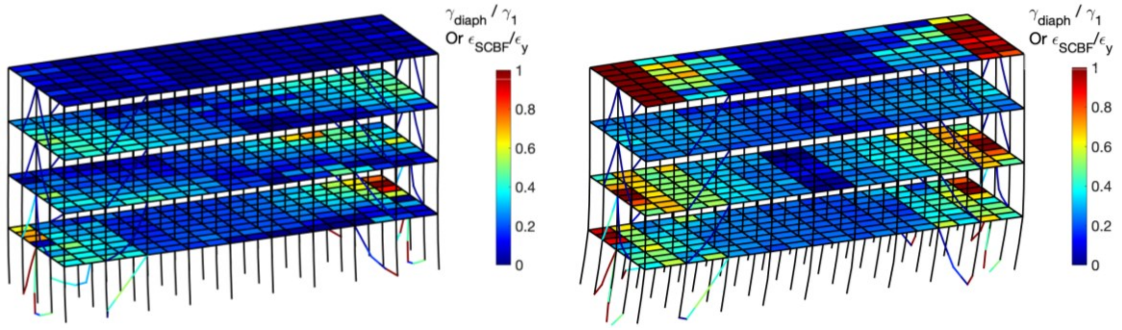

(a) At peak story drift in longitudinal (x) direction

(b) At peak story drift in transverse (y) direction

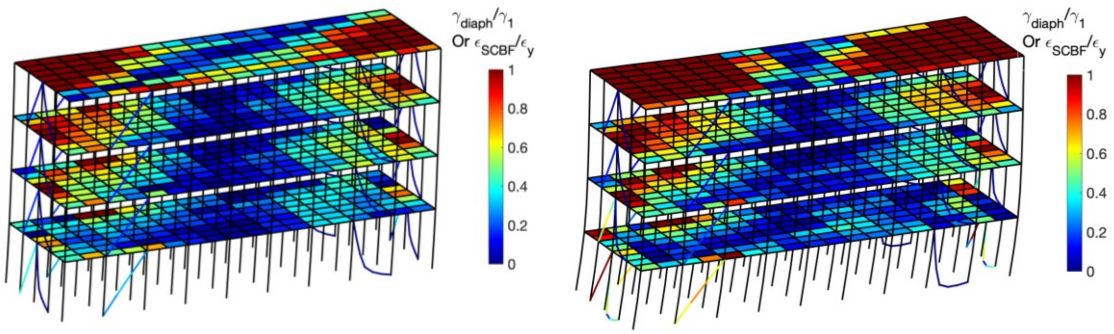

(c) At peak base shear in longitudinal (x) direction

(d) At peak base shear in transverse (y) direction

Figure 5-11. Contour of normalized diaphragm shear angle and normalized SCBF strain of four-story building with Traditional / R_s = 2.0 or 2.5 diaphragm design under MCE-level ground motion.

To illustrate the deformation demands for buildings with different diaphragm designs, the contour of normalized diaphragm shear angle demand and SCBF strain demand are plotted in Figure 5-12. The diaphragm shear angles and SCBF strains are normalized as described previously for Figure 5-11, but in this plot, the maximum deformation demands at any time during the record are used. It can be observed from Figure 5-12 that in each of the three cases, all the SCBF's experienced inelastic deformation.

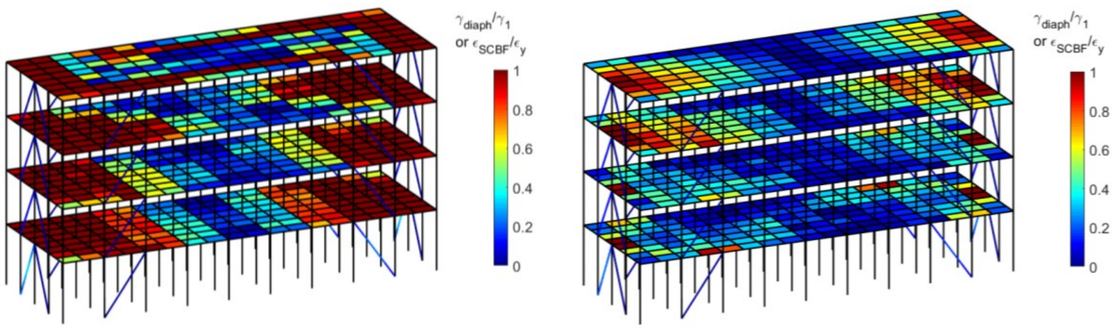

(a) Traditional / R_s = 2.0 or 2.5 diaphragm design

(b) R_s = 1.0 diaphragm design

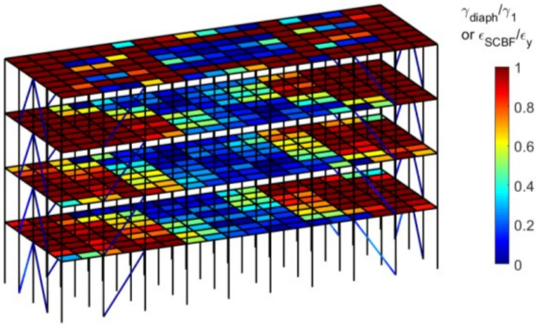

(c) R_s = 3.0 diaphragm design

Figure 5-12. Contour of normalized diaphragm shear angle demand and normalized SCBF strain demand of 4-story building with different diaphragm designs under MCE-level ground motions.

As expected, the diaphragm shear angle demand of the building with Traditional / R_s = 2.0 or 2.5 diaphragm design was larger than that of the building designed with R_s = 1.0. Diaphragm design with R_s = 3.0 experienced large inelastic deformation compared to both Traditional / R_s = 2.0 or 2.5 diaphragm design procedure and R_s = 1.0 diaphragm design procedure. The inelastic deformation in the diaphragm is aligned with the level of ductility assumed in the diaphragm response, i.e., the selected R_s value from the design.

5.5. Statistical Results and Discussion

To evaluate the seismic performance of the SCBF archetype buildings with different diaphragm design procedure, the statistical analysis of the nonlinear response history analysis results is performed across the building archetypes and earthquake records and different levels of hazard. Results are provided and discussed in this section.

5.5.1. Story Drift Analysis

To provide an example for the distribution of median peak story drifts at each story along the archetype buildings, the medians of peak story drifts across the 44-earthquake record records are obtained for twelve-story archetype building with Traditional / R_s = 2.0 or 2.5

diaphragm design (See Figure 5-13). The medians of peak story drifts are calculated for each story in the longitudinal (x) and transverse (y) directions for the SCBF frame and the total SCBF plus diaphragm deflection, and for the resultant story drift (SDR). It should be noted that building collapse based on the story drift criterion can be observed by counting the number of curves hitting/exceeding the 10% story drift limit.

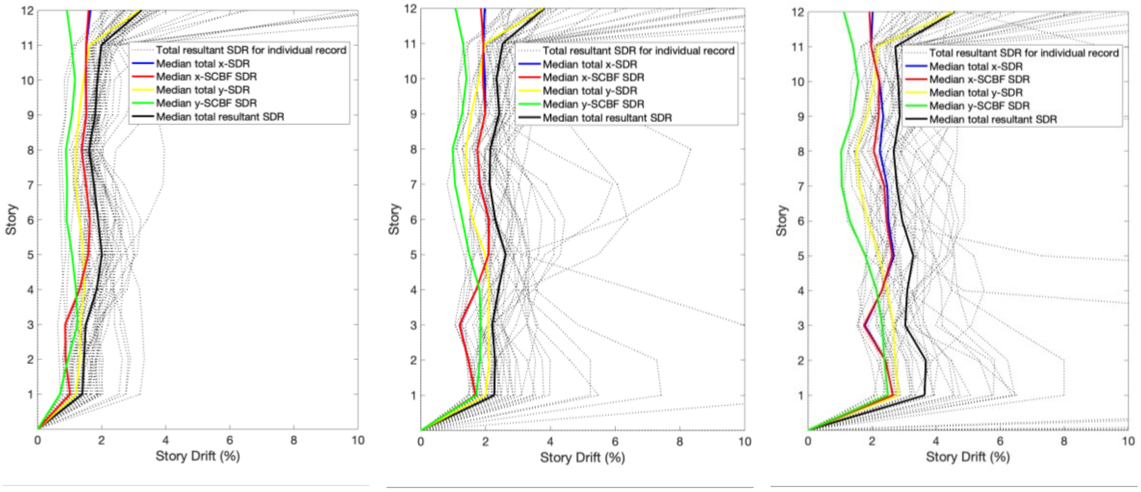

(a) DE (b) MCE (c) $ACMR_{10\%}$

Figure 5-13. Distribution of median peak story drifts at each story along building height of twelve-story archetype buildings with R_s = 2.0 or 2.5 diaphragm design under three levels of ground motions

In Figure 5-13, the median resultant story drift is larger than the median story drift in the longitudinal (x) and transverse (y) direction individually. The difference is obvious specially at the first story and roof of mid-rise SCBF buildings. By observing story drifts in two transvers and longitudinal directions individually, median story drift values in transverse direction and in the roof, level are 3.17 % and 3.68% for DE and MCE-ground motion level, respectively. However, median story drift at DE value is larger than 1.5% which is permitted by *ASCE 7-16* [10] (Drift could be twice the standard design limits of ASCE 7-16 [10] of Table 12.12-1). The median story drift values at MCE-ground motion level are 3.68% which is close to 4% allowable drift limit for Risk Category II non-masonry building taller than four stories. In addition, the median values for resultant story drift are 3.25% at DE and 3.81% at MCE. The larger values for DE-ground motion level indicates that analysis of two-dimensional frames can could prese underestimate peak story drifts.

Since the P-Δ effect is controlled by the story drift in any direction, the resultant story drift is a better estimate of story drift contributing to the P-Δ effect than the longitudinal (x) or transverse (y) direction story drift considered alone which is typically used in conventional frame analysis. This deserves some attention as there is concentrated story drift at the base story where the gravity load is the largest and thus the P-Δ effects are also the worst. Above the first story along the building height, the story drifts are more uniformly distributed with a smaller magnitude in the intermediate stories, while the story drifts in the roof become larger due to the participation of higher modes which is consistent with what is expected based on diaphragm design for SCBF archetype buildings.

For the SCBF frames, the story drifts at the SCBF frames in the transverse (y) direction are typically larger than those in the x direction. This can be explained by the fact that the in-plane stiffness of the diaphragm system in the longitudinal (x) direction is much larger than in the transverse (y) direction. It can also be observed that there is a significant different in peak total story compared to the SCBF brace frame drift due to the in-plane stiffness of the diaphragms in longitudinal and transverse directions. The peak total story drifts considering diaphragm deformations in transverse (y) direction are 1.99% and 3.77% for 1st story and roof of the building at MCE level, which are up to 71% and 14% larger than the peak story drifts at the SCBF frames in the transverse (y) direction, respectively (1.71 % and 1.07% for the 1st story and the roof of the building). It is obvious that the higher mode effect is more pronounced and causes a much larger difference between the total story drifts and the SCBF frame story drifts in the roof. For longitudinal (x) direction, the difference between the values of peak total story drift and peak story drifts at the SCBF frames is negligible as it was expected due to large in-plane stiffness in this direction.

Figure 5-14 to Figure 5-16 show the distribution of median peak resultant story drift, in story drift in the longitudinal (x) direction, and story drift in transverse (y) direction along the building height, for all the SCBF archetype buildings under the three ground motion levels. It can be seen that all the buildings with different diaphragm design procedures follow a similar pattern for the distribution of peak story drift. The median values of peak story drift are larger at the first story compared to the intermediate stories. It was expected because of maximum shear happens at the 1st floor of the building. This observation is also consistent with the static pushover analysis results where the SCBF brace buckling and yielding at the 1st floor of the building is observed. In addition, the median peak story drift is much larger in the roof level of building for all the archetypes. The large values of median peak story drift at roof level can be attributed to the effects of higher modes in the building. This could be described as inherent of diaphragm design with SCBF as vertical lateral force resisting system in *ASCE 7-16*, as it discussed in Chapter 2. The mode shape factor ($z_s = 1.0$) for SCBF as VLFRS in Table 2-2 demonstrates the contribution of higher mode shapes to the inelastic deformation at the roof level of building.

Due to the three-dimensional effect of the analysis, the median peak resultant story drifts range from 3% for buildings under DE-level ground motions, to approximately 10% for buildings under $ACMR_{10\%}$-level ground motions. For one-story archetypes, the median peak resultant story drifts exceed 10% due to significant nonlinearity in both SCBF and diaphragm system in the building. Considering individual values for median peak resultant story drifts for longitudinal (x) or transverse (y) direction, it can be observed that the values as smaller and comparable to the conventional two-dimensional frame analysis. The results from Hsiao *et al.* shows that for SCBF three-story building with $R = 6$, the median peak resultant story drifts varied between 1% to 3% in MCE-ground motion level and 0.3% to 0.5% for DE-ground motion level. In addition, for nine-story building with $R = 6$, median peak resultant story drifts varied between 0.5% to 1.5% in MCE-ground motion level and 0.3% to 0.55% for DE-ground motion level. Finally, median peak resultant story drift varied between 1% to 1.3% in MCE-ground motion level for twenty-story building. The values felled between 0.3% to 0.6% for DE-ground motion level. The results also showed that the largest drift values are concentrated on both roof and 1st story for twenty-story building while the largest drift value only happened in the 1st story for three- and nine-story building. The results from low-rise buildings could be compared with SCBF archetype with $R_s = 1.0$ diaphragm design procedure where the 1st story has the largest median peak resultant story drift. In addition, it can be seen that different diaphragm design procedures could affect the values of median peak resultant story drift especially in the roof of SCBF archetypes. The results show that for eight- and twelve-story SCBF archetype building, largest value of median peak resultant story drift occurs for Traditional design at the roof level while, SCBF archetype with $R_s = 3.0$ diaphragm design procedure has the largest median peak resultant story drift.

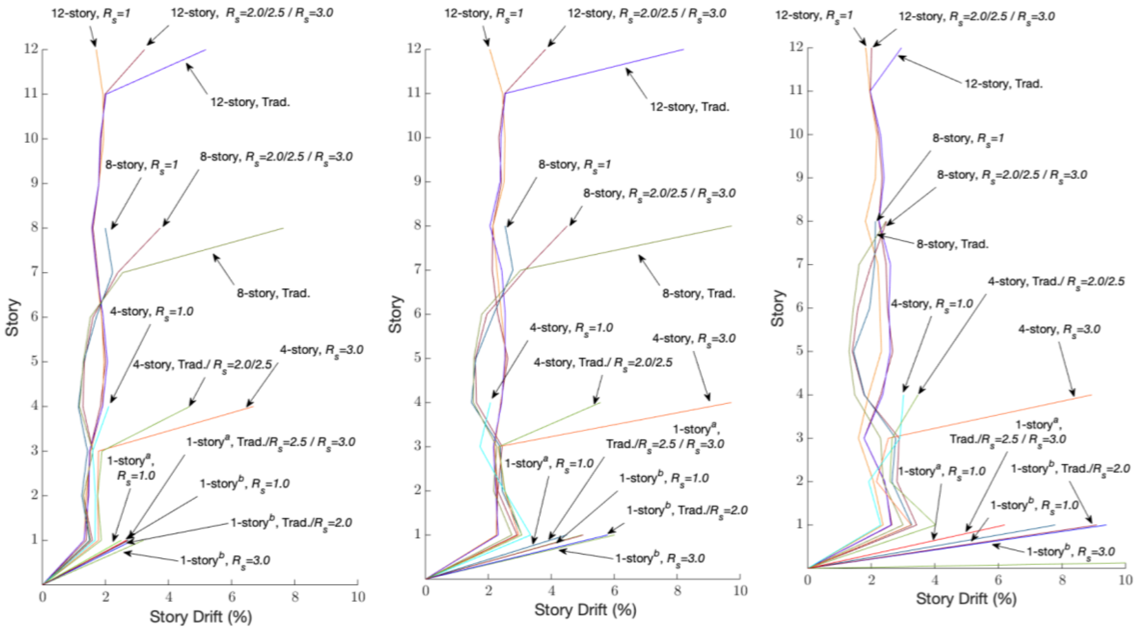

(a) DE (b) MCE (c) ACMR$_{10\%}$

Figure 5-14. Distribution of median peak resultant story drift along building height

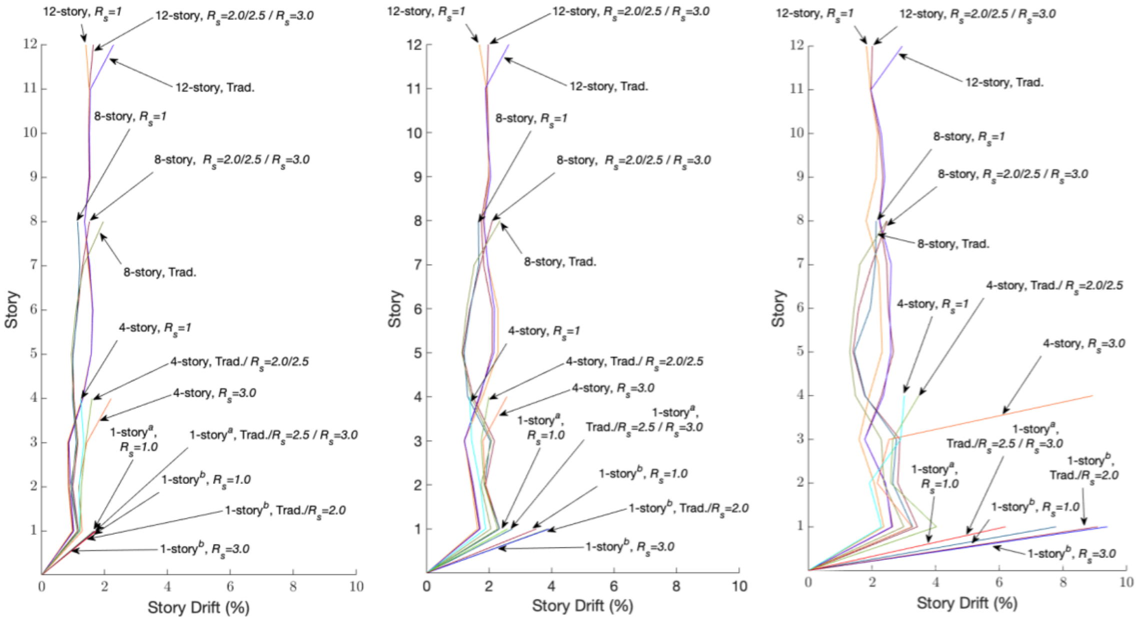

(a) DE (b) MCE (c) ACMR$_{10\%}$

Figure 5-15. Distribution of median peak story drift in longitudinal (x) direction along building height

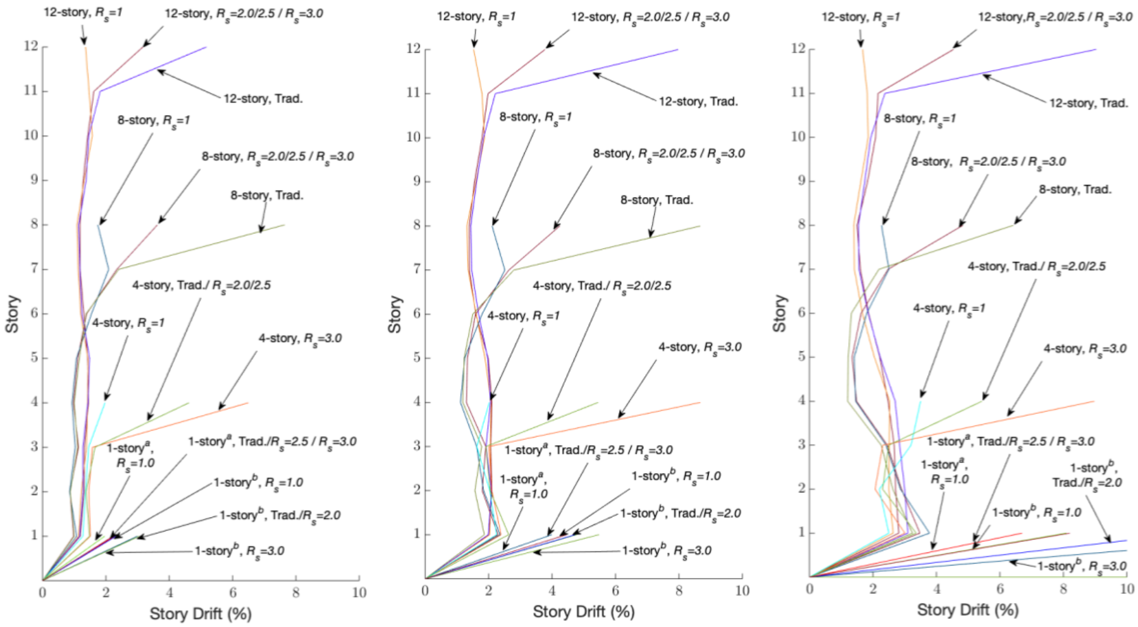

(a) DE (b) MCE (c) ACMR$_{10\%}$

Figure 5-16. Distribution of median peak story drift in transverse (y) direction along building height

5.5.2. Elastic Diaphragm Shear

To evaluate the accuracy of elastic diaphragm forces from different diaphragm design procedure of *ASCE 7-16* [10] Section 12.10.3, the diaphragm shear is calculated for the SCBF archetype building with R_s = 1.0 where diaphragms should remain near elastic. Specifically, the medians of the diaphragm shear demand at the edges, F_{peak} as calculated by the maximum value of the sum of diaphragm shear along the two edges (longitudinal (x) or transverse (y) direction) in the records, are obtained from the analysis results and provided in Table 5-3 for each story of the four-story archetype building. Values for other archetype buildings are given in the Appendix A.3. These values can be viewed as the median peak inertial forces of the diaphragms. As is shown by the contour of diaphragm deformation demand in Figure 5-12, the diaphragms of the four-story building with R_s = 1.0 diaphragm design remained almost elastic under the DE-level ground motions, and therefore the diaphragm shear demands should be comparable to the elastic design shear for diaphragms F_{px} calculated using the alternative diaphragm design procedures. It can be seen in Table 5-4 that ratios of the elastic diaphragm shear demand obtained from the analysis to the design shear given by the $R_s = 1.0$ diaphragm design procedures are relatively close to 1.0, indicating a reasonable accuracy of the prediction of elastic diaphragm shear demand with the design approach. This can be further validated by the average value of $(F_{\mathrm{peak}})_{\mathrm{DE}}/F_{\mathrm{px}}$ to 0.87 across all the archetype buildings. These ratios are shown in Figure 5-17, and one can also observe that the ratio for the roof diaphragm is the largest among the building stories but is close to 1.0. It is therefore concluded that the alternative diaphragm design procedure in *ASCE 7-16* [10] produced elastic diaphragm design forces that are somewhat conservative on average for floors, but generally accurate for the roof for these archetype buildings with flexible roof diaphragms.

Table 5-4. Medians of Diaphragm Shear Demand for four-story Archetype Buildings and Comparison to Design Shear

Diaphragm Design	Story	Median of F_{peak} at DE (kip)			F_{px} (kip)	$(F_{\mathrm{peak}})_{\mathrm{DE}}/F_{\mathrm{px}}$
		x	y	x or y		
$R_s = 1.0$	1	876	968	995	1060	**0.93**
	2	922	1008	1024	1070	**0.95**
	3	781	812	829	1080	**0.76**
	4	810	828	831	823	**1.01**

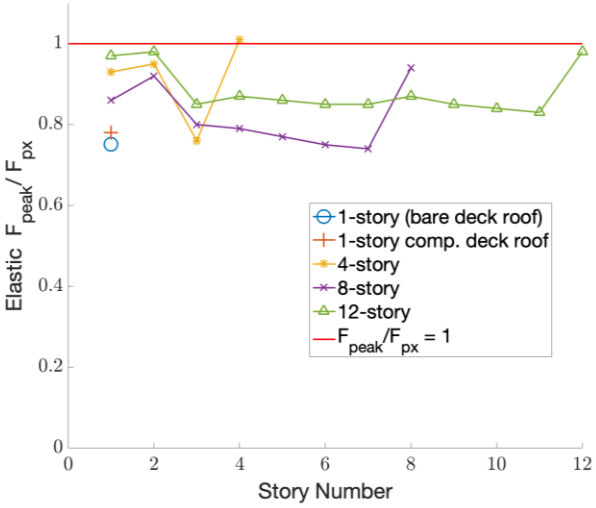

Figure 5-17. Diaphragm shear demand of archetype buildings with $R_s = 1.0$ diaphragm design normalized by diaphragm design shear.

5.5.3. Collapse Ratio Analysis Based on *FEMA* P695

To evaluate the seismic performance of different diaphragm design procedures in SCBF archetype buildings, *FEMA P-695* [38] methodology is utilized to assess the seismic performance factors using nonlinear response history analyses. Seismic performance factors are obtained by analyzing the percentage of ground motions causing collapse, period-based ductility, overstrength and design assumptions for each set of archetypes. Collapse definition for SCBF archetype buildings is in three forms (as it described in Section 5.3):

- Peak resultant story drift ratio exceeds 10% ($\Delta/h>10$).
- Maximum diaphragm shear angle exceeds 4% ($\gamma>0.04$). This limit is determined based on the evaluation of the cantilever diaphragm test and connector test database, in which the majority of the specimens exhibited little residual strength at an average shear angle equal to 4%.
- Convergence failure occurs in the analysis. For those runs of analysis that fail to converge, criteria 1) and 2) are first checked. If neither of these two criteria is met, the time history of story drift at the location where the maximum story drift occurs is examined on a case-by-case basis. Further, conv. represents convergence failure occurring in the analysis.

In addition to the above criterions for collapse, column buckling ratio of all the braced and gravity columns are calculated and monitored by dividing the relative displacement of the middle node in each column by the height of the story. The column considered buckled if the column buckling ratio exceeds 10% ($\delta/\mathrm{h}>0.1$). It should be noted that column buckling does not count as a principal collapse criterion in this study, but it can trigger the collapse in some archetype models and is thus monitored. Total shows the resulting collapse ratio based on the union of the three collapse criteria. In addition, to study the effects of diaphragm rigidity, all the SCBF archetype buildings models are analyzed with rigid diaphragms. Then, the results of rigid diaphragm models are compared to the R_s = 1.0 diaphragm design procedure models. Table 5-5 shows collapse ratios for all the archetype buildings for both rigid diaphragm and R_s = 1.0 diaphragm design procedure.

Table 5-5. Collapse ratio for archetype with rigid and R_s = 1.0 diaphragm design procedure

	Hazard – **ACMR10%**									
Story	*Rigid*					R_s = 1.0				
	Total	$\Delta/h>0.1$	$\gamma>0.04$	$\delta/h>0.1$	conv.	*Total*	$\Delta/h>0.1$	$\gamma>0.04$	$\delta/h>0.1$	conv.
1[a]	45.5	45.5	2.3	0.0	0.0	47.7	47.7	43.2	0.0	0.0
1[b]	68.2	68.2	0.0	0.0	0.0	72.7	72.7	2.2	0.0	0.0
4	63.6	61.4	45.5	52.3	0.0	59.1	54.5	47.7	50.0	0.0
8	50.0	50.0	31.8	43.2	0.0	40.9	40.9	40.9	38.6	0.0
12	29.5	22.7	0.0	9.1	6.8	20.5	13.6	11.4	11.4	6.8

	Hazard – **MCE**									
Story	*Rigid*					R_s = 1.0				
	Total	$\Delta/h>0.1$	$\gamma>0.04$	$\delta/h>0.1$	conv.	*Total*	$\Delta/h>0.1$	$\gamma>0.04$	$\delta/h>0.1$	conv.
1[a]	9.1	9.1	0.0	0.0	0.0	11.4	11.4	0.0	0.0	0.0
1[b]	15.9	15.9	0.0	0.0	0.0	13.6	13.6	2.2	0.0	0.0
4	13.6	13.6	2.2	6.8	0.0	13.6	11.4	11.4	11.4	2.2
8	22.7	22.7	15.9	22.7	0.0	22.7	22.7	15.9	22.7	0.0
12	13.6	11.4	0.0	11.4	2.2	11.4	9.1	6.8	6.8	2.2

	Hazard – **DE**									
Story	*Rigid*					R_s = 1.0				
	Total	$\Delta/h>0.1$	$\gamma>0.04$	$\delta/h>0.1$	conv.	*Total*	$\Delta/h>0.1$	$\gamma>0.04$	$\delta/h>0.1$	conv.
1[a]	0.0	0.0	0.0	0.0	0.0	2.2	2.2	2.2	2.2	0.0
1[b]	0.0	0.0	0.0	0.0	0.0	0.0	0.0	0.0	0.0	0.0
4	2.2	2.2	2.2	2.2	0.0	4.5	2.2	2.2	2.2	2.2
8	4.5	4.5	4.5	4.5	0.0	4.5	4.5	4.5	4.5	0.0
12	0.0	0.0	0.0	0.0	0.0	0.0	0.0	0.0	0.0	0.0

[a]: bare steel deck roof; [b]: concrete-filled deck roof

Based on the individual building evaluation criteria per the *FEMA P-695* [38] methodology, an individual building performance in terms of collapse is considered acceptable if less than 50% of the ground motions at the $ACMR_{10\%}$-ground motion level cause building collapse (Appendix F of *FEMA P-695* [38]). As shown in Table 5-5, one-story bare steel deck roof, eight-story, and twelve-story archetype buildings pass the acceptance criteria (with the number of collapses less than 50%), while the collapse ratios for the four-story and one-story concrete-filled deck roof exceed the *FEMA P-695* [38] criterion. These results are consistent with previous studies in the literature, such as Hsiao *et al.* [19], showing low-rise SCBF archetype buildings designed with $R = 6$ do not provide sufficient strength to fulfill the *FEMA P-695* [38] collapse criteria requirement even if the diaphragm experience negligible inelasticity during earthquake. It is also observed under this level of ground motions, the collapse ratios of the buildings with diaphragm design using $R_s = 1.0$ are close to those with Rigid diaphragm design. The collapse ratio difference increases by increasing the number of stories from 2% for one-story bare steel deck roof building to 9% for eight and twelve-story archetypes where buildings with rigid diaphragm design showing larger collapse ratio compared to diaphragm design using $R_s = 1.0$. This demonstrates that the stronger and stiffer diaphragms can cause more inelasticity to occur in the braces, resulting in larger story drift and more building collapses. For DE and MCE hazard level, the buildings show very similar collapse ratio for both rigid diaphragm and diaphragm design using $R_s = 1.0$. However, the percentage of collapse violate the *FEMA P-695* [38] criteria which are 2% and 10% for DE-level and MCE-level, respectively.

Table 5-6. Triggered collapse ratio for archetype with rigid and R_s = 1.0 diaphragm design procedure

	Hazard – **ACMR10%**									
Story	*Rigid*					R_s = 1.0				
	Total	$\Delta/h>0.1$	$\gamma>0.04$	$\delta/h>0.1$	conv.	*Total*	$\Delta/h>0.1$	$\gamma>0.04$	$\delta/h>0.1$	conv.
1[a]	45.5	45.5	0.0	0.0	0.0	47.7	47.7	0.0	0.0	0.0
1[b]	68.2	68.2	0.0	0.0	0.0	72.7	72.7	0.0	0.0	0.0
4	63.6	61.4	0.0	2.2	0.0	59.1	54.5	0.0	4.6	0.0
8	50.0	45.4	0.0	4.6	0.0	40.9	37.6	0.0	3.3	0.0
12	29.5	22.7	0.0	0.0	6.8	20.5	13.7	0.0	0.0	6.8

	Hazard – **MCE**									
Story	*Rigid*					R_s = 1.0				
	Total	$\Delta/h>0.1$	$\gamma>0.04$	$\delta/h>0.1$	conv.	*Total*	$\Delta/h>0.1$	$\gamma>0.04$	$\delta/h>0.1$	conv.
1[a]	9.1	9.1	0.0	0.0	0.0	11.4	11.4	0.0	0.0	0.0
1[b]	15.9	15.9	0.0	0.0	0.0	13.6	13.6	0.0	0.0	0.0
4	13.6	13.6	0.0	0.0	0.0	13.6	11.4	0.0	0.0	2.2
8	22.7	22.7	0.0	0.0	0.0	22.7	22.7	0.0	0.0	0.0
12	13.6	11.4	0.0	0.0	2.2	11.4	13.7	0.0	0.0	2.2

	Hazard – **DE**									
Story	*Rigid*					R_s = 1.0				
	Total	$\Delta/h>0.1$	$\gamma>0.04$	$\delta/h>0.1$	conv.	*Total*	$\Delta/h>0.1$	$\gamma>0.04$	$\delta/h>0.1$	conv.
1[a]	0.0	0.0	0.0	0.0	0.0	2.2	0.0	0.0	0.0	0.0
1[b]	0.0	0.0	0.0	0.0	0.0	0.0	0.0	0.0	0.0	0.0
4	2.2	2.2	0.0	0.0	0.0	4.5	2.3	0.0	0.0	2.2
8	4.5	4.5	0.0	0.0	0.0	4.5	4.5	0.0	0.0	0.0
12	0.0	0.0	0.0	0.0	0.0	0.0	0.0	0.0	0.0	0.0

[a]: bare steel deck roof; [b]: concrete-filled deck roof

The results from Table 5-5 demonstrates that even archetypes with R_s = 1.0 diaphragm design experiences substantial inelasticity as a part of total ratio of collapse in the buildings. To investigate the effects of each criteria including the diaphragm inelasticity on total collapse ratio, the triggered collapse ratio obtained by comparing the exact first time of observing each collapse criteria. Table 5-6 introduces the triggered collapse ratio of rigid diaphragm design and R_s = 1.0 diaphragm design procedure. It is observed that diaphragm inelasticity does not trigger the collapse of the building for all the models with rigid diaphragm design and diaphragm design with R_s = 1.0. This shows that SCBF low-cycle fatigue is the dominant failure mode for the archetypes. However, for twelve-story archetypes with R_s = 1.0 diaphragm design procedure, column buckling triggers a story drift collapse for a small number of four- and eight-story buildings. These findings are generally consistent with the assumption of elastic diaphragm behavior for an archetype with R_s = 1.0 diaphragm design procedure, observed inelasticity is only occurring in the diaphragm due to other failures creating demands on the diaphragm as collapse progresses.

Table 5-7 shows the total collapse ratio and percentage of failure based on each collapse criteria for archetype buildings with different diaphragm design procedure. For Traditional design, collapse ratio of the archetype buildings tends to become larger as the number of stories increases. For DE- and MCE-ground motion level, all the archetypes except the one-story with concrete-filled steel deck in *DE* level, show a collapse ratio more than *FEMA P-695* [38] single building criteria. Triggered collapse ratios in Table 5-8 reveals that story drift and diaphragm shear angle compete as the dominant failure mode depending on diaphragm design procedure and building height. For SCBF archetype buildings with diaphragm design procedure of R_s = 2.0 or 2.5 and R_s = 3.0, the collapse ratio decreases with increasing the number of stories. The literature is mixed on the effect of story height and collapse probabilities for SCBF's. The finding here is consistent to observations from some studies where two-dimensional frame analysis was performed and low-rise buildings were deemed more vulnerable. For example, in Kircher *et al.* [38] (NIST GCR 10-917-8), two-story SCBF archetype had ACMR values equal to 1.22 indicating large collapse ratio for low-rise SCBF buildings. While six-, twelve- and sixteen-story SCBF archetypes had ACMR values more than acceptable ACMR values which pass the *FEMA P-695* [38] criteria. However, in another more recent study, Kircher *et al.* [55] (FEMA P-2139-4) shows smaller collapse ratio for low-rise SCBF archetypes which is in contrary with the current study and previous studies on SCBF archetypes. Three-dimensional models for a group of four SCBF archetypes (1, 2, 3, and 4-story) have been studied with high and very high seismic design category, different foundation flexibility, and brace configurations. All archetypes are commercial buildings designed for modification response factor of $R = 6$ and seismic response coefficient (C_s) of 0.167*g,* and 0.25*g,* for archetypes with high and very high seismic design category, respectively. The results showed that all archetypes with high seismic design category passed the *FEMA P-695* [38] criterion. However, for archetypes with very high seismic design, two- and four-story buildings have 20% and 19% collapse ratios which is not permitted by *FEMA P-695* [38] criterion. The results also explained the importance of using different bracing configuration by comparing the results of two- and four-story archetypes with SuperX and chevron bracing systems. The comparison of results of *NIST GCR 10-917* study and those of *FEMA P-2139-4* study showed that the significant difference in collapse performance of two-story archetype is primarily due to the large difference in the overstrength of archetypes. The overstrength of two-story archetype in *NIST GCR 10-917* was 1.4 compared to 5.96 for *FEMA P-2139-4*. Another reason might be rooted in the brace configuration if buildings include larger number of braced frames, in order to provide a symmetrical and redundant system. *FEMA P-2139-4* study suggested to design the braces based on optimizing the structural strength instead of material availability, economy or construction limitations. Comparing the overstrength values for one-story bare deck roof and four-story SCBF archetypes in this study, which are 1.85 and 1.96 based on Table 4-2, shows that these values are significantly less than 5.96 from *FEMA P-2139-4* study and close to 1.4 from *NIST GCR 10-917*. This could be the reason that the results from current study shows that mid-rise SCBF archetypes are more vulnerable. In another study, Hsiao *et al.* [54] showed that three-story and six-story SCBF archetypes had *ACMR* values less than acceptable $ACMR_{20\%}$ values which did not pass the *FEMA P695* criteria.

In $\mathrm{ACMR}_{10\%}$-ground motion level, both eight- and twelve-story archetypes have collapse ratio less than 50% which is acceptable based on *FEMA P-695*. Triggered collapse ratio shows significant inelastic behavior for the diaphragm. For buildings with diaphragm design $R_s = 1.0$, collapse ratio is less than archetypes with other diaphragm designs, which shows the contribution of diaphragm inelasticity to the performance of the buildings during earthquake.

Rather than look at mean drift predictions one can look at the distribution. Towards a better description of distribution of maximum SRSS drift (δ) and shear angle (γ), empirical cumulative distribution function (CDF) plots are developed for the archetypes with different diaphragm design. Figure 5-18 and Figure 5-19 show the cumulative distribution function (CDF) plots for archetypes in $ACMR_{10\%}$ hazard level. The fact that the exceedance probabilities generally grow significantly past a story drift of 10% indicates that 10% story drift is a reasonable collapse criterion. The shape of the CDF indicates a measure of how robust the different designs are against the collapse criteria. The curves allow one to understand the impact of the R_s selection of the diaphragm on the collapse probability and to compare when traditional design is similar, or vastly different from the alternative designs with R_s. Lognormal cumulative function (CDF) plots for different hazard level are given in Appendix A4.

Table 5-7. Collapse ratio for all archetype with different diaphragm design procedure

	Hazard – **ACMR10%**																			
	R_s = 1.0					Traditional					R_s = 2.0 or 2.5					R_s = 3.0				
Story	*Total*	C^1	C^2	C3	C^4	*Total*	C^1	C^2	C3	C^4	*Total*	C^1	C^2	C3	C^4	*Total*	C^1	C^2	C3	C^4
1^a	47.7	47.7	43.2	0.0	0.0	81.8	79.5	81.8	0.0	0.0	81.8	79.5	81.8	0.0	0.0	81.8	79.5	81.8	0.0	0.0
1^b	72.7	72.7	2.2	0.0	0.0	79.5	79.5	6.8	0.0	0.0	79.5	79.5	6.8	0.0	0.0	81.8	81.8	9.1	0.0	0.0
4	59.1	54.5	47.7	50.0	0.0	59.1	52.3	54.5	45.5	4.5	59.1	52.3	54.5	45.5	4.5	84.1	65.9	72.7	31.8	6.8
8	40.9	40.9	40.9	38.6	0.0	50.0	31.8	47.7	31.8	2.2	52.3	43.2	45.5	22.7	6.8	52.3	43.2	45.5	22.7	6.8
12	20.5	13.6	11.4	11.4	6.8	79.5	54.5	77.3	13.6	2.2	45.5	25.0	43.2	15.9	4.5	45.5	25.0	43.2	15.9	4.5

	Hazard – **MCE**																			
	R_s = 1.0					Traditional					R_s = 2.0 or 2.5					R_s = 3.0				
Story	*Total*	C^1	C^2	C3	C^4	*Total*	C^1	C^2	C3	C^4	*Total*	C^1	C^2	C3	C^4	*Total*	C^1	C^2	C3	C^4
1^a	11.4	11.4	0.0	0.0	0.0	43.2	38.6	43.2	0.0	0.0	43.2	38.6	43.2	0.0	0.0	43.2	38.6	43.2	0.0	0.0
1^b	13.6	13.6	2.2	0.0	0.0	15.9	15.9	2.2	0.0	0.0	15.9	15.9	2.2	0.0	0.0	18.2	18.2	4.5	0.0	0.0
4	13.6	11.4	11.4	11.4	2.2	31.8	22.7	31.8	4.5	0.0	31.8	22.7	31.8	4.5	0.0	40.9	22.7	31.8	4.5	0.0
8	22.7	22.7	15.9	22.7	0.0	43.2	31.8	38.6	27.3	4.5	38.6	31.8	36.4	20.5	2.2	38.6	31.8	36.4	20.5	2.2
12	11.4	9.1	6.8	6.8	2.2	65.9	43.2	65.9	4.5	2.2	27.3	18.2	25.0	4.5	2.2	27.3	18.2	25.0	4.5	2.2

	Hazard – **DE**																			
	R_s = 1.0					Traditional					R_s = 2.0 or 2.5					R_s = 3.0				
Story	*Total*	C^1	C^2	C3	C^4	*Total*	C^1	C^2	C3	C^4	*Total*	C^1	C^2	C3	C^4	*Total*	C^1	C^2	C3	C^4
1^a	2.2	2.2	2.2	2.2	0.0	6.8	6.8	6.8	0.0	0.0	6.8	6.8	6.8	0.0	0.0	6.8	6.8	6.8	0.0	0.0
1^b	0.0	0.0	0.0	0.0	0.0	0.0	0.0	0.0	0.0	0.0	0.0	0.0	0.0	0.0	0.0	2.2	2.2	0.0	0.0	0.0
4	4.5	2.2	2.2	2.2	2.2	25.0	9.1	25.0	4.5	0.0	25.0	9.1	25.0	4.5	0.0	27.3	9.1	27.3	4.5	0.0
8	4.5	4.5	4.5	4.5	0.0	40.9	22.7	36.4	15.9	4.5	18.2	9.1	18.2	4.5	0.0	18.2	9.1	18.2	4.5	0.0
12	0.0	0.0	0.0	0.0	0.0	40.9	18.2	40.9	45.5	0.0	15.9	9.1	15.9	0.0	0.0	15.9	9.1	15.9	0.0	0.0

Collapse criteria: C^1 : $\Delta/h>0.1$; C^2 : $\gamma>0.04$; C^3 : $\delta/h>0.1$; C^4 : conv. / **Diaphragm System**: 1^a: bare steel deck roof; 1^b: concrete-filled deck roof

Table 5-8. Triggered collapse ratio for all archetype with different

	Hazard – **ACMR10%**																			
	R_s = 1.0					Traditional					R_s = 2.0 or 2.5					R_s = 3.0				
Story	*Total*	C^1	C^2	C3	C^4	*Total*	C^1	C^2	C3	C^4	*Total*	C^1	C^2	C3	C^4	*Total*	C^1	C^2	C3	C^4
1^a	47.7	47.7	0.0	0.0	0.0	81.8	0.0	81.8	0.0	0.0	81.8	0.0	81.8	0.0	0.0	81.8	0.0	81.8	0.0	0.0
1^b	72.7	72.7	0.0	0.0	0.0	79.5	79.5	0.0	0.0	0.0	79.5	79.5	0.0	0.0	0.0	81.8	72.7	9.1	0.0	0.0
4	59.1	54.5	0.0	4.6	0.0	59.1	29.3	16.8	8.5	4.5	59.1	29.3	16.8	8.5	4.5	84.1	7.5	67.3	2.5	6.8
8	40.9	37.6	0.0	3.3	0.0	50.0	5.7	42.1	0.0	2.2	52.3	17.3	28.2	0.0	6.8	52.3	16.8	28.7	0.0	6.8
12	20.5	13.7	0.0	0.0	6.8	79.5	6.8	72.8	0.0	2.2	45.5	13.5	27.5	0.0	4.5	45.5	13.5	27.5	0.0	4.5

	Hazard – **MCE**																			
	R_s = 1.0					Traditional					R_s = 2.0 or 2.5					R_s = 3.0				
Story	*Total*	C^1	C^2	C3	C^4	*Total*	C^1	C^2	C3	C^4	*Total*	C^1	C^2	C3	C^4	*Total*	C^1	C^2	C3	C^4
1^a	11.4	11.4	0.0	0.0	0.0	43.2	0.0	43.2	0.0	0.0	43.2	0.0	43.2	0.0	0.0	43.2	0.0	43.2	0.0	0.0
1^b	13.6	13.6	0.0	0.0	0.0	15.9	15.9	0.0	0.0	0.0	15.9	15.9	0.0	0.0	0.0	18.2	13.7	4.5	0.0	0.0
4	13.6	11.4	0.0	0.0	2.2	31.8	0.0	31.8	0.0	0.0	31.8	0.0	31.8	0.0	0.0	40.9	0.0	40.9	0.0	0.0
8	22.7	22.7	0.0	0.0	0.0	43.2	3.1	35.6	0.0	4.5	38.6	5.9	39.6	0.0	2.2	38.6	2.3	43.2	0.0	2.2
12	11.4	13.7	0.0	0.0	2.2	65.9	2.0	57.1	0.0	6.8	27.3	2.3	22.5	0.0	6.8	27.3	2.3	22.6	0.0	2.2

	Hazard – **DE**																			
	R_s = 1.0					Traditional					R_s = 2.0 or 2.5					R_s = 3.0				
Story	*Total*	C^1	C^2	C3	C^4	*Total*	C^1	C^2	C3	C^4	*Total*	C^1	C^2	C3	C^4	*Total*	C^1	C^2	C3	C^4
1^a	0.0	0.0	0.0	0.0	0.0	6.8	0.0	6.8	0.0	0.0	6.8	6.8	6.8	0.0	0.0	6.8	6.8	6.8	0.0	0.0
1^b	0.0	0.0	0.0	0.0	0.0	0.0	0.0	0.0	0.0	0.0	0.0	0.0	0.0	0.0	0.0	2.2	2.2	0.0	0.0	0.0
4	4.5	2.3	0.0	0.0	2.2	25.0	2.3	22.7	0.0	0.0	25.0	2.3	22.7	0.0	0.0	27.3	1.8	25.5	0.0	0.0
8	4.5	4.5	0.0	0.0	0.0	40.9	0.0	36.4	0.0	4.5	18.2	0.0	18.2	0.0	0.0	18.2	0.0	28.2	0.0	0.0
12	0.0	0.0	0.0	0.0	0.0	40.9	0.0	40.9	0.0	0.0	15.9	0.0	15.9	0.0	0.0	15.9	0.0	15.9	0.0	0.0

Collapse criteria: C^1 : $\Delta/h>0.1$; C^2 : $\gamma>0.04$; C^3 : $\delta/b>0.1$; C^4 : conv. / **Diaphragm System**: 1^a: bare steel deck roof; 1^b: concrete-filled deck roof

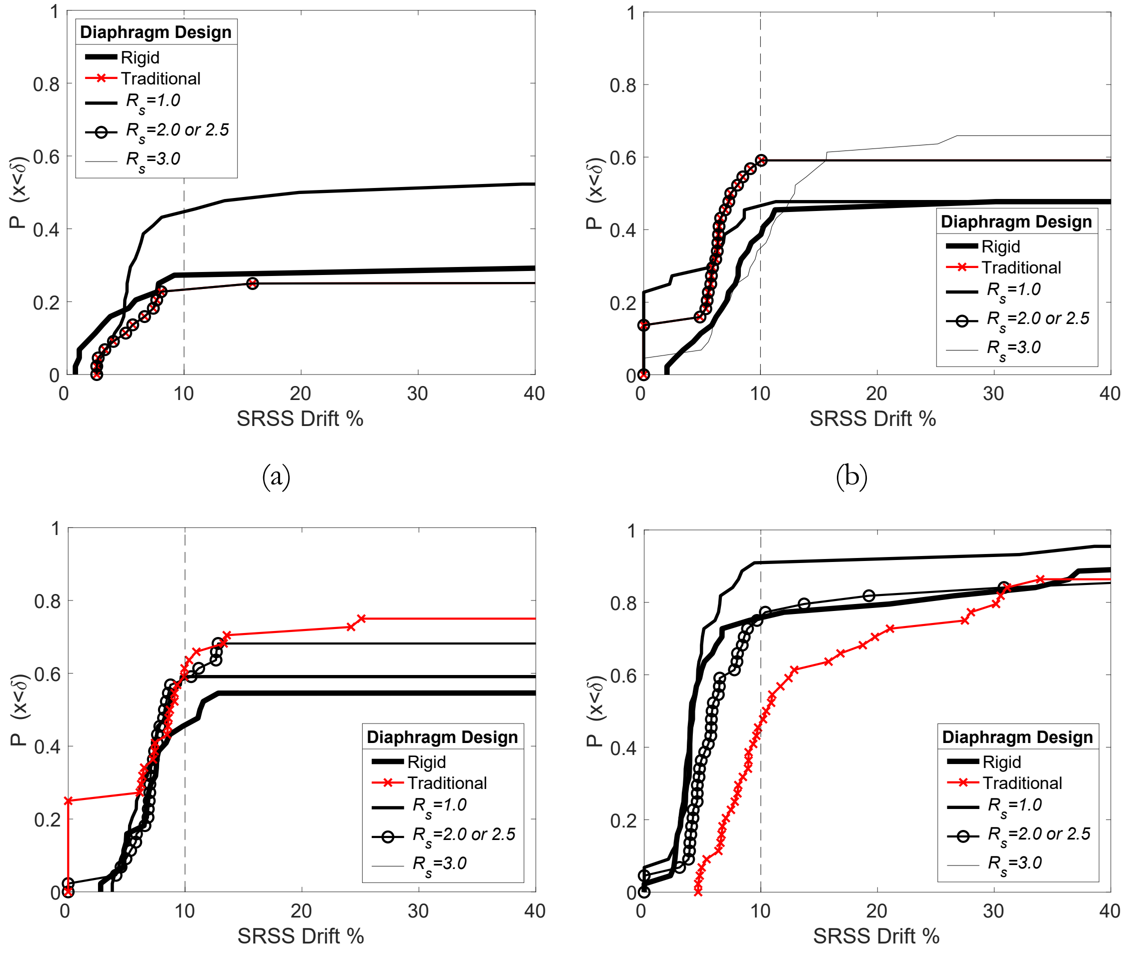

(a)

(b)

(c)

(d)

Figure 5-18. Cumulative distribution function (CDF) plots for SRSS drift for *ACMR*$_{10\%}$ hazard level: (*a*) One-story steel bare deck roof; (*b*) Four-story; (*c*) Eight-story; (*d*) Twelve-story.

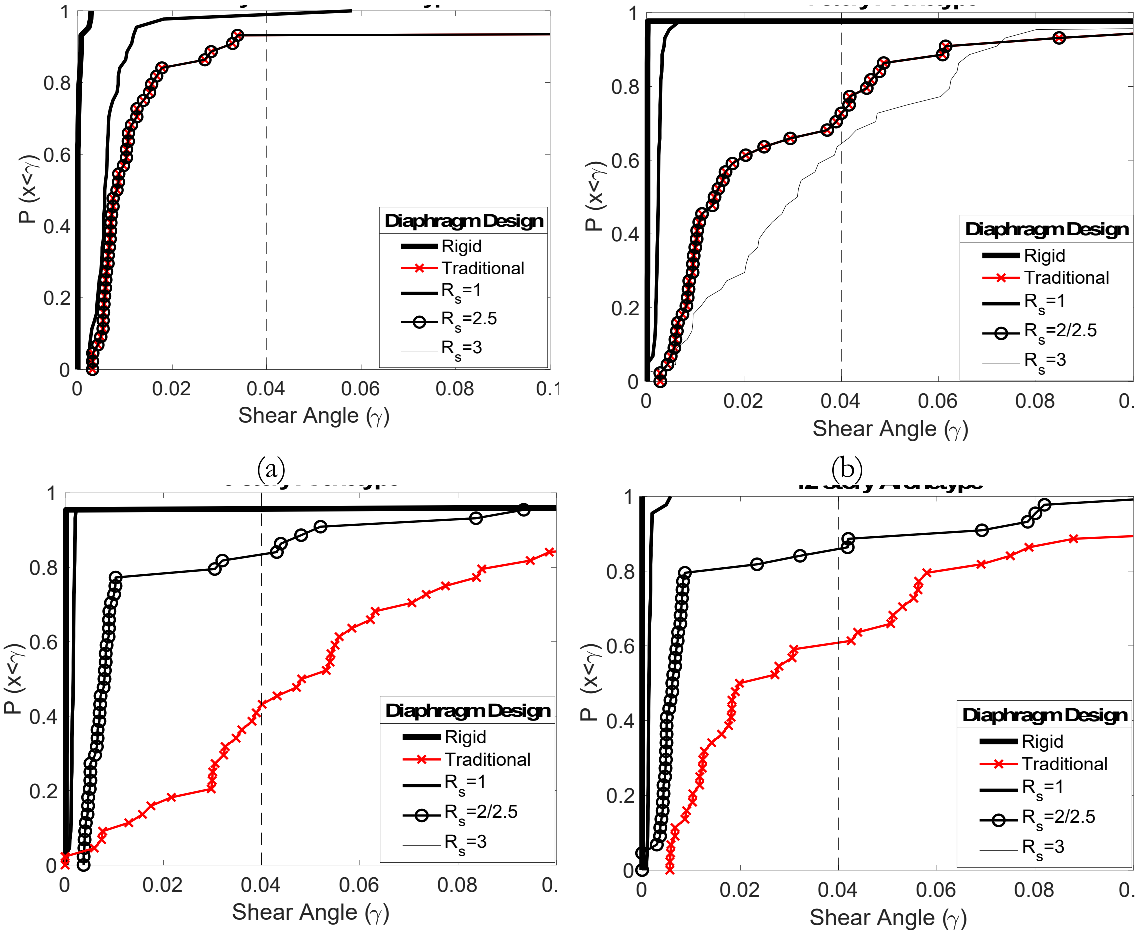

Figure 5-19. Cumulative distribution function (CDF) plots for shear angle for $ACMR_{10\%}$ hazard level: (*a*) One-story steel bare deck roof; (*b*) Four-story; (*c*) Eight-story; (*d*) Twelve-story.

If instead of using the single building criteria of *FEMA P-695* [38] Appendix F-2 uses the conventional criteria for comparing building types, as in Chapter 2 Section 2.4.1 then according to *FEMA P-695* [38], to pass the performance evaluation criteria, individual archetypes must have adjusted collapse margin ratios exceeding $ACMR_{20\%}$. In addition, the adjusted collapse margin ratio averaged across all archetypes in a performance group must exceed $ACMR_{10\%}$. The objective of the *FEMA P-695* [38] methodology is to evaluate the adequacy of seismic response modification coefficients used in design (R, C_d, Ω_o and now extended to R_s) where the collapse potential of the archetypes for different diaphragm designs is specifically extended in this study. This evaluation compares the computed adjusted collapse margin ratio (ACMR) with the acceptable collapse margin ratio, which is based on the collapse margin ratio (CMR).

The collapse margin ratio (CMR) is defined as the ratio of the median spectral acceleration of the collapse level ground motions, $\hat{S}_{CT}$, to the S_{MT} at the fundamental period of the structure, T_1, of the MCE-ground motion level. Table 5-9 shows the ratio of the mean spectra acceleration corresponding to the maximum considered earthquake (MCE), S_{MT}, and design basis earthquake (DE), S_{DT}.

Table 5-9. Mean spectral acceleration corresponding to MCE and DE level

Design Parameters	1-story[a]	1-story[b]	4-story	8-story	12-story
T_0	0.110	0.110	0.110	0.110	0.110
T_s	0.552	0.552	0.552	0.552	0.552
T_L	8.000	8.000	8.000	8.000	8.000
T	0.203	0.304	0.538	0.895	1.209
S_{MS}	1.545	1.545	1.545	1.545	1.545
S_{M1}	0.854	0.854	0.854	0.854	0.854
S_{MT} (*g*)	1.545	1.545	1.586	0.954	0.706
S_{DT}(*g*)	1.030	1.030	1.058	0.636	0.471

[a]: bare steel deck roof; [b]: composite deck roof

To account for statistical variation in the records, the CMR is multiplied by a simplified spectral shape factor (SSF) to obtain the ACMR. It should be noted that according to *FEMA P-695,* the values for ACMR must be divided by 1.2 factor to account the 3D modeling effects. The SSF values are specified and depend on the structural period and the building ductility capacity. Table 5-10 shows the overstrength ($\boldsymbol{\Omega}$), period-based ductility (μ_T) and total system collapse uncertainty (β_{total}) for the archetypes.

Table 5-10. Overstrength, period-based ductility and total system collapse uncertainty (β_{total})

	Diaphragm Design											
	$R_s = 1$			Traditional			$R_s = 2.0$ or 2.5			$R_s = 3$		
Story	$\boldsymbol{\Omega}$	μ_T	β_{total}	$\boldsymbol{\Omega}$	μ_T	β_{total}	$\boldsymbol{\Omega}$	μ_T	β_{total}	$\boldsymbol{\Omega}$	μ_T	β_{total}
1[a]	3.04	2.70	0.506	1.85	2.40	0.485	1.85	2.40	0.485	3.04	2.40	0.485
1[b]	4.59	8.80	0.529	2.20	5.83	0.529	4.58	5.74	0.529	2.21	6.50	0.529
4	1.96	4.11	0.529	1.98	3.51	0.529	1.98	3.51	0.529	1.94	3.80	0.529
8	2.37	3.25	0.529	2.36	3.39	0.529	2.36	3.39	0.529	2.36	3.39	0.529
12	2.31	2.55	0.492	2.30	2.86	0.514	2.30	2.86	0.514	2.30	2.86	0.514
Mean	**2.85**	**4.28**	**0.517**	**2.14**	**3.60**	**0.517**	**2.61**	**3.58**	**0.517**	**2.37**	**3.79**	**0.517**

[a]: bare steel deck roof; [b]: composite deck roof

The median spectral acceleration at collapse initiation is $\hat{S}_{CT}$, which is predicted using the lognormal cumulative function (CDF) plots developed for archetypes based on three values of collapse ratio in each hazard level. Figure 5-20 shows lognormal cumulative distribution (CDF) plot for 4 and 8-story building with diaphragm design $R_s = 2.0$ or 2.5. Lognormal cumulative function (CDF) plots for other archetype buildings are given in of the Appendix A4.

Finally, the SCBF archetypes are evaluated by comparing the calculated *ACMR* to an acceptable $ACMR_{20\%}$ and $ACMR_{10\%}$, which were specified according to the uncertainty factors of structural system, including the quality of design requirements, numerical modeling, and a prescribed set of ground motions. By the *FEMA P695* procedure, 1) the acceptable *AMCR* should reflect conditional probability of collapse of 20% for individual archetype ($AMCR_{20\%}$). The *ACMR* of an individual archetype needed to be greater than the corresponding acceptable $AMCR_{20\%}$ to pass the trial. 2) If the determined *ACMR* was less than the acceptable $ACMR_{10\%}$., the diaphragm design of the performance group does not meet the performance requirements of collapse prevention.

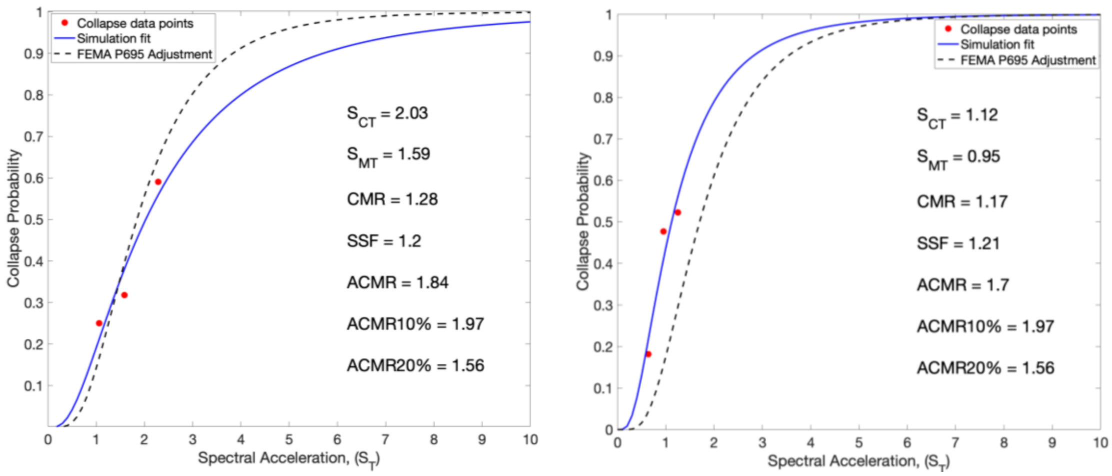

(a) (b)

Figure 5-20. Lognormal cumulative distribution (CDF) plots for diaphragm design with Rs = 2.0 or 2.5: (a) Four-story archetype; (b) Eight-story archetype.

Table 5-11. Summary of evaluation of SCBF archetype buildings using *FEMA P695* methodology

	FEMA P695 Evaluation											
	R_s = 1.0			Traditional			R_s = 2.0 or 2.5			R_s = 3.0		
Story	ACMR	Accep. ACMR 10%	Accep. ACMR 20%	ACMR	Accep. ACMR 10%	Accep. ACMR 20%	ACMR	Accep. ACMR 10%	Accep. ACMR 20%	ACMR	Accep. ACMR 10%	Accep. ACMR 20%
1[a]	2.45	1.91	1.53	1.53	1.86	1.50	1.53	1.86	1.50	1.53	1.86	1.50
1[b]	1.93	1.97	1.56	1.75	1.97	1.56	1.75	1.97	1.56	1.75	1.97	1.56
4	2.06	1.97	1.56	1.84	1.97	1.56	1.84	1.97	1.56	1.35	1.97	1.56
8	2.10	1.97	1.56	2.11	1.97	1.56	1.70	1.97	1.56	1.70	1.97	1.56
12	3.34	1.88	1.51	1.20	1.93	1.54	2.20	1.93	1.54	2.24	1.93	1.54
Mean	2.38	1.97	1.56	1.69	1.97	1.56	1.80	1.97	1.56	1.71	1.97	1.56

[a]: bare steel deck roof; [b]: composite deck roof

Table 5-11 summarizes the results of the evaluation for SCBF archetype buildings with different diaphragm design procedures. Archetype buildings with shorter periods (less floors) generally have lower *ACMR* values than archetypes with longer periods. For diaphragm design with Rs = 1.0, all individual archetypes pass the *FEMA P-695* [38] criteria since have *ACMR* values bigger than AMCR20%. In addition, the performance of the archetype group fulfills the requirement of *FEMA P-695* [38] where the mean value of *ACMR* is bigger than *AMCR10%*. For Traditional diaphragm design procedure, all individual archetypes pass the first criteria of *FEMA P-695* [38] except the twelve-story archetype. However, the mean value of *ACMR* could not pass the second *FEMA P-695* [38] criteria for the performance archetype group. For archetypes with diaphragm design procedure of R_s = 2.0 or 2.5, all individual archetypes pass the *FEMA P-695* [38] criteria since have *ACMR* values bigger than *AMCR20%*. However, for the performance of the archetype group, the mean value of *ACMR* is slightly (difference is around 8%) less than *AMCR10%*. For diaphragm design with R_s = 3.0, all individual archetypes except the four-story archetype pass the *FEMA P-695* [38] criteria. Similar to R_s = 2.0 or 2.5 diaphragm design procedure, Rs = 3.0 diaphragm design procedure could not pass (difference is around 13%) the second *FEMA P-695* [38] criteria for the performance archetype group.

Given that traditional diaphragm design is generally felt to give acceptable behavior for SCBF buildings it is difficult to recommend radical change. The alternative diaphragm design method with R_s = 2 for concrete-filed steel deck floor diaphragms and R_s = 2.5 for bare steel deck roof diaphragms provides the same design as traditional design, or a slightly improved design when higher mode effects are important, as in taller buildings. Further increasing R_s up to 3 may be problematic as evidenced by the performance of the four-story archetype. Decreasing R_s to one appears safe, but likely uneconomical, and explicitly ignores the evidence in O'Brien *et al.* [79] and related work that diaphragm inelasticity exists. Therefore, it is concluded that the alternative diaphragm design procedure with proposed R_s values: R_s = 2 for concrete-filled steel deck diaphragm and R_s = 2.5 for bare steel deck diaphragm may be reasonable for use in design of SCBF buildings.

5.6. Conclusion

To evaluate the seismic performance of SCBF archetype buildings, a series of one-, four-, eight-, and twelve-story SCBF archetype buildings were designed to the current U.S. building code with four different diaphragm designs: a traditional design that uses conventional diaphragm design forces from *ASCE 7-16* [10], a design that uses the seismic demand calculated assuming some diaphragm ductility (values proposed for future editions of the building code of $R_s = 2$ for concrete-filled steel deck floor diaphragms and 2.5 for bare steel deck roof diaphragms), a design with diaphragm demands assuming no diaphragm ductility $R_s = 1.0$, and a design with diaphragm demands assuming significant diaphragm ductility $R_s = 3.0$. Nonlinear response history analyses is used to investigate the behavior of the buildings during earthquake.

Seismic response history analyses show significant inelasticity occurred in the diaphragms as higher modes affected the diaphragm demands. There was also an interaction between diaphragm inelasticity and SCBF inelasticity as the two compounded each other to exacerbate second order effects and cause collapse in some models. Large story drift concentrates at the first story of the building where P-Δ effects are the greatest. For the intermediate stories, the peak story drifts are smaller and more uniformly distributed along the building height, while the peak story drifts near the roof become larger due to higher mode effects. In addition, because of the three-dimensional effect and diaphragm deformation, the predicted peak resultant story drifts can be twice as large as the story drifts along either orthogonal direction of the building. The total story drift considering diaphragm deformation can also be significantly larger than the story drift at the SCBF frames, especially when the diaphragms have smaller in-plane stiffness, which can result in even larger P-Δ effects. Taken together all of these observations indicate conventional three-dimensional or two-dimensional frame analysis with rigid diaphragm assumptions can significantly underestimate the story drifts of a building.

The diaphragms of the archetype buildings remained almost elastic under DE-level ground motions. The diaphragm shear demands for an archetype building with $R_s = 1.0$ diaphragm design were compared to the elastic diaphragm design shear from the *ASCE 7-16* [10] alternative diaphragm design procedure. It was found that ratios of the diaphragm shear demand obtained from the analysis to the design shear given by the alternative diaphragm design procedures in *ASCE 7-16* [10] have an average value of 0.87, indicating a reasonably accurate, but slightly conservative prediction of elastic diaphragm shear demand with the design approach in the studied archetype buildings

The performance of the archetype buildings in terms of collapse was evaluated based on the collapse ratio from the results of nonlinear seismic response history analysis across a suite of scaled earthquake records. For Traditional design, as the number of stories increases, collapse ratios of the archetype buildings tend to become larger since higher mode effects are not considered in the diaphragm design. Collapse ratios of the archetype buildings become smaller with height for all of the alternative diaphragm design options studied: $R_s = 1.0$, $R_s = 2.0$ or 2.5, and $R_s = 3.0$.

In general, the number of collapses associated with $R_s = 1.0$ diaphragm design is close to that with a rigid diaphragm, and these collapses are associated with low-cycle fatigue in SCBF braces. As discussed herein the $R_s = 2.0$ or 2.5 diaphragm design provides designs and performance either consistent with, or improvements from, traditional design. Evaluated per the *FEMA P-695* [38] methodology the $R_s = 2.0$ or 2.5 diaphragm design procedure passes for each individual archetype and nearly passes for the full group. Considering all factors, it is concluded that the diaphragm design procedure with proposed R_s values (R_s = 2 for concrete-filled steel deck floor diaphragms and R_s = 2.5 for bare steel deck roof diaphragms) is reasonable for use in design of these types of structures.

However, it should also be noted that due to the three-dimensional effect in the analysis with the consideration of diaphragm nonlinearity in this study, there are more collapses than expected for multistory buildings under the *DE* and MCE-level ground motions. Future study is desired to further understand the behavior of three-dimensional models that consider diaphragm deformations as compared to the more widely used two-dimensional frame analyses, to investigate the three-dimensional effect on the evaluation of seismic performance of buildings, and to define appropriate performance objectives for the evaluation measures such as collapse ratios.

Chapter 6

Lateral Performance of Metal Building Systems

6.1. Introduction

Metal building systems have the biggest market share of low-rise, non-residential constructions across the United States. Due to the wide range of applications, metal buildings are constructed in different regions including high seismic regions. The observations show a reasonable seismic response for metal buildings in past earthquakes. However, there is a general lack of knowledge concerning the seismic performance of metal building systems due to limited number of computational and experimental studies.

Regarding the investigations on lateral load resisting system in metal buildings, moment frame response has been studied in several studies during the recent years. These studies have been used to update the seismic design guideline for metal buildings consistent with modern performance-based design approach. However, some parts of lateral force resisting system such as rod bracing still use the traditional design limit states established by researchers in 1990s [89]. Lack of knowledge about the potential limit states for rod bracing connection could affect the overall performance of metal building systems in sever seismic events. This chapter aims to provide the research background and objectives for computational modeling of metal building systems in order to provide a better understanding of their seismic performance.

6.2. Metal building Systems

To resist the lateral loads in both directions of metal building, steel moment frames are repetitively built in the transverse direction, while braced frames with rod bracing or shear walls hold the lateral load in the longitudinal direction of the building. Primary steel moment frames fabricated into I-sections from welded plates with the web depth of the members tapered to match the dominant demands, and secondary cold-formed steel purlins and girts running perpendicular to the primary frames. The building skin typically consists of metal roof cladding such as corrugated steel decking, while the walls employ a variety of solutions from lightweight metal cladding to brick, concrete, or masonry. Shows the typical structure of metal building structure. Figure 6-1 shows the typical metal building system.

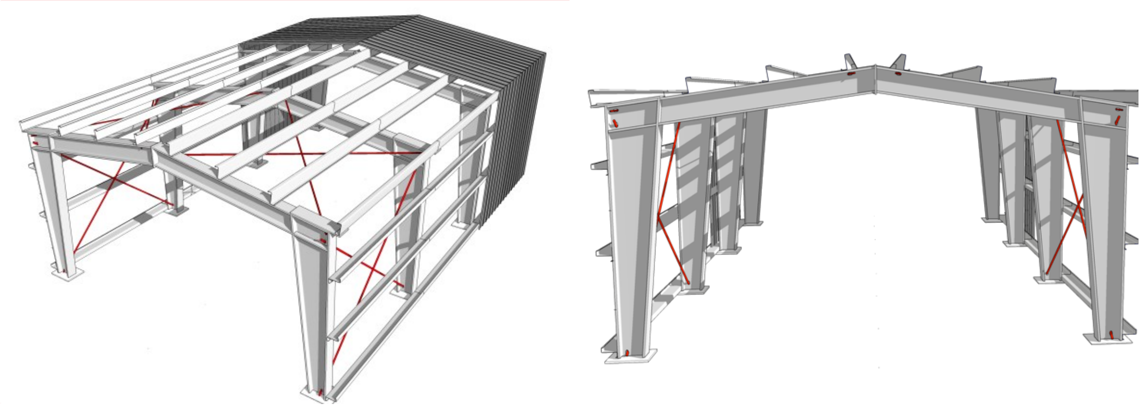
(a) (b)

Figure 6-1. Typical Metal Building System: (a) Three-dimensional view; (b) Front view

6.2.1. Seismic Design of Metal Building Systems

Seismic design of metal buildings typically follows an equivalent lateral force (ELF) approach provided in *ASCE 7-10* [6]. The maximum spectral acceleration for the metal building system derives from the response spectrum divided by the seismic response modification factor (R). According to *ASCE 7-10* [6], the response spectrum can be approximated using the fundamental period of the building in transverse direction. Accuracy of the estimated fundamental period could significantly affect the seismic performance of metal building systems. Using either a small or large value for the estimated natural period could result in a conservative or an unsafe design for the building. Therefore, having a precise estimation of fundamental period using three-dimensional computational models of metal building archetypes could be beneficial for resilient design of buildings.

Different seismic performance factors including the Response Modification Coefficient, R, the Overstrength Factor, Ω, and the Deflection Amplification Factor, C_d are needed for the design. Current practice of designing metal building systems suggests a value equal to 3.5 for seismic response modification factor (R) which is based on ordinary steel moment frames assumption [34]. In addition, Overstrength Factor, Ω, and the Deflection Amplification Factor, C_d values are considered equal to 3 for most of the buildings.

In the design process, different parts of the primary moment frames such as flanges, web, and taper are designed and optimized based on the moment envelope computed using the seismic base shear obtained by different load combinations. It should be noted that due to use of slender flange and web plates and the relatively long unbraced lengths of inner flanges, either lateral-torsional buckling (LTB) or flange local buckling (FLB) is the design limit state to calculate the ultimate strength of metal building moment frame members.

AISC/MBMA Steel Design Guide 25: Frame Design Using Web-Tapered Members [90] is provided the details for these design limit state [34]. The research background and challenges for having a resilient design for both lateral resisting system in two directions are described in the following sections.

6.2.2. Moment Frame Response

In metal buildings, moment frames are considered as ordinary moment frames for the design. However, previous studies showed that current metal building design might be vulnerable due to lack of ductility in the moment frame system [36]. As it described in Section 6.2, lateral-torsional buckling (LTB) or flange local buckling (FLB) are two design limit states due to the lack of flange or web compactness limit for web-tapered frames. Some research studies such as Nethercot and Trahair [91], White and Jung [92], and White and Kim [93] shows the importance of including the influence of adjacent unbraced segments on the LTB strength of prismatic members. In addition to LTB which could be considered as a conservative limit states, underestimating the ultimate strength of the moment frame which should operate as inelastic hinge can cause an unsafe deformation and may lead to premature failures in a large seismic event.

To evaluate the seismic performance of metal building system through experiment, a full-scale quasi-static cyclic test was conducted by Hong and Uang [94] at University of California-San Diego. The experimental results show that the frame deformed elastically up to 2.5%. Subsequently, a decrease in cyclic strength occurred due to lateral-torsional buckling in the flanges. The findings of Hong and Uang [94] study led to the proposal of a drift limit criteria for seismic design approach [95]. In 2013, the capability of the proposed drift limit criteria was investigated with conducting an experimental program on seismic behavior of two primary moment frames connected with girts, purlins, and panels under uniaxial dynamic load [36]. Several ground motion records in different scaled magnitude have been used. The results show that the metal building system never experienced collapse even in high seismic demands. In this study, the primary moment frames accommodated up to 4% drift with some fracture observed. Lateral-torsional buckling was also observed in the main frames. In addition, the results showed that empirical natural period prediction from *ASCE 7-10* [6] is not able to provide an accurate value for actual natural period of the structures. New equations were proposed and validated for empirical natural period prediction.

Lack of knowledge to validate the new drift limit approach and misperceptions regarding the seismic response modification factor, *R*, led to more seismic testing at University of California-San Diego. Observation of failure mode showed that the main frame tapered members could undergo several LTB cycles without fracture. Comparing the experimental results with the predictions from AISC/MBMA Steel Design Guide 25 [90], showed that LTB capacity of the main frames could be determined if the calculation of the critical elastic buckling moment considers the bracing conditions. In 2018, NBM Technologies, Inc. (NBM) [96] investigated seismic performance of metal building systems within the *FEMA P-695* methodology. *ABAQUS* [97] finite element modeling software has been used for three-dimensional high-fidelity models. The findings form also validate the seismic response modification factor (*R*) equal to 3.5 based on *ASCE 7*-10 [6] seismic design procedures. The collapse margin ratio, defined as the spectral acceleration at median collapse probability to the spectral acceleration from the Maximum Considered Earthquake (MCE) was on average across the metal building performance group higher than the acceptable collapse margin ratio corresponding to a 10% collapse probability, with no outliers greater than 20%. These findings confirmed the validity of the existing *ASCE 7-10* [6] equivalent lateral force seismic design procedures for metal buildings in the performance group considered.

6.2.3. Rod Bracing Response

For lateral loads perpendicular to the primary frames, and for diaphragm action in the roof plane, rods in an X-configuration are typically employed within a given bay of the building. The rods connect to the primary frames by running through holes in the web and are anchored by large hillside washers that fit within the holes in the web of the primary frame and are designed to accommodate the X-bracing approach angle that varies based on the building height and bay spacing (see Figure 6-2). Thus, the rod assemblage consists of the rod, the anchorage (hillside washer), and the primary frame member that is penetrated by the rod.

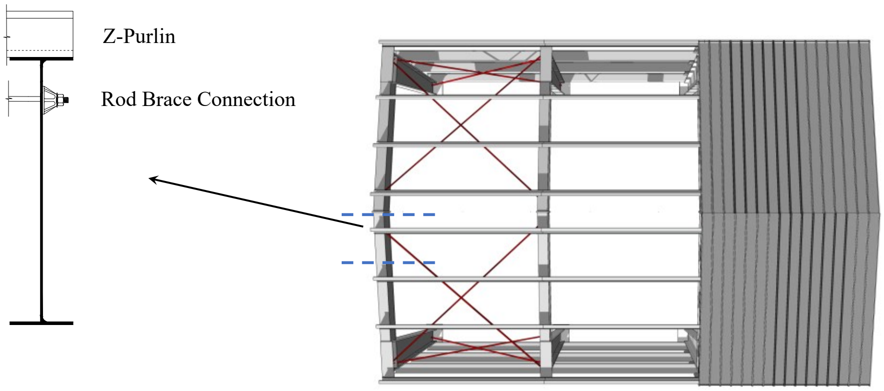

Figure 6-2. Application of rod bracing in metal building system: top view rod bracing detail

Deformation of the web of the primary frame member, accommodation in the hillside washer anchorage, and of the rod itself all contribute to the brace flexibility. The rod, its anchorage, or elements of the primary frame all can potentially be associated with the final limit state of the rod brace assemblage.

In 1992, Sinno completed a study on rod bracing strength that forms the primary methods in use for design of rod bracing anchorages in metal building systems today [98]. Sinno's testing documented the influence of web thickness, transverse web stiffeners, web patch plates, hillside washer details, and rod diameter on strength. Angle of the rod was maintained at 60 degrees from the web for all tests. Sinno's study recommended five limit states be considered: (1) tensile failure of the rod; (2) weld failure of the web-flange connection; (3) web plate shear fracture; (4) web plate punching shear fracture; and (5) web plate tensile fracture. Limit state equations and example problems were provided. After Northridge earthquake in 1994, failure of rod bracing anchorage connection has been reported due to damage to several metal buildings. The evidence shows the failure of five out of six hillside washer-to-web connection in one metal building which was mainly due to the fracture of hillside washer and subsequent pull-through of the rods [99]. However, the fracture of hillside washer has not been included in recommended limit states by Sinno [32]. Moreover, subsequent proprietary testing has brought the applicability of these design limit states into question. The hillside washers have evolved significantly and are now commonly made from ductile steel, as opposed to cast iron as used in the 1992 study. More broadly, steel rods serve as common bracing as well as anchorage in a variety of structures and research on stiffness and strength similar in spirit to this study have been performed on bridges [100], transmission towers [101], rehabilitation for building shear walls [102], and internal diaphragms for large thin-walled box columns [103]. Later on, the results of an experimental program to revisit rod bracing design for metal buildings will be discussed in this study.

6.3. Seismic Performance Evaluation for Metal Building Systems

The main objective of this study is utilizing the experimental test results and specifically the stiffness of rod bracing anchorage connection, conducted by Foroughi *et al.* [37] , into the full three-dimensional computational model of metal building archetype. The findings of this study could be beneficial to have a better prediction of metal building seismic response. It should be noted that an archetype building with members which has same configuration as experimental program, is designed and provided by MBMA. The details about the archetype building are provided in Chapter 8 of this study.

To evaluate the seismic performance of current metal building seismic design with actual values of strength and stiffness for rod bracing system, following analysis has been considered: 1) Modal (vibration) analysis of the archetype to obtain the fundamental period of vibration using three-dimensional model in *OpenSees*; 2) Static nonlinear pushover analysis on each archetype to obtain the system overstrength and period-based ductility; 3) Nonlinear time history response analysis to evaluate the performance of the metal building archetypes using *FEMA P-695* methodology.

6.3.1. Fundamental Response of Metal Building Systems

6.3.1.1. Modal Analysis

Natural period of metal building systems has an important role in seismic design of the building. Inaccurate values for natural period and the mode shapes of the building can result in an overestimation or underestimation in seismic response of structure. Rod bracing assemblage system as a part of lateral force resisting system could affect the values of natural period. Considering smaller stiffness for rod bracing could cause larger natural period for structures. In this study, modal analysis is considered for the metal building archetypes using

OpenSees software. The objectives are obtaining the actual values of natural periods and mode shapes using the test data from [37]. The results from *OpenSees* software will be compared to estimated natural period values obtained by seismic design provisions for metal building systems.

6.3.1.2. Nonlinear Static Pushover Analysis

In this section, nonlinear static pushover analysis is considered to evaluate the static behavior of metal building systems. Ductility and Overstrength of the archetypes with actual values of rod bracing stiffness are two key principles to predict the seismic performance of the buildings. Based on *FEMA P-695* [38] provision, vertical distribution of lateral force at each node should be assigned proportional to the product of the tributary mass and the fundamental mode shape coordinate at the node. To apply the static load for the nonlinear static pushover analysis in transverse direction of the building, a displacement control load pattern is used.

6.3.2. Nonlinear Response History Analysis

To evaluate the seismic performance of the metal buildings with actual values of rod bracing stiffness, nonlinear response history analysis is considered with the archetype models subjected to the suite of *FEMA P-695* [38] far-field earthquake motions. In addition, ground motion scaling of the records to desired hazard levels is planned based on design period of the metal building. Three different ground motion scaling including Design Based Earthquake (*DE*), Maximum Considered Earthquake (*MCE*), and an Adjusted Collapse Margin Ratio ($ACMR_{10\%}$) are considered for nonlinear time history analysis. Figure 6-3 shows the three-dimensional metal building archetype modeling in *OpenSees* Software.

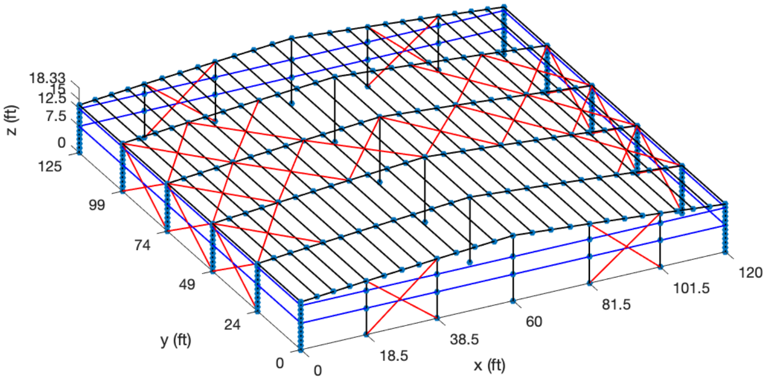

Figure 6-3. Reduced order modeling of metal building archetype using *OpenSees* software

6.4. Conclusion

In this chapter the importance of having an accurate prediction of seismic response for metal building systems is described. The lateral force resisting system in two directions of the building is presented and discussed. The seismic design procedure using *ASCE 7-10* [6] and limit states are provided. Literature review on previous studies for both primarily moment frames and rod bracing are presented. Finally, different parts of computational modeling is described and discussed.

Chapter 7

Fundamental Response of Metal Building Rod Bracing

7.1. Introduction

Rod or cable bracing is often provided in metal buildings to develop lateral resistance against wind or seismic loads in the 'long' direction of the building, i.e., in the direction perpendicular to the primary frames. This bracing is oriented in an X-configuration between frame bays, with bracing termination points occurring in the primary frame webs. The rods or cables connect to the primary frames with hillside washers that accommodate the X-bracing approach angle that vary based on the building height and bay spacing. The hillside washer mounts inside a punched hole in the web, and the performance of the bracing, both stiffness and ultimate capacity, is dependent upon the web out-of-plane plate bending stiffness and web-to-flange weld lengths and orientations, and the location of the anchorage point relative to the frame flanges. X-bracing stiffness also dictates lateral load sharing between frames and exterior cladding.

The primary objective of this section is to experimentally establish the stiffness, strength and applicable limit states for rod assemblages used as braces in metal building primary frames. Twelve rod brace assemblages with differing details related to the geometry of the primary frame members, anchorage of the rod into the frame member, and angle of the rod relative to the framing member were tested in tension until failure. Included herein is a detailed description of the experimental program employed to determine the reported stiffness and strength. The experimental information is intended to be used to validate future improvements to siesmic performance evaluation of metal building archetypes.

7.2. Industry Survey of Rod Anchor Details in Metal Buildings

An important first step in this study was to document typical rod bracing details employed by Metal Building Manufacturers Association (MBMA) members.

7.2.1. Rod and cable bracing – industry survey results

Anchor rods are typically Grade 55 with nominal unthreaded diameters ranging from 0.375 in. to 1.5 in. (Table 3-1, Figure 7-1) with an average of 0.96 in. (COV of 0.41) and the most common rod angle (measured from the web plane) reported was 45 degrees (COV of 0.50) (Figure 7-2). Cable bracing details, although not the focus of this research, were also collected in the survey, with the ASTM A475 extra high strength type as the most popular specified material and a diameter range from 0.25 in. to 1.5 in. with an average of 1.0 in. (COV of 0.48).

Table 7-1. List of SCBF Archetype Buildings for the Study

	Rod Brace		
	Min	Max	Most repeated
Material	ASTM A529	ASTM A572	Gr (50-55)
Diameter, minimum (inches)	0.375	1.000	0.500
Diameter, maximum (inches)	0.625	1.500	1.250
Thread type (Rolled, Cut, Other)			Cut
Nut material			ASTM A563 Grade C HvyHex,D, DH
Double nut? Yes or No			No
washer material specification			ASTM F436

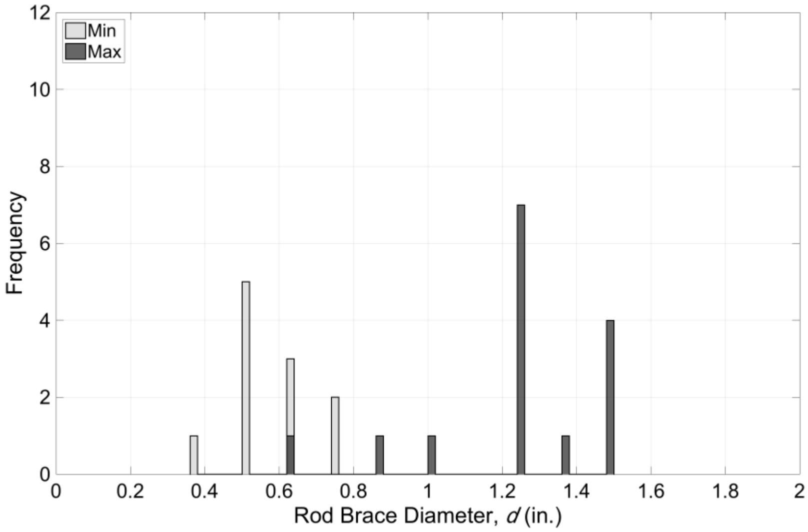

Figure 7-1. Rod brace diameter industry survey results – min and max reported ranges.

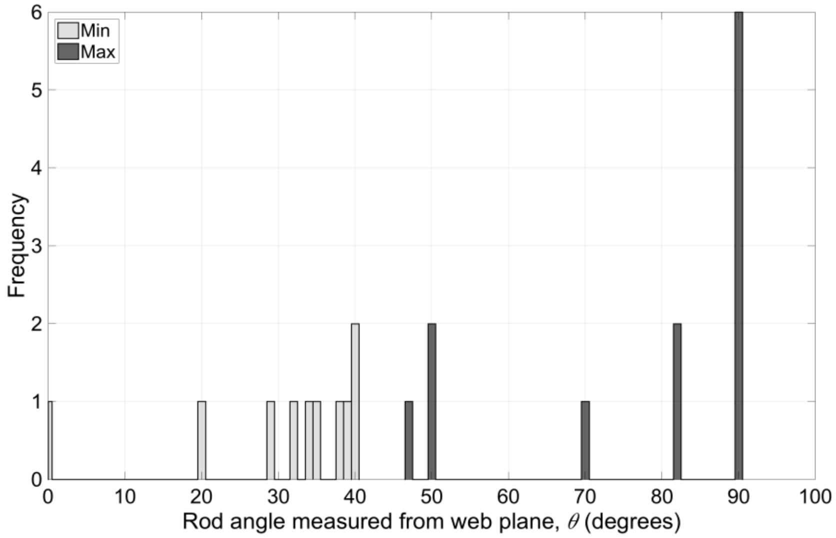

Figure 7-2. Rod brace angle industry survey results – min and max reported ranges where θ is the angle from the web plane to the rod (0 degree result was probably misreported and should be 90 degrees).

Table 7-2. Industry survey results - cable brace material, diameter, and washer details

Cable Brace			
	Min	Max	Most repeated
Material			ASTM A475 Extra high strength
Cable diameter, minimum (inches)	0.250	0.375	0.250
Cable diameter, maximum (inches)	0.626	1.500	1.250
Eyebolt material			ASTM A563 Grade C HvyHex,D, DH
Eyebolt diameter, minimum (inches)	0.500	0.750	0.500
Eyebolt diameter, maximum (inches)	0.750	0.875	0.875
Thread type (Rolled, Cut, Other)			Rolled
Nut material			ASTM A563 Gr. A Hx Nut
Double nut? Yes or No			No
washer material specification			F436, F844

7.2.2. Hillside washer type and details – industry survey results

The most commonly reported rod brace anchor connection in the survey is made with a hardened steel hillside washer shown in Figure 7-3(a) with an oversized web bearing surface, a nipple for engaging the web when the rod is anchored at an angle, and a rounded, ridged bearing surface for the rod nut and washer. One of the member companies responded that they use an aluminum hillside washer, see Figure 7-3 (b).


(a) (b)

Figure 7-3. Hillside washer types reported in the survey: (a) hardened steel with an oversized bearing surface and nipple for engaging web edge; and (b) an aluminum hillside washer.

7.2.3. Primary frame web and flange dimensions and details – industry survey results

Primary frame web and flange dimensions used in a welded built-up cross section are important parameters that influence the rod brace anchor strength limit states and in-service building response. For example, thinner webs are susceptible to local bearing and tearing deformations and the system stiffness they provide is less than a thicker web. Frame web depth varies widely from 7 in. to 72 in. (Table 7-3, Figure 7-4) with an average of 32.1 in. (COV of 0.89), and web thickness from 1/8 in. to 3/4 in. (Table 7-3, Figure 7-5) with an average of 0.34 in. (COV of 0.66). Frame flange width ranges from 5 in. to 16 in. with an average of 7.75 in. (COV of 0.46) as summarized in Table 7-4 (and Figure 7-6). Flange thickness ranges from 3/16 in. to 1.5 in. with an average of 0.65 in. (COV of 0.81) (see Figure

7-7). The most common fabrication detail for the primary frame is a single-sided fillet weld for connecting the web to flanges.

Table 7-3. Industry survey results - web dimensions and details for a metal building primary frame

Web			
	Min	Max	Most repeated
Material			A529, A572 or A1011 Grade 55
Depth, minimum (inches)	7	10	8
Depth, maximum (inches)	60	72	60
Thickness, minimum (inches)	0.120	0.134	0.134
Thickness, maximum (inches)	0.375	0.75	0.5
Connecting web to flanges			Continuous, fillet, Single sided
Connecting web to base plate			Continuous, fillet, Single sided-All Around
Connecting web to end plate			Continuous, fillet, Single sided-All Around

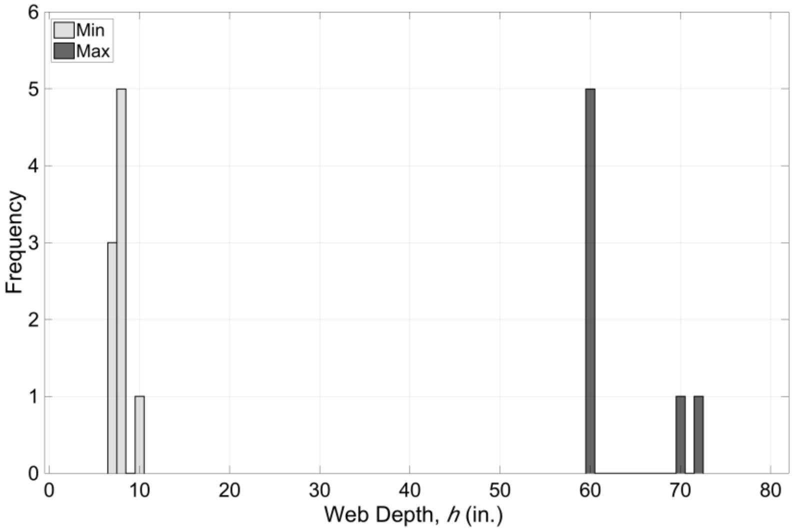

Figure 7-4. Primary frame web depth industry survey results – min and max reported ranges.

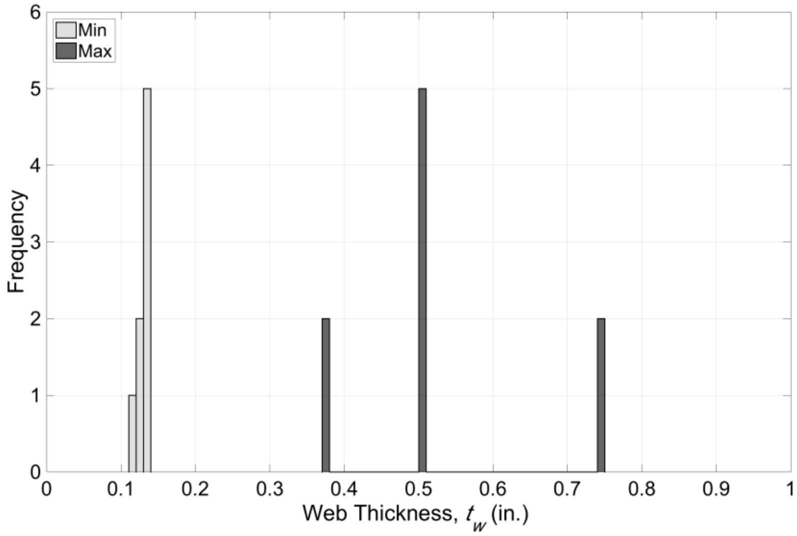

Figure 7-5. Primary frame web thickness industry survey results – min and max reported range.

Table 7-4. Industry survey results - flange dimensions and details for a metal building primary frame

	Flange		
	min	max	Most repeated
Material			ASTM A572, A529, Grade 55
Width (inches)	5	16	6
Thickness (inches)	0.1875	1.5	0.25
Width to thickness ratio	3	32	12

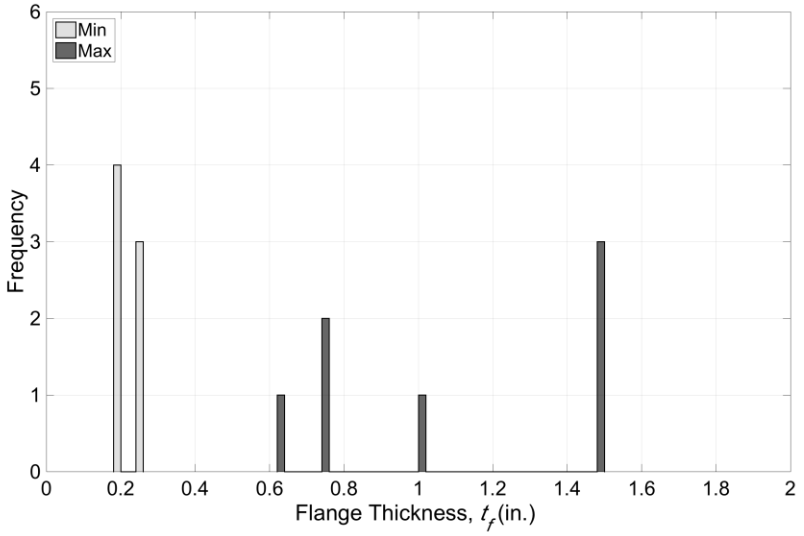

Figure 7-6. Primary frame flange thickness industry survey results – min and max reported ranges.

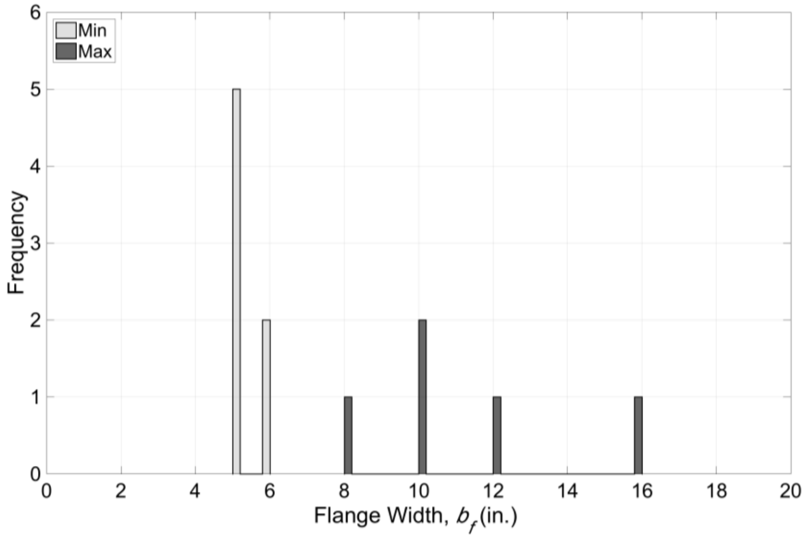

Figure 7-7. Primary frame flange width industry survey results – min and max reported ranges.

7.2.4. Rod brace anchor location and details in primary frame – industry survey results

Industry reported anchor edge distances from the flange ranged from to 2 in. to 4 in., with an average of 2.5 in. (COV of 0.81).

Table 7-5. Industry survey results – anchor hole dimensions and details for a metal building primary frame

Slotted hole			
	Min	Max	Most repeated
Width (inches)	0.688	1.188	1.375
Length (inches)	2.000	4.000	2.500
Edge distance to flanges (inches)	2.000	4.000	2.500
Distances to end plate or base plate (inches)	6.000	6.500	6.000

This industry data is used to design the experimental program presented in the next section. The goal of the testing program is to explore the validity of current MBMA ultimate strength limit states for rod brace anchor connections and to proposed changes to the design methodology if warranted.

7.3. Test specimens

A small section of the primary frame where the rod bracing penetrates through the web, as called out in Fig. 1c by dashed lines, was isolated and selected for testing. Primary frame dimensions and the angle of the rod brace in relation the web of the primary frame member were varied, with the remaining details: material, boundary conditions, rod size, hillside washer size, hole location, etc. held constant as summarized in Table 7-6 and Figure 7-8. The selected dimensions and anchorage details were based on a survey of U.S. metal building manufacturers summarized in [8].

Nomenclature of the specimen dimensions is defined in Figure 7-8.. The nominal web depth (h) is 610 mm and the oval shaped anchor rod hole in the web have a length (L_{hole}) and depth (w_{hole}) of 540 mm and 270 mm, respectively. The rod anchor hole is located at the mid-length of each specimen, with the hole centerline 63.5 mm from the web plate. The length of the rod from the hillside washer to the actuator (L_{rod}) is 1150 mm. All frame members were fabricated with a one-sided fillet weld connecting the flange and web plates, with the specimen oriented in the test frame such that the weld was on the same side as the hillside washer during loading. A minimum of three tests was performed for each configuration.

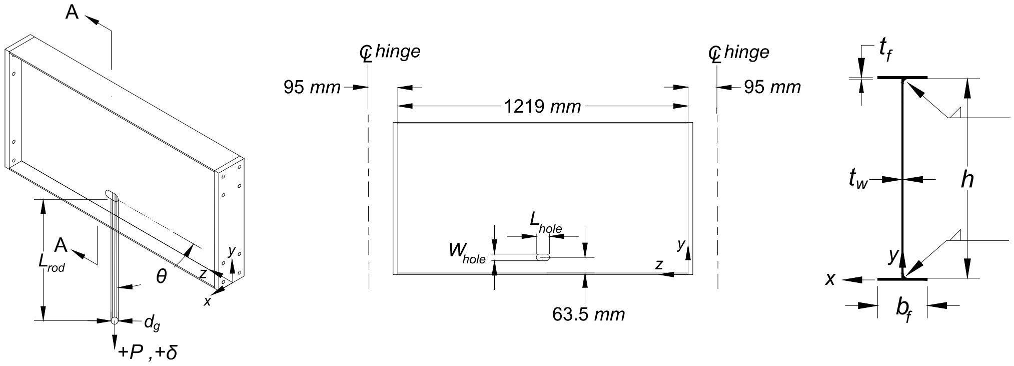

(a) Isometric (b) Elevation (c) Section A-A

Figure 7-8. Metal building primary frame steel plate girder specimen dimension nomenclature.

Table 7-6. Test matrix and nominal specimen dimensions

Specimen Group	Description	Rod angle	Specimen cross-section		
			Web	Flanges	
		θ	t_w	b_f	t_f
		degrees	mm	mm	mm
C	Control	45	4.8	152	6.4
W	Reduce web thickness	45	3.4	152	6.4
F	Increase flange width and thickness	45	4.8	203	13
A	Reduce rod angle	30	4.8	152	6.4

The hillside washer selected is consistent with the style most commonly noted in the industry survey. The washer has a large web bearing surface and utilizes a curved washer on the serrated bolt bearing surface to minimize slip as the anchor is loaded. Washer dimensions are provided in Figure 7-9. The washer nipple (18 mm x 8.9 mm in section) is designed to transmit the bearing force in the web hole. The selected washer has the ability to accommodate a rod angle (measured from the plane of the web) as low as 38 degrees.

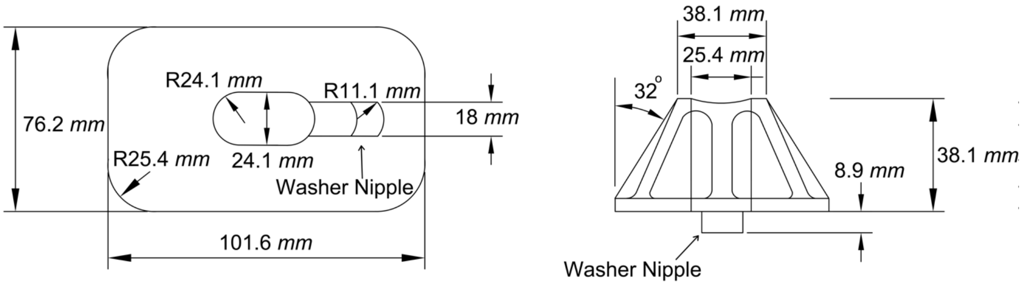

Figure 7-9. Dimensions and details for the hillside washer used for all tests in this research.

7.4. Test setup, loading and instrumentation

The test setup approximates an anchor rod engaging a metal building frame as lateral bracing. Mechanical pin connections bolted to welded end plates are utilized at the specimen ends as shown in Figure 7-10 creating boundary conditions with high warping restraint. The centerline pin-to-pin distance (*L*) of the framing member is 1409 mm. Framing orientation in the test rig is rotated compared to its position in a metal building (in the test frame the rod is anchored near the bottom flange) to minimize eccentricity and deformation in the test rig. The rods are produced with ASTM 1554-55 steel and have a nominal outer unthreaded diameter of 220 mm. Mill certificates provided with the rods recorded their yield stress as 580 MPa.

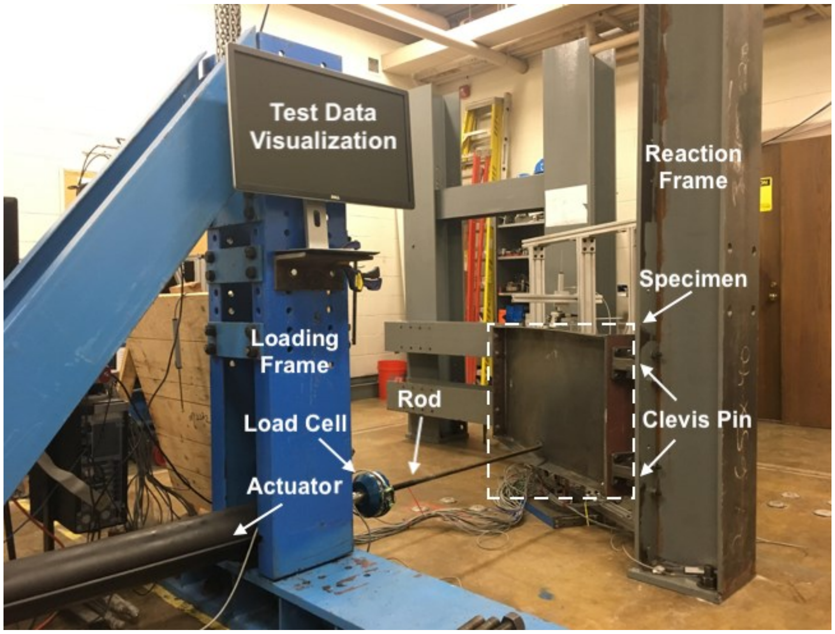

Figure 7-10. Metal building primary frame test setup with rod anchor.

Each specimen was loaded with a hydraulic actuator at a displacement rate of 0.1 mm/sec, total testing time for a specimen was typically 35 minutes. The force in the rod was recorded with a load cell attached to the actuator with an accuracy of +/- 0.4 kN. Elongation of the rod was recorded with an internal actuator LVDT with an accuracy of +/- 0.3 mm. Additional measurements were made with position transducers (accuracy of +/- 0.0015 mm.) that allow the decomposition and study of local web deformation and rigid body rotation and twist as shown in Figure 7-11. A reference load for the testing was established as the nominal predicted tensile strength of the rod, $P_{n,rod}$ = 169 kN. Where $P_{n,rod}$ is calculated as the yield stress (580 MPa) multiplied by the unthreaded rod area (388 mm^2) and then further multiplied by 75% to account for fracture in the threaded plane consistent with *AISC 360-16* [43] .

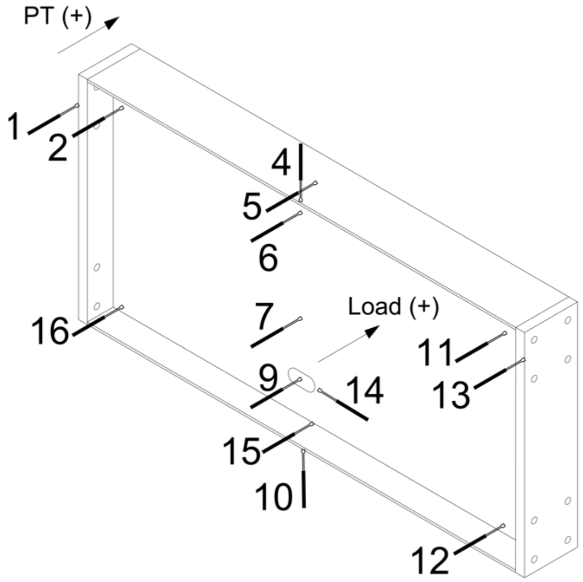

Figure 7-11. Position transducer plan designed to isolate specimen local web and flange deformation, weak axis bending, and torsion deformation.

7.5. Specimen measurements and material properties

Cross-section dimensions were measured in each element: top flange, web, and bottom flange and the results are presented in Table 7-7 as an average of three measurements. Web out-of-straightness relative to the flange centerline was observed in most specimens, and these magnitudes, measured at the specimen mid-length for the bottom flange, are also provided in Table 7-7 where $+\Delta x_{web}$ is in the same direction as $+x$ shown in Figure 7-11.

Tensile coupon tests were performed in accordance with *ASTM E8/E8M-16* [10] on the plate used to manufacture the specimens – 2 web plates and 2 flange plates of different thicknesses. Plates of the same thickness were sourced from the same heat. Average steel yield stress σ_y, steel ultimate stress σ_u, and percent elongation at ultimate, ε_u, are summarized in Table 7-8.

Table 7-7. Measured specimen dimensions

Specimen Name	Top Flange	Web	Bottom Flange	Web out-of-straighness
	b_f	h	b_f	Δ_{xweb}

	mm	*mm*	*mm*	*mm*
C1	152.14	607.91	152.29	-25.40
C2	152.15	607.91	152.02	-19.05
C3	151.91	607.90	152.00	-12.70
C4	151.91	607.90	152.00	-12.70
W1	151.89	608.01	151.97	-5.08
W2	152.23	611.29	151.99	-6.35
W3	152.31	609.60	152.06	-5.59
W4	152.31	609.60	152.06	-5.08
F1	204.04	604.26	203.45	-21.59
F2	204.38	608.33	203.45	-24.13
F3	204.47	608.35	204.22	-25.40
F4	204.47	608.35	204.22	-22.86
A1	151.89	608.58	151.38	-7.62
A2	151.72	608.58	151.72	-12.70
A3	151.97	609.09	151.72	-2.54

Table 7-8. Specimen steel yield stress, ultimate stress, and elongation

Specimen name	Flange					Web				
	t_f	w_{coupon}	s_y	s_u	ε_u	t_w	w_{coupon}	s_y	s_u	ε_u
	mm	mm	MPa	MPa	%	*mm*	mm	MPa	MPa	%
C1	6.3	12.7	492	552	18	4.6	12.6	411	500	25
C2	6.2	12.7	492	552	18	4.6	12.6	411	500	25
C3	6.4	12.7	492	552	18	4.6	12.6	411	500	25
C4	6.4	12.7	492	552	18	4.6	12.6	411	500	25
W1	6.2	12.7	492	552	18	3.4	12.5	332	508	31
W2	6.1	12.7	492	552	18	3.4	12.5	332	508	31
W3	6.2	12.7	492	552	18	3.4	12.5	332	508	31
W4	6.2	12.7	492	552	18	3.4	12.5	332	508	31
F1	12.9	12.6	364	579	34	4.6	12.6	411	500	25
F2	12.9	12.6	364	579	34	4.6	12.6	411	500	25
F3	13.1	12.6	364	579	34	4.6	12.6	411	500	25
F4	13.1	12.6	364	579	34	4.6	12.6	411	500	25
A1	6.5	12.7	492	552	18	4.6	12.6	411	500	25
A2	6.1	12.7	492	552	18	4.6	12.6	411	500	25
A3	6.3	12.7	492	552	18	4.6	12.6	411	500	25

7.6. Rod anchorage connection limit states

Although the number and variation in the test specimens is relatively small, the number of different observed limit states is large. Observed limit states include fracture of the rod, flange local buckling (FLB) of the frame, bearing failure including tearing of the web hole, and slip and shear of the nipple of the hillside washer. The observed limit state for each test is reported in Table 7-9.

Flange local buckling occurred in all but the F series specimens. The rod load at which flange local buckling initiated, $P_{test,FLB}$, is provided in Table 4, and calculated at the intersection of the pre-buckling and post-buckling load-deformation slopes as annotated in Fig. 11. Flange local bucking caused stiffness degradation and rapid out-of-plane anchor deflection and rotation that was eventually arrested by the pin-pin end boundary conditions of the test specimen. The restraint provided by the heavy end plates and the pin boundary conditions reestablished anchor stiffness and load increased until either rod failure or local web bearing and washer disengagement at the peak load for the test, $P_{test,u}$. Figure 7-13 shows typical flange local buckling as observed in the W1 specimen.

Figure 7-12. Typical flange local buckling deformation (W1 test shown).

Web bearing deformation and associated material pileup at the web bearing surface was observed in test groups C, F, and A, and is shown in a typical instance in Figure 7-13. Web tearing, i.e., the nipple of the hillside washer cutting through the web without material pileup is shown in Figure 7-14, and was observed in test group W where the web thickness was reduced from the control (C) configuration. Typically, tests were terminated when the nipple of the hillside washer slipped off the web bearing point or fully or partially sheared off (see Figure 7-15). The lone exception is test C2 where the test was terminated after the rod fractured. Test C1 was terminated by the researchers before reaching ultimate load.

Figure 7-13. Typical web bearing deformation at the hillside washer nipple bearing point (C3 test shown)

Figure 7-14. Typical web tearing deformation at the hillside washer nipple bearing point (W1 test shown)

Figure 7-15. Hillside washer nipple bearing failure (C3 test shown)

7.7. Overall load-deformation response

Overall load-deformation response for the four specimen groups (C, W, F, and A per Table 1) are provided in Figure 7-17 to Figure 7-20. Initial nonlinearity at small loads resolved as the hillside washer settled into bearing against the web. In cases where x_{web} was large and curved in the opposite direction to the applied load, for example test C3, there is a shift in the load-deformation response (see Figure 7-17) as the web snaps through. Localized web deformation continued up to approximately $0.40P_{n,rod}$ with linear pre-peak stiffness that varied as a function of the frame member cross-section dimensions. Flange local buckling deformation initiated in all specimens except those in the F group (a wider, thicker flange) with a typical buckling half-wave as shown in Figure 7-12 developing slightly offset from the centerline.

Table 7-9. Summary of tested response and observed limit states including flange local buckling and peak test load

Specimen Name	Rod load at buckling in test	Buckling half-wavelength	Half-wave offset from anchor location	Rod load at connection failure	Observed limit states
	$P_{test,FLB}$	$L_{cr,test}$	$Dz_{cr,test}$	$P_{test,u}$	
	kN	mm	mm	kN	
C1	82.8	137.00	5.00	terminated early	Flange local buckling (FLB)
C2	83.6	132.00	15.00	179.5	FLB, Rod fracture
C3	79.2	140.00	20.00	169.0	FLB, Web bearing, Washer nipple shear
C4	77.4	134.62	5.00	162.2	FLB, Web bearing, Washer nipple shear
W1	79.0	161.00	15.00	106.6	FLB, Web tearing, Washer nipple slip
W2	75.6	153.00	5.00	101.4	FLB, Web tearing, Washer nipple slip
W3	79.4	156.21	15.00	92.1	FLB, Web tearing, Washer nipple slip
W4	74.8	161.00	10.00	113.4	FLB, Web tearing, Washer nipple slip

F1	No Buckling	No Buckling	No Buckling	135.7	Web bearing, Washer nipple shear
F2	No Buckling	No Buckling	No Buckling	137.0	Web bearing, Washer nipple shear
F3	No Buckling	No Buckling	No Buckling	136.6	Web bearing, Washer nipple shear
F4	No Buckling	No Buckling	No Buckling	132.6	Web bearing, Washer nipple shear
A1	60.0	122.00	5.00	133.4	FLB, Web bearing, Washer nipple slip
A2	65.0	120.00	5.00	135.3	FLB, Web bearing, Washer nipple slip
A3	66.3	125.00	5.00	135.7	FLB, Web bearing, Washer nipple slip

(a) *(b)*

Figure 7-16. Tested specimen group C: (a) Front side view (b) Back side view

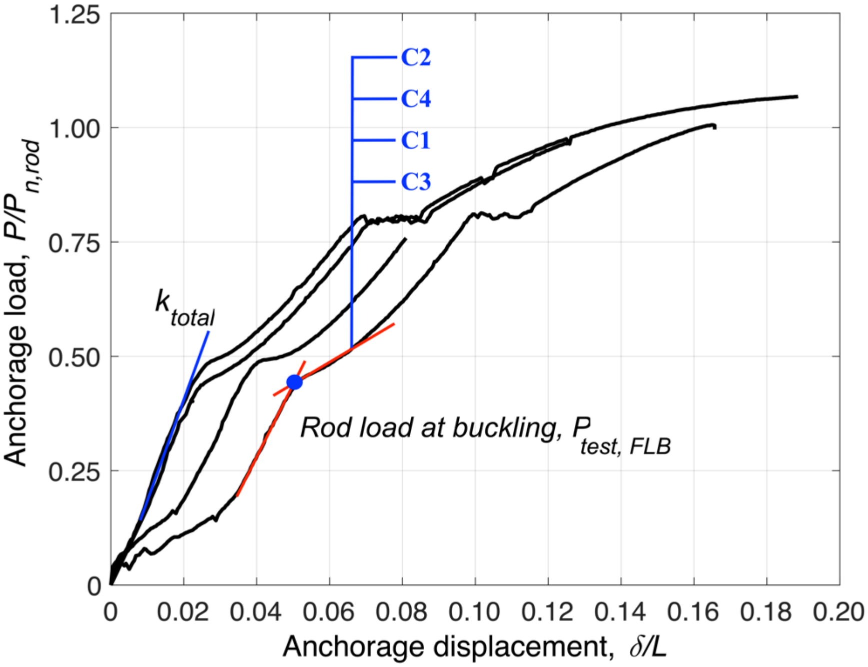

Figure 7-17. Test group C (control) load-deformation response

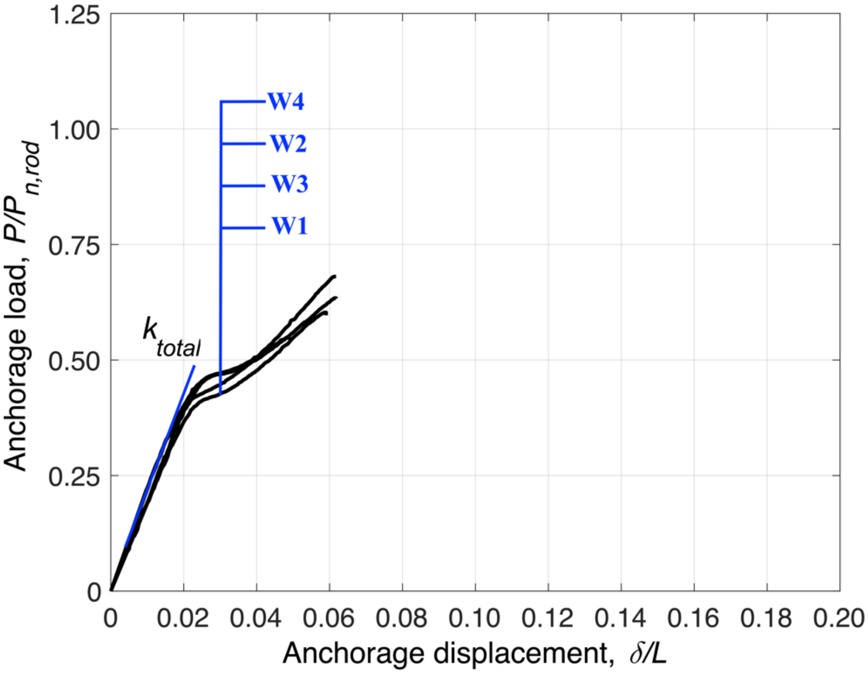

Figure 7-18. Test group W (reduced web thickness) load-deformation response

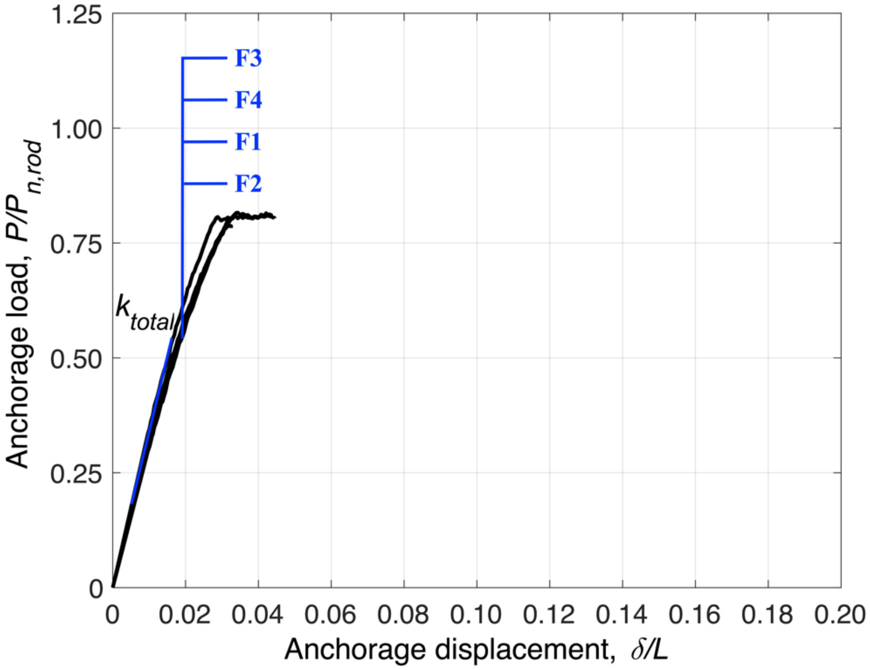

Figure 7-19. Test group F (increased flange width and thickness) load-deformation response

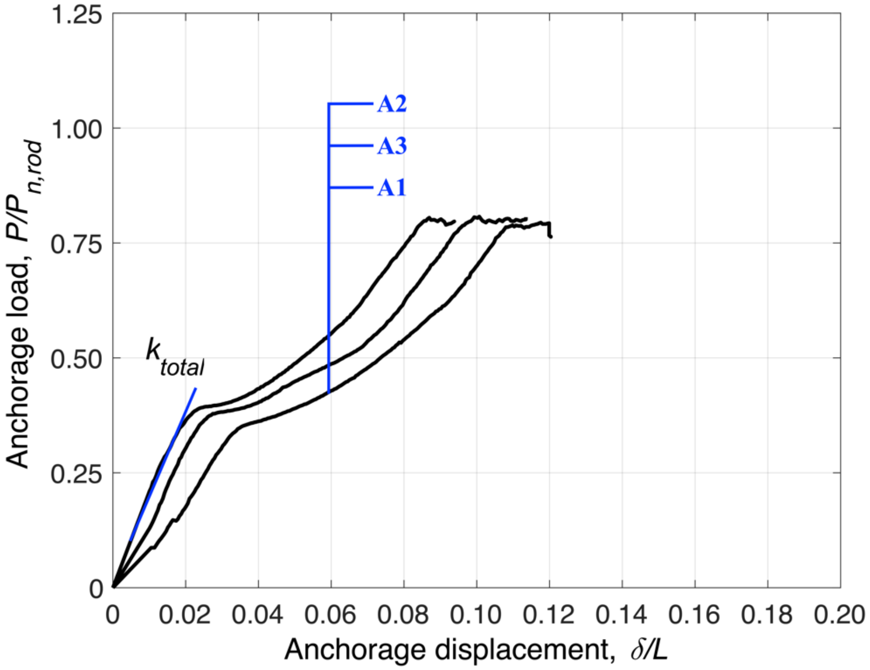

Figure 7-20. Test group A (decreased rod angle) load-deformation response

It is worth noting that the only difference between the C tests (Figure 7-17) and the A tests (Fig. 14) is the rod angle; however, the C specimens are able to develop substantially larger strength and deformation capacity. When the rod is at 60 deg. as in the A tests (instead of 45 deg. in the C tests) the hillside washer has less friction to hold the washer nipple in place and the result, as provided in Table 4, slip and disengagement of the washer is the final limit state in the A series.

7.8. Localized response

The position transducer scheme of Figure 7-11 was designed in part to study local deformations including minor axis bending of the frame member ($\delta_{flexure}$) and local bending in the web (δ_{web}). Per beam theory for a point load a midspan, the minor axis flexure deformation at the anchor ($\delta_{flexure}$) can be defined as,

$$\delta_{flexure} = \frac{\theta_y L}{3} \tag{7-1}$$

where L is the length of the specimen and the specimen rotation (θ_y) at the clevis pin measured as the average of readings from PT_{11} and PT_{12} divided by the distance from the clevis pin to the PTs (140 *mm*). Figure 7-21 provides $\delta_{flexure}$ for the W1 and A1 specimens as an example for minor axis bending deformation.

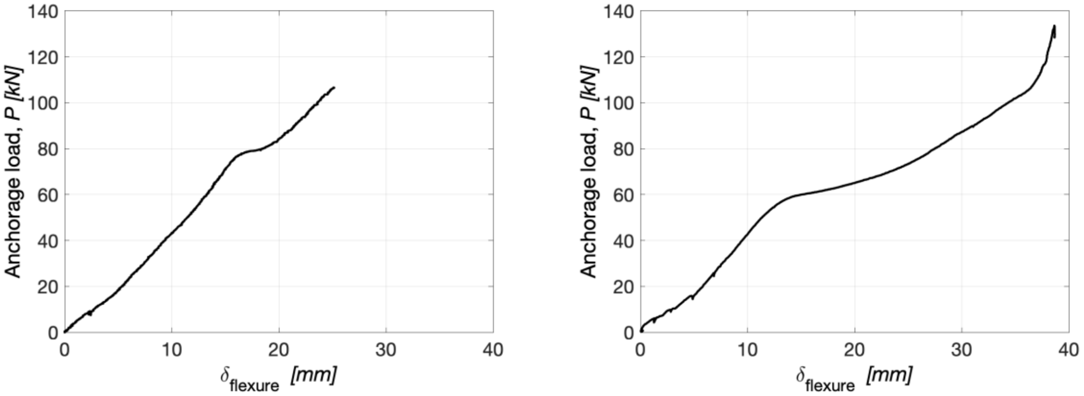

Figure 7-21. Load-flexural deformation (δ_{flexure}) response: (a). W1 Specimen (b). A1 Specimen

Moreover, δ_{web} can be obtained as,

$$\delta_{web} = \delta_{total} - \delta_{flexure} \tag{7-2}$$

where the total deformation (δ_{total}) is measured by PT_9. It should be noted that anchor deformation from twist is not considered in Eq. (2) since it is negligible away from the anchor location. Figure 7-21 provides an example of δ_{web} for the W1 and A1 specimens. Frame flexural stiffness and local web/washer stiffness can be obtained by calculating the slopes from Fig. 16. All data from the PT measurements are available in [37].

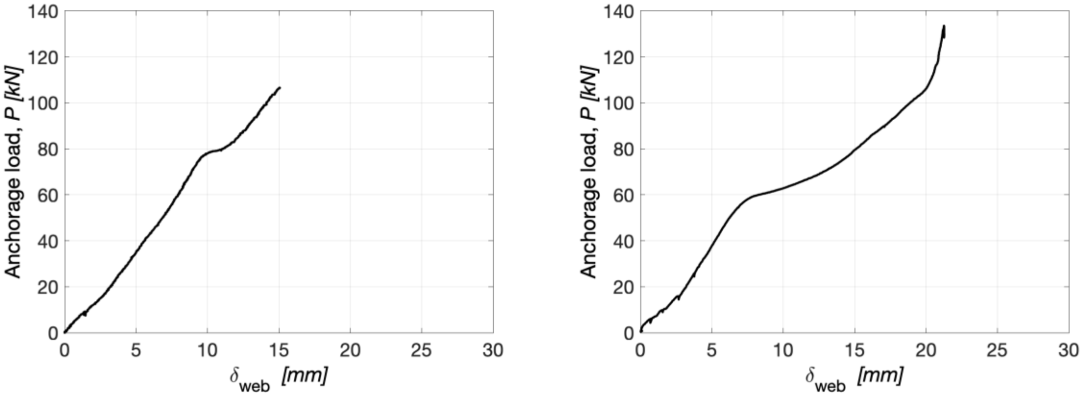

Figure 7-22. Load-web deformation (δ_{web}) response: (a). W1 Specimen (b). A1 Specimen

7.9. Rod brace assemblage connection stiffness

The stiffness of the rod-braced assemblage is determined for each specimen, graphically depicted in Figure 7-17 through Figure 7-20 , and tabulated in Table 7-10. The tangent stiffness at approximately 20% of the expected rod strength (P_{nrod}) averaged over 20% of the load (10 to 30% P_{nrod}) is selected for the reported stiffness. This range is prior to significant flange local buckling or bearing deformations at the access hole. The recorded stiffness varies from 1.9 to 4.1 kN/mm.

Note that the web must be relatively straight to develop the reported stiffness, k_{total}. Large out-of-plane web curvature, opposite in direction to the deformations imposed by the rod, such as that observed in some of the specimens (see Table 7-7) results in stiffness loss at low brace loads (see stiffness offset at low loads for specimens C1 and C3 in Figure 7-17) that is only regained after web snap-through displacement of as much as 25 mm is complete.

The total approximated anchor stiffness (k^*) can idealized as a set of springs in series, some of which may be approximated analytically and some of which are directly measured experimentally. Rod axial stiffness (k_{rod}) is defined as,

$$k_{rod}=EA_{rod}/L_{rod} \tag{7-3}$$

where E is elastic modulus, A_{rod} is the rod area, and L_{rod} is length of the rod. Frame flexural stiffness ($k_{flexure}$) is defined from,

$$k_{flexure}= P/\delta_{flexure} \tag{7-4}$$

where P is the rod force and $\delta_{flexure}$ is per Equation (7-1). Local web/washer ($k_{web/washer}$) stiffness is,

$$k_{web/washer}=P/\delta_{web} \tag{7-5}$$

where δ_{web} is defined in Equation (7-2). The total approximated anchor stiffness (k^*) can be obtained as,

$$k^* = [1/k_{rod} + 1/\ k_{flexure} + 1/\ k_{web/washer}]^{-1} \tag{7-6}$$

The comparison between the total approximated stiffness (k^*) and total experimental stiffness (k_{total}) is provided in Table 7-10. The approximate stiffness k^* is a reasonable predictor for the C and W specimens, but overly stiff for the F and A specimens.

Table 7-10. Rod brace anchor connection deformation and stiffness

Specimen Name	Total experimental stiffness	Component Stiffness				Approximated stiffness to experimental stiffness ratio (k^*/k_{total})
		Axial rod stiffness (Analytical)	Local web deformation (Experimental)	Primary frame weak axis flexure (Experimental)	Total approximated stiffness	
	k_{total}	k_{rod}	k_{web}	$k_{flexture}$	k^*	
	kN/mm	kN/mm	kN/mm	kN/mm	kN/mm	
C1	2.2			Lost data		
C2	2.5					
C3	2.0					
C4	2.6	56.4	7.4	4.3	2.5	0.98
W1	2.8	56.4	7.2	4.3	2.6	0.91
W2	2.4	56.4	10.5	4.2	2.8	1.15
W3	2.7	56.4	10.2	5.0	3.1	1.17
W4	2.7	56.4	9.7	5.0	3.1	1.16
F1	4.1	56.4	9.2	8.7	4.1	1.00
F2	4.1	56.4	27.5	8.1	5.6	1.37
F3	3.9	56.4	12.5	9.2	4.8	1.23
F4	4.0	56.4	17.9	8.8	5.3	1.31
A1	1.9	56.4	7.7	4.4	2.7	1.42
A2	2.5	56.4	9.1	7.4	3.8	1.49
A3	2.4	56.4	7.6	8.3	3.7	1.50

7.10. Discussion and implications for design

Rod bracing commonly provides lateral stiffness for metal building systems. When assessing the supplied brace stiffness some care must be taken to develop an accurate estimate. Deformations to be considered include rod elongation, anchorage accommodation, local plate bending of the web, weak axis flexure of the frame member, and torsion of the frame member for rod braces eccentric to the frame centroid. Initial imperfections induced in fabrication can further reduce the initial stiffness, while having little effect on the ultimate stiffness supplied by the rod brace assemblage. In a typical metal building structural model, the axial stiffness of the rod k_{rod} and the weak axis flexure of the frame (k_{flexure}) would be explicitly included as line elements. Additional flexibility would need to be added to the model to account for the deformations observed in testing. A spring of stiffness, k_{model}, could be added in series with the rod,

$$k_{model} = \left(1/k_{total} - 1/k_{rod} - 1/k_{flexure} \right)^{-1} \tag{7-7}$$

and this would supply a model that has stiffness consistent with the observed testing. Additional guidance and generalization is provided in an addendum report available with [8].

The strength of rod braced assemblages can be controlled by brittle failures such as rod fracture or shear of the nipple in the hillside washer, or more ductile failure modes such as yielding of the rod, bearing in the hole of the web plate of the frame member, or even flange local buckling of the frame member. Current design recommendations provide limited guidance for these failure modes, short of rod fracture and yield, and additional guidance is needed.

The web bearing and shear of the hillside washer may be handled by relatively traditional design checks. A simple connection bearing check based on *AISC 360-16* [43] Section J3 provides a reasonable prediction of the observed bearing limit state (plateaus in Figure 5-17, Figure 7-19, and Figure 7-20). Specifically, the rod strength limited by washer bearing, P_{br}, may be well approximated by

$$P_{br} = 2.4 d_n t_w F_{uw} \Big/ \cos(\theta) \tag{7-8}$$

Where d_{n} is the diameter of the nipple of the hillside washer, t_{w} is the width of the web, F_{uw}, is the ultimate stress of the web, and θ is the rod angle, complete details are provided in the addendum report with [37].

Other limit states are more complex, e.g., the observed flange local buckling is unique. Weak axis bending and torsion of the frame member due to the component of the brace force perpendicular to the frame member and direct compression due to the component of the brace force parallel to the frame member all induce compression in the flange and hence flange local buckling. Based on $P_{\mathrm{test,FLB}}$ as reported in Table 7-9 the plate buckling coefficient for the flange was back-calculated and found to be 0.33 with a standard deviation of 0.02 across the 11 specimens that experienced flange local buckling. This is considerably lower than the plate buckling coefficient assumed in Table B4.1 of [43], due to the unique loading and boundary conditions. If the reduced plate buckling coefficient is used instead of the values assumed in [43] one finds that the non-compact/slender limit, i.e. λ_r, reduces to $0.4\sqrt{E/F_y}$. This value is remarkably close to the traditional compact/non-compact, λ_p, limit of $0.38\sqrt{E/F_y}$. Thus, it is recommended that if the rod is anchored near the flange with details similar to the testing conducted herein that the flange be compact, see the addendum report with [37] for complete details.

Measured experimental stiffness can differ greatly from simplified analytical treatments that do not include all sources of flexibility. For example, metal building engineers typically use springs in series calculation including axial rod stiffness and local primary frame web stiffness where the web is modeled as a simply supported plate with a load at the middle of the plate. This may be overly conservative. In many cases the stiffness and strength of the anchorage is sensitive to the fit between the hillside washer and the fabricated hole. A closer examination of the intended and realized tolerances may provide a means to better understand this sensitivity. Further, while an attempt was made to use a common hillside washer in the tested specimens, the survey of industry did include other potential hillside washer systems. For those specimens failing in bearing or fracture of the nipple for different manufacturers hillside washers will provide different capacities.

As indicated in Figure 7-8 the test specimens are a simplification of a portion of a metal building frame and rod brace. Neither purlins nor purlin-to-frame kickers are included in the specimens; however, these secondary components would be commonly found in actual metal building frames. In the building the component of the brace force perpendicular to the primary frame is resolved through the secondary members. In the test specimen this component is resolved through the pinned ends at the top and bottom flange of the specimen. The tested condition is a stronger/stiffer support than in the building and more concentric with respect to the depth of the frame member; however, it is eccentric from the brace location along the length of the frame member by 704.5 mm. The authors contend that the simplification in the test specimen is reasonable; however, it has two effects that could accentuate the observed flange local buckling: (1) the weak axis bending of the specimen is greater and (2) the warping stresses developed due to torsion may also be greater. As a result, further study with respect to the flange local buckling limit state in this connection appears warranted.

7.11. Conclusion

Metal building systems commonly rely on rod bracing to supply lateral stiffness and diaphragm response for forces perpendicular to the primary frames. Today limited guidance exists on the realized stiffness and strength of these rod brace assemblages; therefore, an experimental study was conducted. A small segment of a metal building frame was isolated, and a test rig developed whereby a rod, with anchorage through the web of a three-plate built-up metal building I-section, anchored with a proprietary hillside washer was pulled in tension until failure. Twelve specimens were conducted, and it was observed that the stiffness of the rod bracing system is sensitive to the elongation of the rod, the local plate bending of the web of the frame member, accommodation in the anchorage system, and potentially weak axis bending and torsion of the frame member itself. A variety of limit states was observed in the testing including brittle failures: rod fracture and shearing of the nipple of the hillside washer that anchors the rod; and more ductile failures: rod yielding, bearing of the web plate, and flange local buckling. Strength when flange local buckling occurs, and ultimate peak strength are both reported for all tested specimens. It is noted that the configuration of the tested specimens may accentuate the flange local buckling limit state in comparison to complete metal building systems. The provided stiffness and strength can be utilized to develop improved design guidance for rod bracing in metal building systems. All the test date are presented in CFSRC report [37].

Chapter 8

Preliminaries for Metal Building System Archetype Three-Dimensional Modeling with Rod Bracing

8.1. Introduction

Despite the wide application of metal building systems, a small number of studies are conducted to investigate the seismic response of metal building systems. In addition, most of the previous studies considers two-dimensional frame modeling which can cause inaccurate prediction of metal building response.

To investigate the seismic response of metal buildings, the current study is proposed using a metal building archetype designed by MBMA based on the configuration of experimental study on rod anchorage connection and stiffness. Using the archetype building with same members configurations does not need any specific calibration that could be problematic and could result in better understanding of seismic response of the building. A three-dimensional model with all the members is considered. Different type of analysis with different ground motion scaling is considered in this study. In this chapter the basic information about the archetype and modeling protocol is provided. It should be noted that this work is ongoing, and the results will be provided in future studies.

8.2. Development of Computational Models for Metal Building Archetypes

To perform the nonlinear dynamic analysis, three-dimensional computational models of metal building archetype is considered using the *OpenSees* [56] software. Details of the archetype simulation are provided in this section.

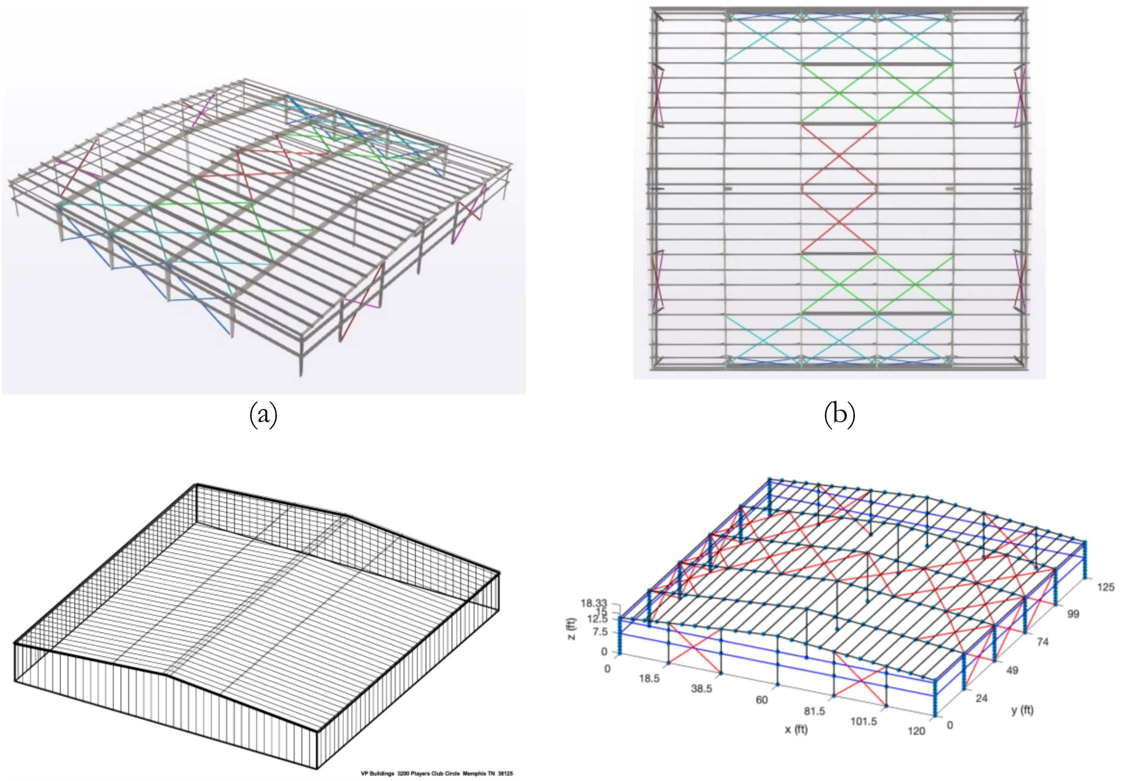

(a) (b)

(a) (c)

Figure 8-1. Metal Building Archetype (*VP Buildings 3200 Club Circle Memphis TN*): (a) Designed Archetype with Rod Bracing (MBMA); (b) Top View of Archetype; (c) Computational model [105]

To study the seismic performance of metal building longitudinal and roof diaphragm bracing systems including the behavior of the rod connections (i.e., hillside washers), a modular 60’ x 125’ metal building archetype was designed in a high seismic area (SDS=1.0, SD1=0.6) by an MBMA member, as shown in Figure 8-1. The detailed design information is provided in the design report as shown in and the material specification is shown in Table 8-1. It should be noted that an additional small point load and moment are applied at the knee joint, to simulate the portion of the frame and roof that extends past the knee joint. These uniform loads account for the specified tribe width equal to 25 ft. In addition, frame self-weight load is not considered in the frame analysis and only considered for calculating the base shear.

Table 8-1. Metal Building Archetype Building Loading and Design Information

Building Roof and Side Loading	Design Parameters
Collateral Gravity (only for roof) = 12.0 psf	$R = 3.5$
Covering + Second. Load (for roof and sides) = 1.89 psf	$\Omega_0 = 2.5$ $C_d = 3.0$
Frame Self-Weight (assumed for seismic, roof and sides): 2.50 psf	T_a (sec)= 0.621
Roof Live Load = 20. psf	$\rho = 1.3$ Risk Category 2 Site Class D $I_e = 1$

8.3. Damping, Elements, Geometric Nonlinearity and Material Modeling

Both material and geometric nonlinearity are considered in the analysis. In addition, nonlinear material models used for columns, rafters, and rod bracing were represented by nonlinear beam-column elements with fiber-section.

The rod-bracing system is detailed in Figure 8-2 for the walls, i.e., the vertical lateral force resisting system and in Figure 8-3 for the roof, i.e., the “horizontal” lateral force resisting system or diaphragm. It should be noted that the design choices for the rod diameter, angle and girder or column web thicknesses are consistent with the rod-bracing specimens tested in Foroughi et al. (2018). Accordingly, the experimental results can be used almost directly in the nonlinear modeling of the vertical and horizonal lateral force resisting systems.

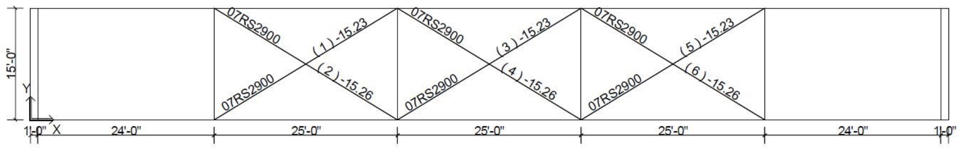

Diagonal Bracing Member Design Summary: Sidewall 4

Mem. No.	Bracing Shape	Length (ft)	Angle	Design Axial (k)	Seismic Factor	Stress Factor	Stress Ratio	Governing Load Case	Design Status	Comment
1	R 0.875	28.98	31.0	-15.23	1.3000	1.0000	0.884	1.2D+1.2CG+1.0E>+1.0EG+	passed	
2	R 0.875	28.98	31.0	-15.26	1.3000	1.0000	0.886	1.2D+1.2CG+1.0<E+1.0EG+	passed	
3	R 0.875	28.98	31.0	-15.23	1.3000	1.0000	0.884	1.2D+1.2CG+1.0E>+1.0EG+	passed	
4	R 0.875	28.98	31.0	-15.26	1.3000	1.0000	0.886	1.2D+1.2CG+1.0<E+1.0EG+	passed	
5	R 0.875	28.98	31.0	-15.23	1.3000	1.0000	0.884	1.2D+1.2CG+1.0E>+1.0EG+	passed	
6	R 0.875	28.98	31.0	-15.26	1.3000	1.0000	0.886	1.2D+1.2CG+1.0<E+1.0EG+	passed	

Figure 8-2. Wall rod layout and sizing for metal building archetype [105]

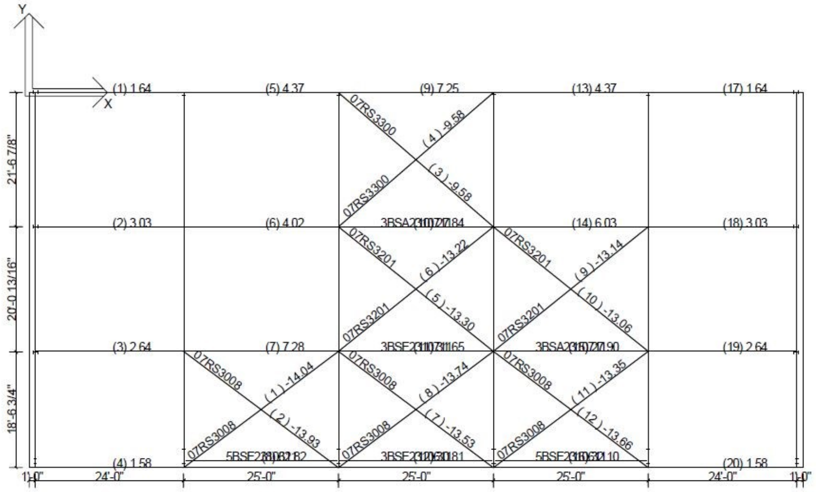

Diagonal Bracing Member Design Summary: Roof A

Mem. No.	Bracing Shape	Length (ft)	Angle	Design Axial (k)	Seismic Factor	Stress Factor	Stress Ratio	Governing Load Case	Design Status	Comment
1	R 0.875	30.66	38.2	-14.04	1.3000	1.0000	0.815	1.2D+1.2CG+1.0E>+1.0EG+	passed	
2	R 0.875	30.66	38.2	-13.93	1.3000	1.0000	0.809	1.2D+1.2CG+1.0<E+1.0EG+	passed	
3	R 0.75	32.98	42.1	-9.58	1.3000	1.0000	0.762	1.2D+1.2CG+1.0<E+1.0EG+	passed	
4	R 0.75	32.98	42.1	-9.58	1.3000	1.0000	0.762	1.2D+1.2CG+1.0E>+1.0EG+	passed	
5	R 0.875	32.07	40.0	-13.30	1.3000	1.0000	0.772	1.2D+1.2CG+1.0<E+1.0EG+	passed	
6	R 0.875	32.07	40.0	-13.22	1.3000	1.0000	0.767	1.2D+1.2CG+1.0E>+1.0EG+	passed	
7	R 0.875	30.66	38.2	-13.53	1.3000	1.0000	0.785	1.2D+1.2CG+1.0<E+1.0EG+	passed	
8	R 0.875	30.66	38.2	-13.74	1.3000	1.0000	0.797	1.2D+1.2CG+1.0E>+1.0EG+	passed	
9	R 0.875	32.07	40.0	-13.14	1.3000	1.0000	0.763	1.2D+1.2CG+1.0E>+1.0EG+	passed	
10	R 0.875	32.07	40.0	-13.06	1.3000	1.0000	0.758	1.2D+1.2CG+1.0<E+1.0EG+	passed	
11	R 0.875	30.66	38.2	-13.35	1.3000	1.0000	0.775	1.2D+1.2CG+1.0E>+1.0EG+	passed	
12	R 0.875	30.66	38.2	-13.66	1.3000	1.0000	0.793	1.2D+1.2CG+1.0<E+1.0EG+	passed	

Figure 8-3. Roof rod layout and sizing for metal building archetype [105]

Geometric nonlinearity was considered by including the gravity loads and using the P-Delta coordinate transformation algorithm in *OpenSees* [56] for the columns. For the braces, Corotational coordinate transformation algorithm in *OpenSees* [56] is applied to capture a precise response of the rod bracing system. Shows the details for material designations.

Table 8-2. Material designations for metal building archetype

Materials	ASTM Designation	Grade
Brace Rods	ASTM572, A510	GRADE 55
Hot Rolled Mill Shapes	A36, A529, A572, A588, A922	GRADE 36 or 50
Hot Rolled Angles	A529, A572, A588, A922	GRADE 50
Cladding	A653, A792	GRADE 50 or 80
Cold-formed Light Gage Shapes	A653, A1011	GRADE 60

To perform the nonlinear time history analyses, Rayleigh damping with a critical damping ratio equal to 5% for the 1st modes was used for the metal building archetype models. ElasticBeamColumn element is utilized for both girts and purlins.

8.4. Rod Bracing Connection, Panel Zone, and Base Plate Modeling

To simulate the actual rod bracing connection stiffness, panel zone rigidity, and base plate inelastic behavior, zero-length nonlinear rotational spring element using Steel02 material model is utilized. The computational model is considered to calibrated against experimental data. Figure 8-4 shows the typical juncture of rafter-to-column and rod bracing to rafter and column connections. The typical rob brace connection and hillside washer used in the archetype and previously tested is shown in Figure 8-5.

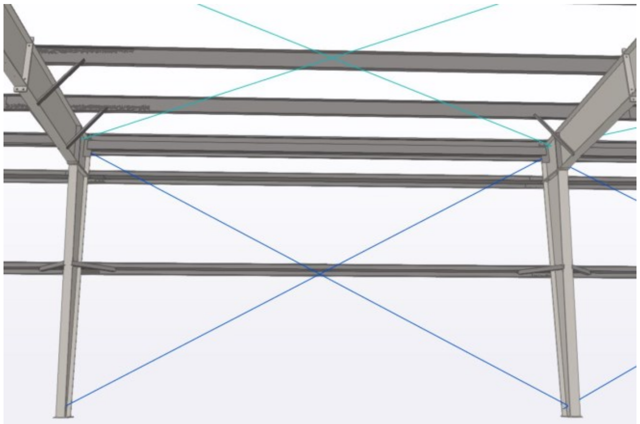

Figure 8-4. Typical juncture of rafter-to-column and rod bracing to rafter and column connections

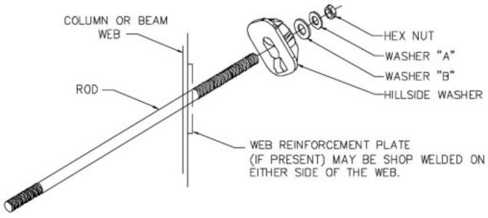

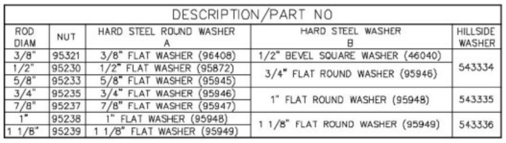

DESCRIPTION/PART NO				
ROD DIAM	NUT	HARD STEEL ROUND WASHER A	HARD STEEL WASHER B	HILLSIDE WASHER
3/8"	95321	3/8" FLAT WASHER (96408)	1/2" BEVEL SQUARE WASHER (46040)	543334
1/2"	95230	1/2" FLAT WASHER (95872)	3/4" FLAT ROUND WASHER (95946)	
5/8"	95233	5/8" FLAT WASHER (95945)		
3/4"	95235	3/4" FLAT WASHER (95946)	1" FLAT ROUND WASHER (95948)	543335
7/8"	95237	7/8" FLAT WASHER (95947)		
1"	95238	1" FLAT WASHER (95948)	1 1/8" FLAT ROUND WASHER (95949)	543336
1 1/8"	95239	1 1/8" FLAT WASHER (95949)		

Figure 8-5. Typical hillside washer detail for rod-brace systems based on rod diameter [105]

8.5. Metal Building Roof System

The through fastened roof (TRF) system shown in Figure 8-6 is potentially an alternative diaphragm element in metal building systems, though typically it is not designed for this purpose. Dynamic seismic analysis of the archetype system can potentially shed light on the interaction of the rod-bracing system with the TRF system and can help with considering the effect of TRF in the diaphragm design of metal building systems.

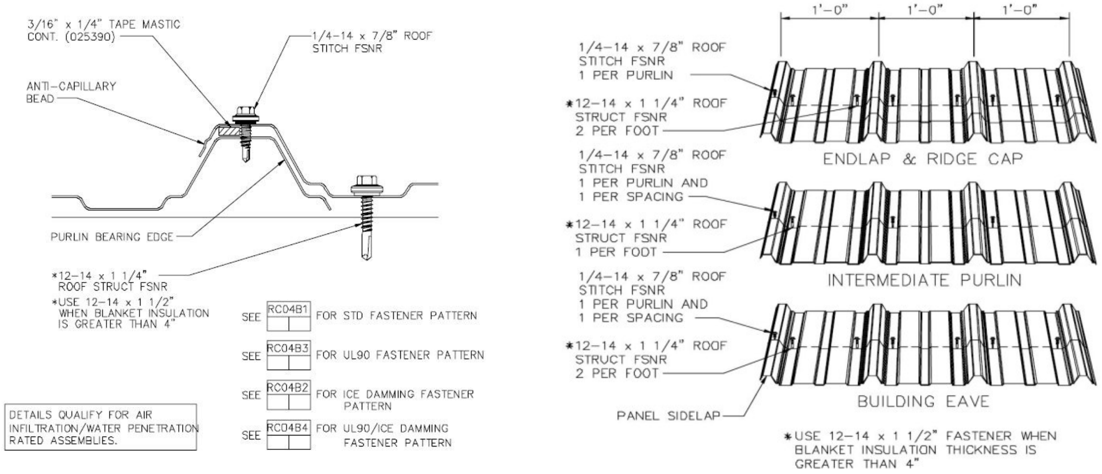

Figure 8-6. Typical through fastened panel detailing for roof and walls [105]

8.6. Basic Ideas and Future Work

To provide a resilient design for metal building systems, it is important to consider the actual values for material properties, geometry and dimensions, and lateral force system resisting stiffness. Three-dimensional modeling of metal building archetypes by considering different key modeling parameters and utilizing experimental values for rod bracing stiffness could provide the ability to improve the knowledge about the seismic behavior of metal building systems.

8.7. Conclusion

Metal building archetypes is presented, and key design parameters for modeling are described and discussed. A framework for seismic performance analysis of metal building systems is provided for future studies.

Chapter 9

Conclusion and Future work

9.1. Major Contribution

This dissertation is devoted to improvement of resilient design for steel braced buildings. This study has two major contributions:

1) The seismic response of conventional steel buildings with special concentrically braced frames (SCBF), as the vertical force resisting system, and different diaphragm design procedures based on *ASCE 17-16* are studied. A series of one-, four-, eight-, and twelve-story SCBF archetype buildings were designed to the current U.S. building code with four different diaphragm designs: a traditional design that uses conventional diaphragm design forces from *ASCE 7-16* [10], a design that uses the seismic demand calculated assuming some diaphragm ductility (values proposed for future editions of the building code of $R_s = 2$ for concrete-filled steel deck floor diaphragms and 2.5 for bare steel deck roof diaphragms), a design with diaphragm demands assuming no diaphragm ductility $R_s = 1.0$, and a design with diaphragm demands assuming significant diaphragm ductility $R_s = 3.0$. Nonlinear response history analyses is used to investigate the behavior of the buildings during earthquake.

2) Lateral response of a typical metal building system with focus on experimental determination of stiffness for rod bracing anchorage connections is conducted. The research study summarized herein revisits rod bracing design for metal buildings, focusing on local strength limit states including web bearing and tearing and documenting frame-anchor load-deformation response up to anchor failure. The work started with an industry survey of common rod anchor bracing details. The survey gleaned metal building frame geometry (flange, web dimensions) and anchor geometry (angle relative to web, location of anchor in the frame cross-section) that were used to design a test matrix for an experimental program. The results from the testing program are reviewed and discussed, concluding with a comparison of the observed limit states to those laid out by [98] that are currently being used by MBMA members. An archetype building is designed by MBMA with same configuration of the experimental study members in order to computational modeling. Finally, a framework is presented for future studies. In what follows, the major contributions are summarized.

9.1.1. SCBF Archetype Building Designed with Different Diaphragm Design Procedures

The results from modal analysis of three-dimensional models showed that current rigid diaphragm assumption could result in inaccurate fundamental natural period for the building. The natural period of the one-story building with bare deck shows 66% different compared to the results from *SAP 2000* analyzed with rigid diaphragm assumption. The results from this study shows that the difference increase for low-rise buildings. In general, having semi-rigid diaphragm, design with higher R_s values for alternative diaphragm design procedure, could result in larger natural period for the building. In addition, natural period for SCBF archetypes has larger difference compared to same archetype buildings with BRBF as vertical lateral force resisting system. This finding was expected since SCBF are less ductile compare to BFBF braced frame steel buildings.

Static response of the building shows three regions for SCBF archetype response. In all the computational models, SCBF buckling and yielding are the dominant failure modes. However, in the one-story archetype with bare steel deck roof the diaphragm failure is observed as failure mode and cause 50% decrease in peak value compared to $R_s = 1$ diaphragm design procedure. The response of other archetypes in nonlinear pushover analysis shows that diaphragm design procedures based on *ASCE 7-16* [10] could not affect the overall static response of the SCBF archetype since the brace failure is dominant failure mode. The observations show that the ductility decrease for taller archetypes as it was expected.

Seismic response history analyses show significant inelasticity occurred in the diaphragms as higher modes affected the diaphragm demands. There was also an interaction between diaphragm inelasticity and SCBF inelasticity as the two compounded each other to exacerbate second order effects and cause collapse in some models.

Large story drift concentrates at the last story of the building, where second order effects the building, are the greatest. For the intermediate stories, the peak story drifts are smaller and more uniformly distributed along the building height, while the peak story drifts near the become larger due to large base shear forces.

In addition, because of the three-dimensional effect and diaphragm deformation, the predicted peak resultant story drifts can be twice as large as the story drifts along either orthogonal direction of the building. The total story drift considering diaphragm deformation can also be significantly larger than the story drift at the SCBF frames, especially when the diaphragms have smaller in-plane stiffness, which can result in even larger P-Δ effects. All indicating conventional three-dimensional or two-dimensional frame analysis with rigid diaphragm assumptions can significantly underestimate the story drifts of a building.

The diaphragm shear demands for an archetype building with $R_s = 1.0$ diaphragm design were compared to the elastic diaphragm design shear from the *ASCE 7-16* [10] alternative diaphragm design procedure. It was found that ratios of the diaphragm shear demand obtained from the analysis to the design shear given by the alternative diaphragm design procedures in *ASCE 7-16* [10] have an average value of 0.87, indicating a reasonably accurate, but slightly conservative prediction of elastic diaphragm shear demand with the design approach in the studied archetype buildings

The performance of the archetype buildings in terms of collapse shows that as the number of stories increases for Traditional design, collapse ratios of the archetype buildings tend to become larger since higher mode effects are not considered in the diaphragm design. Collapse ratios of the archetype buildings become smaller with height for all of the alternative diaphragm design options studied: $R_s = 1.0$, $R_s = 2.0$ or 2.5, and $R_s = 3.0$. In general, the number of collapses associated with $R_s = 1.0$ diaphragm design is close to that with a rigid diaphragm, and these collapses are associated with low-cycle fatigue in SCBF braces. As discussed herein the $R_s = 2.0$ or 2.5 diaphragm design provides designs and performance either consistent with, or improvements from, traditional design. Evaluated per the *FEMA P-695* [38] methodology the $R_s = 2.0$ or 2.5 diaphragm design procedure passes for each individual archetype and nearly passes for the full group. Considering all factors, it is concluded that the diaphragm design procedure with proposed R_s values ($R_s = 2$ for concrete-filled steel deck floor diaphragms and

R_s = 2.5 for bare steel deck roof diaphragms) is reasonable for use in design of these types of structures.

9.1.2. Lateral Response of Metal Building

Metal building systems commonly rely on rod bracing to supply lateral stiffness and diaphragm response for forces perpendicular to the primary frames. Today limited guidance exists on the realized stiffness and strength of these rod brace assemblages; therefore, an experimental study was conducted. A small segment of a metal building frame was isolated, and a test rig developed whereby a rod, with anchorage through the web of a three-plate built-up metal building I-section, anchored with a proprietary hillside washer was pulled in tension until failure.

Twelve specimens were conducted, and it was observed that the stiffness of the rod bracing system is sensitive to the elongation of the rod, the local plate bending of the web of the frame member, accommodation in the anchorage system, and potentially weak axis bending and torsion of the frame member itself.

A variety of limit states was observed in the testing including brittle failures: rod fracture and shearing of the nipple of the hillside washer that anchors the rod; and more ductile failures: rod yielding, bearing of the web plate, and flange local buckling. Strength when flange local buckling occurs, and ultimate peak strength are both reported for all tested specimens. It is noted that the configuration of the tested specimens may accentuate the flange local buckling limit state in comparison to complete metal building systems. The provided stiffness and strength can be utilized to develop improved design guidance for rod bracing in metal building systems.

The experimental information is intended to be used in three-dimensional metal building archetype models to validate future improvements to: bracing provisions for primary frame members, diaphragm stiffness predictions when rod bracing is employed, and strength prediction equations for rod brace assemblages.

9.2. Future work

Three-dimensional modeling for seismic evaluation of buildings could provide for a better resilient design for buildings. In what follows, the future paths based on the work conducted in this study are briefly explained.

9.2.1. Semi-Rigid Diaphragm System

To improve our knowledge of the capabilities of three-dimensional modeling for buildings with semi-rigid diaphragm, it is necessary to study other methods for modeling the diaphragm response. Observations from 2011 Christchurch earthquake [104] shows that diaphragm behavior could be affected by trampoline phenomenon in the diaphragm system. So, developing advanced shell element diaphragm models for dynamic loads in *OpenSees* could improve the modeling by better considering the out-of-plane response of the diaphragm system.

One of the main advantages of the three-dimensional modeling for the archetypes is the ability to consider the torsional behavior of the buildings with irregularities in both diaphragm and vertical lateral force resisting system. The current study only considered the SCBF archetype buildings with regular geometry. Thus, comprehensive studies on archetype with irregularities in both VLFRS and diaphragm system could be beneficial to have better understanding of diaphragm behavior.

Multi-hazard studies could be another window into the future of research on resilient design for steel structures. Having both seismic and fire hazards in three-dimensional modeling of steel archetype buildings could be beneficial for both resilient design and post-disaster management.

9.2.2. Metal Building System

Metal building response can significantly change by different parameters such as geometry, design and location of the building. Having more archetype models could be beneficial for having a better understanding of seismic performance of the building.

Fire in industrial buildings can result in a complete loss of function. Again, multi-hazard studies could be an interesting subject for metal buildings since these buildings usually show reasonable performance in earthquakes. Having fire in addition to earthquakes in three-dimensional models could provide more knowledge regarding the resilient design for the metal building industry.

References

[1] Jaiswal KS, Petersen MD, Rukstales K, Leith WS. Earthquake Shaking Hazard Estimates and Exposure Changes in the Conterminous United States. Earthquake Spectra 2015;31:S201–20. https://doi.org/10.1193/111814EQS195M.

[2] Jaiswal K, Bausch D, Rozelle J, Holub J, McGowan S. Hazus® estimated annualized earthquake losses for the United States. Federal Emergency Management Agency; 2017.

[3] Building Science - Earthquake Publications | FEMA.gov n.d. https://www.fema.gov/emergency-managers/risk-management/building-science/earthquakes (accessed February 15, 2021).

[4] American National Standards Institute - ANSI Home. American National Standards Institute - ANSI n.d. https://www.ansi.org/ (accessed February 15, 2021).

[5] FEMA F. 445. Next-Generation Performance-Based Seismic Design Guidelines Program Plan for New and Existing Buildings. Redwood City 2006.

[6] ASCE. Minimum design loads for buildings and other structures, American Society of Civil Engineers; 2010.

[7] Rodriguez ME, Restrepo JI, Blandón JJ. Seismic design forces for rigid floor diaphragms in precast concrete building structures. Journal of Structural Engineering 2007;133:1604–15.

[8] Earthquake Engineering Research Institute n.d. https://www.eeri.org/ (accessed February 15, 2021).

[9] Sabelli R, Sabol TA, Easterling WS. Seismic design of composite steel deck and concrete-filled diaphragms. NEHRP Seismic Design Technical Brief No 2011;5.

[10] ASCE. Minimum design loads for buildings and other structures, American Society of Civil Engineers; 2016.

[11] New initiative for steel diaphragm research. Construction Specifier 2016. https://www.constructionspecifier.com/smdi-and-aisc-partner-to-establish-sdii/ (accessed February 15, 2021).

[12] Sabelli R, Roeder CW, Hajjar JF. Seismic Design of Steel Special Concentrically Braced Frame Systems n.d.:36.

[13] Adamo & Associates Structural Engineers (adamostructural) - Profile | Pinterest n.d. https://www.pinterest.com/adamostructural/ (accessed February 15, 2021).

[14] Asada H, Sen AD, Li T, Berman JW, Lehman DE, Roeder CW. Seismic performance of chevron-configured special concentrically braced frames with yielding beams. Earthquake Engineering & Structural Dynamics 2020;49:1619–39. https://doi.org/10.1002/eqe.3320.

[15] Grabner KDM. Performance assessment of special concentrically-braced frames in moderate seismic regions 2018.

[16] Grabner KD, Fahnestock LA. Seismic stability of special concentrically braced frames in a moderate seismic region. Proceedings of the Structural Stability Research Council Annual Stability Conference, Louis, MI, USA, 2019, p. 2–5.

[17] Speicher MS, Harris JL. Collapse prevention seismic performance assessment of new special concentrically braced frames using ASCE 41. Engineering Structures 2016;126:652–66. https://doi.org/10.1016/j.engstruct.2016.07.064.

[18] Li T. Seismic performance of special concentrically braced frames in deep basins during subduction-zone earthquakes. Engineering Structures 2019:17.

[19] Hsiao P-C, Lehman DE, Roeder CW. Evaluation of the response modification coefficient and collapse potential of special concentrically braced frames 2013:18.

[20] Lumpkin EJ, Hsiao P-C, Roeder CW, Lehman DE, Tsai C-Y, Wu A-C, et al. Investigation of the seismic response of three-story special concentrically braced frames. Journal of Constructional Steel Research 2012;77:131–44. https://doi.org/10.1016/j.jcsr.2012.04.003.

[21] Tremblay R. Inelastic seismic response of steel bracing members. Journal of Constructional Steel Research 2002;58:665–701.

[22] Hsiao P-C, Lehman DE, Roeder CW. Improved analytical model for special concentrically braced frames. Journal of Constructional Steel Research 2012:16.

[23] Sen AD, Roeder CW, Berman JW, Lehman DE, Li C-H, Wu A-C, et al. Experimental investigation of chevron concentrically braced frames with yielding beams. Journal of Structural Engineering 2016;142:04016123.

[24] Lehman DE, Roeder C w, Herman D, Johnson S, Kotulka B. Improved seismic performance of gusset plate connections. Journal of Structural Engineering 2008;134:890–901.

[25] Bradley CR. Experimental investigation of post-elastic failure mechanisms in low-ductility braced frames and the implications for collapse performance. PhD Thesis. Tufts University, 2016.

[26] Stoakes C. Beam-column connection flexural behavior and seismic collapse performance of concentrically braced frames. PhD Thesis. University of Illinois at Urbana-Champaign, 2012.

[27] Sizemore JG. Inelastic behavior and seismic collapse prevention performance of low-ductility steel braced frames. PhD Thesis. University of Illinois at Urbana-Champaign, 2017.

[28] O'Reilly GJ, Goggins J. Experimental testing of a self-centring concentrically braced steel frame. Engineering Structures 2021:111521. https://doi.org/10.1016/j.engstruct.2020.111521.

[29] Uriz P. Towards earthquake resistant design of concentrically braced steel structures. University of California, Berkeley; 2005.

[30] Hammad A, Moustafa MA. Numerical analysis of special concentric braced frames using experimentally-validated fatigue and fracture model under short and long duration earthquakes. Bull Earthquake Eng 2020. https://doi.org/10.1007/s10518-020-00997-8.

[31] Hsiao P-C, Lehman DE, Roeder CW. A model to simulate special concentrically braced frames beyond brace fracture. Earthquake Engineering & Structural Dynamics 2013;42:183–200.

[32] Alexander Newman PE. Metal building systems: design and specifications. McGraw-Hill Education; 2015.

[33] Metal Building Product Systems. Nucor Building Systems n.d. https://www.nucorbuildingsystems.com/products/ (accessed February 15, 2021).

[34] Smith MD. Seismic testing and analytical studies for the development of new seismic force resisting systems for metal buildings. PhD Thesis. UC San Diego, 2013.

[35] Foroughi H, Ji C, Moen CD, Schafer BW. Experimental determination of stiffness and strength for metal building system rod bracing. Journal of Constructional Steel Research 2020;171:106149. https://doi.org/10.1016/j.jcsr.2020.106149.

[36] Uang CM, Smith MD, Shoemaker WL. Earthquake simulator testing of metal building systems. Structures Congress 2011, 2011, p. 693–704.

[37] Foroughi H, Ji C, Schafer BW, Moen CD. Strength and stiffness of metal building rod brace anchor connections 2018.

[38] Kircher C, Deierlein G, Hooper J, Krawinkler H, Mahin S, Shing B, et al. Evaluation of the FEMA P-695 methodology for quantification of building seismic performance factors. FEFEDERAL EMERGENCY MANAGEMENT AGENCY 2010.

[39] CSI S. Integrated Software for Structural Analysis and Design. Computers and Structures Inc, Berkeley, California, USA, Sa 2000.

[40] ANSI/AISC 341. Seismic provisions for structural steel buildings. ANSI/AISC 341–16. AISC 2016;60601.

[41] ANSI A. Specification for structural steel buildings. ANSI/AISC 360-16 2016.

[42] Code UB. International building code. International Code Council, USA 1997.

[43] Mattingly J, Chen H. AISI Newly Developed Standard AISI S310-13, North American Standard for the Design of Profiled Steel Diaphragm Panels 2014.

[44] Sabelli R, Roeder CW, Hajjar JF. Seismic design of steel special concentrically braced frame systems. NEHRP, Gaithersburg, USA, Seismic Design Technical Brief 2013;8.

[45] Baiguera M. An innovative dual concentrically-braced moment-resisting steel frame for increased seismic resilience. PhD Thesis. Heriot-Watt University. School of Energy, Geoscience, Infrastructure & Society, 2017.

[46] Xie Q. State of the art of buckling-restrained braces in Asia. Journal of Constructional Steel Research 2005;61:727–48.

[47] Clark PW. Design procedures for buildings incorporating hysteretic damping devices. International Post-SMiRT Conference Seminar on Seismic Isolation, Korea, 1999.

[48] Kersting RA, Fahnestock LA, López WA. Seismic design of steel buckling-restrained braced frames. NIST GCR 2015:15–917.

[49] Wei G, Eatherton MR, Foroughi H, Torabian S, Schafer BW. Seismic Behavior of Steel BRBF Buildings Including Consideration of Diaphragm Inelasticity. 2020.

[50] Muir L, Thornton W. Vertical bracing connections-analysis and design. Steel Design Guide 29, American Institute of Steel Construction 2014.

[51] VERCO DECKING, INC. Nucor. STEEL FLOOR DECK CATALOG VF5. Nucor; 2014.

[52] VERCO DECKING, INC. Nucor. STEEL FLOOR DECK CATALOG VF4. Nucor; 2014.

[53] Fang C-H, Leon RT. Seismic behavior of symmetric and asymmetric steel structures with rigid and semirigid diaphragms. Journal of Structural Engineering 2018;144:04018186.

[54] Chen C-H, Mahin S. EXAMPLE COLLAPSE PERFORMANCE EVALUATION OF STEEL CONCENTRICALLY BRACED SYSTEMS n.d.:10.

[55] Kircher C, Berman J, Cobeen K, Dolan D, Filiatrault A, Harris G, et al. Short-Period Building Collapse Performance and Recommendations for Improving Seismic Design (FEMA P-2139-4). FEFEDERAL EMERGENCY MANAGEMENT AGENCY 2020.

[56] Mazzoni S, McKenna F, Scott MH, Fenves GL. OpenSees command language manual. Pacific Earthquake Engineering Research (PEER) Center 2006;264.

[57] Shea GH. Recommended lateral force requirements and commentary. Structural Engineers Association of California; 1999.

[58] Vukobratović V, Ruggieri S. Floor Acceleration Demands in a Twelve-Storey RC Shear Wall Building. Buildings 2021;11:38.

[59] Bull DK. Understanding the complexities of designing diaphragms in buildings for earthquakes. Bulletin of the New Zealand Society for Earthquake Engineering 2004;37:70–88.

[60] Jain SK, Mandal UK. Dynamics of Buildings with V-Shaped Plan. Journal of Engineering Mechanics 1992;118:1093–112. https://doi.org/10.1061/(ASCE)0733-9399(1992)118:6(1093).

[61] Barron JM, Hueste MBD. Diaphragm effects in rectangular reinforced concrete buildings. Structural Journal 2004;101:615–24.

[62] Jain SK, Jennings PC. Analytical models for low-rise buildings with flexible floor diaphragms. Earthquake Engineering & Structural Dynamics 1985;13:225–41.

[63] Ju SH, Lin MC. Comparison of Building Analyses Assuming Rigid or Flexible Floors n.d.:7.

[64] Tremblay R, Stiemer SF. Seismic behavior of single-storey steel structures with a flexible roof diaphragm. Canadian Journal of Civil Engineering 1996;23:49–62.

[65] Fleischman RB, Farrow KT. Dynamic behavior of perimeter lateral-system structures with flexible diaphragms. Earthquake Engineering & Structural Dynamics 2001;30:745–63.

[66] Tremblay R, Rogers CA. Seismic design of low-rise steel buildings with flexible steel roof deck diaphragms – a Canadian perspective. Steel Construction 2011;4:242–50. https://doi.org/10.1002/stco.201110032.

[67] Sadashiva VK, MacRae GA, Deam BL, Spooner MS. Quantifying the seismic response of structures with flexible diaphragms. Earthquake Engineering & Structural Dynamics 2012;41:1365–89.

[68] Koliou M, Filiatrault A, Kelly DJ, Lawson JW. Numerical framework for seismic collapse assessment of rigid wall-flexible diaphragm structures. Tenth US National Conference on Earthquake Engineering: Anchorage, AK, 2014.

[69] Koliou M, Filiatrault A, Kelly DJ, Lawson J. Distributed yielding concept for improved seismic collapse performance of rigid wall-flexible diaphragm buildings. Journal of Structural Engineering 2016;142:04015137.

[70] Tremblay R, Archambault M-H, Filiatrault A. Seismic Response of Concentrically Braced Steel Frames Made with Rectangular Hollow Bracing Members. J Struct Eng 2003;129:1626–36. https://doi.org/10.1061/(ASCE)0733-9445(2003)129:12(1626).

[71] Tremblay R, Poncet L. Seismic Performance of Concentrically Braced Steel Frames in Multistory Buildings with Mass Irregularity. J Struct Eng 2005;131:1363–75. https://doi.org/10.1061/(ASCE)0733-9445(2005)131:9(1363).

[72] Speicher MS, Dukes JD, Wong KK. Collapse risk of steel special moment frames per FEMA P695. Gaithersburg, MD: National Institute of Standards and Technology; 2020. https://doi.org/10.6028/NIST.TN.2084.

[73] Roeder CW, Lumpkin EJ, Lehman DE. Seismic Performance Assessment of Concentrically Braced Steel Frames n.d.:19.

[74] Chen C-H, Mahin S. Seismic Collapse Performance of Concentrically Steel Braced Frames. Structures Congress 2010, Orlando, Florida, United States: American Society of Civil Engineers; 2010, p. 1265–74. https://doi.org/10.1061/41130(369)115.

[75] Stoakes CD, Fahnestock LA. Three-Dimensional Finite Element Simulation of the Seismic Behavior of Multitier Concentrically Braced Frames. Structures Congress 2014, Boston, Massachusetts, United States: American Society of Civil Engineers; 2014, p. 2675–86. https://doi.org/10.1061/9780784413357.234.

[76] Torabian S, Eatherton MR, Easterling WS, Hajjar JF, Schafer BW. SDII Building Archetype Design v1. 0 2017.

[77] Popov EP, Black RG. Steel struts under severe cyclic loadings. Journal of the Structural Division 1981;107:1857–81.

[78] Fell BV, Kanvinde AM, Deierlein GG, Myers AT. Experimental investigation of inelastic cyclic buckling and fracture of steel braces. Journal of Structural Engineering 2009;135:19–32.

[79] O'Brien P, Eatherton MR, Easterling WS. Characterizing the load-deformation behavior of steel deck diaphragms using past test data. 2017.

[80] Martin E. Inelastic response of steel roof deck diaphragms under simulated dynamically applied seismic loading. 2004.

[81] Essa HS, Tremblay R, Rogers CA. Behavior of roof deck diaphragms under quasistatic cyclic loading. Journal of Structural Engineering 2003;129:1658–66.

[82] Avellaneda Ramirez RE, Easterling WS, Schafer BW, Hajjar JF, Eatherton MR. Cyclic Testing of Composite Concrete on Metal Deck Diaphragms Undergoing Diagonal Tension Cracking. 12th Canadian Conference on Earthquake Engineering, 2019.

[83] Luttrell LD. Steel Deck Institute diaphragm design manual 2006.

[84] Standard AA. Building Code Requirements for Structural Concrete (ACI 318-14). American Concrete Institute, 2014.

[85] Mirghaderi R, Ahlehagh S. Effect of Reduced Brace Section on Behavior of SCBF Bracings. AIP Conference Proceedings, vol. 1020, American Institute of Physics; 2008, p. 1044–51.

[86] Richards PW. Seismic column demands in ductile braced frames. Journal of Structural Engineering 2009;135:33–41.

[87] Rai DC, Goel SC. Seismic evaluation and upgrading of chevron braced frames. Journal of Constructional Steel Research 2003;59:971–94.

[88] Flores F, Charney F, Lopez-Garcia D. The influence of gravity column continuity on the seismic performance of special steel moment frame structures. Journal of Constructional Steel Research 2016;118:217–30.

[89] Sinno RR. X-Bracing Anchorage Connection. Journal of Structural Engineering 1993;119:3360–83.

[90] Kaehler RC, White DW, Kim YD. Frame design using web-tapered members. American Institute of Steel Construction; 2011.

[91] Nethercot DA, Trahair NS. Lateral buckling approximations for elastic beams. Structural Engineer 1976;54.

[92] White DW, Jung S-K. Unified flexural resistance equations for stability design of steel I-section members: Uniform bending tests. Journal of Structural Engineering 2008;134:1450–70.

[93] White DW, Duk Kim Y. Unified flexural resistance equations for stability design of steel I-section members: Moment gradient tests. Journal of Structural Engineering 2008;134:1471–86.

[94] Hong, J.K. and Uang, C.M. Cyclic Performance Evaluation of a Metal Building System with Web-Tapered Members. Report No. SSRP-06/23, Department of Structural Engineering, University of California, San Diego; 2006.

[95] Hong, J.K. and Uang, C.M. Development of A Seismic Design Procedure for Metal Building Systems. Report No. SSRP-07/17, Department of Structural Engineering, University of California, San Diego, La Jolla, CA; 2007.

[96] Moen, C.D. Torabian, S., and Schafer, B.W. Evaluation of Metal Building System Seismic Response Modification Coefficients. NBM Technologies Report, 2019.

[97] Abaqus, G. Abaqus 6.11. Dassault Systemes Simulia Corporation, Providence, RI, USA; 2011.

[98] Sinno, R. R. X-Bracing Anchorage Connection Under Static and Seismic Loading Conditions. MBMA Final Report No. 9006, Engineering and Industrial Research Station, Mississippi State University;1992.

[99] Miller. J. R. Performance of Pre-engineered Buildings in the CA Earthquake, Metal Constr. News; 1994.

[100] Helwig, T., Yura, J. Steel bridge design handbook: Bracing system design.13; 2015.

[101] Albermani, F., Mahendran, M., and Kitipornchai, S. Upgrading of transmission towers using a diaphragm bracing system, Eng. Struct. 26(6); 2004; 735-744.

[102] Kurata, M., Leon, R. T., DesRoches, R., Nakashima, M., Steel plate shear wall with tension-bracing for seismic rehabilitation of steel frames, J. Constr. Steel Res. 71;2012; 92-103.

[103] Hsu, H.L., Juang, J. L. Performance of thin-walled box columns strengthened with internal braces, Thin-Walled Struct. 37(3);2000; 241-58.

[104] Alizadeh, S., et al. In-Plane Diaphragm Issues for Steel Buildings in Seismic Zones. 16th World Conference on Earthquake, 16WCEE. 2017.

[105] VP Buildings "Erection Drawings and Details" private communication to author; 2019.

Appendix

A1. Member Sizes of Archetype Buildings

The sizes of beams, columns, and SCBF braces of the archetype buildings are given in Table A-1, Table A-2, and Table A-3, respectively.

Table A-1 Beam Sizes of Archetype Buildings*

Archetype building	**Story**	**Longitudinal (x) direction**				**Transverse (y) direction**			
		Edge Beam			**Interior**	**Edge Beam**			**Interior**
		At SCBF	**Chord[D1]**	**Chord[D2]**	**beam**	**At SCBF**	**Collector[D1]**	**Collector[D2]**	**beam**
1-story[a]	1	14X38	14X38	14X38	12X26	12X35	12X35	14X38	14X38
1-story[b]	1	24X76	24X76	24X76	16X26	16X40	16X40	24X76	21X48
4-story	1	24X103	21X62	24X84	16X31	21X93	16X40	16X45	21X48
	2	24X94	“	“	“	21X83	“	“	21X48
	3	24X84	“	“	“	21X68	“	“	21X48
	4	24X38	14X38	16X57	12X26	14X26	14X26	14X38	14X38
8-story	1-4	24x103	16x40	24X84	16x31	21x111	21x62	18x50	21x48
	5	“	“	“	“	21x83	“	“	“
	6	24x94	“	“	“	21x73	“	“	“
	7	24x94	“	“	“	21x73	“	“	“
	8	14x38	14x26	16x77	12x26	14x26	14x38	14x38	14x38
12-story	1	24x162	21x62	24x94	16x31	21x132	16x40	18x60	12x26
	2	24x162	“	“	“	21x111	“	“	“
	3	21x131	“	“	“	“	“	“	“
	4	21x103	“	“	“	“	“	“	“
	5-8	“	“	“	“	“	“	“	“
	9	24x94	“	“	“	21x83	“	“	“
	10-11	“	“	“	“	“	“	“	“
	12	14x38	14x38	16x77	21x48	14x26	14x26	14x38	14x38

[a]: bare steel deck roof; [b]: composite deck roof ;

* All section are wide flange beams (W)

[D1] : Traditional /Rs = 2.0 or 2.5 / Rs = 3.0 Diaphragm design; [D2] : Rs = 1.0 Diaphragm design

Table A-2 Column Sizes of Archetype Buildings*

Archetype building	Story	Edge column					Interior column
		At SCBF (long x direction)	At SCBF (short y direction)		Corner	Other	
			Zipper	Outer			
1-story[a]	1	14X68	14X48	14X48	10X30	10X30	10X30
1-story[b]	1	14X68	14X68	14X68	10X30	10X30	10X30
4-story	1-2	14X159	14X176	14X132	10X33	10X39	10X49
	3-4	14X159	14X74	14X48	10X30	10X33	10X30
8-story	1-2	14x370	14x370	14x342	10x45	10x60	10x77
	3-4	14x257	14x257	14x233	10x33	10x49	10x54
	5-6	14x145	14x193	14x132	10x33	10x39	10x45
	7-8	14x68	14x68	14x48	10x30	10x33	10x30
12-story	1-2	14x605	14x665	14x665	10x60	12x87	12x120
	3-4	14x455	14x500	14x455	10x49	10x77	12x87
	5-6	14x342	14x342	14x342	10x45	10x60	10x77
	7-8	14x233	14x257	14x233	10x33	10x49	10x54
	9-10	14x143	14x145	14x132	10x33	10x39	10x45
	11-12	14x68	14x74	14x48	10x30	10x33	10x30

[a]: bare steel deck roof; [b]: composite deck roof

* All section are wide flange beams (W)

Table A-3 SCBF brace Sizes of Archetype Buildings

Archetype building	Story	Direction	
		Longitudinal (x)	Transverse (y)
1-story[a]	1	HSS 5x5x1/2	HSS 4.5x4.5x3/8
1-story[b]	1	HSS 6x6x1/2	HSS 6x6x3/8
4-story	1	HSS 10x10x5/8	HSS 10x10x5/8
	2	HSS 8x8x5/8	HSS 8x8x5/8
	3	HSS 7x7x5/8	HSS 7x7x5/8
	4	HSS 6x6x3/8	HSS 6x6x3/8
8-story	1-4	HSS 10x10x5/8	HSS 10x10x5/8
	5	HSS 10x10x5/8	HSS 8x8x5/8
	6	HSS 8x8x5/8	HSS 7x7x5/8
	7	HSS 7x7x5/8	HSS 6x6x5/8
	8	HSS 6x6x3/8	HSS 6x6x3/8
12-story	1	HSS 12x12x3/4	HSS 12x12x3/4
	2-3	HSS 12x12x3/4	HSS 10x10x5/8
	4-8	HSS 10x10x5/8	HSS 10x10x5/8
	9	HSS 8x8x5/8	HSS 8x8x5/8
	10	HSS 8x8x5/8	HSS 7x7x5/8
	11	HSS 7x7x5/8	HSS 7x7x5/8
	12	HSS 6x6x3/8	HSS 6x6x3/8

[a]: bare steel deck roof; [b]: composite deck roof

A2. Modification of Pinching4 Backbone Parameters for Diaphragm Models

The backbone parameters (stresses and strains) of the Pinching4 material model were modified as follows so that the diaphragm shear strength per unit length is consistently represented. The equations used for the modification are derived based on Figure A-1.

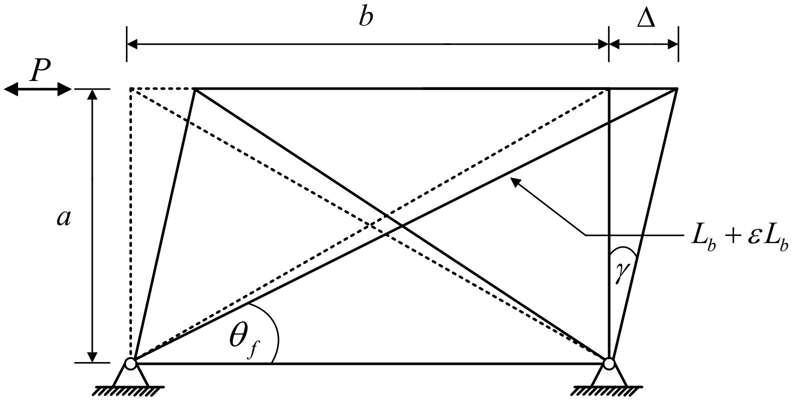

(a) Diaphragm test specimen

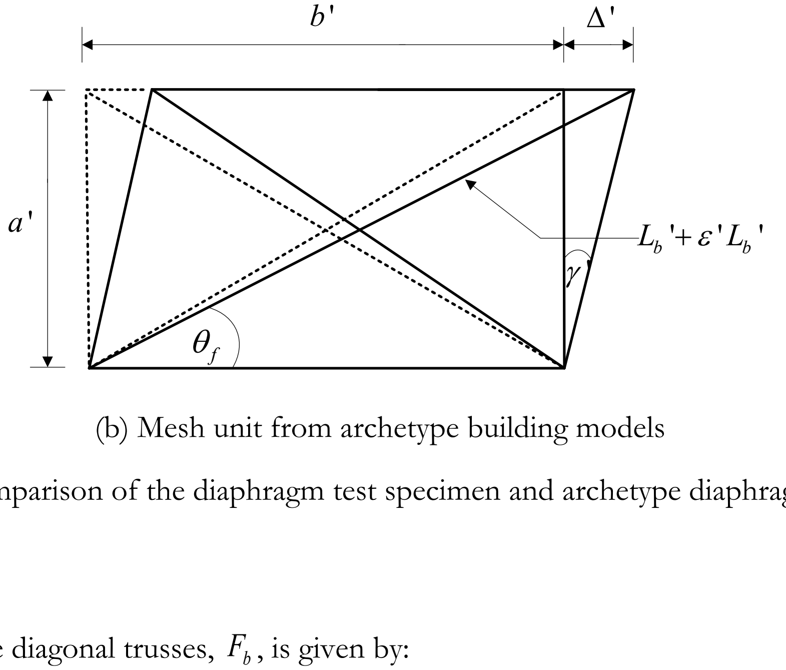

(b) Mesh unit from archetype building models

Figure A-1 Comparison of the diaphragm test specimen and archetype diaphragm mesh unit

1) Stresses

The force in the diagonal trusses, F_b, is given by:

$$F_{bi} = \sigma_i A \tag{A-1}$$

where σ is the stress in the diagonal trusses, A is the area of the diagonal trusses and i is the number ranging from 1 to 4 (corresponding to the Pinching4 stress values).

The relationship between the force, P, and F_b can be established using:

$$\cos\theta = \frac{P_i}{2F_{bi}} \tag{A-2}$$

where θ is the angle in undeformed position (initial angle) which can obtained using:

$$\theta = \tan^{-1}\left(a/b\right) \tag{A-3}$$

where b is the span of the diaphragm specimen and a is the depth of the diaphragm specimen. Substituting Equation A-2 into Equation A-1 yields:

$$P_i = 2\sigma_i A\cos\theta \tag{A-4}$$

The shear strength per unit length of the specimen, S, can be found by dividing Equation A-4 by the span of the diaphragm:

$$S_i = \frac{2}{b}\sigma_i A\cos\theta \tag{A-5}$$

Then the modified stresses for the archetype building models, σ_i', can be obtained using:

$$S_i = \frac{2}{b'}\sigma_i' A'\cos\theta' \tag{A-6}$$

$$\sigma_i' = \frac{b' S_i}{2A'\cos\theta'} \tag{A-7}$$

where b' and A' are the span of each mesh unit and the area of the diagonal trusses in the archetype building models, respectively, and θ' is the initial angle that can be obtained by:

$$\theta' = \tan^{-1}\left(a'/b'\right) \tag{A-8}$$

where a' is the depth of each mesh unit in the archetype building models.

2) Strains

The relationship between the diaphragm deflection, Δ, and the strain in the truss member, ε, can be established (based on the deformed geometry) using:

$$\cos\theta_f = \frac{b+\Delta}{L_b + \varepsilon L_b} \tag{A-9}$$

where θ_f is the angle in deformed position (final angle) and L_b is the undeformed length of the truss member which can be obtained using:

$$L_b = \sqrt{b^2 + a^2} \tag{A-10}$$

The diaphragm deflection, Δ, is given by:

$$\Delta = \gamma a \tag{A-11}$$

where γ is the shear angle. Substituting Equation A-11 into Equation A9 yields:

$$\gamma_i = \frac{1}{a}\left[\left(L_b + \varepsilon_i L_b\right)\cos\theta_f - b\right] \tag{A-12}$$

Then the modified strains for the archetype building model, ε_i', can be obtained using:

$$\gamma_i = \frac{1}{a'}\left[\left(L_b' + \varepsilon_i' L_b'\right)\cos\theta_f' - b'\right] \tag{A-13}$$

$$\varepsilon_i' = \frac{1}{L'\cos\theta_f'}\left(\gamma_i a' + b'\right) - 1 \tag{A-14}$$

where L_b' is the undeformed length of the truss member in each mesh unit in the archetype building model and all other terms were defined previously.

A3. Lognormal Cumulative Distribution Function (CDF) fitting

The median spectral acceleration at collapse initiation is $\hat{S}_{CT}$ is predicted using the lognormal cumulative function (CDF) plots developed for archetypes based on three values of collapse ratio in each hazard level. To do the fitting, minimum of unconstrained multivariable function (*fmincon*) in MATLAB is simply used to minimize the difference of three data points belongs to collapse ratios in DE-, MCE-, and ACMR$_{10\%}$-ground motion level and a lognormally distributed function. Then, $\hat{S}_{CT}$ is obtained using 50% collapse probability in lognormal CDF plots.

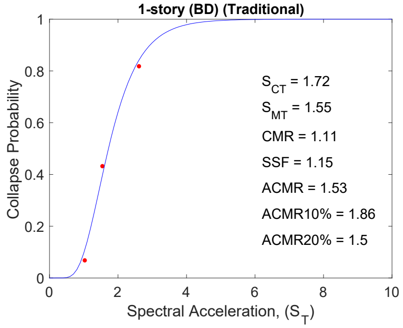
1-story (BD) (Traditional)

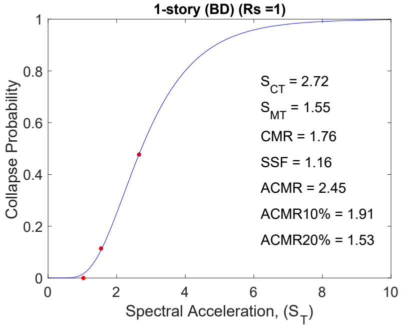
1-story (BD) (Rs =1)

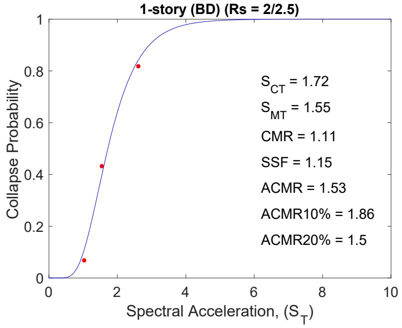
1-story (BD) (Rs = 2/2.5)

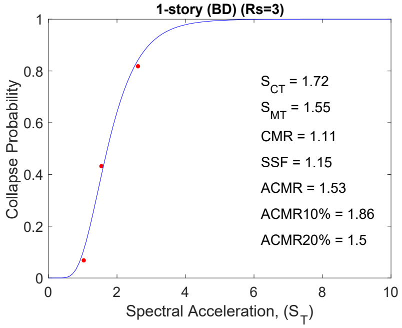
1-story (BD) (Rs=3)

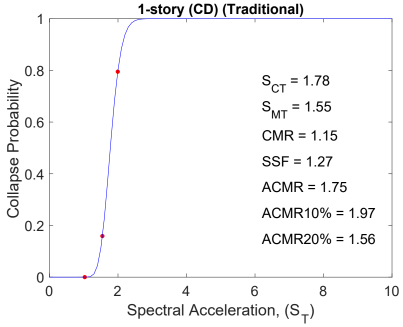
1-story (CD) (Traditional)

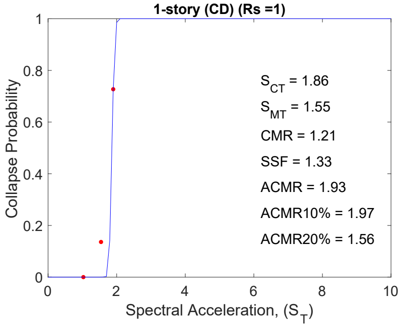
1-story (CD) (Rs =1)

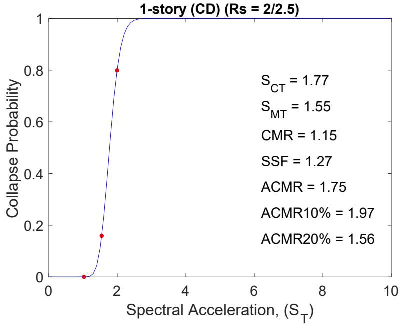
1-story (CD) (Rs = 2/2.5)

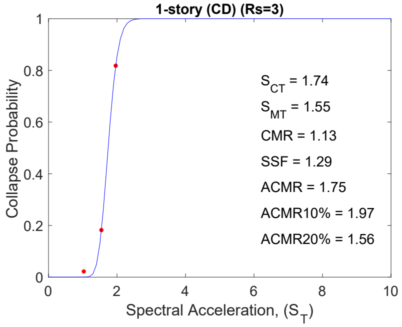
1-story (CD) (Rs=3)

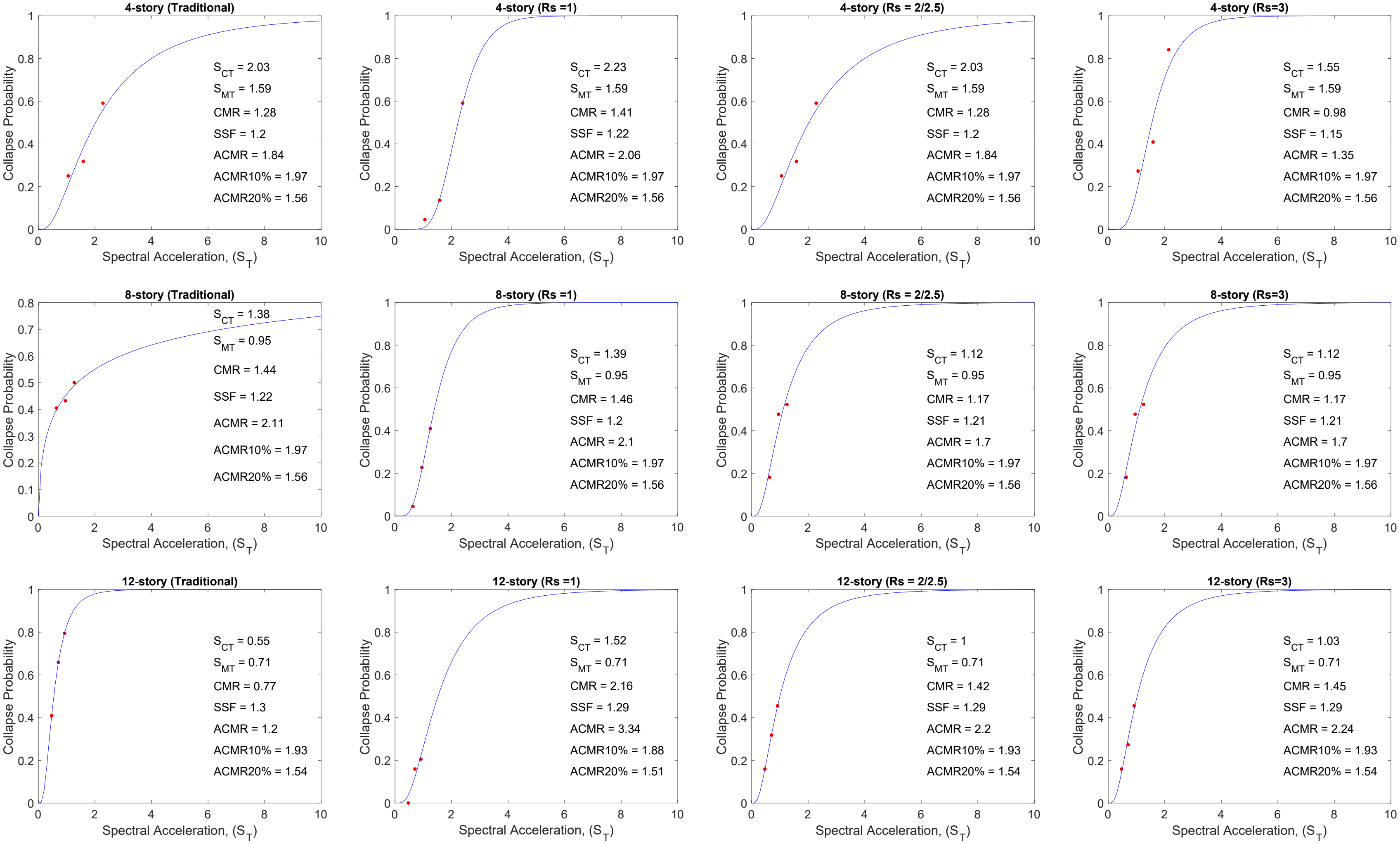
4-story (Traditional)

4-story (Rs =1)

4-story (Rs = 2/2.5)

4-story (Rs=3)

8-story (Traditional)

8-story (Rs =1)

8-story (Rs = 2/2.5)

8-story (Rs=3)

12-story (Traditional)

12-story (Rs =1)

12-story (Rs = 2/2.5)

12-story (Rs=3)

Figure A-2 Lognormal CDF plots for all the archetype buildings with different diaphragm design

A4. Median of Peak Story Drifts and Diaphragm Shear Demands

Table A-4 and Table A-5 provide details for the medians of peak story drifts and diaphragm shear demands of the archetype buildings from the nonlinear response history results.

Table A-4 Medians of Peak Story Drifts at Each Story of Archetype Buildings under Three Ground Motion Levels

Archetype Building	Diaphragm Design	Story	Median of Peak Story Drift at Each Story (%)								
			DE			MCE			$ACMR_{10\%}$		
			x	y	Result.	x	y	Result.	x	y	Result.
1-story[a]	R_s = 1.0	1	1.8	2.0	2.4	2.1	4.1	4.4	6.3	6.4	6.5
	Trad. / R_s = 1.0 / R_s = 2.0 / R_s = 3.0	1	1.7	2.2	2.6	2.3	4.4	4.7	7.1	8.1	8.2
1-story[b]	R_s = 1.0	1	1.7	2.1	2.7	3.7	4.3	5.1	8.0	8.1	8.3
	Trad.	1	1.8	2.5	3.0	4.1	5.2	5.9	9.9	14	15
	R_s = 2.5	1	1.8	2.5	3.0	4.1	5.1	5.9	9.9	14	15
	R_s = 3.0	1	1.9	2.5	3.5	4.3	5.9	6.1	13	21	25
4-story	R_s = 1.0	1	1.1	1.2	1.4	2.1	2.6	3.1	2.0	2.5	3.1
		2	1.2	1.3	1.2	2.0	2.3	2.5	2.1	2.6	2.6
		3	1.4	1.6	1.8	1.7	1.9	2.1	2.5	2.3	2.7
		4	1.1	1.2	1.4	1.5	3.1	3.4	2.2	3.0	4.1
		whole building	1.1	1.2	1.4	1.6	2.3	2.5	2.1	2.3	3.6
	Trad. / R_s = 2.0* or 2.5**	1	1.2	1.5	1.9	2.5	2.9	3.4	2.2	2.6	3.5
		2	1.3	1.4	1.8	2.0	2.3	2.8	2.1	2.9	2.3
		3	1.4	1.6	1.9	1.7	1.9	2.3	2.7	2.5	2.8
		4	1.6	4.6	4.7	2.0	5.5	5.6	3.5	5.4	5.9
		whole building	1.3	1.6	1.9	2.0	2.6	3.1	3.9	4.6	5.6
	R_s = 3.0	1	1.3	1.5	1.8	2.5	2.7	3.3	2.4	3.0	3.4
		2	1.2	1.4	1.7	2.1	2.3	2.8	2.3	2.5	2.8
		3	1.4	1.6	1.8	1.8	2.0	2.3	2.5	2.3	3.4
		4	2.2	6.5	6.7	2.6	8.7	9.7	8.9	9.0	13.0
		whole building	1.4	1.5	1.8	2.3	2.5	3.0	4.5	4.2	6.1
8-story	R_s = 1.0	1	2.2	2.0	2.8	2.4	2.5	2.9	2.6	2.9	3.2
		2	1.8	1.6	2.4	2.5	2.5	2.8	2.6	2.4	2.6
		3	1.1	1.0	1.4	2.0	1.6	2.3	2.4	2.4	2.5
		4-6	1.0-1.1	0.9-1.6	1.2-1.7	1.2-1.4	1.1-1.8	1.4-2.2	1.8-1.9	1.4-1.8	1.8-2.6
		7	1.2	2.1	2.2	1.6	2.5	2.8	2.1	2.5	3.7
		8	1.2	1.7	2.0	1.7	2.1	2.6	2.2	2.3	3.1
		whole building	1.2	1.6	1.8	1.7	2.0	2.5	2.2	2.4	3.1
	Trad.	1	2.1	2.0	2.8	2.4	3.2	3.3	3.1	3.2	3.3
		2	1.8	1.6	2.4	2.5	2.5	2.6	2.7	2.4	2.6
		3	1.1	1.0	1.4	2.0	1.7	2.4	2.8	2.4	3.5
		4-6	1.0-1.1	0.9-1.5	1.1-1.7	1.2-1.4	1.1-1.8	1.4-2.2	1.4-1.8	1.4-1.8	1.9-2.6
		7	1.2	2.1	2.2	1.7	2.5	2.8	2.1	2.5	3.7
		8	1.2	1.8	2.0	1.7	2.2	2.5	2.2	2.3	3.1
		whole building	1.1	1.6	1.9	1.7	1.7	2.4	2.1	2.3	3.3
	R_s = 2.0* or 2.5** / R_s = 3.0	1	2.2	1.8	3.0	2.4	3.0	3.2	2.8	2.9	3.3
		2	1.8	1.6	2.5	2.5	2.4	2.6	2.3	2.5	2.5
		3	1.2	1.1	1.6	2.2	1.9	2.4	2.9	2.4	2.3
		4-6	1.0-1.2	1.0-1.4	1.3-1.6	1.2-1.5	1.3-1.5	1.6-2.0	1.4-1.7	2.3-1.6	1.8-2.3
		7	1.3	2.3	2.4	1.7	2.6	3.2	2.0	2.4	3.7
		8	1.5	3.6	3.7	2.1	4.2	4.5	2.5	4.8	6.2

		whole building	1.2	1.5	2.0	1.9	2.3	2.8	2.2	2.5	3.5
12-story	$R_s = 1.0$	1	1.0	1.2	1.3	1.6	2.0	2.3	2.4	2.7	3.4
		2	0.9	1.1	1.4	1.4	2.0	2.2	2.0	2.5	3.1
		3	0.8	1.4	1.5	1.2	2.0	2.1	1.6	2.5	2.8
		4	1.3	1.4	1.9	1.8	2.0	2.4	1.9	2.5	2.8
		5-10	1.4-1.5	1.2-1.5	1.7-2.0	1.9-2.3	1.3-1.9	2.1-2.5	1.8-2.3	1.4-2.0	2.2-2.8
		11	1.5	1.5	1.9	1.9	1.8	2.4	1.9	1.8	2.7
		12	1.4	1.3	1.7	1.7	1.5	2.0	1.8	1.7	2.5
		whole building	1.5	1.3	1.8	1.9	2.0	2.3	2.1	1.8	2.1
	Trad.	1	1.0	1.2	1.3	1.7	2.0	2.3	2.6	3.1	4.2
		2	0.9	1.3	1.5	1.5	2.1	2.2	2.4	3.0	4.0
		3	0.9	1.3	1.5	1.2	1.9	2.2	1.7	2.8	3.3
		4	1.3	1.4	1.9	1.7	2.1	2.4	2.3	2.7	3.3
		5-10	1.4-1.5	1.1-1.5	1.5-2.0	1.8-2.2	1.4-2.0	2.0-2.5	2.2-2.6	1.5-2.2	2.5-3.3
		11	1.5	1.8	2.0	1.9	2.2	2.5	2.0	2.4	2.8
		12	2.3	5.1	5.2	2.6	7.0	8.0	3.0	9.0	9.9
		whole building	1.5	1.3	1.8	1.9	2.0	2.4	2.4	2.3	3.2
	$R_s = 2.0$* or 2.5** / $R_s = 3.0$	1	1.0	1.2	1.4	1.6	2.0	2.3	2.6	2.8	3.6
		2	0.8	1.3	1.4	1.4	2.1	2.3	2.4	2.7	3.6
		3	0.8	1.3	1.5	1.2	2.0	2.2	1.7	2.6	3.0
		4	1.3	1.4	1.8	1.7	2.1	2.3	2.3	2.4	3.1
		5-10	1.3-1.6	1.2-1.4	1.7-2.0	1.7-2.1	1.4-2.0	2.1-2.6	2.2-2.7	1.8-2.2	2.0-3.0
		11	1.5	1.6	2.0	1.9	2.0	2.5	1.9	2.1	2.8
		12	1.6	3.1	3.2	2.0	3.7	3.8	2.0	4.5	4.6
		whole building	1.5	1.3	1.8	1.8	2.0	2.3	2.3	2.2	3.0

^{a}: bare steel deck roof; ^{b}: composite deck roof

*: $R_s = 2.0$ with concrete-filled steel deck; **: $R_s = 2.5$ with bare steel deck (roof)

Table A-5 Medians of Diaphragm Shear Demands for Archetype Buildings and Comparison to Design Shear

Archetype Building	Diaphragm Design	Story	Median of F_{peak} (kip)									F_{px} (kip)	$\frac{F_{peak}}{F_{px}}$
			DE			MCE			ACMR$_{10\%}$				
			x	y	x or y	x	y	x or y	x	y	x or y		
1-story[a]	R_s = 1.0	1	203	281	285	247	350	351	273	399	403	419	0.68
	Trad. / R_s = 1.0 / R_s = 2.0 / R_s = 3.0	1	292	358	361	374	419	424	396	450	468	262	1.38
1-story[b]	Trad.	1	341	616	618	461	718	720	483	809	812	542	1.14
	R_s = 1.0	1	368	699	702	498	809	810	513	898	901	867	0.81
	R_s = 2.5	1	343	622	623	459	719	722	481	809	813	542	1.15
	R_s = 3.0	1	350	634	656		726	742	501	812	833	542	1.21
4-story	R_s = 1.0	1	876	968	995	1061	1227	1207	1191	1258	1252	1060	0.93
		2	922	1008	1024	1051	1172	1225	1089	1188	1270	1070	0.95
		3	781	812	829	835	903	1003	1093	926	1051	1080	0.76
		4	810	828	831	857	865	865	861	990	996	823	1.01
	Trad. / R_s = 2.0** or 2.5**	1	592	731	749	895	953	964	900	991	1012	524	1.43
		2	548	667	697	784	874	895	903	941	978	532	1.31
		3	716	783	800	931	957	961	943	1001	1021	630	1.27
		4	553	568	573	586	601	602	696	727	732	377	1.52
	R_s = 3.0	1	638	757	791	787	981	1010	849	1027	1091	524	1.51
		2	631	745	770	782	899	940	890	957	1020	524	1.47
		3	610	655	744	710	772	825	729	765	851	524	1.42
		4	386	399	420	406	432	436	411	443	444	274	1.53
8-story	R_s = 1.0	1	621	782	820	911	1051	1153	1008	1181	1281	1012	0.81
		2	991	716	862	923	997	1130	1012	1193	1303	980	0.88
		3	631	691	777	879	954	1001	971	1013	1103	948	0.82
		4	680	739	760	742	861	873	881	934	958	916	0.83
		5	532	632	698	631	745	775	654	778	801	883	0.79
		6	591	640	647	668	691	726	619	695	731	851	0.79
		7	871	901	929	857	998	1039	994	1087	1123	1272	0.73
		8	851	862	884	861	888	888	854	871	896	982	0.90
	Trad.	1	792	873	902	912	1087	1246	969	1398	1461	524	1.72
		2	707	781	812	881	921	1074	1074	1186	1233	524	1.55
		3	681	697	770	861	902	985	991	1001	1123	524	1.47
		4	657	711	734	834	881	893	870	912	963	524	1.40
		5	601	675	697	731	761	811	797	834	861	524	1.33
		6	623	678	686	684	701	767	673	694	781	524	1.31
		7	661	689	718	703	746	795	695	787	804	524	1.37
		8	431	462	475	431	486	503	423	480	501	273	1.74
	R_s = 2.0* or 2.5** / R_s = 3.0	1	901	931	965	1119	1254	1312	1321	1411	1503	524	1.84
		2	798	840	844	965	1070	1101	1033	1111	1267	524	1.61
		3	680	751	786	823	967	1000	923	1020	1120	524	1.50
		4	701	759	791	811	865	901	873	900	971	524	1.51
		5	598	634	702	687	759	781	798	821	836	524	1.34
		6	591	634	686	638	716	771	687	745	791	524	1.31
		7	632	681	723	702	751	801	723	788	813	524	1.38
		8	583	610	612	613	637	641	628	634	644	327	1.87
12-story	R_s = 1.0	1	813	903	932	1006	1273	1309	1203	1494	1589	1024	0.91
		2	796	907	943	999	1023	1289	1118	1390	1551	1003	0.94
		3	693	789	853	923	1087	1211	1087	1280	1533	981	0.87
		4	700	781	844	890	982	1075	1011	1131	1221	959	0.88
		5	673	701	788	791	862	932	871	923	1046	938	0.84
		6	598	673	787	678	793	837	796	899	1024	916	0.86
		7	599	683	743	701	800	893	789	832	946	895	0.83
		8	634	710	768	693	789	874	707	801	900	873	0.88
		9	534	593	672	616	721	759	597	712	798	851	0.79
		10	598	693	770	617	758	878	626	763	891	1054	0.73
		11	834	998	1108	923	1003	1178	956	1011	1188	1560	0.71
		12	894	973	990	988	995	996	981	997	998	1032	0.96

	Trad.	1	853	972	1001	1101	1283	1323	1346	1523	1723	524	1.91
		2	859	934	964	1009	1111	1273	1288	1467	1653	524	1.84
		3	785	891	949	953	1045	1231	1076	1233	1534	524	1.81
		4	631	788	891	831	962	1120	989	1112	1311	524	1.70
		5	630	743	854	762	801	996	923	1050	1101	524	1.63
		6	611	711	812	721	805	970	714	850	991	524	1.55
		7	617	717	822	619	713	918	681	791	963	524	1.57
		8	512	678	755	517	695	849	518	699	921	524	1.44
		9	512	673	702	513	691	769	513	791	873	524	1.34
		10	493	588	697	523	631	746	555	653	777	524	1.33
		11	563	682	712	571	687	732	577	700	764	524	1.36
		12	476	481	490	480	485	493	482	488	492	262	1.87
	R_s = 2* or 2.5** / R_s = 3.0	1	865	909	969	963	1013	1286	1101	1346	1603	524	1.85
		2	791	880	943	899	1007	1212	988	1233	1489	524	1.80
		3	720	832	928	741	990	1173	966	1100	1346	524	1.77
		4	688	781	891	699	902	1043	887	1003	1247	524	1.70
		5	641	747	807	650	841	943	696	991	1094	524	1.54
		6	601	738	802	633	798	936	645	803	998	524	1.53
		7	587	686	739	613	731	861	633	773	937	524	1.41
		8	555	660	713	581	693	761	594	706	843	524	1.36
		9	544	618	681	546	700	749	557	697	787	524	1.30
		10	549	660	686	570	675	723	581	731	779	524	1.31
		11	550	652	666	589	669	701	599	691	735	524	1.27
		12	599	613	623	602	617	633	621	634	641	344	1.81

[a]: bare steel deck roof; [b]: composite deck roof

*: R_s = 2.0 with concrete-filled steel deck; **: R_s = 2.5 with bare steel deck (roof)